Hämäläinen, M.; Hari, R.; Ilmoniemi, Risto; Knuutila, J.; Lounasmaa, O.V.

# Magnetoencephalography - theory, instrumentation, and applications to noninvasive studies of the working human brain

*Published in:*
Reviews of Modern Physics

*DOI:*
10.1103/RevModPhys.65.413

Published: 01/01/1993

*Document Version*
Publisher's PDF, also known as Version of record

# Magnetoencephalography—theory, instrumentation, and applications to noninvasive studies of the working human brain

Matti Hämäläinen, Riitta Hari, Risto J. Ilmoniemi, Jukka Knuutila, and Olli V. Lounasmaa

*Low Temperature Laboratory, Helsinki University of Technology, 02150 Espoo, Finland*

Magnetoencephalography (MEG) is a noninvasive technique for investigating neuronal activity in the living human brain. The time resolution of the method is better than 1 ms and the spatial discrimination is, under favorable circumstances, 2–3 mm for sources in the cerebral cortex. In MEG studies, the weak 10 fT–1 pT magnetic fields produced by electric currents flowing in neurons are measured with multichannel SQUID (superconducting quantum interference device) gradiometers. The sites in the cerebral cortex that are activated by a stimulus can be found from the detected magnetic-field distribution, provided that appropriate assumptions about the source render the solution of the inverse problem unique. Many interesting properties of the working human brain can be studied, including spontaneous activity and signal processing following external stimuli. For clinical purposes, determination of the locations of epileptic foci is of interest. The authors begin with a general introduction and a short discussion of the neural basis of MEG. The mathematical theory of the method is then explained in detail, followed by a thorough description of MEG instrumentation, data analysis, and practical construction of multi-SQUID devices. Finally, several MEG experiments performed in the authors' laboratory are described, covering studies of evoked responses and of spontaneous activity in both healthy and diseased brains. Many MEG studies by other groups are discussed briefly as well.

## CONTENTS

## I. INTRODUCTION

### A. General comments

The human brain is the most complex organized structure known to exist, and, for us, it is also the most important. There are at least $10^{10}$ neurons in the outermost layer of the brain, the cerebral cortex. These cells are the active units in a vast signal handling network, which includes $10^{14}$ interconnections or synapses. When information is being processed, small currents flow in the neural system and produce a weak magnetic field which can be measured noninvasively by a SQUID magnetometer, placed outside the skull, provided that thousands of nearby neurons act in concert. This relatively novel method of recording, called magnetoencephalography (MEG), has already produced several pieces of new information about the functioning of the human brain, and it is expected that MEG will become increasingly more important in the near future as clinical applications emerge. In many MEG measurements, an area in the brain that has been activated by a stimulus, such as a sound or a picture, can be located by analyzing the detected magnetic fields. A typical signal, evoked by a tone burst, is shown in Fig. 1. In addition, spontaneous brain activity has also been studied successfully.

In this introduction, we shall briefly consider the basics of magnetoencephalography. Section II of this review explains the neuronal basis of MEG. In Secs. III and IV we discuss the theory of the method in detail. Section V contains a thorough description of SQUID instrumentation as applied to magnetoencephalographic measurements. Finally, in Sec. VI, we present several illustrative examples of our own MEG studies and review briefly some of the work from other laboratories.

The MEG method is based on the superconducting quantum interference device or SQUID, a sensitive detector of magnetic flux, introduced in the late 1960s by James Zimmerman (Zimmerman *et al.*, 1970). The first SQUID measurement of magnetic fields of the brain was carried out at the Massachusetts Institute of Technology by David Cohen (Cohen, 1972). He measured the spontaneous $\alpha$ activity of a healthy subject and the abnormal brain activity of an epileptic patient. Evoked responses were first recorded a few years later (Brenner *et al.*, 1975; Teyler *et al.*, 1975).

SQUID magnetometers are used also in studies of magnetic fields emanating from several other organs of the human body, notably the heart. The whole area of research is referred to as biomagnetism. In the context of estimating the distribution of electrical sources within

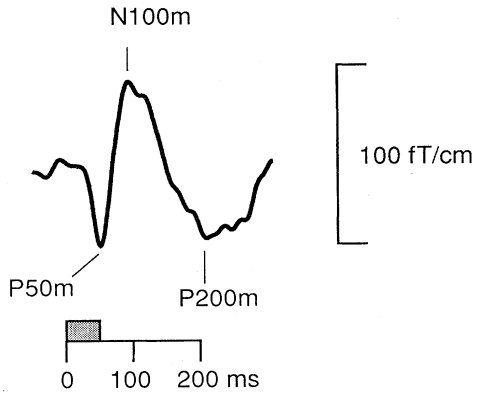


FIG. 1. Typical magnetic response as a function of time, measured close to the subject's auditory cortex. The signal was evoked by a 50-ms tone, illustrated by the hatched bar on the time axis. 150 single responses were averaged. The signal consists of the following parts: a small deflection (P50m) at about 50 ms after the stimulus onset, a prominent peak (N100m) at 100 ms, and yet another peak (P200m) at about 200 ms. *P* indicates that the corresponding deflection in electric potential (EEG) measurements is positive at the top of the head; *N*, that it is negative; and *m* refers to "magnetic."

the body, these studies are often called magnetic source imaging (MSI), and sometimes magnetic-field tomography or current-flow imaging.

Present understanding of brain functions is based mainly on experiments using small mammals. Spontaneous neural activity can be recorded by microelectrodes inserted into well-defined brain areas. These sites may also be stimulated selectively. The effects of brain damage on behavior and on the cerebral electrical activity of the animal also provide important information. Although extremely useful, animal models can never substitute for studies on humans when functions characteristic to man are of interest. Human brain activity may be recorded directly during surgery on patients suffering from drug-resistant epilepsy or cerebral tumors. However, for ethical reasons, such studies are restricted to small areas in the vicinity of the damaged tissue.

Exploration of the human brain is of the utmost intellectual interest: the whole humanity depends on our minds. Although a great deal has been learned about cerebral anatomy and physiology, the fundamental question of how the brain stores, retrieves, and processes information is still largely unknown. Neural computers, which will handle information in a way similar to the brain, are becoming useful tools of analysis and decision making. Recent developments in this new field of computing (Kohonen, 1988, 1990) are thus an important source of inspiration for studies of the functional principles applied by the human brain and vice versa. In addition, many interesting questions in basic and clinical neuroscience can be investigated by magnetoencephalography.

The main emphasis in MEG recordings so far has been on basic research. Clinical applications are now in their early stages of development. To understand the dynamics of brain activity, one can monitor the temporal and spatial changes in the active cortical areas. It is also possible to study in detail the reactivity of various brain regions to changes in the stimulus sequence. Responses to speech sounds form an especially interesting branch of research. Language is a typically human function, and the complete noninvasiveness of MEG allows studies of brain mechanisms associated with speech production and perception in healthy persons under a wide variety of conditions.

Many important imaging methods of the human brain are available today (Pechura and Martin, 1991). Anatomical structures can now be investigated precisely by means of computer-assisted x-ray tomography (CAT; see Lauterbur, 1973 and Hinz, 1988) and by magnetic-resonance imaging (MRI; see Damadian, 1972, Lauterbur, 1973, and Hinshaw and Lent, 1983). Both these techniques provide high-quality but static pictures of living tissues. Functional information about the brain can be obtained with single-photon-emission computed tomography (SPECT; Knoll, 1983) and with positron-emission tomography (PET; see ter-Pogossian *et al.*, 1975, Kessler *et al.*, 1987, and Jaszczak, 1988). A newly developed echo-planar technique allows functional imaging with MRI as well, with one-second time resolution (Belliveau *et al.*, 1991; Stehling *et al.*, 1991; Ogawa *et al.*, 1992). All these methods permit studies of the brain without opening the skull, but the subject is exposed to x rays, to radioactive tracers, or to time-varying and strong static magnetic fields.

Electroencephalography (EEG), the measurement of electric potential differences on the scalp, is a widely applied method of long clinical standing. MEG is closely related to EEG. In both methods, the measured signals are generated by the same synchronized neuronal activity in the brain. The time resolution of MEG and EEG is in the millisecond range, orders of magnitude better than in the other methods mentioned above. Thus with MEG and EEG it is possible to follow the rapid changes in cortical activity that reflect ongoing signal processing in the brain; the electrical events of single neurons typically last from one to several tens of milliseconds.

A very important advantage of MEG and EEG is that they are completely noninvasive. One only measures brain activity as a result of sensory stimuli such as sounds, touch, or light, or even when no stimuli are given. The very rapid development of the MRI technique has provided an ideal medium for linking the functional MEG information to anatomical data. Several groups are now working towards routine use of magnetic-resonance images in conjunction with MEG.

The interested reader may wish to consult other review articles or books. The September 1979 and 1992 issues of Scientific American are devoted to brain research. The books by Kuffler *et al.* (1984), Kandel and Schwartz (1991), and Thompson (1985) are general introductions to the human brain; the text by Thompson is, in particular, to be recommended for physicists. The books edited by Williamson *et al.* (1983), Grandori *et al.* (1990), and by Sato (1990) are more specialized treatises on biomagnetism and magnetoencephalography. Review articles on MEG have been written, for example, by Williamson and Kaufman (1981, 1989), Romani *et al.* (1982), Hari and Ilmoniemi (1986), Romani and Narici (1986), Hoke (1988), Hari and Lounasmaa (1989), and by Hari (1990, 1991). Specialized information is available in the proceedings of international conferences on biomagnetism, edited by Erné, Hahlbohm, and Lübbig (1981), Romani and Williamson (1983), Weinberg *et al.* (1985), Atsumi *et al.* (1988), Williamson *et al.* (1989), and by Hoke *et al.* (1992).

Magnetocardiography (MCG) is methodologically closely related to MEG: instead of the brain, the heart is being investigated (Nenonen and Katila, 1991a, 1991b; Nenonen *et al.*, 1991). Much of the theory and practice of MEG, discussed in Secs. III, IV, and V of this review, applies to MCG as well. However, the volume conductor geometry is much more complicated for the thorax than for the head, whereas the brain is functionally far more complicated than the heart. New uses of multi-SQUID devices are to be expected now that more reliable and higher-sensitivity sensors have become available, and at a lower cost than before (Ryhänen *et al.*, 1989). For exam-

ple, geomagnetic instruments (for reviews, see Clarke, 1983 and Ilmoniemi *et al.*, 1989) and magnetic monopole detectors (Cabrera, 1982; Tesche *et al.*, 1983) have been used for some time already.

### B. The human brain

Figure 2 is a drawing of the human brain viewed from the left side, with some of the anatomical features identified. In MEG one is usually concerned with the uppermost layer of the brain, the cerebral cortex, which is a 2–4 mm thick sheet of gray tissue. The cortex has a total surface area of about 2500 $cm^2$, folded in a complicated way, so that it fits into the cranial cavity formed by the skull. The brain consists of two hemispheres, separated by the longitudinal fissure. The left and right halves, in turn, are divided into lobes by two deep grooves. The Rolandic fissure runs down the side of both hemispheres, while the Sylvian fissure is almost horizontal. There are four lobes in both halves of the cortex: frontal, parietal, temporal, and occipital.

Most regions of the cortex have been mapped functionally. For example, the primary somatosensory cortex S1, which receives tactile stimuli from the skin, is located posterior to the Rolandic fissure. The area in the frontal lobe just anterior to the Rolandic fissure contains neurons concerned with integration of muscular activity: each site of the primary motor cortex (M1) is involved in the movement of a specific part of the body. Figure 3 illustrates representations of the body surface on S1 and M1 (Penfield and Rasmussen, 1950); large areas of cortex are devoted to those body parts which are most sensitive to touch (e.g., lips) or for which accurate control of movement is needed (fingers). S1 and M1 on the left side of the brain monitor and control the right side of the body and vice versa.

The primary auditory cortex (A1) is in the temporal lobe buried within the Sylvian fissure, while the primary visual cortex (V1) is in the occipital lobe at the back of the head. Most of the remaining regions are known as association areas; they respond in a more complex way to external stimuli.

### C. Basics of magnetoencephalography

A sensory stimulus initially activates a small portion of the cortex. This process is associated with a primary current source related to the movement of ions due to their chemical concentration gradients (see Sec. II). In addition, passive ohmic currents are set up in the surrounding medium. This so-called volume current completes the loop of ionic flow so that there is no buildup of charge. The magnetic field is generated by both the primary and the volume currents. Figure 4(a) illustrates a localized source, approximated by a current dipole, the returning volume currents, and the magnetic-field lines around the dipole.

If the primary source and the surrounding conductivi-

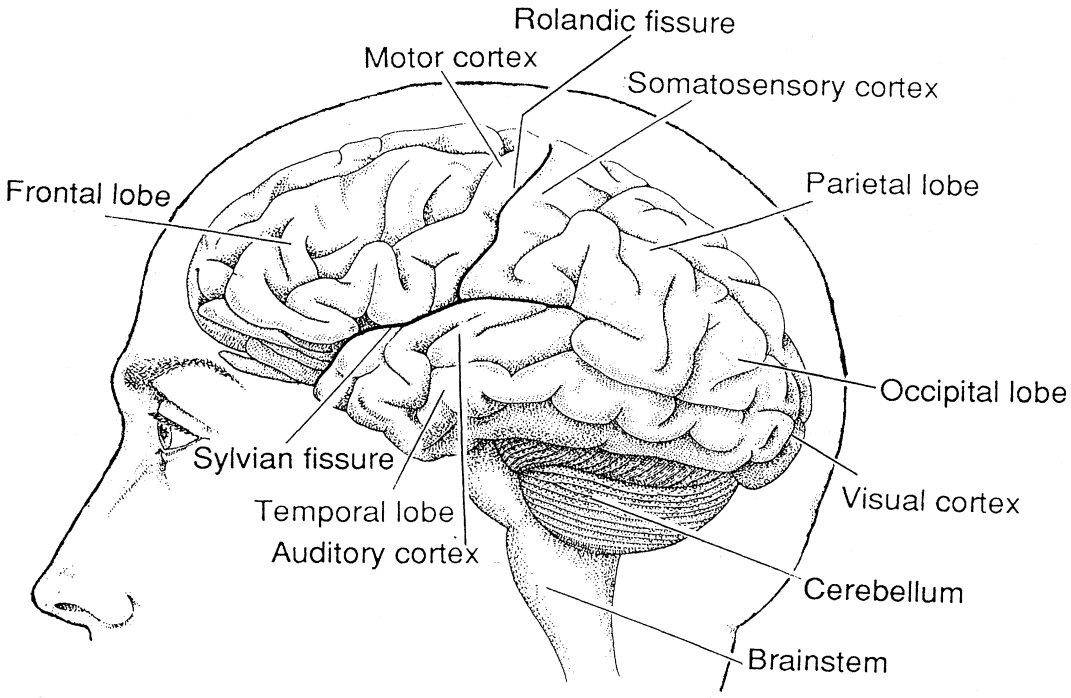


FIG. 2. Human brain seen from the left side. Some of the important structural landmarks and special areas of the cerebral cortex are indicated.

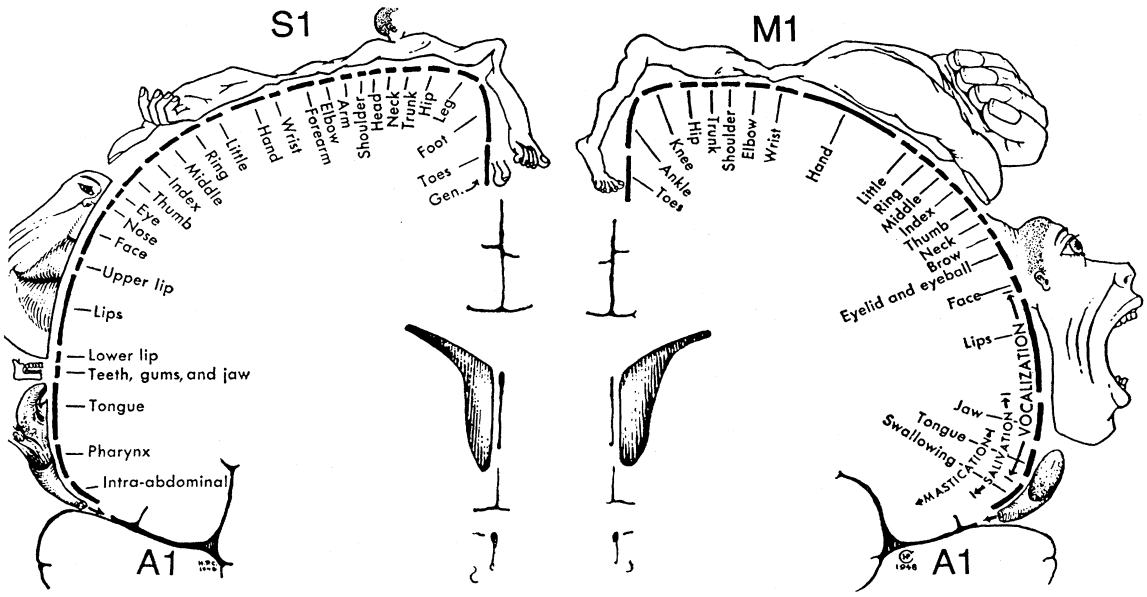


FIG. 3. Representations of different body parts on the somatosensory (S1) and motor (M1) cortices. These "homunculi" are based on direct cortical stimulation of awake humans during brain surgery. The picture illustrates a transsection of the brain in a plane parallel to the face [see Fig. 13(a)]. The two halves are separated by the longitudinal fissure, which has been widened here for clarity. The locations of the left and right primary auditory cortices A1 in the upper surface of the temporal lobe are shown as well. Modified from Penfield and Rasmussen (1950).

ty distribution are known, the resulting electric potential (EEG) and magnetic field (MEG) can be calculated from Maxwell's equations. This forward problem will be discussed in Sec. III. Figure 5 illustrates the magnetic- and electric-field patterns due to a current dipole in a spherical head model. It follows from the linearity of Maxwell's equations that once we possess the solution for the elementary current dipole, the fields of more complex sources can be obtained readily by superposition.

In certain finite conductor geometries the volume current causes an equal but opposite field to that generated by the primary current. The net external field is then zero. For example, only currents that have a component tangential to the surface of a spherically symmetric conductor produce a magnetic field outside; radial sources are thus externally silent. Therefore, MEG measures mainly activity from the fissures of the cortex, which often simplifies interpretation of the data. Fortunately, all primary sensory areas of the brain—auditory, soma-

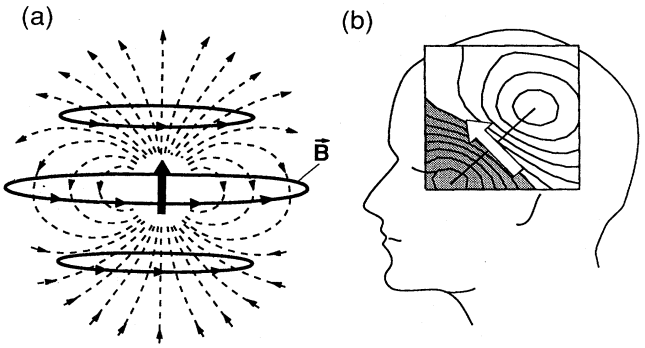


FIG. 4. Magnetic field of a current dipole. (a) Current dipole (large arrow) in a homogeneous conducting medium. Examples of volume currents (dashed curves) and magnetic-field lines **B** (solid curves) produced by the primary current are shown as well. (b) Example of the topographic field map calculated from the measured MEG signals. The simple geometrical construction for locating the equivalent current dipole in the brain is also illustrated: the dipole is midway between the field extrema (compare with Fig. 5).

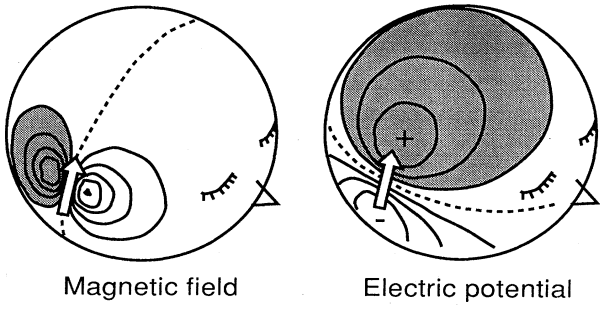


FIG. 5. Schematic illustration of idealized magnetic-field and electric-potential patterns produced by a tangential dipole (white arrow). The head was approximated with a four-compartment sphere consisting of the brain, the cerebrospinal fluid, the skull, and the scalp. From noninvasive measurements of the MEG or EEG field distributions, the active area in the brain can be determined by a least-squares fit to the data.

tosensory, and visual—are located within fissures.

In interpreting MEG and EEG data, one is dealing with the electromagnetic inverse problem, i.e., with the deduction of the source currents responsible for the externally measured field. Hermann von Helmholtz showed in 1853 that this problem has no unique solution. One must, therefore, use source models, such as current dipoles, or special estimation techniques to interpret the data (see Sec. IV).

The current dipole is a popular source model in MEG research. It is used to approximate the flow of electrical current in a small area. A typical strength of a dipole, caused by the synchronous activity of probably tens of thousands of neurons, is 10 nA m.

For a single current-dipole source, the map of the radial magnetic field $B_r$ has one maximum and one minimum. The dipole is halfway between the field extrema, at a right angle to the line joining them (see Fig. 5). Figure 4(b) illustrates a typical topographic field distribution. The magnitude, direction, and position of the source can be deduced unambiguously from the map (Williamson and Kaufman, 1981; Romani *et al.*, 1982a), provided that the dipolar assumption is valid, i.e., the source currents are limited to a small region of the brain.

In practice the optimal solution is found by fitting the theoretical and measured field patterns in the least-squares sense. The outcome of this procedure is commonly called the equivalent current dipole (ECD; see Sec. IV.G).

Figure 5 shows that the MEG and EEG field distributions are mutually orthogonal. Data obtained by these two techniques complement each other, and both methods have their own advantages. In determining the locations of source activity in the brain, MEG has better spatial accuracy than EEG, a few millimeters under favorable conditions (see Sec. IV.D). This is because electrical potentials measured on the scalp are often strongly influenced by various inhomogeneities in the head, making accurate determination of the activated area difficult. The magnetic field, in contrast, is mainly produced by currents that flow in the macroscopically relatively homogeneous intracranial space. Because of the poor electrical conductivity of bone, the irregular currents in the skull and on the scalp are weak and can be ignored as contributors to the external magnetic field.

### D. Detection of neuromagnetic fields

Neuromagnetic signals are typically 50–500 fT, one part in $10^9$ or $10^8$ of the earth's geomagnetic field. The only detector that offers sufficient sensitivity for the measurement of these tiny fields is the SQUID (Lounasmaa, 1974; Ryhänen *et al.*, 1989), schematically illustrated in Fig. 6. The SQUID is a superconducting ring, interrupted by one or two Josephson (1962) junctions. These weak links limit the flow of the supercurrent and are characterized by the maximum critical current $I_c$ that can be sustained without loss of superconductivity. dc SQUIDs,

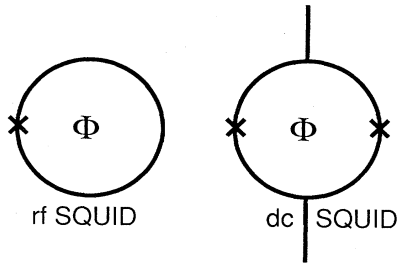


FIG. 6. Schematic illustration of an rf and a dc SQUID. The Josephson (1962) junctions are indicated by crosses. The magnetic flux Φ threads the superconducting loop of the SQUID, changing the impedance around (rf SQUID) or across (dc SQUID) the loop. This can be detected (dc SQUID) by feeding a current and measuring the voltage or (rf SQUID) by inductive coupling (see Sec. V.D).

with two junctions, are preferred, because the noise level is lower in them than in rf SQUIDs (Clarke, 1966; Clarke *et al.*, 1976).

Quantum-mechanical phase coherence of charge carriers in a bulk superconductor gives rise to magnetic-flux quantization in a solid superconducting ring: the magnetic flux Φ through the loop must be an integral multiple of the so-called flux quantum, $\Phi_0 = h/2e = 2.07$ fWb (see Sec. V.D.1). In an external magnetic field, this is accomplished by supercurrents that flow along the surface of the ring so as to precisely cancel any deviations from the quantization condition. The weak links of the SQUID alter the compensation of the external field by the circulating current, thus making it easier to exploit flux quantization for the measurement of the magnetic field. A schematic illustration of the usual experimental arrangement for MEG measurements is shown in Fig. 7(a). We shall discuss the theory and practice of SQUIDs as applied to MEG measurements thoroughly in Sec. V.D.

The magnetic signals from the brain are extremely weak compared with ambient magnetic-field variations (see Fig. 8). Thus rejection of outside disturbances is of utmost importance. Significant magnetic noise is caused, for example, by fluctuations in the earth's geomagnetic field, by moving vehicles and elevators, by radio, television, and microwave transmitters, and by the omnipresent power-line fields. The electrical activity of the heart also generates a field, which on the chest is two to three orders of magnitude larger than the signals from the brain outside the head.

The sensitivity of the SQUID measuring system to external magnetic noise is greatly reduced by the proper design of the flux transformer, a device normally used for bringing the magnetic signal to the SQUID. For example, an axial first-order gradiometer consists of a pickup (lower) coil and a compensation coil, which are identical in area and connected in series but wound in opposition [see Fig. 7(b)]. This system of coils is insensitive to spatially uniform changes in the background field, but responds to inhomogeneous changes. Therefore, if the

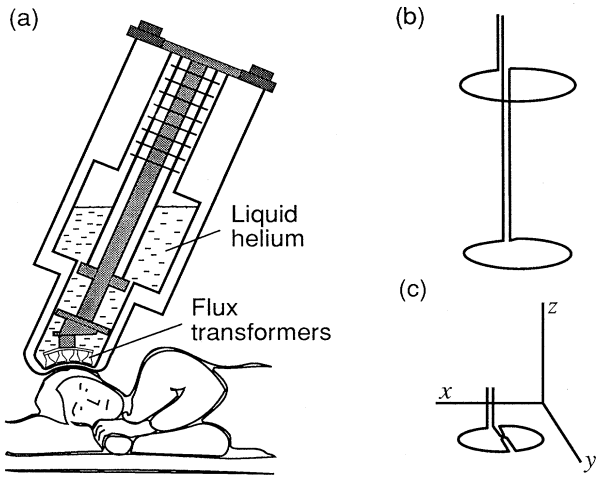


FIG. 7. Detection of cerebral magnetic fields. (a) Typical experimental arrangement during a MEG measurement. The subject lies on a nonmagnetic bed with his head supported by a vacuum cast to prevent movements. The bottom of the helium dewar, with the flux-transformer pickup coils near its tip, is brought as close to his head as possible. Auditory stimuli are presented via plastic tubes and earpieces (not shown) from loudspeakers outside the shielded room. (b,c) Two superconducting flux transformers employed in brain research: the axial gradiometer (b) measures $\Delta B_z/\Delta z$ (approximately $B_z$ at the lower loop) and the planar gradiometer (c) $\Delta B_z/\Delta x$ (approximately $\partial B_z/\partial x$). Flux transformer (b) detects two field extrema, one on each side of the dipole [see Figs. 4(b) and 27], while with (c) the maximum signal is recorded above the dipole (see Fig. 27). Note that when referring to individual magnetic sensors, we use coordinate systems that are fixed to each sensor unit separately.

signal of interest arises near the lower coil, it will cause a much greater change of field in the pickup loop than in the more remote compensation coil, thus producing a net change in the output. In effect, the lower loop picks up the signal, while the upper coil compensates for variations in the background field. For still better rejection of external disturbances, MEG measurements are usually performed in a magnetically shielded room (see Fig. 9 and Sec. V.B.1).

Processing of incoming information by the brain can be studied by recording responses to sensory stimuli. In many experiments, spontaneous brain activity, such as the $\alpha$ rhythm (see Sec. VI.D.1), or incoherent background events are sources of noise. Thus signals resulting from many successive stimuli must be averaged; in this way the evoked responses emerge from the background noise. For localization of the active brain area, measurements must be made over many sites, typically at

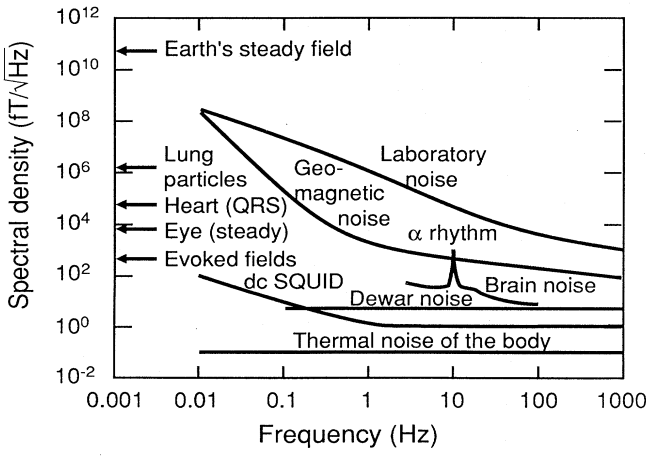


FIG. 8. Peak amplitudes (arrows) and spectral densities of fields due to typical biomagnetic and noise sources.

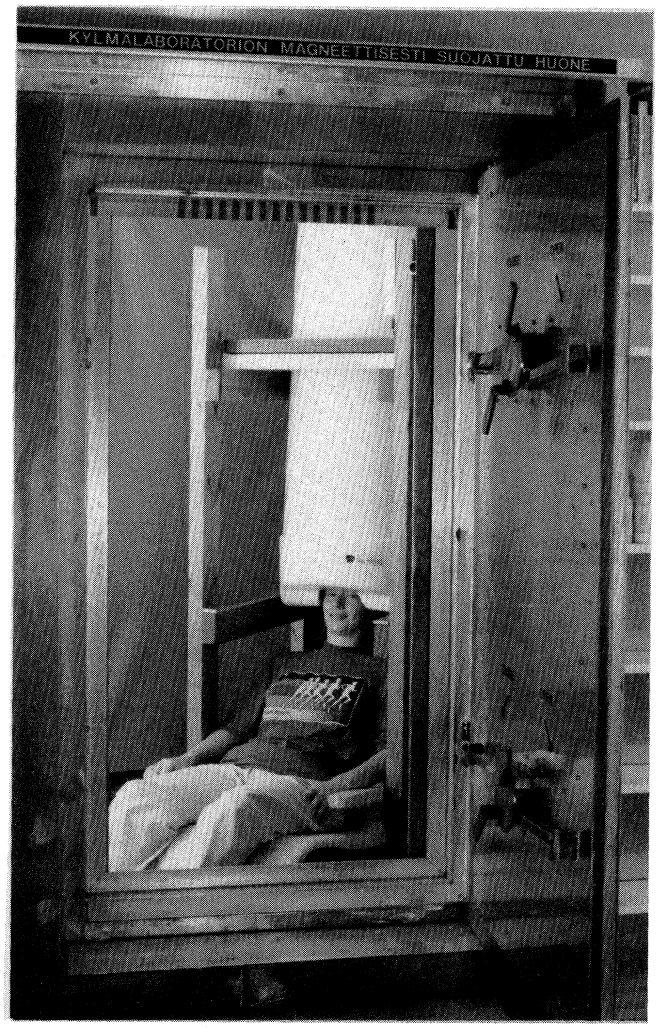


FIG. 9. View of the interior of the magnetically shielded room at the Helsinki University of Technology (Kelhä *et al.*, 1982). During actual measurements the subject is usually left alone and the double doors are closed. The room is a cube of 2.4-m inner dimensions with three layers of $\mu$-metal, which are effective for shielding at low frequencies of the external magnetic noise spectrum (particularly important for biomagnetic measurements), and three layers of aluminum, which attenuate very well the high-frequency band. The shielding factor is $10^3$–$10^4$ for low-frequency magnetic fields and about $10^5$ for fields of 10 Hz and above. The subject has her head inside a 122-channel neuromagnetometer (see Fig. 41 and Sec. V.F.6).

20 to 60 points separated by about 3 cm. At each location the stimulus must be repeated 20 to 500 times in order to obtain an adequate signal-to-noise ratio. This is a potentially tedious and time-consuming procedure that also endangers the reliability of the data: the subject cannot be expected to remain in the same state of vigilance throughout a long measurement session.

Indeed, the main drawback of the MEG method in the past was the long time needed to gather data for a topographic field map [see Fig. 4(b)] from which the activated cortical site could be deduced. An instrument that records the whole magnetic-field pattern at once is clearly very useful. Several MEG groups and companies are already constructing and using such multi-SQUID magnetometers. A photograph of the 24-channel neurogradiometer in Helsinki is shown in Fig. 10; this instrument employs planar gradiometric flux transformers, whose construction was schematically illustrated in Fig. 7(c).

An example of MEG data recorded with this system is shown in Fig. 11. A typical auditory evoked response was detected as a function of time over the left temple. The main peak occurs approximately 100 ms after the stimulus onset. The locations of the largest signals imply that the equivalent current dipole is beneath unit 8, in the auditory cortex at the upper surface of the temporal lobe, pointing down (see Sec. V.B.2).

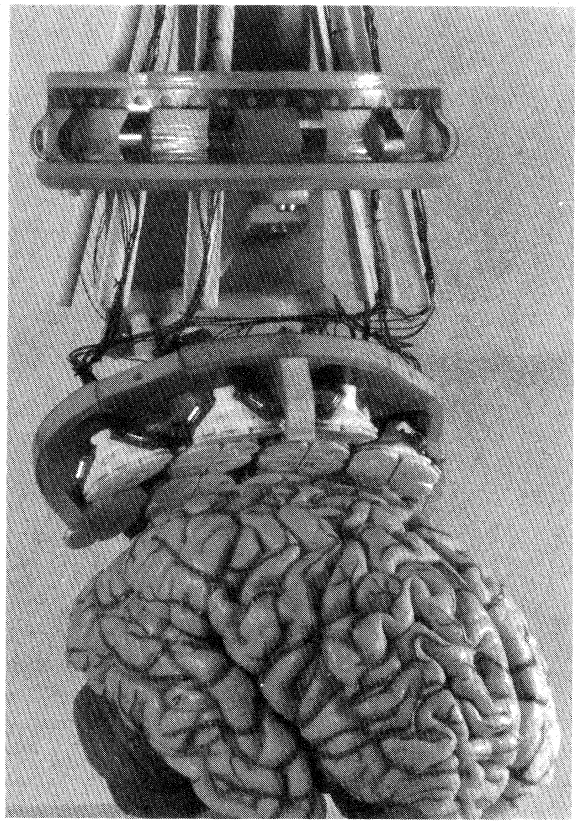

FIG. 10. The 24-channel neurogradiometer in Helsinki (Kajola *et al.*, 1989; Ahonen *et al.*, 1991) at a typical measurement distance above a model of the brain. During an actual measurement the instrument is, of course, in a helium dewar and the brain is inside the skull! The measuring head of the gradiometer and the tip of the dewar are concave so that they fit as closely as possible to the subject's head.

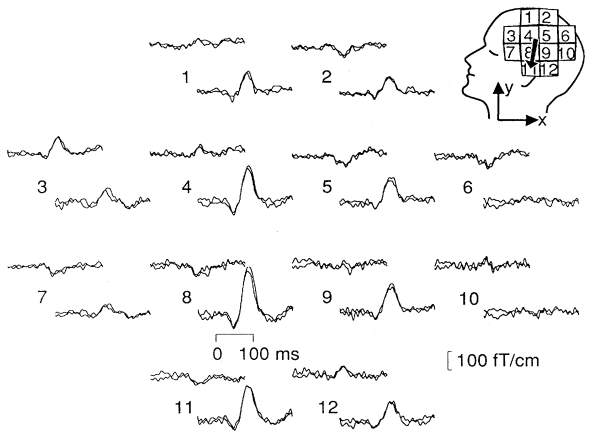


FIG. 11. Typical auditory responses evoked by short tones. The approximate location of the magnetometer is depicted on the schematic head. The magnetic-field gradient as a function of time is illustrated at 12 locations (see Figs. 10 and 37) for two orthogonal directions at each site, $\partial B_z/\partial y$ above and $\partial B_z/\partial x$ below. The Cartesian coordinate system is individually determined at the site of each sensor unit [see Fig. 7(c)]. Two traces, both corresponding to averages of 66 individual responses, are superimposed in each case to show the repeatability of the responses. The stimulus has been given at $t=0$ (time scale below the data of unit 8). The arrow on the head shows the location of the equivalent current dipole in the auditory cortex during the largest peak of the response.

### E. Magnetic fields from the human body

The strongest electrophysiological signals are generated by the heart and by skeletal muscles. Typically, the amplitude of the QRS peak, corresponding to contraction of the cardiac muscle, is several tens of picoteslas. However, the clinically more important signals from the cardiac conducting system, which are superimposed on the field due to contraction of the muscle, are less than 1 pT in amplitude (Fenici *et al.*, 1983).

From the normal awake brain, the largest field intensity is due to spontaneous activity. The so-called $\alpha$ rhythm, observed over the posterior parts of the head, is 1–2 pT in amplitude (see Sec. VI.D.1). Abnormal conditions, such as epileptic disorders, may elicit spontaneous spikes of even larger amplitude (see Sec. VI.E). Typical evoked fields following sensory stimulation are weaker by an order of magnitude or more; i.e., their strengths are only several tens or hundreds of femtoteslas. The ultimate limit for the sensitivity of a biomagnetometer is determined by the thermally induced magnetic noise in the body tissues. This background is, however, only on the order of 0.1 $\mathrm{fT}/\sqrt{\mathrm{Hz}}$ (Varpula and Poutanen, 1984).

The brain itself produces magnetic fields that are often irrelevant to the experiment being conducted (see Fig. 12). This background activity limits the signal-to-noise ratio in measurements made with the best SQUID magnetometers. Of course, during studies of spontaneous brain activity, this subject "noise" is actually the signal! In contrast to instrumental noise, the background activity is correlated between the different magnetometer channels and can, at least in principle, be taken into account in the data analysis. If the noise source is different from the signal source, the two can be separated in multichannel recordings.

The spectral density of the cerebral background activity is typically 20–40 $fT/\sqrt{Hz}$ below about 20 Hz, decreasing towards higher frequencies and showing peaks at the spontaneously occurring rhythms of the brain, e.g., around 10 Hz (Maniewski *et al.*, 1985; Knuutila and Hämäläinen, 1988).

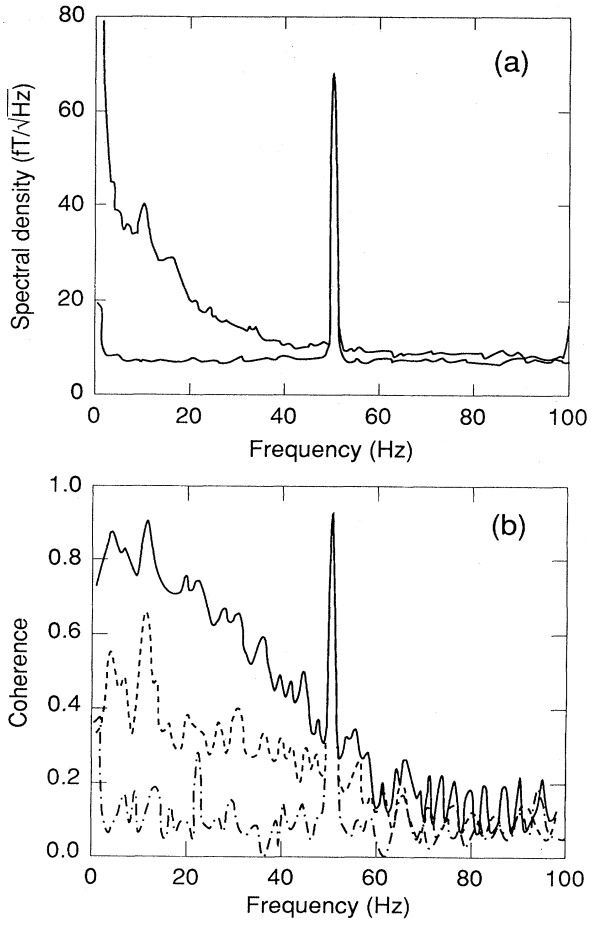


FIG. 12. Background activity of the brain over the left temporal lobe for a subject with his eyes open; an axial first-order gradiometer was used: (a) spectral density of the noise spectrum with (upper curve) and without (lower curve) a subject; (b) normalized coherence functions measured between channels separated by 36.5 mm (solid curve) and 73 mm (dashed line). The dot-dashed curve shows the coherence between channels without a subject. The prominent peak at 50 Hz is caused by the power-line frequency. From Knuutila and Hämäläinen (1988).

There are many other magnetic signals originating from the human body (see Fig. 8). Ionic currents in the eye give rise to a static 10-pT field, which also has a changing component during eye movements and blinks. The fields due to inhaled or digested magnetized particles, often observed in the lungs of welders or iron foundry workers, may be several nanoteslas in amplitude.

## II. NEURAL BASIS OF MAGNETOENCEPHALOGRAPHY

In this section, the structure of the human cerebral cortex and some neuronal functions are described in such detail that the reader may gain an understanding of the brain's electrical activity and the ensuing electromagnetic field.

### A. Constituents of the brain

The principal building blocks of the brain are neurons and glial cells, the latter being more abundant by a factor of 10. The glia are important for structural support, for the maintenance of proper concentrations of ions, and for the transport of nutrients and other substances between blood vessels and brain tissue. Specialized glial cells, the oligodendrocytes, form an insulating myelin sheath around certain nerve fibers, thereby speeding signal transmission. Neurons are the information-processing units. Their cell bodies and dendrites are concentrated in the gray matter, the largest part of which is the cerebral cortex forming the surface of the brain. In addition, there is gray matter in subcortical nuclei, like the thalamus, but these structures do not directly interest us here because MEG signals are mainly due to cortical currents.

The interior of the brain is largely occupied by nerve fibers; this tissue is called white matter because of the bright appearance of the myelinated axons (see Sec. II.B), which form connections between different cortical areas as well as from the cortex to other brain structures and to the periphery. There are also many links between the two hemispheres, the most conspicuous of them being the corpus callosum.

Anatomy has implications for neuromagnetism in three ways. First, local, cellular-level structures determine how neuronal electrical events produce macroscopic current sources. Second, the electrical conductivity as a function of location on a macroscopic length scale is needed for the solution of the forward problem (see Sec. III.E.2). Third, knowledge of the brain's anatomy can be utilized in the solution of the inverse problem (see Sec. IV.E). In particular, if we assume that the source currents are confined to the gray matter, the three-dimensional localization problem becomes essentially two-dimensional, thereby improving the accuracy. In practice, the distribution of gray matter in the brain, as well as the shape of the cranium, can be determined with

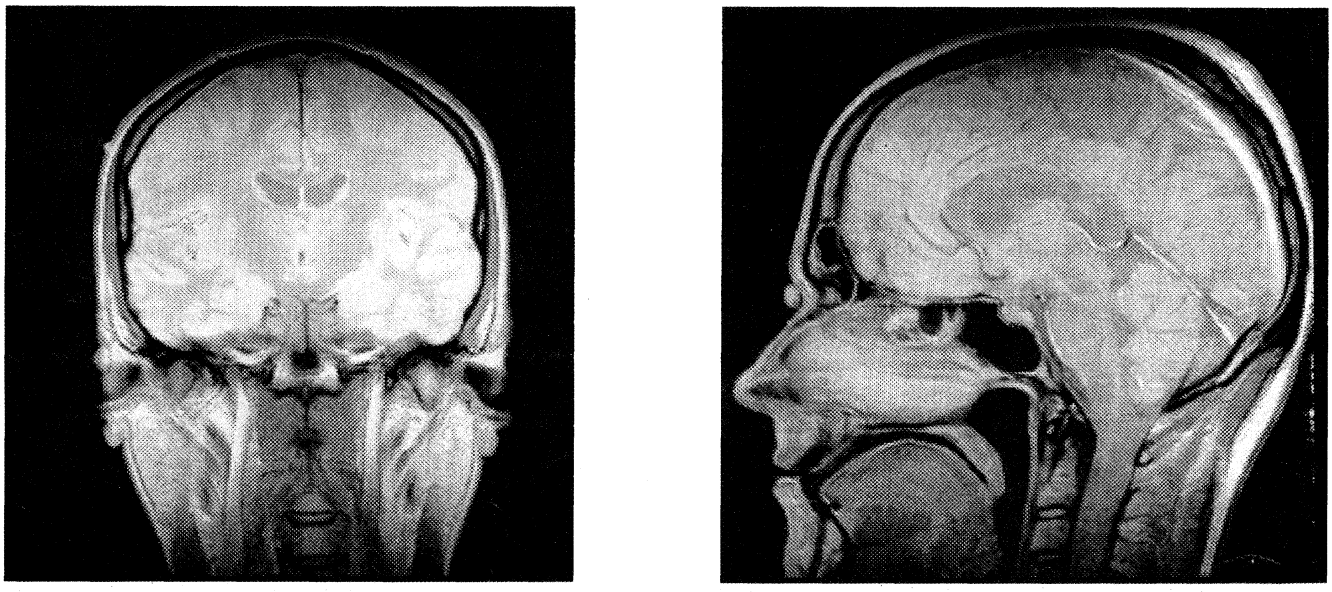

FIG. 13. Coronal section (a) at the level of the ears and sagittal (longitudinal) section (b) near the head midline of MRI's made on one of the authors; many important brain structures are clearly seen. The images were acquired with the Siemens 1.0-T MRI system at the Helsinki University Central Hospital.

magnetic-resonance imaging. Two magnetic-resonance (MR) images of a human head are illustrated in Fig. 13.

The detailed structure of the head is quite complicated. The brain is surrounded by membranes which, although thin, may have to be taken into account when precise analysis of the cerebral magnetic field is attempted. In addition, the electrical conductivity of brain tissue is highly anisotropic: the white matter conducts 10 times better along an axon fiber than in the transverse direction. At the present level of analysis, we largely ignore these complications; in fact, we usually consider the whole intracranial volume as a homogeneous conductor. Refinement of the volume conductor models presented in this review will be useful only when there are tools to measure the details of conductivity and to take them properly into account in the analysis.

### B. The neuron

Figure 14 shows the visual cortex of a rat in cross section. Only a small percentage of the neurons is seen because a selective stain has been applied to the tissue. Neurons can send electrical impulses, so-called action potentials, to other neurons nearby or to distant parts of the brain (see Sec. II.E). A neuron (see Fig. 15) consists of the cell body (the soma), which contains the nucleus and much of the metabolic machinery, the dendrites, which are threadlike extensions that receive stimuli from other cells, and the axon, a single long fiber that carries the nerve impulse away from the soma to other cells. The two principal groups of cortical neurons are the pyrami-

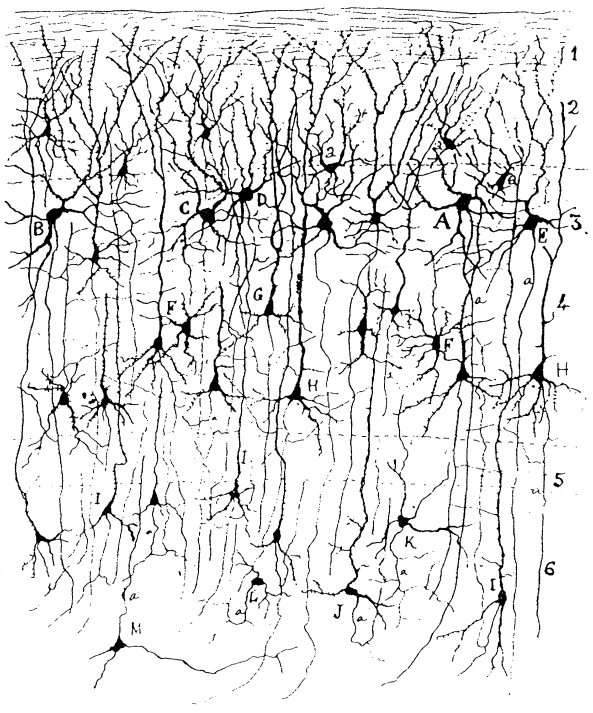


FIG. 14. Transverse section through the gray matter of rat cortex; the thickness of the sheet, from top to bottom, is in humans about 3 mm. A prominent pyramidal neuron (*H*) is illustrated in the middle and two stellate cells (*F*) nearby. The tissue was prepared by the Golgi method, which stains about 1% of the neurons. This picture was drawn by Ramón y Cajal in 1888.

dal and the stellate cells (see Fig. 14). The former are relatively large; their apical dendrites from above reach out parallel to each other, so that they tend to be perpendicular to the cortical surface. Since neurons guide the current flow, the resultant direction of the electrical current flowing in the dendrites is also perpendicular to the cortical sheet of gray matter; this is important for MEG studies.

The dendrites and the soma have typically thousands of synapses (connections) from other neurons. The intracellular potential is increased by input through the excitatory synapses, but decreased by inhibitory input. Most excitatory synapses are on the dendrites; inhibitory synapses often attach to the soma. The neuron fires an action potential when the potential at the axon hillock reaches a certain threshold level.

Schematic illustrations of three synapses are shown in Fig. 15(a). When a pulse arrives along the axon of the presynaptic cell, special transmitter molecules are liberated from the synaptic vesicles into the 50-nm-wide synaptic cleft. These molecules diffuse quickly through the gap and some of them attach themselves to receptors on the surface of the postsynaptic cell. As a result, the receptor molecules change their shape, opening ion channels through the membrane. The ensuing flow of charge (mainly $Na^+$, $K^+$, and $Cl^-$ ions) changes the membrane potential in the second cell; this event is called the postsynaptic potential [PSP; see Sec. II.D and Fig. 16(a)]. The channels are ion selective; depending on the receptor that is activated, only certain types of ions may pass through the membrane.

### C. Ion mechanisms

The neuron, like other cells, is surrounded by a membrane, a 10-nm-thick liquid-crystal bilayer of phospholipids. The insulating membrane divides the tissue into intracellular and extracellular compartments with different ion concentrations. This difference is maintained by special protein molecules on the membrane that pump selected ions against the concentration gradient and also serve as passive ion channels. The most important is the Na–K pump, which moves three $Na^+$ ions out and two $K^+$ ions into the cell in one duty cycle. Although the pump gives rise to a current through the membrane, the increase of the resting voltage due to this current is only a few mV. In a quiescent neuron, the intra-

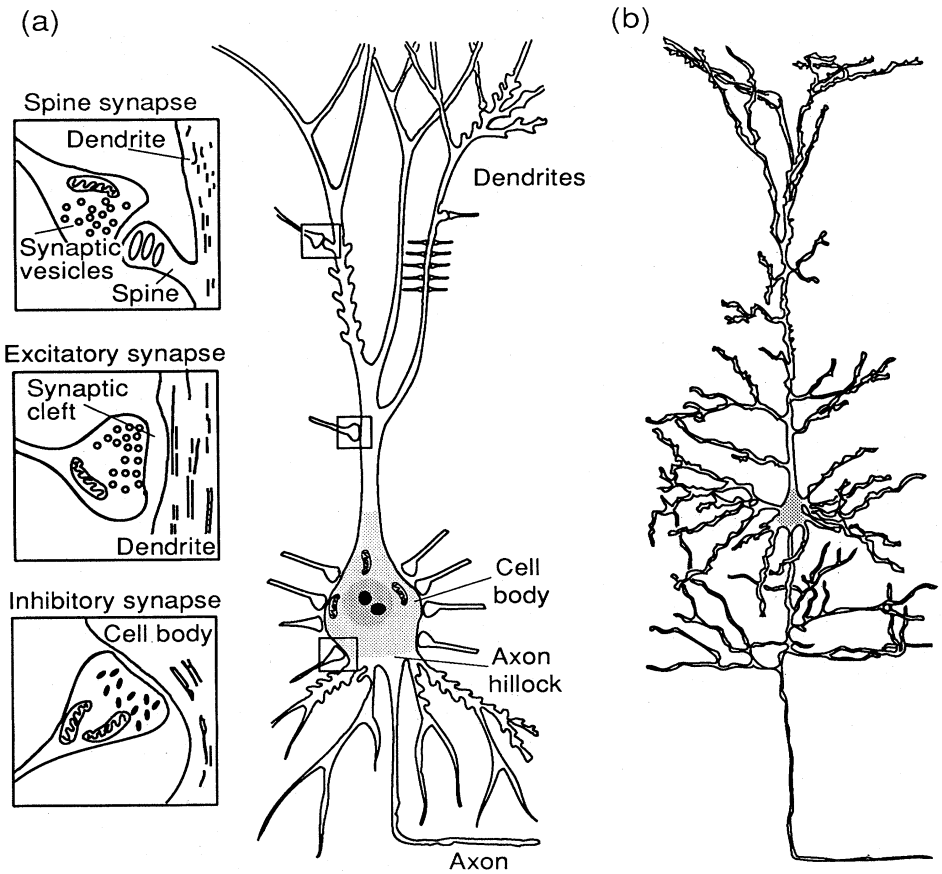


FIG. 15. Cortical neuron. (a) Schematic illustration of a pyramidal neuron and three magnified synapses (modified from Iversen, 1979); (b) pyramidal neuron, redrawn from Ramón y Cajal.

cellular concentrations of $Na^+$ and $K^+$ are about 20 and 140 mmol/liter, respectively, whereas the corresponding extracellular concentrations are about 140 and 5 mmol/liter. The intra- and extracellular concentrations of $Cl^-$ are about 20 and 120 mmol/liter, respectively.

The equilibrium voltage across the cell membrane is determined by the requirement that the diffusive and ohmic currents, in addition to the pump currents, be balanced for each type of ion. In the inactive state, the permeability of potassium dominates that of sodium; i.e., the diffusion coefficient $P(K^+)$ for $K^+$ through the membrane is much higher than $P(Na^+)$. When $K^+$ ions diffuse out of the cell, the interior becomes more negative. The equilibrium potential is determined by thermodynamics: the concentration $C$ of each ion type tends toward thermal equilibrium between the two compartments according to the Boltzmann expression

$$C \sim \exp(-|e|V/k_B T) .$$

From this, the Nernst equation is obtained:

$$V = V_{\text{in}} - V_{\text{ext}} = \frac{k_B T}{|e|} \ln \left[ \frac{C_{\text{ext}}}{C_{\text{in}}} \right] . \tag{1}$$

Here, $V_{\text{in}}$ and $V_{\text{ext}}$ are the intracellular and extracellular potentials, $k_B T$ is the thermal energy, and $e$ denotes the electron charge.

Applying the Nernst equation to concentrations mentioned above, we obtain the equilibrium membrane voltages (inside with respect to the outside) at the body temperature $T = 310$ K: $V(K^+) = -89$ mV, $V(Cl^-) = -48$ mV, and $V(Na^+) = +52$ mV. When these three most important ion types are simultaneously taken into account, the voltage over the membrane becomes

$$V = \frac{k_B T}{|e|} \ln \left[ \frac{P(K^+)C_{\text{ext},K^+} + P(Na^+)C_{\text{ext},Na^+} + P(Cl^-)C_{\text{in},Cl^-}}{P(K^+)C_{\text{in},K^+} + P(Na^+)C_{\text{in},Na^+} + P(Cl^-)C_{\text{ext},Cl^-}} \right] = -70 \text{ mV} . \tag{2}$$

This is Goldman's (1943) equation. Because the permeabilities $P(K^+)$ and $P(Cl^-)$ are large, the resting potential is between the equilibrium values for $K^+$ and $Cl^-$. When the permeabilities change as a result of synaptic excitation or inhibition, or in the course of an action potential, the voltage across the membrane follows Eq. (2).

### D. Postsynaptic potentials

When transmitter molecules released to the synaptic cleft (see Fig. 15) arrive at the postsynaptic cell, the permeability of the membrane for specific ions is altered and the potential in the vicinity of the membrane changes. This causes an electric field and a current along the interior of the postsynaptic cell. The resulting current flows into the cell if sodium channels open; it flows out if potassium or chloride channels are activated. In the former case, the cell is depolarized and there is an excitatory PSP [see Fig. 16(a)]; in the latter case, the cell is hyperpolarized and thereby inhibited.

The strength of the current source decreases with the distance from the synapse. The length constant of the exponential decay is $\lambda = (g_m r_s)^{-1/2}$, where $g_m$ and $r_s$ are the conductance of the membrane and the resistance of the intracellular fluid per unit length, respectively (Scott, 1977). In a cortical neuron, $\lambda$ is typically 0.1–0.2 mm. From a distance, the PSP looks like a current dipole oriented along the dendrite, with strength $Q = I\lambda$. The current $I$ through the synapse can be calculated from the change of voltage $\Delta V$ during a PSP: $I = \Delta V/(\lambda r_s)$. Since $r_s = 4/(\pi d^2 \sigma_{\text{in}})$, where $d$ is the diameter of the dendrite and $\sigma_{\text{in}}$ is the intracellular conductivity, $Q = \pi d^2 \sigma_{\text{in}} \Delta V/4$. Inserting typical values, $d = 1$ $\mu$m, $\sigma_{\text{in}} = 1$ $\Omega^{-1}\text{m}^{-1}$, and $\Delta V = 25$ mV, we find that $Q \approx 20$ fA m for a single PSP.

Usually, the current-dipole moments required to explain the measured magnetic-field strengths outside the head are on the order of 10 nA m. Therefore, about a million synapses must be simultaneously active during a typical evoked response. Since there are approximately $10^5$ pyramidal cells per $\text{mm}^2$ of cortex and thousands of synapses per neuron, the simultaneous activation of as

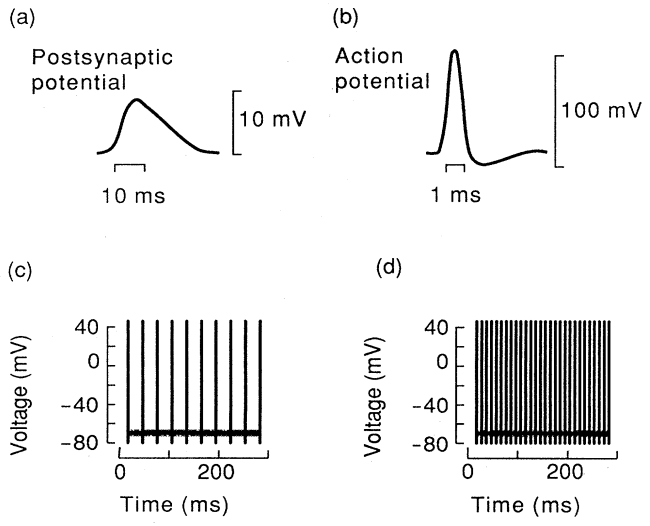


FIG. 16. Schematic illustrations of (a) a postsynaptic potential and (b) an action potential as a function time. Action potentials increase in frequency, but not in amplitude, with the intensity of the stimulus, which is stronger in (d) than in (c). Voltage $V = V_{\text{in}} - V_{\text{ext}}$ [see Eqs. (1) and (2)].

few as one synapse in a thousand over an area of one square millimeter would suffice to produce a detectable signal. In practice, activation of larger areas is necessary because there is partial cancellation of the generated electromagnetic fields owing to source currents flowing in opposite directions in neighboring cortical regions. This is also illustrated by a more realistic estimate based on measured current densities, 100–250 nA/mm$^2$ (Freeman, 1975; Kraut *et al.*, 1985). Assuming this estimate over an effective thickness of 1 mm, a dipole moment of 10 nA m would correspond to 40 mm$^2$ of active cortex (Chapman *et al.*, 1984). On the other hand, if the relevant distance is taken to be the length constant $\lambda = 0.2$ mm (Kuffler *et al.*, 1984), the area would be 5 times larger (Hari, 1990).

### E. Action potentials

Signal transfer along an axon is based on the ability of the membrane to alter its permeability to $Na^+$ and $K^+$ ions. The change is due to the opening of voltage-sensitive channels as a result of an approaching action potential [see Fig 16(b) and Sec. II.C]. When such a voltage pulse travels along an axon, there is a solitary wave of depolarization followed by a repolarization of longer spatial extent. An action potential is initiated when the voltage at the axon hillock [see Fig. 15(a)] reaches the firing threshold of about $-40$ mV. During this stage the interior of the cell is positive for a short time [see Fig. 16(c)]. This change of potential triggers the neighboring region; the action potential thus travels along the axon with undiminished amplitude like the wave of falling pieces in a chain of dominoes. The membrane potential provides the energy needed to propagate the unattenuated pulse. When the excitatory input becomes stronger, the amplitude of the action potential remains the same, but the frequency of firing increases [see Figs. 16(c) and 16(d)].

Over straight portions of a nerve fiber of uniform thickness, the action potential can be approximated by two oppositely oriented current dipoles. Their separation depends on the conduction velocity $v$ and is about 1 mm in an unmyelinated cortical axon where $v \approx 1$ m/s; the magnitude of each dipole is about 100 fA m. Since the two dipoles are opposite, they form a current quadrupole. A dipolar field, produced by synaptic current flow, decreases with distance as $1/r^2$, more slowly than the $1/r^3$-dependent quadrupolar field. Furthermore, temporal summation of currents flowing in neighboring fibers is more effective for synaptic currents, which last tens of milliseconds, than for action potentials, which have a duration of 1 ms only. Thus EEG and MEG signals are produced in large part by synaptic current flow, which is approximately dipolar. Action potentials have, however, been detected both electrically and magnetically in peripheral tissue. They also might contribute significantly to high-frequency electromagnetic fields outside the skull, but this has not been demonstrated so far.

Wikswo *et al.* (1980) reported the first measurements of the magnetic field of a peripheral nerve. They used the sciatic nerve in the hip of a frog; the fiber was threaded through a toroid in a saline bath. When action potentials were triggered in the nerve, a biphasic magnetic signal of about 1 ms duration was detected. Later, the magnetic field of an action potential propagating in a single giant crayfish axon was recorded as well (Roth and Wikswo, 1985). The measured transmembrane potential closely resembled that calculated from the observed magnetic field. From these two sets of data, it was possible to determine the intracellular conductivity. Recently it has become possible to record magnetic compound action fields (CAFs) associated with electrical impulses propagating along human peripheral nerves (Wikswo, 1985; Wikswo, Abraham, and Hentz, 1985; Wikswo, Henry, *et al.*, 1985; Wikswo and Roth, 1985; Erné *et al.*, 1988; Hari, Hällström, *et al.*, 1989).

Figure 17 shows that the noninvasively recorded CAFs near the elbow peak at 6–7 ms after median nerve stimulation at the wrist. The response is monophasic at most locations, with opposite polarities on the two sides of the nerve, the latency becoming longer as the measurement site is moved closer to the central nervous system (CNS).

## III. NEURAL GENERATION OF ELECTROMAGNETIC FIELDS

### A. Quasistatic approximation of Maxwell's equations

The previous section described structural details of the brain as well as neuronal electrical activity. When the conductivity $\sigma$ and the electric current generators in the brain are known, Maxwell's equations and the continuity equation $\nabla \cdot \mathbf{J} = -\partial \rho / \partial t$ can be used to calculate the electric field $\mathbf{E}$ and the magnetic field $\mathbf{B}$; $\mathbf{J}$ and $\rho$ are the total current density and the charge density, respectively.

We can simplify the treatment of Maxwell's equations from the outset by noting two facts. First, the permeabil-

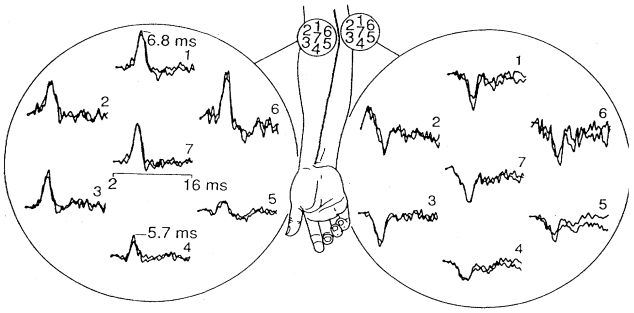


FIG. 17. Compound action fields after electric stimulation of the right median nerve at the wrist. The measurements were made twice (two superimposed traces) at both sites with a 7-channel gradiometer, and about 1000 single responses were averaged. The course of the median nerve along the arm is shown schematically. From Hari, Hällström, *et al.* (1989).

ity of tissue in the head is that of free space, i.e., $\mu=\mu_0$. Second, we can adopt the quasistatic approximation, which means that in the calculation of $\mathbf{E}$ and $\mathbf{B}$, $\partial\mathbf{E}/\partial t$ and $\partial\mathbf{B}/\partial t$ can be ignored as source terms. Let us first see why this is so.

We start from Maxwell's equations:

$$\nabla\cdot\mathbf{E}=\rho/\epsilon_0 , \tag{3}$$

$$\nabla\times\mathbf{E}=-\partial\mathbf{B}/\partial t , \tag{4}$$

$$\nabla\cdot\mathbf{B}=0 , \tag{5}$$

$$\nabla\times\mathbf{B}=\mu_0(\mathbf{J}+\epsilon_0\partial\mathbf{E}/\partial t) . \tag{6}$$

In a passive nonmagnetic medium, $\mathbf{J}$ is the sum of ohmic volume current and the polarization current, viz.,

$$\mathbf{J}=\sigma\mathbf{E}+\partial\mathbf{P}/\partial t , \tag{7}$$

where $\mathbf{P}=(\epsilon-\epsilon_0)\mathbf{E}$ is the polarization; $\epsilon$ is the permittivity of the material.

In neuromagnetism, we generally deal with frequencies that are below 100 Hz; cellular electrical phenomena contain mostly frequencies below 1 kHz. Let $\sigma$ and $\epsilon$ be uniform and let us consider electromagnetic phenomena at frequency $f$ ($j=\sqrt{-1}$):

$$\mathbf{E}=\mathbf{E}_0(\mathbf{r})\exp(j2\pi ft) . \tag{8}$$

With Eqs. (6) and (7),

$$\nabla\times\mathbf{B}=\mu_0[\sigma\mathbf{E}+(\epsilon-\epsilon_0)\partial\mathbf{E}/\partial t+\epsilon_0\partial\mathbf{E}/\partial t] .$$

For the quasistatic approximation to be valid, it is necessary that the time-derivative terms be small compared to ohmic current: $|\epsilon\partial\mathbf{E}/\partial t|\ll|\sigma\mathbf{E}|$, i.e., $2\pi f\epsilon/\sigma\ll 1$. With $\sigma=0.3\ \Omega^{-1}\,\mathrm{m}^{-1}$ (value for brain tissue), $\epsilon=10^5\epsilon_0$, and $f=100$ Hz, we find $2\pi f\epsilon/\sigma=2\times10^{-3}\ll 1$.

In addition, $\partial\mathbf{B}/\partial t$ must be small. From Eqs. (4) and (6),

$$\begin{aligned}\nabla\times\nabla\times\mathbf{E}&=-\frac{\partial}{\partial t}(\nabla\times\mathbf{B})\\&=-\mu_0\frac{\partial}{\partial t}(\sigma\mathbf{E}+\epsilon\partial\mathbf{E}/\partial t)\\&=-j2\pi f\mu_0(\sigma+j2\pi f\epsilon)\mathbf{E} .\end{aligned} \tag{9}$$

Solutions of this equation have spatial changes on the characteristic length scale

$$\lambda_c=|2\pi f\mu_0\sigma(1+j2\pi f\epsilon/\sigma)|^{-1/2} .$$

With the above parameters, $\lambda_c=65$ m, i.e., much longer than the diameter of the head. This implies that the contribution of $\partial\mathbf{B}/\partial t$ to $\mathbf{E}$ is small. Therefore, the quasistatic approximation appears justified. This does not mean that we should forget time-dependent phenomena altogether. For example, the capacitive current through the cell membrane is significant in determining the properties of the action potential (see Sec. II.E). Nevertheless, this so-called displacement current, $\epsilon_0\partial\mathbf{E}/\partial t$, need not be taken into account in the calculation of $\mathbf{B}$.

In the quasistatic approximation, since $\nabla\times\mathbf{E}=0$, the electric field can be expressed with a scalar potential,

$$\mathbf{E}=-\nabla V . \tag{10}$$

The use of $V$ considerably simplifies derivations of formulas for electromagnetic fields; we shall employ it extensively.

### B. Primary current

It is useful to divide the current density $\mathbf{J}(\mathbf{r})$ produced by neuronal activity into two components. The volume or return current, $\mathbf{J}^v(\mathbf{r})=\sigma(\mathbf{r})\mathbf{E}(\mathbf{r})$, is passive. It is the result of the macroscopic electric field on charge carriers in the conducting medium. Everything else is the primary current $\mathbf{J}^p$:

$$\mathbf{J}(\mathbf{r})=\mathbf{J}^p(\mathbf{r})+\sigma(\mathbf{r})\mathbf{E}(\mathbf{r})=\mathbf{J}^p(\mathbf{r})-\sigma(\mathbf{r})\nabla V(\mathbf{r}) . \tag{11}$$

This definition would be meaningless without reference to the length scale. Here $\sigma(\mathbf{r})$ is the macroscopic conductivity; cellular-level details are left without explicit attention. In other words, the whole cortex is modeled as a homogeneous conductor. The division in Eq. (11) is illustrative in that neural activity gives rise to primary current mainly inside or in the vicinity of a cell, whereas the volume current flows passively everywhere in the medium. By finding the primary current, we locate the source of brain activity. It should be emphasized that $\mathbf{J}^p$ is to be considered the driving "battery" in the macroscopic conductor; although the conversion of chemical gradients to current is due to diffusion, the primary current is largely determined by the cellular-level details of conductivity. In particular, the membranes, being good electrical insulators, guide the flow of both intracellular and extracellular currents.

If the events are considered on the cellular level, it is customary to speak about the impressed rather than the primary current.

### C. Current dipole

A current dipole $\mathbf{Q}$, approximating a localized primary current, is a widely used concept in neuromagnetism. $\mathbf{Q}$ at $\mathbf{r}_Q$ can be thought of as a concentration of $\mathbf{J}^p(\mathbf{r})$ to a single point:

$$\mathbf{J}^p(\mathbf{r})=\mathbf{Q}\delta(\mathbf{r}-\mathbf{r}_Q) , \tag{12}$$

where $\delta(\mathbf{r})$ is the Dirac delta function. The letter $\mathbf{Q}$ is used here to avoid confusion with $\mathbf{p}$, the symbol for a charge dipole. In EEG and MEG applications, a current dipole is used as an equivalent source for the unidirectional primary current that may extend over several square centimeters of cortex. Although the current dipole is usually a model for a layer of primary current, it is sometimes convenient to consider $\mathbf{Q}$ as a line element of current $I$ pumped from a sink at $\mathbf{r}_1$ to a source at $\mathbf{r}_2$;

then, $\mathbf{Q}=I(\mathbf{r}_2-\mathbf{r}_1)$.

$\mathbf{Q}$ is closely related to the dipole term $\mathbf{J}_0$ in the current multipole expansion (Katila, 1983): $\mathbf{J}_0=\int \mathbf{J}^p(\mathbf{r})dv$. For the primary current distribution (12), $\mathbf{J}_0=\mathbf{Q}$.

### D. Integral formulas for $V$ and B

The forward problem in neuromagnetism is to calculate the magnetic field $\mathbf{B}(\mathbf{r})$ outside the head from a given primary current distribution $\mathbf{J}^p(\mathbf{r}')$ within the brain. In the quasistatic approximation,

$$\mathbf{B}(\mathbf{r})=\frac{\mu_0}{4\pi}\int \frac{\mathbf{J}(\mathbf{r}')\times\mathbf{R}}{R^3}dv' , \tag{13}$$

where $\mathbf{r}$ is the point where the field is computed, $\mathbf{R}=\mathbf{r}-\mathbf{r}'$, and the primed symbols refer to quantities in the source region. This is the Ampère–Laplace law, the continuous counterpart of the Biot–Savart law which applies to closed wire loops. Inserting the identities

$$\mathbf{R}/R^3=-\nabla(1/R)=\nabla'(1/R) ,$$

where

$$\nabla=\mathbf{e}_x\partial/\partial x+\mathbf{e}_y\partial/\partial y+\mathbf{e}_z\partial/\partial z$$

and

$$\nabla'=\mathbf{e}_x\partial/\partial x'+\mathbf{e}_y\partial/\partial y'+\mathbf{e}_z\partial/\partial z' ,$$

and $\mathbf{J}\times\nabla'(1/R)=(\nabla'\times\mathbf{J})/R-\nabla'\times(\mathbf{J}/R)$ into Eq. (13) and transforming the volume integral of $\nabla'\times(\mathbf{J}/R)$ into a surface integral, we find for a current density that approaches zero sufficiently fast when $\mathbf{r}'$ goes to infinity

$$\mathbf{B}(\mathbf{r})=\frac{\mu_0}{4\pi}\int \frac{\nabla'\times\mathbf{J}(\mathbf{r}')}{R}dv' . \tag{14}$$

With $\mathbf{J}=\mathbf{J}^p-\sigma\nabla V$ and $\nabla\times(\sigma\nabla V)=\nabla\sigma\times\nabla V$,

$$\mathbf{B}(\mathbf{r})=\frac{\mu_0}{4\pi}\left[\int \frac{\nabla'\times\mathbf{J}^p(\mathbf{r}')}{R}dv'-\int \frac{\nabla'\sigma\times\nabla' V}{R}dv'\right] . \tag{15}$$

The first term in this equation is the direct contribution of $\mathbf{J}^p$ to the magnetic field, the second is due to $\mathbf{J}^v$. We notice that there is no contribution from $\mathbf{J}^v$ if $\nabla'\sigma=0$; i.e., in an infinite homogeneous conductor the magnetic field is obtained directly from $\mathbf{J}^p$.

Since $\nabla\sigma\times\nabla V=-\nabla\times(V\nabla\sigma)$, a comparison of Eqs. (13), (14), and (15) shows that

$$\mathbf{B}(\mathbf{r})=\frac{\mu_0}{4\pi}\int(\mathbf{J}^p+V\nabla'\sigma)\times\frac{\mathbf{R}}{R^3}dv' . \tag{16}$$

Because the source of the magnetic field is the total current $\mathbf{J}$, both $\mathbf{J}^p$ and $\sigma\mathbf{E}$ contribute. However, in Eq. (16), $\sigma\mathbf{E}$ is replaced by an equivalent fictitious current $V\nabla\sigma$, which, in general, has no direct physical meaning. Taking the divergence of Eq. (11), we obtain

$$\nabla\cdot\mathbf{J}^p=\nabla\cdot\mathbf{J}+\nabla\cdot(\sigma\nabla V) . \tag{17}$$

From Eq. (6), since the divergence of a curl vanishes, $\nabla\cdot\mathbf{J}=0$ in the quasistatic approximation. Thus we obtain

$$\nabla\cdot(\sigma\nabla V)=\nabla\cdot\mathbf{J}^p . \tag{18}$$

With proper boundary conditions, this equation can be solved for $V$ either analytically in special cases or numerically with finite element techniques. Once $V$ is known, it is straightforward to compute $\mathbf{B}$ from Eq. (16).

### E. Piecewise homogeneous conductor

#### 1. Integral equations for $V$ and B

If the conductor is assumed to consist of homogeneous parts, $\nabla\sigma$ is nonzero only at the boundaries, and it is possible to write the second term of Eq. (16) as a sum of surface integrals over boundaries. The regions of different conductivity will be denoted by $G_i$, $i=1,\ldots,m$, their boundaries by $\partial G_i$, their conductivities by $\sigma_i$, and the surfaces between $G_i$ and $G_j$ by $S_{ij}$. The unit vector normal to the surface $S_{ij}$ at $\mathbf{r}'$ from region $i$ to $j$ is denoted by $\mathbf{n}_{ij}(\mathbf{r}')$ (see Fig. 18).

Inserting Eq. (11) into Eq. (13), we find

$$\mathbf{B}(\mathbf{r})=\mathbf{B}_0(\mathbf{r})-\frac{\mu_0}{4\pi}\sum_{i=1}^{m}\sigma_i\int_{G_i}\nabla' V\times\frac{\mathbf{R}}{R^3}dv' , \tag{19}$$

where

$$\mathbf{B}_0(\mathbf{r})=\frac{\mu_0}{4\pi}\int_G \mathbf{J}^p(\mathbf{r}')\times\frac{\mathbf{R}}{R^3}dv' \tag{20}$$

is the magnetic field produced by $\mathbf{J}^p$ alone. With the vector identities

$$\nabla\times(V\nabla(1/R))=\nabla V\times\nabla(1/R)$$

and

$$\int_G \nabla\times\mathbf{u}dv=\int_S d\mathbf{S}\times\mathbf{u} ,$$

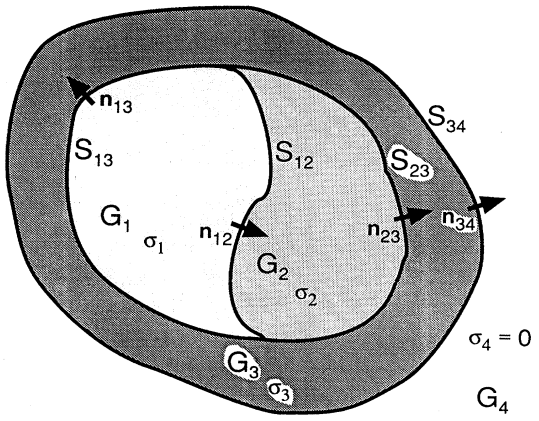


FIG. 18. Multicompartment conductivity model. Each region $G_i$ has uniform conductivity $\sigma_i$. Unit vectors normal to the surfaces are denoted by $\mathbf{n}_{ij}$.

we find

$$\int_{G_i}\nabla' V\times\frac{\mathbf{R}}{R^3}dv'=\int_{G_i}\nabla' V\times\nabla'\frac{1}{R}dv'$$
$$=-\int_{\partial G_i}V\nabla'\frac{1}{R}\times d\mathbf{S}' \ , \tag{21}$$

where $d\mathbf{S}'=\mathbf{n}(\mathbf{r}')dS'$; $\mathbf{n}(\mathbf{r}')$ is a unit vector perpendicular to $\partial G_i$ and pointing out from $G_i$. Combining the terms from all $S_{ij}$, we arrive at (Geselowitz, 1970)

$$\mathbf{B}(\mathbf{r})=\mathbf{B}_0(\mathbf{r})+\frac{\mu_0}{4\pi}\sum_{ij}{}'(\sigma_i-\sigma_j)\int_{S_{ij}}V(\mathbf{r}')\frac{\mathbf{R}}{R^3}\times d\mathbf{S}'_{ij} \ , \tag{22}$$

where the prime signifies summation over all boundaries.

It is now evident that in the calculation of the magnetic field, the volume currents can be replaced by an equivalent surface current distribution

$$-(\sigma_i-\sigma_j)V(\mathbf{r}')\mathbf{n}_{ij}(\mathbf{r}')$$

on each interface $S_{ij}$. These are often called secondary currents, but, in fact, they are only a mathematical tool for simplifying the solution of the forward problem.

In order to compute $\mathbf{B}$ from Eq. (22), we must calculate $V$ on $S_{ij}$. Of course, we could start with Eq. (18) directly, but it turns out that one can derive a surface integral equation for the electric potential which involves $V$ on the boundaries only.

By applying Green's second identity,

$$\int_G(\phi\nabla^2\psi-\psi\nabla^2\phi)dv=\int_S(\phi\nabla\psi-\psi\nabla\phi)\cdot d\mathbf{S} \ ,$$

we find

$$\sum_{i=1}^{m}\sigma_i\int_{G_i}\left[\frac{1}{R}\nabla'^2V-V\nabla'^2\frac{1}{R}\right]dv'$$
$$=\sum_{ij}{}'\int_{S_{ij}}\left[\sigma_i\left[\frac{1}{R}\nabla'_iV-V\nabla'\frac{1}{R}\right]\right.$$
$$\left.-\sigma_j\left[\frac{1}{R}\nabla'_jV-V\nabla'\frac{1}{R}\right]\right]\cdot d\mathbf{S}'_{ij} \ , \tag{23}$$

where $\nabla'_i$ means that the gradient at the boundary is taken inside region $i$. Since the current density $\sigma\nabla V\cdot\mathbf{n}$ is continuous across $S_{ij}$, the right-hand side of Eq. (23) reduces to

$$-\sum_{ij}{}'(\sigma_i-\sigma_j)\int_{S_{ij}}V\nabla'\frac{1}{R}\cdot d\mathbf{S}'_{ij} \ . \tag{24}$$

On the left-hand side we make use of

$$\nabla'^2\frac{1}{R}=-4\pi\delta(\mathbf{R}) \tag{25}$$

and of Eq. (18) to obtain the result (Geselowitz, 1967)

$$V(\mathbf{r})\sigma(\mathbf{r})=\sigma_0V_0(\mathbf{r})$$
$$-\frac{1}{4\pi}\sum_{ij}{}'(\sigma_i-\sigma_j)\int_{S_{ij}}V(\mathbf{r}')\frac{\mathbf{R}}{R^3}\cdot d\mathbf{S}'_{ij} \ . \tag{26}$$

Here, the unit conductivity $\sigma_0=1/(\Omega m)$ is needed to get the dimensions right. $V_0(\mathbf{r})$ is the potential due to $\mathbf{J}^p$ in an infinite homogeneous medium with unit conductivity, viz.,

$$V_0(\mathbf{r})=-\frac{1}{4\pi\sigma_0}\int_G\mathbf{J}^p(\mathbf{r}')\cdot\nabla'\frac{1}{R}dv'$$
$$=\frac{1}{4\pi\sigma_0}\int_G\frac{\nabla'\cdot\mathbf{J}^p}{R}dv' \ . \tag{27}$$

In order to obtain the integral equation for $V$ on the surfaces $S_{ij}$, we let $\mathbf{r}$ in Eq. (26) approach a point on $S_{ij}$. Making use of the limiting value (Vladimirov, 1971)

$$\lim_{\mathbf{r}_0\to\mathbf{r}\in S_{ij}}\int_{S_{ij}}V(\mathbf{r}')\frac{\mathbf{r}_0-\mathbf{r}'}{|\mathbf{r}_0-\mathbf{r}'|^3}\cdot d\mathbf{S}'_{ij}$$
$$=-2\pi V(\mathbf{r})+\int_{S_{ij}}V(\mathbf{r}')\frac{\mathbf{R}}{R^3}\cdot d\mathbf{S}'_{ij} \ , \tag{28}$$

we obtain an integral equation for $V(\mathbf{r})$:

$$(\sigma_i+\sigma_j)V(\mathbf{r})=2\sigma_0V_0(\mathbf{r})$$
$$+\frac{1}{2\pi}\sum_{ij}{}'(\sigma_i-\sigma_j)\int_{S_{ij}}V(\mathbf{r}')d\Omega_{\mathbf{r}}(\mathbf{r}'), \tag{29}$$

where $\mathbf{r}\in S_{ij}$. Note that

$$d\Omega_{\mathbf{r}}(\mathbf{r}')=-|\mathbf{r}-\mathbf{r}'|^{-3}(\mathbf{r}-\mathbf{r}')\cdot d\mathbf{S}'_{ij}$$

is the solid angle subtended at $\mathbf{r}$ by the surface element $d\mathbf{S}'_{ij}$ at $\mathbf{r}'$.

### 2. Spherically symmetric conductor

If the conductor is spherically symmetric, the field $\mathbf{B}$ outside can be obtained without explicit reference to the volume currents. To show this for spherical shells, we first note that in Eq. (22) the contribution of volume currents to the radial field component

$$B_r=\mathbf{B}(\mathbf{r})\cdot\mathbf{e}_r=\mathbf{B}(\mathbf{r})\cdot\mathbf{r}/|\mathbf{r}|$$

vanishes, since

$$(\mathbf{r}-\mathbf{r}')\times\mathbf{n}(\mathbf{r}')\cdot\mathbf{e}_r=(\mathbf{r}-\mathbf{r}')\times\frac{\mathbf{r}'}{|\mathbf{r}'|}\cdot\frac{\mathbf{r}}{|\mathbf{r}|}=0 \ . \tag{30}$$

Therefore, $B_r$ can be calculated simply from Eq. (13) with $\mathbf{J}$ replaced by $\mathbf{J}^p$, viz.,

$$B_r=\frac{\mu_0}{4\pi}\int\mathbf{J}^p(\mathbf{r}')\times\frac{\mathbf{R}}{R^3}\cdot\mathbf{e}_r dv' \ . \tag{31}$$

If the source is a current dipole $\mathbf{Q}$ at $\mathbf{r}_Q$, Eq. (31) reduces to

$$B_r=-\frac{\mu_0}{4\pi}\frac{\mathbf{Q}\times\mathbf{r}_Q\cdot\mathbf{e}_r}{|\mathbf{r}-\mathbf{r}_Q|^3} \ . \tag{32}$$

Furthermore, since $\nabla\times\mathbf{B}=0$ outside the conductor, $\mathbf{B}$ can be derived from the magnetic scalar potential:

$\mathbf{B}=-\mu_0\nabla U$. Since $\nabla\cdot\mathbf{B}=0$, $U$ is harmonic and uniquely determined by its normal derivative on the surface of the conductor and by the requirement that it vanish at infinity. On a sphere, the normal derivative $\partial U/\partial r = -B_r/\mu_0$. Integrating, we find

$$U(\mathbf{r})=\frac{1}{\mu_0}\int_{t=1}^{\infty} B_r(t\mathbf{r})dt \ . \tag{33}$$

This shows that even though the tangential field components are affected by the volume currents in a spherically symmetric conductor, they can be computed without knowing the conductivity profile $\sigma=\sigma(r)$. Derivations of **B**, in rectangular coordinates using Eq. (33), were presented by Ilmoniemi *et al.* (1985) and by Sarvas (1987). The result from the latter publication is

$$\mathbf{B}(\mathbf{r})=\frac{\mu_0}{4\pi}\frac{F\mathbf{Q}\times\mathbf{r}_Q-(\mathbf{Q}\times\mathbf{r}_Q\cdot\mathbf{r})\nabla F(\mathbf{r},\mathbf{r}_Q)}{F(\mathbf{r},\mathbf{r}_Q)^2} \ , \tag{34}$$

where

$$F(\mathbf{r},\mathbf{r}_Q)=a(ra+r^2-\mathbf{r}_Q\cdot\mathbf{r})$$

and

$$\nabla F(\mathbf{r},\mathbf{r}_Q)=(r^{-1}a^2+a^{-1}\mathbf{a}\cdot\mathbf{r}+2a+2r)\mathbf{r} -(a+2r+a^{-1}\mathbf{a}\cdot\mathbf{r})\mathbf{r}_Q \ ,$$

with $\mathbf{a}=(\mathbf{r}-\mathbf{r}_Q)$, $a=|\mathbf{a}|$, and $r=|\mathbf{r}|$.

An important point is seen from Eq. (31). If the primary current is radial, $\mathbf{J}^p(\mathbf{r}')=J^p(\mathbf{r}')\mathbf{r}'/|\mathbf{r}'|$, $B_r$ vanishes. Since $B_r=0$, $U=0$ and thus also $\mathbf{B}=0$. This is true for any axially symmetric current in an axially symmetric conductor (Grynszpan and Geselowitz, 1973). A source in the center of the sphere will produce no magnetic field outside: in Eq. (32), $B_r=0$ if $\mathbf{r}_Q=0$. Note that the properties of **B** cited above for the spherically symmetric conductor are also valid for a horizontally layered conductor $[\sigma=\sigma(z)]$, since this is a limiting case of a sphere. Thus $B_z$ generated by a current dipole located within a horizontally layered conductor is given by

$$B_z=\frac{\mu_0}{4\pi}\frac{\mathbf{Q}\times(\mathbf{r}-\mathbf{r}_Q)\cdot\mathbf{e}_z}{|\mathbf{r}-\mathbf{r}_Q|^3} \ . \tag{35}$$

Therefore, in a spherically symmetric conductor, MEG is sensitive only to the tangential component of the primary current. This means that the method is optimal for detecting activity in fissures.

The electric scalar potential $V$ on the surface of a spherically symmetric conductor is affected by the conductivity profile. For example, if a poorly conducting layer (skull) is placed between two good conductors (brain and scalp), $V$ will be attenuated on the scalp and the potential pattern due to a dipole inside will be more widespread than in a homogeneous sphere. Another difference from **B** is that both radial and deep sources contribute significantly to $V$. Its computation in general requires the evaluation of a series expansion in spherical harmonics (Arthur and Geselowitz, 1970; de Munck, 1988), which is more time consuming than the computation of **B** from the simple analytical expressions.

### 3. Realistically shaped conductor models

If the regions $G_i$ of the piecewise homogeneous conductor are arbitrarily shaped, **B** must be computed numerically. In the boundary element method (BEM), based on Eqs. (22) and (29), each surface $S_i$, here indexed with a single subscript for simplicity, is tessellated into $n_i$ suitable triangles, $\Delta_1^i,\ldots,\Delta_{n_i}^i$ (Barnard *et al.*, 1967; Lynn and Timlake, 1968; Horacek, 1973). Assuming further that the potential is constant, $V(\mathbf{r})=V_k^i$, on each triangle $\Delta_k^i$ and integrating Eq. (29) over one of them, a set of $n_i$ linear equations is obtained for $V_k^i$ at triangles belonging to surface $i$, $k=1,\ldots,n_i$, viz.,

$$\mathbf{V}^i=\sum_{j=1}^{m}\mathbf{H}^{ij}\mathbf{V}^j+\mathbf{g}^i \ . \tag{36}$$

The column vectors $\mathbf{g}^i$ and the matrices $\mathbf{H}^{ij}$ are in this constant-potential approximation defined by

$$g_k^i=\frac{1}{\mu_k^i}\frac{2}{\sigma_i^-+\sigma_i^+}\int_{\Delta_k^i}V_0(\mathbf{r}')dS_i' \tag{37}$$

and

$$H_{kl}^{ij}=\frac{1}{2\pi}\left[\frac{\sigma_j^--\sigma_j^+}{\sigma_i^-+\sigma_i^+}\right]\frac{1}{\mu_k^i}\int_{\Delta_k^i}\Omega_{\Delta_l^j}(\mathbf{r}')dS_i' \ , \tag{38}$$

respectively. Here $\sigma_i^-$ and $\sigma_i^+$ are the conductivities inside and outside surface $S_i$, respectively; $\mu_k^i$ is the area of the $k$th triangle $\Delta_k^i$ on $S_i$; and $\Omega_{\Delta_l^j}(\mathbf{r}')$ is the solid angle subtended by $\Delta_l^j$ at $\mathbf{r}'$ (Barnard *et al.*, 1967; van Oosterom and Strackee, 1983). In practice, $H_{kl}^{ij}$ are often approximated by replacing $\Omega_{\Delta_l^j}(\mathbf{r})$ on each $\Delta_k^i$ by its value at the centroid $\mathbf{c}_k^i$ of the triangle. Alternatively, one can use a numerical integration formula to improve the accuracy (Nenonen *et al.*, 1991). The matrix elements $H_{kl}^{ij}$ depend only on the conductor geometry and thus only the source term $g_k^i$ needs to be recalculated for each source configuration.

The accuracy and speed of BEM can be improved by using higher-order approximations for $V(\mathbf{r})$ on each $\Delta_k^i$. If the potential is allowed to vary linearly within $\Delta_k^i$, we can designate the potential values at the vertices of the tessellated surface as unknowns in the discretization (Urankar, 1990; de Munck, 1992). Since on a closed triangulated surface with $n_i$ triangles we have $n_i'=n_i/2+2$ vertices, the number of equations in (36) drops to about one-half and the computations become, therefore, significantly faster. Furthermore, the potential is now continuous over $S_i$. The exact gains in accuracy and speed are yet to be determined, but we expect that the computational burden can be significantly reduced while retaining at least the same level of precision.

The linear-potential approach highlights two different

aspects in the calculation of $V_k^i$. First, we must have an accurate enough description of the geometry. Second, we shall have to leave enough degrees of freedom for the potential on each surface element to reproduce the high spatial frequencies present in the fields of nearby sources.

Even with a more complex potential variation on $\Delta_k^i$, we suffer from the errors caused by replacing the original smooth surface by a polyhedron. This problem can be alleviated by improving the accuracy of the matrix elements $H_{kl}^{ij}$, which relate the potential values at adjacent elements on the surface $S_j$ (Heller, 1990).

The electric potential is defined only up to an additive constant, which implies that Eq. (36) has no unique solution. This ambiguity can be removed by deflation (Barnard *et al.*, 1967), meaning that the $\mathbf{H}^{ij}$ are replaced by

$$\mathbf{C}^{ij}=\mathbf{H}^{ij}-\frac{1}{N}\mathbf{e}_i\mathbf{e}_j^T , \tag{39}$$

where $\mathbf{e}_i$ is a unit vector with $n_i$ components and $T$ denotes the transpose. The deflated equations have a unique solution, which also applies to Eq. (36). The resulting equations can be solved by an iterative method such as the Gauss–Seidel algorithm. However, as was demonstrated by Oostendorp and van Oosterom (1989), the linear equations can often be solved explicitly, resulting in considerable savings of computing time if the potential of several different sources must be evaluated. Once $V$ on each $S_i$ is available, $\mathbf{B}$ can be obtained from Eq. (22) by direct integration:

$$\mathbf{B}(\mathbf{r})=\mathbf{B}_0(\mathbf{r})+\frac{\mu_0}{4\pi}\sum_{j=1}^{m}(\sigma_j^- -\sigma_j^+)\sum_{k=1}^{n_j}\int_{\Delta_k^j}V(\mathbf{r}')\frac{\mathbf{R}}{R^3}\times d\mathbf{S}_j' . \tag{40}$$

If there is only a single interface, i.e., when one is dealing with a bounded homogeneous conductor, the solution of Eq. (36) is straightforward. However, modeling the head by a poor conductor (the skull) between two much better conductors (the brain tissue and the scalp) requires modifications in the standard numerical approach in order to produce accurate results.

Meijs and Peters (1987) found that numerical errors in computing $V$ may be excessive because the ratio in the conductivity of the skull to that of the brain and the scalp is less than 0.1. The first suggested solution for this numerical instability was the use of the Richardson extrapolation (Richardson and Guant, 1927; Meijs, Peters, *et al.*, 1987). This approach relies on the assumption that the correct potential distribution can be obtained by estimating an asymptote on the basis of two solutions with different grid densities. However, there is no guarantee that the assumption is valid for this particular problem.

Later, Hämäläinen and Sarvas (1989) used the isolated-problem approach, which decomposes the potential on the interfaces as $V(\mathbf{r})=W_0(\mathbf{r})+W(\mathbf{r})$, where $W_0$ is the solution in the case of a perfectly insulating skull and $W(\mathbf{r})$ is a correction term that vanishes as the skull's conductivity approaches zero. With this technique, the numerical calculation of $V(\mathbf{r})$ is divided into two steps: (1) computation of $W_0(\mathbf{r})$, which is the solution for the brain-shaped homogeneous conductor; and (2) solution of the integral equations for $W(\mathbf{r})$.

Simulations presented by Hämäläinen and Sarvas (1989) show that, in a spherically symmetric conductor, the isolated problem yields accurate results. They also demonstrated that the currents in the skull and on the scalp contribute negligibly to $\mathbf{B}$ and proposed that, in practice, it is sufficient to use a brain-shaped homogeneous conductor in the analysis of MEG data.

## IV. INVERSE PROBLEM

### A. General

The neuromagnetic inverse problem is to estimate the cerebral current sources underlying a measured distribution of the magnetic field. We shall limit our discussion to this task and shall not elaborate on the physiological interpretation in this section, although we shall keep constantly in mind that neuromagnetic fields arise in the brain, which imposes constraints on the sources that our measurements might reveal. Many of our results are, however, valid for other applications as well.

We shall use several standard results and terms from linear analysis, numerical mathematics, and estimation theory. For more complete treatment on these methods, we recommend the textbooks by Golub (1989), Press *et al.* (1992), and by Silvey (1978).

It was shown by Helmholtz (1853) that a current distribution inside a conductor $G$ cannot be retrieved uniquely from knowledge of the electromagnetic field outside. There are primary current distributions that are either magnetically silent ($\mathbf{B}=0$ outside $G$), electrically silent ($\mathbf{E}=0$ outside $G$), or both. A simple example of a magnetically silent source that produces an electric field is a radial dipole in a spherically symmetric conductor. An example of the opposite case is a current loop, which is electrically silent but which produces a magnetic field. In general, if $\mathbf{J}^p$ is solenoidal ($\nabla\cdot\mathbf{J}^p=0$), $V=0$ as a consequence of Eq. (18).

If $|\mathbf{J}^p|$ is constant over a closed surface $S$ inside a homogeneous subregion of $G$ and $\mathbf{J}^p$ is normal to $S$, $V_0$ in Eq. (26) will vanish, since

$$\begin{aligned}V_0(\mathbf{r})&=\frac{J^p}{4\pi}\int_S\mathbf{n}(\mathbf{r}')\cdot\nabla'\frac{1}{R}dS'\\&=\frac{J^p}{4\pi}\int_G\nabla'\cdot\nabla'\frac{1}{R}dv'=0 ,\end{aligned} \tag{41}$$

and thus $V=0$. Now $\mathbf{B}$ can be computed from Eq. (20), giving

$$\begin{aligned}\mathbf{B}(\mathbf{r})&=\frac{\mu_0}{4\pi}J^p\int_S\mathbf{n}(\mathbf{r}')\times\nabla'\frac{1}{R}dS'\\&=\frac{\mu_0}{4\pi}J^p\int_G\nabla'\times\nabla'\frac{1}{R}dv'=0 .\end{aligned} \tag{42}$$

Thus this source produces no electromagnetic field outside the conductor.

Because of the nonuniqueness, we must confine ourselves to finding a solution among a limited class of source configurations. Methods for handling this restricted inverse problem are the main subject of this section. Even the limited problem may be difficult to solve in a satisfactory way. Small experimental errors can produce large inaccuracies in the solution: the problem is often ill-conditioned.

### B. Lead field

As was shown in Sec. III.D, both **B** and **E** are linearly related to $\mathbf{J}^p$. Thus, if $b_i$ is the output of a magnetometer, there is a vector field $\mathcal{L}_i(\mathbf{r})$ satisfying

$$b_i = \int \mathcal{L}_i(\mathbf{r})\cdot\mathbf{J}^p(\mathbf{r})dv \ . \tag{43}$$

$\mathcal{L}_i$ is called the lead field; it describes the sensitivity distribution of the $i$th magnetometer (Malmivuo, 1976; Tripp, 1983). $\mathcal{L}_i$ depends on the conductivity $\sigma=\sigma(\mathbf{r})$ and on the coil configuration of the magnetometer.

Similarly, if $V_i$ is a potential difference between two electrodes, we can find the corresponding electric lead field $\mathcal{L}_i^E$ such that

$$V_i = \int \mathcal{L}_i^E(\mathbf{r})\cdot\mathbf{J}^p(\mathbf{r})dv \ . \tag{44}$$

The lead field, as defined by Eq. (43), is readily obtained if one is able to compute the magnetic field $\mathbf{B}=\mathbf{B}(\mathbf{Q},\mathbf{r}')$, caused by any dipole **Q** at any position $\mathbf{r}_Q$. This requires knowledge of the conductivity distribution $\sigma(\mathbf{r})$ so that the effect of volume currents can be properly taken into account. For **Q** at $\mathbf{r}_Q$, $\mathbf{J}^p(\mathbf{r})=\mathbf{Q}\delta(\mathbf{r}-\mathbf{r}_Q)$. Inserting this dipolar primary current distribution into Eq. (43), we obtain

$$B_i(\mathbf{Q},\mathbf{r}_Q)=\mathcal{L}_i(\mathbf{r}_Q)\cdot\mathbf{Q} \ . \tag{45}$$

From this relation, all three components of $\mathcal{L}_i(\mathbf{r}_Q)$ can be found for any $\mathbf{r}_Q$.

If the magnetometer consists of a set of planar coils with normals $\mathbf{n}_j$, $j=1,\ldots,m$, we find

$$B_i(\mathbf{Q},\mathbf{r}_Q)=\sum_{j=1}^{m}\int_{S_j}\mathbf{B}(\mathbf{Q},\mathbf{r}_Q)\cdot\mathbf{n}_j dS_j \ , \tag{46}$$

where the directions of the normals $\mathbf{n}_j$ have been chosen to take correctly into account the winding sense of the coils, so that a field satisfying $\mathbf{B}\cdot\mathbf{n}_j>0$ yields a positive signal at the output. The integration extends over $S_j$, the area of coil $j$.

As an illustration of the form of $\mathcal{L}_i(\mathbf{r})$, Fig. 19 shows the lead fields of magnetometers on the $z$ axis which are sensitive to the radial field component $B_z$, the tangential field component $B_x$, and a tangential derivative of the radial field component, $\partial B_z/\partial x$. We assume a spherically symmetric conductor and display the lead field distributions on one shell.

### C. Value of different measurements

$B_r$ can be calculated for a spherically symmetric conductor directly from $\mathbf{J}^p$ with the Ampère–Laplace law. However, as was shown in Sec. III.E.2, the two tangential components also can be obtained analytically, without any reference to the actual conductivity profile $\sigma(\mathbf{r})=\sigma(r)$. This means that, from the computational point of view, all field components can be utilized easily and that there is no preferred component.

One of the first derivations of the magnetic field due to current dipoles in conductors of simple shapes was presented by Cuffin and Cohen (1977). They concluded that $B_r$ should be preferred in practical measurements because of the zero contribution from volume currents. This would be the case if nonidealities in the conductor geometry would distort the tangential components more than $B_r$, so that by measuring just the radial field one could justify the use of the simple sphere model in a wide range of actual conductor shapes. However, there is no evidence to support this conjecture.

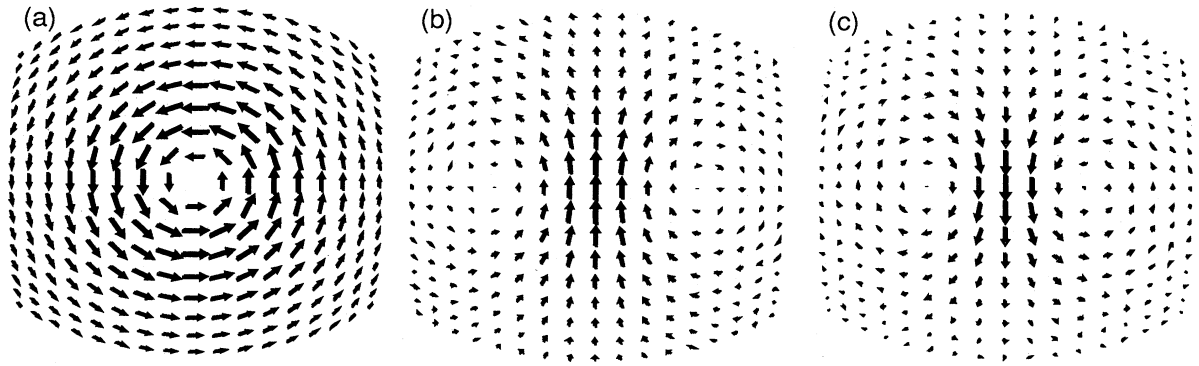


FIG. 19. Two-dimensional projections of the lead field $\mathcal{L}(\mathbf{r})$ of point magnetometers measuring (a) $B_z$, (b) $B_x$, and (c) of a gradiometer measuring $\partial B_z/\partial x$, sampled on a surface whose radius is 90 mm. Each signal coil is located at $x=y=0$, $z=125$ mm.

It has been shown (Hari and Ilmoniemi, 1986) that the sphere model gives good results even if the actual conductor is spheroidal, provided that the sphere model is fitted to the local radius of curvature in the area of interest. Later, simulations with realistically shaped conductor models (Hämäläinen and Sarvas, 1989) showed that nonidealities in the conductor shape produce equal distortions in all three components of the magnetic field. This result is, of course, to be expected from the fact that any component of the field can be computed from the distribution of any other component by integrating Eq. (6) in the current-free space outside the source region.

Instead of measuring just one or two components of **B**, one can also design short-baseline coils to measure their derivatives. An example is the so-called 2D coil (Cohen, 1979), which senses an off-diagonal derivative, such as $\partial B_z/\partial x$ [see Fig. 7(c)]. A multichannel gradiometer with pairs of such coils, orthogonally oriented at 12 locations, has been developed (Kajola *et al.*, 1989; Ahonen *et al.*, 1991; see Fig. 37). Simulations (Knuutila and Hämäläinen, 1989) and actual measurements have shown that this arrangement is highly effective. Furthermore, since the gradient $\sqrt{(\partial B_z/\partial x)^2+(\partial B_z/\partial y)^2}$ ($z$ is the sensitivity axis of a detector) peaks right above a current-dipole source, a less extensive set of sensors is needed to pick up the essential field data from a local source (see Fig. 27).

### D. Comparison of magnetoencephalography and electroencephalography

Although no final evaluation of the capabilities of MEG and EEG can be given at present, several important differences as well as similarities of the two methods may be stated with confidence.

As was shown in Sec. IV.B, both EEG and MEG provide a projection of the primary current distribution on the respective lead fields. Thus MEG and EEG are formally on an equal footing. Both techniques measure weighted integrals of the primary current distribution. Their differences are the following:

(1) The lead fields $\mathcal{L}_i$ and $\mathcal{L}_i^E$ are different. In the spherical model, MEG is sensitive only to the tangential component of $\mathbf{J}^p$, i.e., $\mathcal{L}_i \cdot \mathbf{r}=0$, whereas EEG senses all primary current components. In addition, the magnitude of $\mathcal{L}_i$ falls off more quickly than $\mathcal{L}_i^E$ near the center of the sphere, $\mathcal{L}_i=0$ at the origin.

(2) $\mathcal{L}_i^E$ is affected by the conductivities of the skull and the scalp much more than $\mathcal{L}_i$. Therefore, interpretation of EEG signals will require more precise knowledge of the thicknesses and conductivities of the tissues in the head. In the spherical model, concentric inhomogeneities do not affect the magnetic field at all, whereas they have to be taken into account in the analysis of EEG data.

(3) The instrumentation necessary for MEG is more sophisticated and, therefore, more expensive than that for EEG.

(4) MEG measurements can be accomplished more quickly, since no electrode contact to the scalp needs to be established. On the other hand, the subject has to be immobile during the MEG measurements, whereas telemetric and long-term EEG recordings are possible.

The absolute accuracies of both EEG and MEG source determinations are, at present, a somewhat open question, based on simulations and theoretical calculations on one hand, and on experiments with several technical deficiencies on the other.

A recent example about the controversial aspects of comparisons between MEG and EEG is the discussion evoked by a paper by Cohen *et al.* (1990). These authors claimed that MEG is only marginally more accurate than EEG in locating cerebral electrical activity. The paper has been criticized by Hari *et al.* (1991) and by Williamson (1991) on methodological grounds. More comprehensive discussions of this topic are available (Anogianakis *et al.*, 1992; van den Noort *et al.*, 1992).

In their study, Cohen and co-workers had the rare opportunity to form artificial current dipoles inside patients' heads by feeding current through depth electrodes that had been inserted into the brains of several epileptic patients to monitor their abnormal cerebral activity. The precise position of each source was determined from roentgenograms. A definite comparison between the ability of MEG and EEG to locate the sources thus appeared possible.

Cohen *et al.* (1990) measured the electric field with 16 scalp electrodes and the magnetic field with a single-channel rf SQUID magnetometer from 16 sites outside the head. The locations of the test dipoles were calculated on the basis of MEG and EEG measurements, respectively. An 8-mm average error for MEG and a 10-mm error for EEG source location were reported.

The critique of the study of Cohen and co-workers can be summarized as follows.

(1) Nearly radial current dipoles, optimal for EEG but barely detectable by MEG, were used as test sources. As a result, the signal-to-noise ratio for MEG was reduced considerably.

(2) The dipoles were 16 mm long, although they were assumed to be pointlike in the data analysis. This affects EEG results as well, but also tends to obscure possible differences between the capabilities of MEG and EEG.

(3) The magnetic field was inappropriately sampled.

(4) Twice as many signals were averaged for EEG than for MEG, which gave further advantage to EEG in the comparison.

(5) No attempt to fit the sphere model to the local curvature of the head was reported. This alone may cause an uncertainty comparable to the total reported error.

(6) No error estimates were given for the "real" source locations determined from the roentgenograms.

Two of the test sources happened to be tangential. The reported error in the magnetic site determinations was only 5.5 mm. This remaining uncertainty can be fully accounted for by the experimental inadequacies mentioned

above. Therefore, the results reported by Cohen *et al.* (1990) actually support the superiority of MEG in locating a tangential dipole source. This is in line with the 3-mm maximum error found by Yamamoto *et al.* (1988) in locating dipoles within a sphere and a model skull. Furthermore, these authors reported a similar precision in determining the site of a cortical source. Unfortunately, similar model experiments are much harder to perform for EEG, because the conductivity distribution of the skull and scalp is difficult to implement in a model head.

EEG and MEG are complementary in the sense that measurement with one technique will not always reveal everything that can be found with the other method. Therefore, the best results are obtained by combining information from both techniques.

### E. Combination of magnetoencephalography with tomographic imaging methods

Computer-assisted x-ray tomography (CAT) and magnetic-resonance imaging (MRI) provide accurate images of the brain's anatomy with millimeter resolution. Positron-emission tomography (PET) gives information about metabolic activity with a spatial resolution of about 4 mm, but the time resolution is tens of seconds.

One can foresee the combination of these imaging methods with MEG and EEG at several levels. Provided that the coordinate systems for MEG and MRI have been aligned, one can superimpose the locations of brain activity, found by MEG, on the MRI's (George *et al.*, 1989; Schneider *et al.*, 1989; Suk *et al.*, 1989; Hämäläinen, 1991). It is then possible to compare the locations of source estimates with the actual sites of anatomical structures (see Fig. 20) or in patients with pathological findings within the brain.

High-quality anatomical images allow the use of individually shaped realistic conductor models. Here, however, one meets serious practical difficulties. For example, reliable automatic segmentation of the shape of the brain from MRI's is not trivial. At present, some human intervention is needed to produce correct results. With the outline of the structure of interest at hand, it is relatively easy to construct the corresponding triangulation needed for boundary element modeling. Up to now, MRI's have been used this way only in special cases (see, for example, Meijs, 1988).

The accuracy of the inverse problem solutions can be improved by bringing in complementary information to restrict the set of possible source configurations. With the assumption that MEG mainly reflects the activity in the tangential part of cortical currents, one could, at least in principle, extract the geometry of the cortex from MR images and use the result as a constraint in the source estimation procedures.

### F. Probabilistic approach to the inverse problem

#### 1. The general solution

A study of the restricted inverse problem involves estimation theory: the unknown current sources must be found on the basis of noisy and incomplete measurements. Furthermore, *a priori* information and modeling inaccuracies need to be incorporated into the analysis.

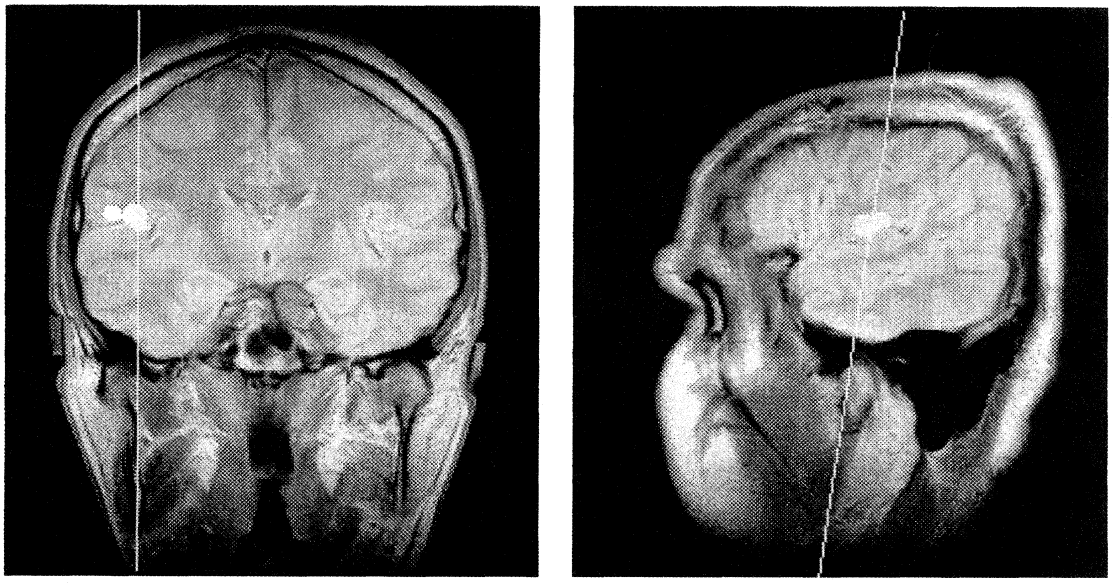

FIG. 20. Example of source locations superimposed on coronal (a) and sagittal (b) MR images. The white lines indicate transsection levels of the companion slice. The white dots show positions of equivalent current dipoles corresponding to the 100-ms deflections of auditory evoked responses in independent repeated measurements. All source locations are within a sphere of 15 mm in diameter (Hämäläinen, 1991).

Before describing any source estimation methods, it is instructive to give a mathematical discussion of the relevant concepts. With this solid foundation we can then more easily formulate the underlying assumptions and establish the theoretical validity of the practical methods used in source analysis.

A general probabilistic approach to problems of this kind has been introduced (Tarantola and Valette, 1982; Tarantola, 1987) and also applied to the neuromagnetic inverse problem (Clarke, 1989). This method is sometimes called "Bayesian," although the approach of Tarantola (1987), on which the following treatment is based, is more general.

We assume that the unknown current distribution can be identified by a finite-dimensional parameter vector $\mathbf{x}$ and the magnetic field to be measured by a vector $\mathbf{b}$. The actual observation, disturbed by noise, is denoted by $\mathbf{b}_{\text{obs}}$. Before and after the measurement, the statistics of $\mathbf{x}$ are described with prior and posterior distributions, respectively. The corresponding probability density functions will be denoted by $\rho_x(\mathbf{x})$ and $\psi_x(\mathbf{x})$.

We shall assume a measurement with known noise statistics; i.e., for any $\mathbf{b}$, we know the conditional density $\nu(\mathbf{b}_{\text{obs}}|\mathbf{b})$. The forward model is described by $\theta(\mathbf{b}|\mathbf{x})$, giving the chances for $\mathbf{b}$ to occur for a given $\mathbf{x}$. With these assumptions one can show (Tarantola, 1987) that the posterior density is

$$\psi_x(\mathbf{x})=C_0\rho_x(\mathbf{x})\int \nu(\mathbf{b}_{\text{obs}}|\mathbf{b})\theta(\mathbf{b}|\mathbf{x})d\mathbf{b} \ , \tag{47}$$

where $C_0=1/[\int \rho_x(\mathbf{x})\int \nu(\mathbf{b}_{\text{obs}}|\mathbf{b})\theta(\mathbf{b}|\mathbf{x})d\mathbf{b}\,d\mathbf{x}]$ is a normalization constant.

Equation (47) nicely separates the sources of information giving rise to $\psi_x(\mathbf{x})$. First, the *a priori* knowledge of $\mathbf{x}$ is embedded in $\rho_x(\mathbf{x})$. Second, the measurement noise, which gives rise to deviations from the correct values, is accounted for by $\nu(\mathbf{b}_{\text{obs}}|\mathbf{b})$. Finally, since the forward model is described by the probability density $\theta(\mathbf{b}|\mathbf{x})$, it is, at least in principle, straightforward to include modeling uncertainties such as an imprecisely known conductor geometry.

If, in addition, the errors of the instrument are independent of input, i.e., $\mathbf{b}_{\text{obs}}=\mathbf{b}+\eta_b$ and $\eta_b$ is described by a known probability density function $f_b(\eta_b)$, $\nu(\mathbf{b}_{\text{obs}}|\mathbf{b})=f_b(\eta_b)$ and Eq. (47) becomes

$$\psi_x(\mathbf{x})=C_0\rho_x(\mathbf{x})\int f_b(\mathbf{b}_{\text{obs}}-\mathbf{b})\theta(\mathbf{b}|\mathbf{x})d\mathbf{b} \ . \tag{48}$$

Assuming now a model function $\mathbf{b}=\mathbf{g}(\mathbf{x})$ which accurately describes the forward problem, e.g., the computation of the magnetic field of a current dipole in the sphere model, we can take $\theta(\mathbf{b}|\mathbf{x})=\delta(\mathbf{b}-\mathbf{g}(\mathbf{x}))$, where $\delta(\mathbf{x})$ is again the Dirac delta function and, consequently,

$$\psi_x(\mathbf{x})=C_0\rho_x(\mathbf{x})f_b(\mathbf{b}_{\text{obs}}-\mathbf{g}(\mathbf{x})) \ . \tag{49}$$

### 2. Gaussian errors

If $\eta_b$ is normally distributed, its probability distribution is completely determined by the covariance matrix $\boldsymbol{\Sigma}=E\{\eta_b\eta_b^T\}$ and by the mean $E\{\eta_b\}$, which is assumed to be zero. Under these assumptions, $\psi_x(\mathbf{x})$ corresponding to the measurement $\mathbf{b}_{\text{obs}}$ is

$$\psi_x(\mathbf{x})=C_0\rho_x(\mathbf{x})\exp\{-\tfrac{1}{2}[\mathbf{b}_{\text{obs}}-\mathbf{g}(\mathbf{x})]^T\boldsymbol{\Sigma}^{-1}[\mathbf{b}_{\text{obs}}-\mathbf{g}(\mathbf{x})]\} \ . \tag{50}$$

If the only *a priori* information about $\mathbf{x}$ is that it is confined to a given region, $\rho_x(\mathbf{x})$ can be assumed constant in this volume and zero elsewhere. With $\rho_x$ constant, it is readily seen that the maximum-likelihood estimate (MLE) $\mathbf{x}_0$ for $\mathbf{x}$, corresponding to the maximum *a posteriori* density, is found by minimizing the weighted sum of squares

$$S(\mathbf{x})=[\mathbf{b}_{\text{obs}}-\mathbf{g}(\mathbf{x})]^T\boldsymbol{\Sigma}^{-1}[\mathbf{b}_{\text{obs}}-\mathbf{g}(\mathbf{x})] \ , \tag{51}$$

i.e., through the conventional least-squares search. If the neural source is modeled by a current dipole, the MLE is commonly called the equivalent current dipole (ECD).

If $\mathbf{g}(\mathbf{x})$ is a nonlinear function, the parameter vector $\mathbf{x}_0$ can be found using some iterative numerical technique, for example, the Marquardt (1963) algorithm. On the other hand, if $\mathbf{g}(\mathbf{x})$ is linear, i.e., $\mathbf{g}(\mathbf{x})=\mathbf{A}\mathbf{x}$, where $\mathbf{A}$ is a matrix, $\mathbf{x}_0$ can be obtained directly by multiplying the measurement $\mathbf{b}_{\text{obs}}$ by the pseudoinverse of $\mathbf{A}$ (Albert, 1972), i.e., $\mathbf{x}_0=\mathbf{A}^{\dagger}\mathbf{b}_{\text{obs}}$.

According to the Gauss–Markov theorem (Silvey, 1978), the MLE minimizing $S(\mathbf{x})$ is also the minimum-variance linear unbiased estimator for $\mathbf{x}$, provided that $\mathbf{g}(\mathbf{x})$ is a linear function of $\mathbf{x}$. The treatment presented above shows that, under the assumption of Gaussian errors, the least-squares estimate is well established even if $\mathbf{g}(\mathbf{x})$ is nonlinear.

### 3. Alternative assumptions for noise

The above derivation, which started from the general equation for the posterior density, Eq. (47), allows us to incorporate more general or alternative assumptions at any stage of the computation. For example, if we expect that there will be outliers in the measured data, we might consider a long-tailed probability density for the measurement errors, e.g., the exponential density

$$f_b(\eta_b)=C_0\exp\left[-\sum_i |\eta_i|/\sigma_i\right] \ , \tag{52}$$

where $\sigma_i=E\{\eta_i^2\}$. We then obtain an estimate for the parameters $\mathbf{x}$ that is robust against outliers in $\mathbf{b}$. If we want to find the MLE, the criterion corresponding to Eq. (51) is now

$$R(\mathbf{x})=\sum_i |\mathbf{b}_{\text{obs},i}-\mathbf{g}_i(\mathbf{x})|/\sigma_i \ , \tag{53}$$

which is often called the $L_1$-norm criterion.

### 4. Confidence regions

In addition to the MLE, we would also like to determine a confidence region for $\mathbf{x}$. The Bayesian confidence

region is defined as the smallest collection of values of $\mathbf{x}$ making up a given total posterior probability (Silvey, 1978). This region contains the most probable parameter vectors on the basis of a given measurement, and thus any value outside it is less plausible than any value inside. If $\mathbf{g}(\mathbf{x})$ is nonlinear, the Bayesian confidence region is tedious to compute. One possibility of finding this region is by appropriately sampling $\psi(\mathbf{x})$ and then sorting the values in decreasing order. The points corresponding to the highest probabilities then make up the confidence region.

If $\mathbf{g}(\mathbf{x})$ is linear and the errors are Gaussian, the determination of the Bayesian confidence region becomes much easier. The linear approximation may also be used if $\mathbf{g}(\mathbf{x})$ in the vicinity of $\mathbf{x}_0$ can be reasonably well approximated by

$$\mathbf{g}(\mathbf{x}) \simeq \mathbf{J}(\mathbf{x}-\mathbf{x}_0)+\mathbf{g}(\mathbf{x}_0) , \tag{54}$$

where $\mathbf{J}$ is the Jacobian of $\mathbf{g}(\mathbf{x})$ at $\mathbf{x}_0$: $J_{ij}=\partial g_i/\partial x_j|_{\mathbf{x}=\mathbf{x}_0}$. It can then be shown (Sarvas, 1987) that the $p$-percentage confidence region for $\mathbf{x}$ is an $\mathbf{x}_0$-centered $m$-dimensional ellipsoid given by

$$(\mathbf{x}-\mathbf{x}_0)^T\mathbf{Q}(\mathbf{x}-\mathbf{x}_0) < c_m^2 , \tag{55}$$

where $c_m^2$ is the $p$-percentage point of the $\chi_m^2$-distribution and $\mathbf{Q}=\mathbf{J}^T\boldsymbol{\Sigma}^{-1}\mathbf{J}=\mathbf{V}^T\boldsymbol{\Lambda}^{-2}\mathbf{V}$, the last form being the eigenvalue decomposition. The ellipsoid can be characterized by its volume, which is given by the product of the diagonals of $\Lambda$, times a constant that depends on $m$. Alternatively, one could determine the size of the smallest rectangular box whose faces are parallel to the coordinate planes.

In practice one is often interested in finding the extremal values of some linear combination $\alpha=\mathbf{a}^T\mathbf{x}$ of the model parameters in the confidence ellipsoid. It can be shown (Sarvas, 1987) that these limits are given by

$$\begin{aligned}|\mathbf{a}^T(\mathbf{x}-\mathbf{x}_0)| &< c_m^2\sqrt{\mathbf{a}^T\mathbf{V}^T\boldsymbol{\Lambda}^2\mathbf{V}\mathbf{a}} \\ &= c_m^2\sqrt{\mathbf{a}^T\mathbf{Q}^{-1}\mathbf{a}} .\end{aligned} \tag{56}$$

For instance, to determine the confidence limits for $x_i$, we take $\mathbf{a}=(\delta_{1i},\ldots,\delta_{ni})^T$, where $\delta_{ij}$ is the Kronecker delta function, giving $|x_i-x_{0i}| < c_m^2\sqrt{Q_{ii}^{-1}}$.

### 5. Marginal distributions

Instead of using the maximum-likelihood estimate and the Bayesian confidence set to characterize $\psi_x(\mathbf{x})$, it is sometimes useful to study $\psi_x(\mathbf{x})$ itself. However, since it has many variables, the form of $\psi_x(\mathbf{x})$ is generally very hard to imagine. The problem can be overcome by studying some marginal densities of $\psi_x(\mathbf{x})$. In this case the probability densities are computed via integration over a subset $x_{k_1},\ldots,x_{k_p}$, $1\le p<n$, of the components of $\mathbf{x}$. The resulting marginal density $\psi_m$ is a function of the remaining variables $x_{k_{p+1}},\ldots,x_{k_n}$ only, viz.,

$$\begin{aligned}\psi_m &= \psi_m(x_{k_{p+1}},\ldots,x_{k_n}) \\ &= \int\cdots\int \psi(\mathbf{x})dx_{k_1}\cdots dx_{k_p} .\end{aligned} \tag{57}$$

In practice, the computation of marginal densities is a tedious task, since it involves numerical integration over multiple variables. However, if $\mathbf{g}(\mathbf{x})$ is a linear function, it can be integrated analytically. Moreover, if $\mathbf{x}$ can be decomposed into two parts, $\mathbf{x}_1=(x_{k_1},\ldots,x_{k_p})^T$ and $\mathbf{x}_2=(x_{k_{p+1}},\ldots,x_{k_m})^T$, so that the dependence of $g$ on $\mathbf{x}_2$ is linear, i.e.,

$$\mathbf{g}(\mathbf{x}) = \mathbf{A}(\mathbf{x}_1)\mathbf{x}_2 , \tag{58}$$

the integration over $\mathbf{x}_2$ can be performed analytically (Hämäläinen *et al.*, 1987). If the source model consists of $k$ current dipoles, the linear part contains the components of the dipoles and the nonlinear part their locations. Then $\psi_m(\mathbf{x}_1)=\psi_m(x_1,y_1,z_1,\ldots,x_k,y_k,z_k)$ is the marginal density of all dipole locations. If the model consists of only one dipole, $\psi_m$ is a function of three variables and one can easily plot its contour lines, for example, on a set of parallel planes. If there are several dipoles, it is, in principle, possible to integrate numerically over all but one of their locations to reduce the number of variables to three.

Using marginal densities, one can also consider the confidence limits for a single parameter which describe the variance of one parameter when the others are allowed to attain any values. Assuming a constant $\rho_x(\mathbf{x})$ and the linearization given by Eq. (54), it is straightforward to show that the posterior density of Eq. (50) can be integrated over all but one of the parameters $x_1,\ldots,x_m$. The marginal density for $x_k$ then becomes

$$\psi_m(x_k)=\frac{1}{\sqrt{2\pi}\tilde{\sigma}_k}\exp\left[-\frac{(x_k-x_{0k})^2}{2\tilde{\sigma}_k^2}\right] , \tag{59}$$

where $\tilde{\sigma}_k=\sqrt{(Q^{-1})_{kk}}$. It is easy to see that the $p$-percentage confidence interval for $x_k$ is

$$|x_k-x_{0k}| < c\tilde{\sigma}_k , \tag{60}$$

where $c$ is chosen from the $x\sim N(0,1)$ distribution so that $P\{|x|<c\}=p/100$.

## G. The equivalent current dipole

### 1. Finding dipole parameters

The dipolar appearance of the magnetic-field pattern due to a localized cortical current source was first revealed in a study of the somatosensory evoked field (Brenner *et al.*, 1978). The estimates of the location, amplitude, and orientation of the dipole were based on a simple geometrical construction utilizing the shape of the field map. If $B_z$ is measured on the plane $z=z_0$ above a

horizontally layered conductor, the relation between the field pattern and the dipolar source is particularly simple. The dipole lies below the midpoint of the field extrema and is perpendicular to the plane passing through the minimum and the maximum and parallel to the $z$ axis. It can be shown easily that the depth $d$ of the dipole is related to the distance $\Delta$ between the extrema by $d=\Delta/\sqrt{2}$. A similar approach can be used for a dipole embedded in a spherical conductor (Williamson and Kaufman, 1981).

The standard method of estimating the location of a simple source is to determine the equivalent current dipole by a nonlinear least-squares search (Tuomisto *et al.*, 1983). In the so-called moving-dipole model, the source is assumed to be dynamic so that its location, orientation, and strength are allowed to change with time. The data are fitted separately for each time instant, with temporal correlations ignored.

The dipole model is useful even for identifying multiple, simultaneously active sources lying far away from each other, as demonstrated by measurements of activity in the first and second somatosensory cortices S1 and S2 (Hari *et al.*, 1984). In this case the orientations of the sources are particularly favorable for MEG. When both S1 and S2 are simultaneously active, the latter in both hemispheres, the magnetic-field pattern for each dipole is distinct and the existence of three separate sources is evident. In contrast, the electric potential distributions are smeared and largely overlapping, which makes it difficult to see that there are, indeed, three spatially separated sources (see Sec. VI.C.2 and Figs. 54 and 55).

### 2. Estimation of noise

We saw in Sec. IV.F that estimates of noise levels as well as their correlations are needed, both in the least-squares fitting and in the confidence-region calculations, to establish the proper covariance matrix $\Sigma$. Below we shall assume no correlations between the channels. Therefore, $\Sigma=\mathrm{diag}(\sigma_1,\ldots,\sigma_n)$, where the $\sigma_i$'s contain the effects of both the environmental (see Sec. V.A) and subject noise sources (see Sec. I.E).

We can use several approaches to find the noise level estimates for individual channels. If we are averaging several responses, $\sigma_i$ may be obtained from the standard errors of the mean. However, if we apply digital filtering to the data, individual responses must be filtered *before* computing the standard errors, which is a nonlinear operation and, therefore, does not commute with filtering.

If our data have a base line containing only background activity, we can simply use the values sampled within the base line and calculate their standard deviation. However, we lose information about any time dependence of $\sigma_i$, such as possible variations of incoherent background activity during the response.

Still another possibility is to compute alternating subaverages of the evoked responses by reversing the sign of every second response. If the length of the subaverages is kept small, the responses are likely to be very similar and one obtains an estimate for the noise. Since one is now dealing with a linear operation, digital filters can be applied to the subaverages to account correctly for their effects. The outcome of the model validation tests and the sizes of the confidence regions depend crucially on the reliability of the $\sigma_i$'s. Therefore, we suggest that several methods should be applied and their results compared.

### 3. Validity of the model

To describe how well the field pattern of an equivalent current dipole, which is determined by means of a least-squares search, agrees with the experimental data, the goodness-of-fit value,

$$g=1-\sum_{i=1}^{n}(b_i-\hat{b}_i)^2\Big/\sum_{i=1}^{n}b_i^2\ , \tag{61}$$

is used; here $b_1,\ldots,b_n$ are the experimental data and $\hat{b}_1,\ldots,\hat{b}_n$ are the values given by the equivalent dipole. This choice of $g$ is analogous to the measure widely used in linear regression analysis (Kaukoranta, Hämäläinen, *et al.*, 1986). If $g=1$, the model agrees completely with the measurement. If $g=0$, the model is irrelevant and does not describe the measurements any better than a zero field would. Deviations of $g$ from 1 are caused by measurement noise and by the inadequacy of the source model.

With reliable estimates for $\sigma_i$ it is also useful to consider the $\chi^2$ value:

$$\chi^2_{\mathrm{obs}}=\sum_{i=1}^{n}\frac{(b_i-\hat{b}_i)^2}{\sigma_i^2}\ . \tag{62}$$

With Gaussian errors in the measured data, $\chi^2_{\mathrm{obs}}$ is distributed as $\chi^2_{n-r}$, where $r$ is the number of model parameters. For a dipole in a spherically symmetric conductor, $r=5$. The probability $P_{\mathrm{obs}}=P\{\chi^2_{n-r}<\chi^2_{\mathrm{obs}}\}$ then gives a quantitative measure for the goodness of the model. If $P_{\mathrm{obs}}\approx 1$, the model represents the data well and adding more sources is not reasonable. Correspondingly, a low probability indicates that the dipole model is unsatisfactory. However, with our relatively small $n$, $P_{\mathrm{obs}}$ changes quite rapidly from 0 to 1 when the $\sigma_i$'s increase. Therefore, if the noise levels are over- or underestimated, one easily obtains misleading results (Supek and Aine, 1993). Overestimation of $\sigma_i$ leads to missing some of the details in the actual source configuration, while their underestimation may fool the experimenter to a more complex model than is actually allowed by the noisy data.

### 4. Confidence limits

The problem of finding suitable and adequate confidence limits for the dipole model has been discussed by several authors (Okada *et al.*, 1984; Kaukoranta, Hämäläinen, *et al.*, 1986; Hämäläinen *et al.*, 1987; Stok,

1987; Hari, Joutsiniemi, and Sarvas, 1988). Stok compared the single-parameter linear confidence limits of Eq. (60) with those given by a Monte Carlo experiment. His data are, at least qualitatively, in agreement with Hari *et al.*, who showed that the true Bayesian confidence set will be highly nonsymmetrical (banana-shaped) in the dipole-depth–dipole-strength plane (see Fig. 21). The same is also evident from a comparison of the linear and nonlinear confidence sets (Hämäläinen *et al.*, 1987). Therefore, care must be exercised when the accuracy of estimates for the current dipole depth is determined. However, for superficial current sources it is sufficient to consider the linear approximation given by Eqs. (55) and (56).

It is useful to calculate the confidence limits in the longitudinal direction (in the direction of the ECD), in the transverse direction (perpendicular to the dipole and its location vector), and in depth (along the location vector). Comparing the limits given by Eq. (56) in these three directions, one finds that the deviation in the transverse direction is smallest, being about half of the deviations in the longitudinal direction and in depth. This difference can be qualitatively understood from the effect that dipole displacements have on the field pattern (Cohen and Cuffin, 1983).

Another point of concern is the resemblance between the field distributions produced by a single dipole, a side-by-side dipole pair, and a dipole distribution along a line. Simulations indicate (Cuffin, 1985) that the application of the single-dipole model to the interpretation of the field produced by a side-by-side distributed source results in an equivalent dipole that is deeper and stronger than the actual one (Okada, 1985). This is a serious problem, since the modeling error is only weakly reflected in the goodness-of-fit measure $g$ (Hari, Joutsiniemi, and Sarvas, 1988).

### H. Multidipole models

#### 1. Formulation of the problem

The obvious generalization of the single-dipole model is an assumption of multiple, spatially separated dipolar sources. If the distance between the individual dipoles is sufficiently large ($>4$ cm) and their orientations are favorable, the field patterns may show only minor overlap and they can be fitted individually using the single-dipole model. An example of this approach is the separation of activities from the first and second somatosensory cortices (Sec. VI.C.2). Similarly, if the temporal behaviors of the dipoles differ, it is often possible to recognize each source separately.

However, when the sources overlap both temporally and spatially, we must resort to a multidipole calculation to obtain correct results. An effective approach to this modeling problem is to take into account the spatiotemporal course of the signals as a *whole* instead of considering each time sample *separately*. This method was first applied to EEG analysis (for a review, see Scherg, 1990), but the same approach can be used in MEG studies as well (Scherg *et al.*, 1989).

The basic assumption of the model is that there are several dipolar sources that maintain their position and, optionally, also their orientation throughout the time interval of interest. However, the dipoles are allowed to change their amplitudes in order to produce a field distribution that matches the experimental values.

We shall denote the measured and predicted data by the matrices $M_{jk}$ and $B_{jk}$, respectively, where

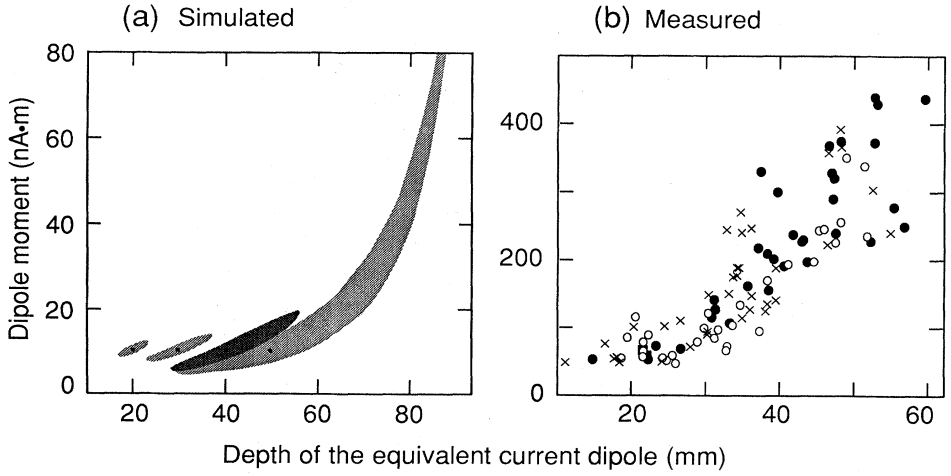


FIG. 21. Correlation between strength and depth of a dipole. (a) Simulated 95% confidence regions in the dipole-depth–dipole-strength plane. A 10-nA m dipole was placed either 20, 30, 40, or 50 mm beneath the surface in a spherical conductor with 100-mm radius. The noise level was 30 fT. (b) Depth-strength dependence of ECDs for different magnetic phenomena [magnetic counterparts of K-complexes (○), vertex waves (●), and slow waves (×) observed during sleep]. The source determination was based on nonaveraged spontaneous signals, and the strongest depth-strength dependence is illustrated. Modified from Hari (1991a).

$j=1,\ldots,n$ indexes the measurement points and $k=1,\ldots,m$ corresponds to the time instants $t_k$ under consideration. We seek the minimum for the conventional least-squares error function

$$S=\|\mathbf{M}-\mathbf{B}(x_1,\ldots,x_q)\|_F^2 , \tag{63}$$

where $x_1,\ldots,x_q$ are the unknown model parameters, whereas $\|\cdot\|_F^2$ denotes the square of the Frobenius norm:

$$\|\mathbf{A}\|_F^2=\sum_{i=1}^{n}\sum_{j=1}^{m}A_{ij}^2=\mathrm{Tr}(\mathbf{A}^T\mathbf{A}) . \tag{64}$$

We assume $p$ dipoles located at $\mathbf{r}_d$, $d=1,\ldots,p$, and further restrict our attention to the spherical conductor model so that any measurement is insensitive to radially oriented dipoles. There will be $p_1$ fixed-orientation dipoles and $p_2$ dipoles with a variable orientation ($p=p_1+p_2$). Therefore, we want to retrieve $r=p_1+2p_2$ dipole wave forms, one for each fixed-orientation and two for each variable-orientation dipole.

With these assumptions, the data predicted by the model can be written as

$$\mathbf{B}^{(n\times m)}=\mathbf{G}^{(n\times 2p)}(\mathbf{r}_1,\ldots,\mathbf{r}_p)\mathbf{R}^{(2p\times r)}\mathbf{Q}^{(r\times m)} , \tag{65}$$

where the dimensions of each matrix appear as superscripts. Here $\mathbf{G}$ is a gain matrix composed of the unit dipole signals

$$G_{j,2d-1}=b_j(\mathbf{r}_d,\mathbf{e}_\theta) ,$$
$$G_{j,2d}=b_j(\mathbf{r}_d,\mathbf{e}_\varphi),\quad d=1,\ldots,p,\quad j=1,\ldots,n , \tag{66}$$

where $b_j(\mathbf{r}_d,\mathbf{e}_\theta)$ and $b_j(\mathbf{r}_d,\mathbf{e}_\varphi)$ are the signals that would be produced by unit dipoles at $\mathbf{r}_d$, pointing in the directions of the unit vectors $\mathbf{e}_\theta$ and $\mathbf{e}_\varphi$ of the spherical coordinate system, respectively.

The matrix $\mathbf{R}$ contains the differentiation between fixed- and variable-orientation dipoles:

$$\mathbf{R}=\begin{bmatrix}
\cos\beta_1 & 0 & \cdots & & \cdots & \cdots & 0 \\
\sin\beta_1 & 0 & \cdots & & \cdots & \cdots & 0 \\
0 & \cos\beta_2 & 0 & & \cdots & \cdots & 0 \\
0 & \sin\beta_2 & 0 & & \cdots & \cdots & 0 \\
 & & & \ddots & & & \\
0 & \cdots & \cdots & & 0 & \cos\beta_{p_1} & 0 \\
0 & \cdots & \cdots & & 0 & \sin\beta_{p_1} & 0 \\
0 & \cdots & \cdots & & 0 & \cdots & \mathbf{I}^{(2p_2)}
\end{bmatrix} , \tag{67}$$

where $\mathbf{I}^{(2p_2)}$ is the $2p_2\times 2p_2$ identity matrix. If all the orientations are varying, $r=2p_2=2p$ and $\mathbf{R}=\mathbf{I}^{(2p)}$. The fixed dipoles form angles $\beta_k$, $k=1,\ldots,p_1$, with respect to $\mathbf{e}_\theta$.

Finally, the first $p_1$ rows of $\mathbf{Q}$ [see Eq. (65)] contain the amplitude time series of the fixed dipoles at $t_k$, $k=1,\ldots,m$, while the remaining $2p_2$ rows are the time series of the two components of each of the variable-orientation dipoles.

### 2. Selecting the correct model

Before minimizing Eq. (63), correct values must be chosen for $p_1$ and $p_2$, the number of fixed- and variable-orientation dipoles, respectively.

The conventional method for doing this (de Munck, 1990) is based on an analysis of the singular-value decomposition (SVD) of the measured data

$$\mathbf{M}=\mathbf{U}\Lambda\mathbf{V}^T , \tag{68}$$

where $\Lambda$ is a diagonal matrix containing the singular values of $\mathbf{M}$ while $\mathbf{U}$ and $\mathbf{V}$ are unitary matrices formed by its left and right singular vectors, respectively.

It can be shown (de Munck, 1990) that among all $\mathbf{B}$'s of rank $r$ the minimum of Eq. (63), $S_{\min}$, satisfies

$$S_{\min}\geq\sum_{k=r+1}^{\mathrm{rank}(\mathbf{M})}\lambda_k^2 , \tag{69}$$

where $\lambda_k$ are the singular values of $\mathbf{M}$, arranged in decreasing order. We obtain for the goodness of fit

$$g\leq\sum_{k=1}^{r}\lambda_k^2\Big/\sum_{k=1}^{\mathrm{rank}(\mathbf{M})}\lambda_k^2 . \tag{70}$$

Equations (69) and (70) tell us to what extent the measured data can be explained by $r$ sources that have linearly independent wave forms and spatial distributions detected by our set of sensors. This does not mean, however, that the sources are necessarily dipolar.

A reasonable value for $r$ can be obtained either by comparing $\lambda_k/\sqrt{m}$ ("effective noise level") with the estimated noise level of the measurements (Wax and Kailath, 1985; Yin and Krishnaiah, 1987) or just by studying the general behavior of $S_{\min}$ when $r$ is increased. Examples of $g_{\max}$ and $\lambda_k/\sqrt{m}$ as functions of $r$ are depicted in Fig. 22.

However, as was pointed out by Mosher *et al.* (1990), even if the dipole model is correct and we have chosen $r$ such that the remaining $S_{\min}$ can be explained by noise, we still have an ambiguity in dividing the available $r$ degrees of freedom between variable-orientation and fixed dipoles under the constraint $p_1+2p_2=r$.

### 3. Linear optimization

If the model consists only of variable-orientation dipoles, $\mathbf{R}=\mathbf{I}$ and the data are given by

$$\mathbf{B}=\mathbf{G}(\mathbf{r}_1,\ldots,\mathbf{r}_p)\mathbf{Q} .$$

Assuming that the dipole locations $\mathbf{r}_d$, $d=1,\ldots,p$, are known, the remaining minimization problem

$$S_{\min}=\min_{\mathbf{Q}}\|\mathbf{GQ}-\mathbf{M}\|_F^2 \tag{71}$$

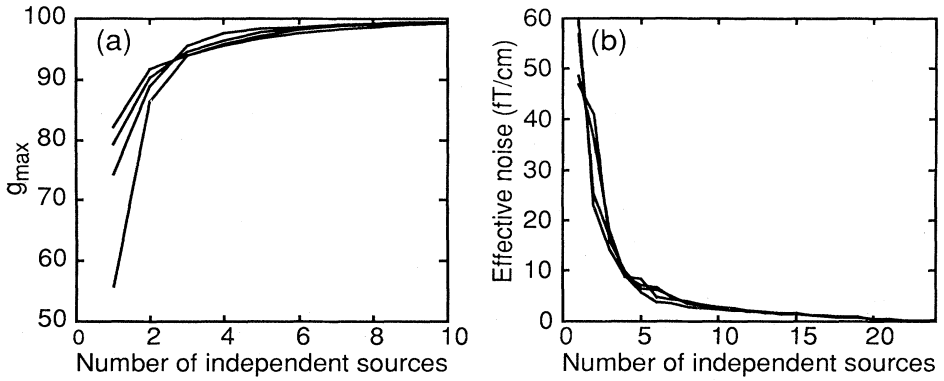


FIG. 22. Characteristics of multiple-source modeling. (a) Behavior of $g_{max}$ as a function of the number of independent sources. The curves were calculated from somatosensory measurements performed with a 24-channel gradiometer. Four different fingers were stimulated; the time range considered in the analysis was 0–100 ms. The data were bandpass filtered to 0.05–100 Hz. (b) Level of noise corresponding to the residual field, which cannot be explained by the given number of independent sources.

is linear with the solution

$$\hat{\mathbf{Q}}=\mathbf{G}^{\dagger}\mathbf{M} , \tag{72}$$

where the dagger denotes the pseudoinverse. In fact, $\mathbf{G}\hat{\mathbf{Q}}$ is the projection of $\mathbf{M}$ to the column space of $\mathbf{G}$: $\mathbf{G}\hat{\mathbf{Q}}=\mathbf{P}_{\|}\mathbf{M}$, whereas

$$S_{\min}=\|(\mathbf{I}-\mathbf{G}\mathbf{G}^{\dagger})\mathbf{M}\|_F^2=\|\mathbf{P}_{\perp}\mathbf{M}\|_F^2 , \tag{73}$$

where $\mathbf{P}_{\perp}$ is a projector to the left nullspace of $\mathbf{G}$. When one minimizes over the nonlinear parameters $\mathbf{r}_d$, $d=1,\ldots,p$, Eq. (73) can be used to find $S_{\min}$ at each iteration step of the nonlinear optimization algorithm.

In the traditional approach of Scherg (1990), all dipoles have fixed orientations. He includes the orientation angles in the set of nonlinear parameters, and $\mathbf{Q}$ is found by the above linear approach. For this purpose one just replaces $\mathbf{G}$ in Eqs. (71)–(73) by $\tilde{\mathbf{G}}=\mathbf{G}\mathbf{R}$.

Subsequently, it was proposed (de Munck, 1990) that the orientation angles could be found by a linear approach. However, this variation requires an iteration between two linear optimizations and may, therefore, be even more time consuming than finding the orientations by nonlinear minimization.

Recently it was shown (Mosher *et al.*, 1990) that one could start with variable-orientation dipoles only and then find an optimal orientation for the fixed dipoles. In this procedure, Eq. (72) is first applied to find $\hat{\mathbf{Q}}$ for $r$ variable-orientation dipoles. Then, $2\times m$ submatrices $\hat{\mathbf{Q}}_k$, $k=1,\ldots,p$, are formed, each containing two successive rows of $\hat{\mathbf{Q}}$. One then finds the best rank-one approximation for $\hat{\mathbf{Q}}_k$ through the SVD, viz.,

$$\hat{\mathbf{Q}}_k\approx\mathbf{v}_{1k}[\lambda_{1k}\mathbf{u}_{1k}^T] , \tag{74}$$

where $\lambda_{1k}$ is the larger of the two singular values of $\hat{\mathbf{Q}}_k$, while $\mathbf{u}_{1k}$ and $\mathbf{v}_{1k}$ are the corresponding left and right singular vectors, respectively. From Eq. (74) we can readily identify $v_{1k}=(\cos\beta_k \sin\beta_k)^T$. The term in brackets is the time series for the fixed dipole. The variable-orientation and fixed-dipole cases can be combined simply by applying Eq. (74) to fixed dipoles only.

### 4. Finding dipole positions

#### *a. The multiple-signal-classification approach*

The remaining nonlinear optimization for $\mathbf{r}_d$, $d=1,\ldots,p$, has been one of the central problems in multidipole modeling. This stems mainly from the fact that reasonable initial guesses are difficult to make. In addition, the calculation may get trapped into a local minimum and $S_{\min}$ is never reached.

So far the selection of the initial dipole positions has been based mainly on heuristic methods. Although an expert-system approach has been proposed (Palfreyman *et al.*, 1989), we are still at a stage where the expertise and physiological intuition of the experimenter are crucial for providing reasonable solutions. Consequently, the results may strongly depend on the person who is in charge of the analysis. Especially when MEG is applied in clinical practice it is of vital importance to provide the means to remove these ambiguities.

In the next two sections we shall concentrate on an elegant, recently proposed approach (Mosher *et al.*, 1992) for searching the optimal locations of several simultaneously active current dipoles. This method is identical with the MUSIC algorithm (multiple signal classification), introduced earlier in another context (Schmidt, 1986).

The basic idea is to find the parameters giving rise to $S_{\min}$ in four steps: (1) Decide the number of variable-orientation and fixed dipoles. (2) Find the best projector, $\mathbf{P}_{\perp}$ [Eq. (73)], regardless of $\mathbf{G}$ and $\mathbf{R}$, assuming a certain combination of variable-orientation and fixed dipoles. (3) Find $\mathbf{G}$ and $\mathbf{R}$ for which $\mathbf{I}-(\mathbf{G}\mathbf{R})(\mathbf{G}\mathbf{R})^{\dagger}$ is as close as possible to the optimal projector. Equivalently, one may

require that $\mathbf{GR}$ be orthonormal to $\mathbf{P}_\perp$. (4) Find the dipole time series with the methods described in the previous section.

*b. Variable-orientation dipoles*

Following Mosher *et al.* (1992) we shall consider first variable-orientation dipoles only ($r=2p_2$). For convenience, it will be assumed that $n<m$ and that $\text{rank}(\mathbf{M})=n$. The rank of $\mathbf{P}_\perp$ is $n-r=n-2p_2$ and the optimal $\mathbf{P}_\perp$ minimizes

$$S_\perp=\|\mathbf{P}_\perp\mathbf{M}\|_F^2 \ . \tag{75}$$

We can again make use of the SVD of $\mathbf{M}$ and write

$$\begin{aligned}\mathbf{M}&=\sum_{k=1}^{r}\lambda_k\mathbf{u}_k\mathbf{v}_k^T+\sum_{k=r+1}^{n}\lambda_k\mathbf{u}_k\mathbf{v}_k^T\\&\equiv\mathbf{M}_\parallel+\mathbf{M}_\perp \ ,\end{aligned} \tag{76}$$

where $\mathbf{M}_\parallel$ is the best rank-$r$ approximation of $\mathbf{M}$, and $\mathbf{M}_\perp$ is the corresponding orthogonal complement projection. Therefore,

$$\mathbf{M}_\parallel=\mathbf{P}_\parallel\mathbf{M}=\mathbf{U}_\parallel\mathbf{U}_\parallel^T\mathbf{M} \quad \text{and} \quad \mathbf{M}_\perp=\mathbf{P}_\perp\mathbf{M}=\mathbf{U}_\perp\mathbf{U}_\perp^T\mathbf{M} \ , \tag{77}$$

where

$$\mathbf{U}_\parallel=(\mathbf{u}_1,\ldots,\mathbf{u}_r) \quad \text{and} \quad \mathbf{U}_\perp=(\mathbf{u}_{r+1},\ldots,\mathbf{u}_n) \ . \tag{78}$$

The best orthogonal projector minimizing $S_\perp$ is thus $\mathbf{P}_\perp=\mathbf{U}_\perp\mathbf{U}_\perp^T$.

We next proceed to find $\mathbf{G}$ such that

$$S_G=\|\mathbf{G}^T\mathbf{P}_\perp\|_F^2 \tag{79}$$

is minimized. We write $\mathbf{G}=(\mathbf{G}_1,\ldots,\mathbf{G}_{p_2})$, where the $\mathbf{G}_k$'s are $n\times 2$ submatrices containing the unit dipole fields. If, indeed, the source is a collection of $p_2$ variable-orientation dipoles, each $\mathbf{G}_d$ must be orthogonal to $\mathbf{P}_\perp$. Therefore, it is meaningful to investigate the "scanning function" (Mosher *et al.*, 1992)

$$S_v(\mathbf{r})=\|\mathbf{P}_\perp\tilde{\mathbf{G}}_d(\mathbf{r})\|_F^2 \ , \tag{80}$$

where $\tilde{\mathbf{G}}_d=\mathbf{G}_d/\|\mathbf{G}_d\|$ is a normalized gain matrix. Normalization is necessary to distinguish orthogonality from small values due to small gain.

The algorithm for finding the dipole positions now readily emerges. One computes $S_v(\mathbf{r})$ in a grid of viable dipole positions and searches for minima. If our assumptions are correct, we should find exactly $p_2$ minima. Of course, the situation may be complicated by noise and, therefore, it is instructive to provide a contour plot of $S_v(\mathbf{r})$ or $1/S_v(\mathbf{r})$ on plane intersections to get a comprehensive picture of the situation. Since we are just moving one dipole, the search can be accomplished quite quickly.

*c. Fixed-orientation dipoles*

For fixed-orientation dipoles we need to find the optimal orientations as well. Now, however, $r=p_1$. We proceed as in the previous subsection, except that $\mathbf{G}$ is replaced by $\mathbf{GR}$ and that in the final step our scanning function is

$$\begin{aligned}S_f(\mathbf{r})&=\min_{\mathbf{m}_k}\frac{\|\mathbf{U}_\perp\mathbf{G}_k(\mathbf{r})\mathbf{m}_k\|_2^2}{\|\mathbf{G}_k(\mathbf{r})\mathbf{m}_k\|_2^2}\\&=\min_{\mathbf{m}_k}\frac{\mathbf{m}_k^T\mathbf{G}_k(\mathbf{r})^T\mathbf{P}_\perp\mathbf{G}_k(\mathbf{r})\mathbf{m}_k}{\mathbf{m}_k^T\mathbf{G}_k(\mathbf{r})^T\mathbf{G}_k(\mathbf{r})\mathbf{m}_k} \ ,\end{aligned} \tag{81}$$

where $\mathbf{m}_k=(\cos\beta_k \sin\beta_k)^T$, and $\|\cdot\|_2$ denotes the Euclidean norm of a vector.

It can be shown (Mosher *et al.*, 1992) that

$$S_f(\mathbf{r})=\lambda_{\min}[\mathbf{U}_{\mathbf{G}_k}(\mathbf{r})^T\mathbf{P}_\perp\mathbf{U}_{\mathbf{G}_k}(\mathbf{r})] \ , \tag{82}$$

where $\lambda_{\min}[\cdot]$ denotes the minimum eigenvalue of the bracketed $2\times 2$ matrix and $\mathbf{U}_{\mathbf{G}_k}^T$ is the matrix formed by the left singular vectors of $\mathbf{G}_k$. To find the dipole positions we can again construct a contour plot of $S_f(\mathbf{r})$ or $1/S_f(\mathbf{r})$ and search for extrema.

*d. The combined case*

When there are both fixed- and variable-orientation dipoles, $r=p_1+2p_2$, we can proceed as in the fixed-dipole case. If we hit a location of a variable-orientation dipole while evaluating Eq. (82), $\mathbf{G}_k\mathbf{m}_k$ is orthogonal to $\mathbf{P}_\perp$ for all $\mathbf{m}_k$ and, therefore, both eigenvalues of the bracketed term in Eq. (82) are close to zero. Therefore, we can always use the fixed-orientation dipole scanning method. To detect the variable-orientation dipoles we may, in addition, compute $S_v(\mathbf{r})$ and check whether it is at a minimum as well.

*e. Applications and limitations*

The appeal of the scanning method is that one can sort out the feasible source positions relatively quickly. Mosher *et al.* (1992) have also shown with both simulations and applications to actual measurements that the method, indeed, produces reasonable results. However, if there are strongly correlating sources whose field patterns overlap, the predictions will, in general, be misleading. The $r$ independent sources are no longer dipolar and, therefore, we cannot find a set of $r$ single-dipole gain submatrices $\mathbf{G}_k$ which are perpendicular to $\mathbf{P}_\perp$.

## I. Current-distribution models

One can also search for more general solutions of the neuromagnetic inverse problem instead of working with source models in the strict sense described above. Starting from the definition of $\mathcal{L}_i(\mathbf{r})$ in Eq. (43), an alternative description exists for the nonuniqueness of the inverse problem. Only current distributions that yield $b_i\neq 0$ for at least one $i$ can be detected. The extreme simplicity of assuming one or a few pointlike sources can be replaced by an unambiguous solution with minimal assumptions.

The first attempt of this kind was the minimum-norm estimate (MNE; Hämäläinen and Ilmoniemi, 1984; Ilmoniemi *et al.*, 1985; Sarvas, 1987; Hämäläinen and Ilmoniemi, 1993). Subsequently, the approach was further refined (Clarke *et al.*, 1989; Crowley *et al.*, 1989; Ioannides *et al.*, 1989; Wang *et al.*, 1992). A related procedure, using Fourier-space methods, was introduced by Kullmann and Dallas (1987). Furthermore, recent work by Ioannides *et al.* (1990) indicates that the point-source and distributed-source methods can be naturally linked by introducing restrictions to the set of feasible current source candidates.

### 1. Minimum-norm estimates

In the following, primary current distributions will be considered as elements of a function space $\mathcal{F}$ that contains all square-integrable current distributions confined to a known set of points $G$ inside a conductor. $\mathcal{F}$ will be called the current space. The set $G$ into which $\mathbf{J}^p$ is confined may be a curve, a surface, a volume, or a combination of discrete points, depending on the nature of the problem. When referring to current distributions as elements of the current space, we use capital letters. The inner product of $J_1^p \in \mathcal{F}$ and $J_2^p \in \mathcal{F}$ is defined by

$$\langle J_1^p, J_2^p \rangle = \int_G \mathbf{J}_1^p(\mathbf{r}) \cdot \mathbf{J}_2^p(\mathbf{r}) dG \ . \tag{83}$$

The overall amplitude of a current distribution is described by its norm, viz.,

$$\|J^p\|^2 = \langle J^p, J^p \rangle = \int_G |\mathbf{J}^p(\mathbf{r})|^2 dG \ . \tag{84}$$

From Eq. (43) it is evident that measurements of $b_i = \langle \mathcal{L}_i, J^p \rangle, i = 1, \ldots, n$, only yield information about primary currents lying in the subspace $\mathcal{F}'$ that is spanned by the lead fields: $\mathcal{F}' = \text{span}(\mathcal{L}_1, \ldots, \mathcal{L}_n)$.

The idea of a MNE is that we search for an estimate $J^*$ for $J^p$ that is confined to $\mathcal{F}'$. Then, $J^*$ will be a linear combination of the lead fields,

$$J^* = \sum_{j=1}^{n} w_j \mathcal{L}_j \ , \tag{85}$$

where $w_j$ are scalars to be determined from the measurements. Requiring that $J^*$ reproduce the measured signals, $\langle \mathcal{L}_i, J^* \rangle = b_i = \langle \mathcal{L}_i, J^p \rangle$, we obtain a set of linear equations $\mathbf{b} = \mathbf{\Pi w}$, where

$$\mathbf{b} = (b_1, \ldots, b_n)^T \ , \quad \mathbf{w} = (w_1, \ldots, w_n)^T \ ,$$

and $\mathbf{\Pi}$ is an $n \times n$ matrix containing the inner products of the lead fields, $\Pi_{ij} = \langle \mathcal{L}_i, \mathcal{L}_j \rangle$. With this notation, Eq. (85) can be compactly written as $J^* = \mathbf{w}^T \mathcal{L}$, where $\mathcal{L} = (\mathcal{L}_1, \ldots, \mathcal{L}_n)^T$.

The term *minimum-norm estimate* derives its name from the fact that $J^*$ is the current distribution with the smallest overall amplitude that is capable of explaining the measured signals in the sense of the norm defined by Eq. (84). The nonuniqueness of the inverse problem is manifested by the fact that the actual current distribution producing $b$ may be any current of the form $J = J^* + J_\perp$, where $J_\perp$ satisfies $\langle J_\perp, \mathcal{L}_i \rangle = 0$, $i = 1, \ldots, n$. In other words, any primary current distribution to which the measuring instrument is not sensitive may be added to the solution.

Figure 23 illustrates some of the concepts discussed above. Three dimensions of the current space are depicted. Two of the axes are in the plane defined by the lead fields $\mathcal{L}_1$ and $\mathcal{L}_2$; the third axis is perpendicular to all lead fields of the magnetometer array under consideration. In general, the primary current distribution $J^p$ is not confined to the subspace $\mathcal{L}_\parallel$ spanned by the lead fields, but contains a component in the complement subspace $\mathcal{L}_\perp$. A measurement will give only the projection of $J^p$ on $\mathcal{L}_\parallel$, which is the minimum-norm estimate $J^*$.

### 2. Regularization

If the lead fields are linearly independent, which is generally the case when the measurements are made at different locations, the inner-product matrix $\mathbf{\Pi}$ is nonsingular and

$$\mathbf{w} = \mathbf{\Pi}^{-1} \mathbf{b} \ . \tag{86}$$

However, the $\mathcal{L}_i$'s in $\mathcal{F}'$ may be almost linearly dependent. Thus $\Pi$ can possess some very small eigenvalues, which causes large errors in the computation of $\mathbf{w}$.

To avoid this numerical instability, the solution must be regularized (Sarvas, 1987). This means that directions in $\mathcal{F}'$ with poor coupling to the sensors are suppressed. Let $\mathbf{\Pi} = \mathbf{V \Lambda V}^T$, with $\mathbf{V}^T \mathbf{V} = \mathbf{I}$ and $\mathbf{\Lambda} = \text{diag}(\lambda_1, \ldots, \lambda_n)$, where $\lambda_1 > \lambda_2 > \cdots \lambda_n > 0$ are the eigenvalues of $\mathbf{\Pi}$. Then, $\mathbf{\Pi}^{-1} = \mathbf{V \Lambda}^{-1} \mathbf{V}^T$. Regularization may be carried out by replacing $\mathbf{\Lambda}^{-1}$ by

$$\tilde{\mathbf{\Lambda}}^{-1} = \text{diag}(\lambda_1^{-1}, \ldots, \lambda_k^{-1}, 0, \ldots, 0)$$

to obtain a regularized inverse $\tilde{\mathbf{\Pi}}^{-1} = \mathbf{V} \tilde{\mathbf{\Lambda}}^{-1} \mathbf{V}^T$. The cutoff value $k < n$ is selected so that the regularized MNE does not contain excessive contribution from noise. The

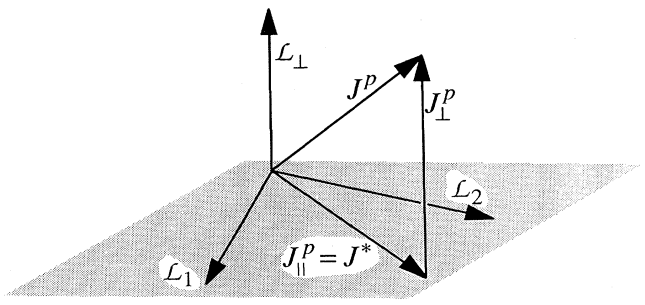


FIG. 23. Minimum-norm estimate $J^*$ visualized as a projection of the current vector $J^p$ into a subspace spanned by the lead fields $\mathcal{L}_1$ and $\mathcal{L}_2$. For simplicity, $n = 2$ measurement channels were assumed. Generalization to a typical multidimensional case with $n \simeq 100$ is straightforward.

resulting estimate does not reproduce exactly the measured signals, but the misfit $\mathbf{b}-\tilde{\mathbf{b}}$, where $\tilde{\mathbf{b}}=\mathbf{\Pi}\tilde{\mathbf{w}}=\mathbf{\Pi}\tilde{\mathbf{\Pi}}^{-1}\mathbf{b}$, is in accordance with experimental errors (Sarvas, 1987). In terms of current distributions, regularization means that those "eigenleads" that correspond to small eigenvalues and are hard to measure with sufficient signal-to-noise ratio are ignored. The regularized minimum-norm solution is

$$\tilde{J}^{*}=(\tilde{\mathbf{\Pi}}^{-1}\mathbf{b})^{T}\mathcal{L} \ . \tag{87}$$

Examples of MNE's for primary currents in a horizontally layered conductor were discussed by Hämäläinen and Ilmoniemi (1984). The source to be estimated was an assembly of current dipoles lying in the plane. The MNE's approximated reasonably well the locations of the original sources. However, since lead fields given by Eq. (43) are solenoidal ($\nabla\cdot\mathcal{L}_i=0$), the minimum-norm estimates also will be solenoidal and thus nonsolenoidal currents are not properly reconstructed.

Analogous simulations for a spherically symmetric conductor were computed by Hämäläinen and Ilmoniemi (1993). MNE's were also applied to the analysis of visual evoked responses (Ahlfors *et al.*, 1992; see also Fig. 24). The effect of regularization on these data is shown in Fig. 25.

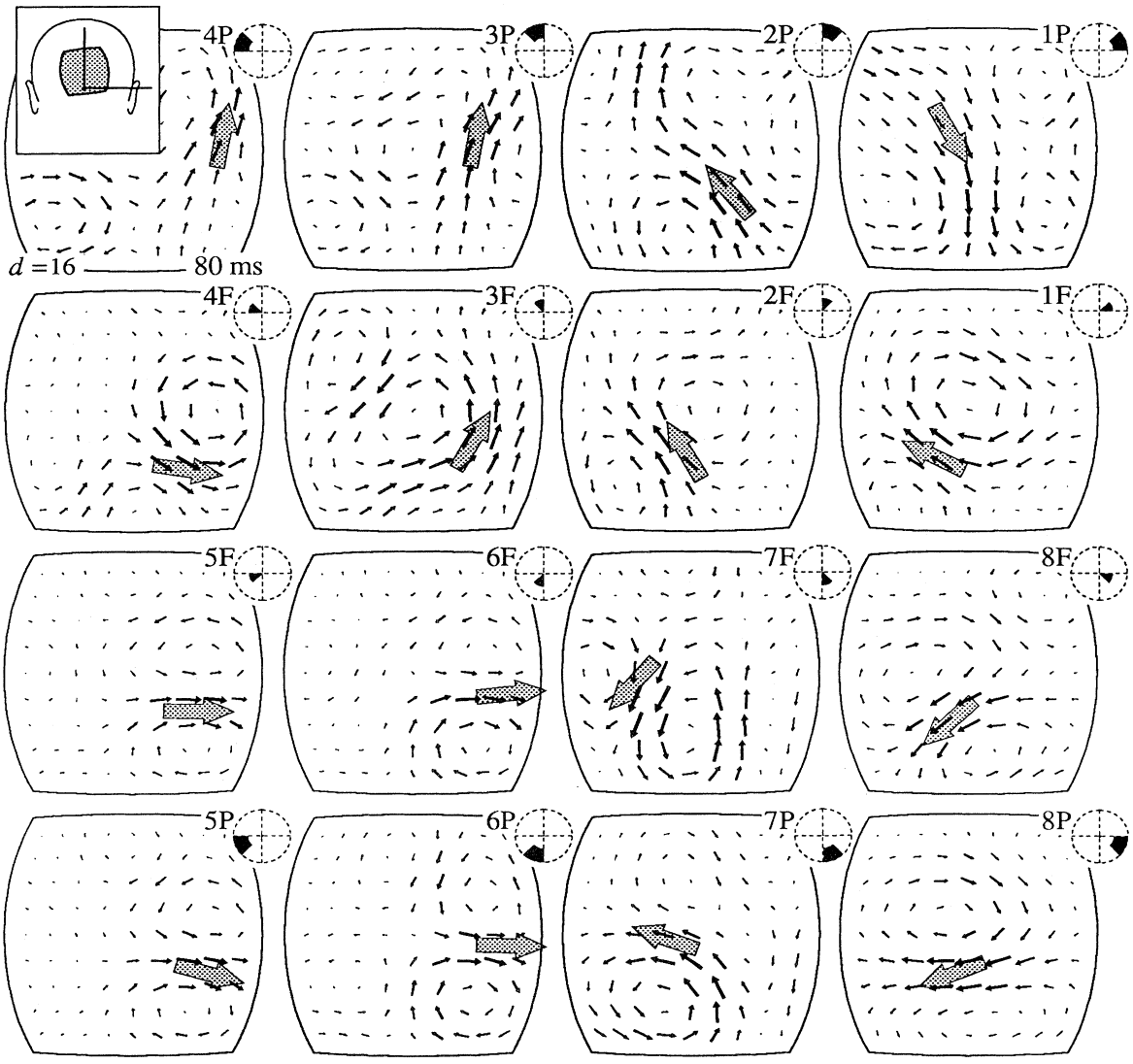


FIG. 24. Minimum-norm estimates (small arrows) and equivalent current dipoles (shadowed arrows) calculated from evoked visual MEG data. Different octants of the visual field were stimulated with foveal (*F*; second and third row) and parafoveal (*P*; first and last row) checkerboard patterns. The magnetic field was recorded with a 24-channel gradiometer over the occipital cortex (see Fig. 37 and inset at the upper left corner). Modified from Ahlfors *et al.* (1992).

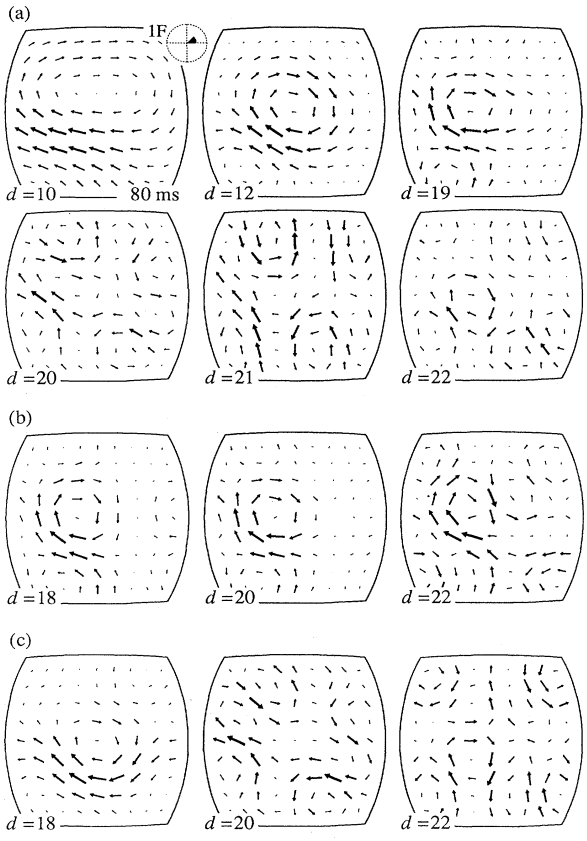


FIG. 25. Effect of regularization on the data shown in Fig. 24. In (a), 60 responses were averaged, while (b) and (c) represent two trials of 20 stimulus repetitions from the same measurement location. The value of $d$ at the lower left corner of each map indicates how many eigenleads out of the possible 24 were used. For more details, see Sec. IV.I.2. Modified from Ahlfors *et al.* (1992).

### 3. Minimum-norm estimates with *a priori* assumptions

Minimum-norm estimates versus single- or multidipole models represent two extreme approaches to source modeling. The MNE is an optimal estimate when minimal prior information is assumed or used. The dipole model is preferable when one knows that only a small patch of the cortex produced the measured field. However, this is often an oversimplification. In such a case, if supplementary information is available, solutions that are intermediate between the MNE and the dipole model can be obtained.

An interesting iterative approach has been introduced by Ioannides *et al.* (1990). The method is able to resolve localized sources, at least in simulations, without any prior assumption about their number or sites. The iterative distributed-source approach assumes a weighting function in the inner product of two current distributions, viz.,

$$\langle J_1, J_2 \rangle_\omega = \int_G \omega(\mathbf{r}) \mathbf{J}_1(\mathbf{r}) \cdot \mathbf{J}_2(\mathbf{r}) dG \ . \tag{88}$$

The solution is obtained as the limiting value of a sequence of current estimates $J^{(k)}$, $k = 0, 1, \ldots$ . Each of the estimates is computed as in the minimum-norm solution of Eq. (87). However, the weight function employed to calculate the dot-product matrix $\mathbf{\Pi}$ changes at each iteration and, therefore, one actually has a sequence $\Pi^{(k)}$ of inner-product matrices as well. For $k = 0$, $\omega^{(0)}(\mathbf{r}) = 1$; thus $J^{(0)} = J^*$ is the minimum-norm solution. In successive iterations the weight function depends on the previous estimate, $\omega^{(k)} = f(J^{(k-1)})$. The two particular functions tried by Ioannides *et al.* were the square and the square root of $J^{(k-1)}$. The resulting source estimates are well localized and they seem to be able to reproduce the sites of simulated point sources remarkably well.

Since the inner products must be recalculated during each iteration, this procedure is computationally demanding. Ioannides *et al.* (1990) have utilized a transputer system to speed up the calculations. Even so, they had to alleviate the computational burden by choosing a suitable set of lead fields to be used as basis functions. The important feature of this method is that it can reveal the number and locations of activated areas, with the only prior assumption being that there is a small number of localized sources.

Quite recently, a weighting function that increases monotonically with source depth has been applied to differentiate cortical and thalamic activity (Ribary *et al.*, 1991). Although the preliminary results are promising, it is not yet clear whether the two source regions that were observed to have a constant phase shift can be reconstructed consistently or if the observations are due to biasing the analysis with the desired enhancement of deep sources. The results clearly call for additional experiments for verification and other modeling approaches to confirm the source locations and their temporal behavior.

## J. Future trends

Because of the nonuniqueness of the neuromagnetic inverse problem, it is necessary to combine MEG data with supplementary information. Only the first steps in this direction have been taken. We need a system in which MRI gives structural information, PET and the functional MRI provide metabolic blood flow data, and EEG supplements MEG in obtaining data about signal processing in the brain. The improved accuracy of anatomic information and the combination of MEG with EEG will necessitate considerable improvements in modeling the conductivity of the head. The variable thickness and conductivity of the skull, holes in the cranium, cavities filled with highly conducting cerebrospinal fluid, white matter with its considerable anisotropy as well as anisotropy of the cortex itself, all have to be taken into account, unless one can prove that some of these complications are not important in practice.

We also need more refined filtering methods for the estimation of signal wave forms from noisy data. In addition, much emphasis must be put on the development of techniques for handling signals that arise from a multitude of simultaneous sources.

## V. INSTRUMENTATION FOR MAGNETOENCEPHALOGRAPHY

In this section we shall discuss instrumentation for neuromagnetic recordings in detail. To a large extent, the same principles and methods can be applied to studies of cardiac signals (MCG), geomagnetic applications, and monopole detectors or to any measurement employing multiple, simultaneously active SQUID magnetometers (Ilmoniemi *et al.*, 1989).

### A. Environmental and instrumental noise sources

In a laboratory environment, the magnetic noise level is several orders of magnitude higher than the biomagnetic signals to be measured. Electric motors, elevators, power lines, etc., all cause disturbances. In urban areas, trains and trolleys can be a nuisance, in particular if they are dc operated. In this case, removal of the power-line frequency and its harmonics with comb filters does not help; the frequency band of the disturbances overlaps that of the signals. In laboratories that are near public roads, moving automobiles and buses may also cause significant interference.

In addition, various laboratory and hospital instruments generate strong noise. In particular, superconducting magnets used in magnetic-resonance imaging (MRI) systems (Hutchinson and Foster, 1987) produce fields that are larger than the brain signals by 14–15 orders of magnitude. However, the main field of an MRI magnet is highly stable under normal operation, posing no severe problem. The gradients used in the image formation, typically on the order of 10 mT/m, are rapidly switched on and off. This is much more troublesome. A safe separation between an MEG system, operated inside a magnetically shielded room, and an MRI installation is a few tens of meters, which may be difficult to arrange in some hospitals.

Even if the interference is well outside the measurement band, problems may still occur. For example, radio-frequency fields, due to broadcasting, laboratory instruments, or computers, may ruin the experiments by decreasing the SQUID gain and increasing the noise level.

Static fields can cause flux trapping in the superconducting structures of the SQUID, which also results in a degraded performance. If the measuring device is not well supported, large disturbances due to vibrations will be seen in the magnetometer output.

Many stimulus generators also produce artefacts. Therefore, sounds are typically presented to the subject via plastic tubes and earpieces, and electric stimuli in somatosensory experiments are delivered through tightly twisted pairs of wires. The video monitor employed for visual stimuli is also a source of noise. If a magnetically shielded room is used, the monitor must be outside, behind a hole in the wall. Visual stimuli can also be led into the room via a mirror system or along optic fibers.

Eye movements and blinks are important biological sources of artefacts; both may be time-locked to the stimuli, especially if they are strong or infrequent. Sometimes the magnetic field due to cardiac activity can contaminate cerebral measurements. The peak field due to the heart's contraction, measured over the chest, is two orders of magnitude larger than that of typical evoked brain responses. However, the heart is farther away. Cardiac disturbances can usually be dealt with by signal averaging as well (see Sec. V.B.4). Electric currents in other muscles evoke magnetic fields, too, but such artefacts have not produced any significant problems during MEG recordings.

In addition, artefacts may be caused by mechanical movements of the body in the rhythm of the heartbeat or breathing. Therefore, all magnetic material on the subject, such as spectacles, watches, and hooks, must be removed.

Besides man-made disturbances, naturally occurring geomagnetic fluctuations constitute a significant source of noise, especially at low frequencies. Below 1 Hz, the spectral density of such field variations can exceed $1\text{pT}/\sqrt{\text{Hz}}$ (Fraser-Smith and Buxton, 1975). However, inside a shielded room and measured with a gradiometer (see Sec. V.B.1 and V.B.2), the total noise reduction can be 100 dB or more, and the contribution of geomagnetic fluctuations is negligible.

With modern thin-film dc SQUIDs, the magnetometer noise can be well below the level of the brain signals. Field sensitivities of a few $\text{fT}/\sqrt{\text{Hz}}$ have been reported, for example, by Maniewski *et al.* (1985), Knuutila, Ahlfors, *et al.* (1987), and Cantor *et al.* (1991). The limiting factor for the intrinsic noise of the magnetometers is the thermal noise in the SQUID itself; contributions from the state-of-the-art electronics are negligible. Decreased instrumental noise has revealed, however, new sources of disturbances that were not seen previously. Thermal noise generated in the aluminum foils used as radiation shields in Dewars is now a main factor limiting sensitivity if other external environmental disturbances have been eliminated. The fundamental noise barrier for measurements is the Nyquist current noise of the conducting human body. Fortunately, being on the order of $0.1\ \text{fT}/\sqrt{\text{Hz}}$ (Varpula and Poutanen, 1984), it is negligible compared with instrumental noise.

For amplitudes and spectra of various noise sources, as well as of some biomagnetic signals, see Fig. 8.

### B. Noise reduction

#### 1. Shielded rooms

The most straightforward and reliable way of reducing the effect of external magnetic disturbances is to perform

the measurements in a magnetically shielded room. To make such an enclosure, four different methods exist: ferromagnetic shielding, eddy-current shielding, active compensation, and the recently introduced high-$T_c$ superconducting shielding. Many rooms have been built for biomagnetic measurements utilizing combinations of these techniques.

The first shielded enclosure for biomagnetic measurements was constructed at the Massachusetts Institute of Technology (Cohen, 1970a). This room has its walls made of three ferromagnetic moly-permalloy layers and two sheets of aluminum in the form of a 26-faced polyhedron. With active compensation and "shaking," a shielding factor of 59 dB at 0.1 Hz was obtained. Above 10 Hz, the shielding was 100 dB (Cohen, 1970b). For active compensation, field sensors such as flux-gate magnetometers are employed to control the current fed to pairs of orthogonal Helmholtz coils around the room to eliminate the external field. Shaking is performed by applying a strong continuous 60-Hz field on the ferromagnetic layers so as to increase the effective permeability at other frequencies.

In our laboratory, a cubic shield with inner dimensions of 2.4 m was built in 1980 (Kelhä *et al.*, 1982). This room (see Fig. 9) consists of three shells made of high-permeability $\mu$-metal, sandwiched between aluminum plates. It attenuates external fields by 90–110 dB above 1 Hz; below 0.01 Hz the shielding factor is 45 dB. After demagnetization, a remanent field of 5 nT has been measured inside. At low frequencies, there is an option for active compensation, resulting in a 10–20 dB increase in the shielding factor. Active shielding, however, is presently not in use; the improved shielding is, in practice, superfluous when first-order gradiometers are employed. The better performance at higher frequencies is due to eddy currents induced in the high-conductivity aluminum layers. The plates of each shell were welded together at their edges to allow for the flow of eddy currents which oppose changes in the external magnetic field.

At the Physikalisch-Technische Bundesanstalt in Berlin a heavy shield has been built of six layers of $\mu$-metal and one layer of copper (Mager, 1981). In the frequency range 1–100 Hz, the shielding factor is comparable to that of the Helsinki room (Erné, Hahlbohm, Scheer, and Trontelj, 1981), although the Berlin room is superior at lower frequencies.

Several shielded rooms for basic biomagnetic research and for clinical use have been constructed commercially by Vacuumschmelze GmbH (see the Appendix for address). These enclosures are made of two ferromagnetic $\mu$-metal layers with inner dimensions of $3\times4\times2.4$ m$^3$. The shielding factor varies from about 50 dB at 1 Hz to 80 dB at 100 Hz. The Vacuumschmelze room is a compromise between performance and price. With suitable gradiometers it offers a sufficiently quiet space for practically all types of biomagnetic measurements. Two other commercial manufacturers have also entered the market, Amuneal Corporation and Takenaka Corporation (see the Appendix for addresses).

Less expensive shielded rooms can be made from thick aluminum plates. Several such enclosures, based solely on eddy-current shielding, have been built (Zimmerman, 1977; Malmivuo *et al.*, 1981; Stroink *et al.*, 1981; Nicolas *et al.*, 1983; Vvedensky, Naurzakov, *et al.*, 1985). The wall thickness in these rooms is about 5 cm; the shielding factor is proportional to frequency, being about 50 dB at 50 Hz.

The newest shielding method is to employ high-$T_c$ superconductors to make whole-body shields (Matsuba *et al.*, 1992). The first shield of this type will consist of a horizontal tube of 1-m diameter and 3-m length, closed at one end. The open end will have a set of ferromagnetic cylinders to increase the effective length of the tube. The expected shielding factor, based on calculations and on a 1/10-scale model experiment, is 160 dB, more than enough for all practical purposes.

The ultimate performance of magnetically shielded rooms is determined by Nyquist current noise in the conducting walls. The effect of this noise source is most significant in eddy-current shields; it can be reduced if the innermost layer is made of $\mu$-metal (Varpula and Poutanen, 1984; Maniewski *et al.*, 1985; Nenonen and Katila, 1988).

### 2. Gradiometers

In addition to or instead of shielded rooms, external magnetic disturbances can be reduced with gradiometric coil configurations. Even inside shielded enclosures, mechanical vibrations of the Dewar in the remanent magnetic field and nearby noise sources, such as the heart, disturb the measurements, so that simple magnetometers [see Fig. 26(a)] are rendered practically useless.

A first-order axial gradiometer, in which an oppositely wound coaxial coil is connected in series with the pickup coil, is shown in Figs. 7(b) and 26(d). This arrangement is insensitive to a homogeneous magnetic field which im-

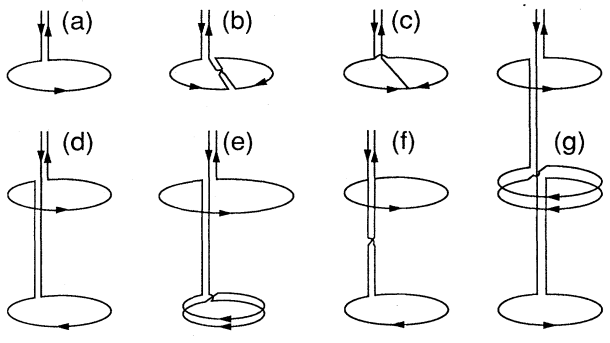


FIG. 26. Various types of flux transformers: (a) magnetometer; (b) series planar gradiometer; (c) parallel planar gradiometer; (d) symmetric series axial gradiometer; (e) asymmetric series axial gradiometer; (f) symmetric parallel axial gradiometer; and (g) second-order series axial gradiometer.

poses an opposite net flux through the lower (pickup) and the upper (compensation) coils. The first-order gradiometer is thus effective in measuring the inhomogeneous magnetic fields produced by nearby signal sources, whereas the more homogeneous fields of distant noise generators are effectively canceled. If the pickup coil is close to the subject's head and the distance between the two coils (the base line) is at least 4–5 cm, the magnetic field produced by the brain is sensed essentially by the lower coil only.

In general, an adequate base line for an axial gradiometer is 1–2 times the typical distance to the source. This provides sufficient far-field rejection without severe attenuation of the signal (Vrba *et al.*, 1982; Duret and Karp, 1983). One should note, however, that noise from nearby sources, such as the Dewar, cannot be avoided with gradiometric techniques. Therefore, with modern SQUIDs, further improvement requires reduction of the Dewar noise, which is probably mostly due to thermal currents in the thin metallic layers of superinsulation.

Other possibilities for arranging first-order axial gradiometer coils are shown in Figs. 26(e) and 26(f). In Fig. 26(e), an asymmetric first-order gradiometer is illustrated. Because the inductance of its compensation coil is smaller than that of the pickup loop, a better sensitivity is obtained than with a symmetric gradiometer. In Fig. 26(f), the pickup and compensation coils are connected in parallel instead of in series; this reduces the total inductance by a factor of 4 from the configuration in Fig. 26(d). The parallel connection is easier to match to the signal coil of a SQUID, which has a small inductance. A disadvantage is that homogeneous magnetic fields give rise to shielding currents in the detection coil that couple to neighboring gradiometer channels. In Fig. 26(d), a planar, off-diagonal, so-called double-D gradiometer (Cohen, 1979) is shown, with the coils connected in series. A parallel version of this gradiometer is illustrated in Fig. 26(c).

Figure 26(g) shows a second-order axial gradiometer in which two first-order gradiometers are connected together in opposition so that the detection coil is insensitive to both homogeneous fields and uniform field gradients. This arrangement further improves the cancellation of magnetic fields generated by distant sources. Successful experiments with second-order gradiometers of this type have been performed in unshielded environments (Kaufman and Williamson, 1987). A disadvantage of higher-order gradiometers is that to avoid reduction of the signal energy coupled to the SQUID the height of the coil may become impractically long (see also Fig. 27).

Traditionally, most neuromagnetic measurements have been performed with axial gradiometers. However, off-diagonal planar configurations of Figs. 26(b) and 7(c) have advantages over axial coils: the double-D construction is compact in size and it can be fabricated easily with thin-film techniques. The locating accuracies of planar and axial gradiometer arrays are essentially the same for typical cortical sources (Erné and Romani, 1985; Knuutila *et al.*, 1985; Carelli and Leoni, 1986). The base line of planar sensors is typically shorter than that of conventional axial gradiometers; this may be advantageous if measurements have to be performed in very noisy environments. In addition, the spatial sensitivity pattern (see below) of off-diagonal gradiometers is narrower and shallower. These sensors thus collect their signals from a more restricted area near the sources of interest and there is less overlap between lead fields.

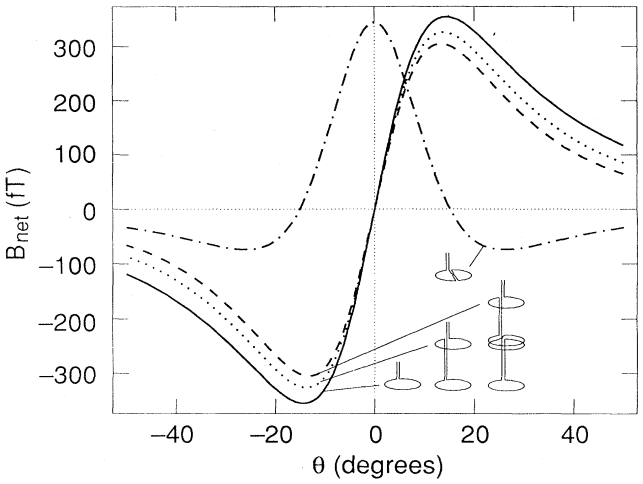


FIG. 27. Amplitudes of magnetic signals due to a tangential current dipole in a spherically symmetric volume conductor. $B_{net}$, the difference signal between the gradiometer loops, is calculated perpendicular to the dipole along a circle passing through it, as the field would be recorded by a magnetometer, an axial first-order gradiometer, an axial second-order gradiometer, and a planar first-order gradiometer (see Fig. 26). The radius of the spherical surface where the measurements are performed is 100 mm and the dipole is assumed to be at $\theta=0°$, 30 mm below the surface. The dipole moment is 10 nA m, and the base lengths of the axial and planar gradiometers are 60 mm and 15 mm, respectively. Note that for the planar gradiometer the maximum signal is just above the source.

The "signal profiles" of a magnetometer, a first-order and a second-order axial gradiometer, and a planar gradiometer are illustrated in Fig. 27, calculated for a current-dipole source in a spherically symmetric volume conductor [see Eq. (34)]. The double-D gradiometer gives its maximum response just over the source, with the direction of the source current being perpendicular to that of the field gradient. Since the maximum signal is obtained directly above the source instead of at two locations on both sides, as with conventional axial gradiometers (see Fig. 27), the area where measurements must be made to obtain the dipolar field pattern can be smaller. Note also that the signals of the first- and second-order axial gradiometers are 8 and 15% smaller, respectively, than that of the magnetometer.

To obtain cancellation of homogeneous fields, one has to make the effective turns-area products of the pickup and compensation coils equal. In wire-wound gradiometers, an initial imbalance of a few percent is typical. It can be reduced by changing the effective areas of the coils

with movable superconducting pieces (Aittoniemi *et al.*, 1978; Duret and Karp, 1983). Three tabs are needed to adjust the $x$, $y$, and $z$ components separately. Usually, a final imbalance of about 1–10 ppm can be achieved. Another possibility is to place small pieces made of magnetically soft material outside of the Dewar (Thomas and Duret, 1988). Although superconducting tabs are suitable for balancing single-channel instruments, their use in multichannel devices is too complicated. Furthermore, even after careful balancing at low frequencies, a balance at rf frequencies is not guaranteed.

## 3. Electronic noise cancellation

As we mentioned already, active compensation of external fields is a practical technique in conjunction with shielded rooms. Another possibility is to apply electronic cancellation directly to the measured signals. The system may include additional "reference" sensors measuring the three magnetic-field components and possibly some of the field gradients as well. These compensation channels are insensitive to brain signals, since they are positioned far away from the subject's head, but they detect distant noise sources.

The reference channels can be employed to remove common-mode disturbances from the gradiometer output caused by imbalance. For example, for a planar first-order gradiometer, which measures the derivative $\partial B_z/\partial x = G_x$, where $x$, $y$, and $z$ refer to a local coordinate system of the sensor, the corrected output is

$$G_x^{\rm corr}(t) = G_x^{\rm meas}(t) - C_x B_x^{\rm ref}(t) - C_y B_y^{\rm ref}(t) - C_z B_z^{\rm ref}(t) \ , \tag{89}$$

where $C_x$, $C_y$, and $C_z$ are experimentally determined imbalance coefficients and $B_x^{\rm ref}(t)$, $B_y^{\rm ref}(t)$, and $B_z^{\rm ref}(t)$ are the reference signals. In multi-SQUID systems, the reference channels can be employed to subtract terms common to all channels and caused by the homogeneous and gradient components of disturbing fields. Assuming that $\Psi_j$ are the outputs of the reference channels, including gradiometers, the compensated outputs ($i = x,y,z$) of the first-order gradiometer signal channels are

$$G_i^{\rm corr}(t) = G_i^{\rm meas}(t) - \sum_{j=1}^{N} W_{ij}(t)\Psi_j(t) \ , \tag{90}$$

where $W_{ij}(t)$ are subtraction coefficients that depend on the character of the disturbing field. They are, in general, time dependent.

In New York University a system was adopted where balancing was improved electronically, using analog hardware (Williamson *et al.*, 1985). In addition to five second-order gradiometers near the subject's head, extra channels measured the three magnetic-field components and the axial derivative of the radial component. With this system, rejection of external noise in an unshielded environment improved by about 20 dB. Still, the noise level could not be reduced sufficiently for some measurements, although many successful experiments were performed (Kaufman and Williamson, 1987). A magnetically shielded room has now been installed at NYU as well.

Electronic balancing by applying the compensation digitally with a software algorithm offers much more versatility (Robinson, 1989; Vrba *et al.*, 1989). The weights $W_{ij}(t)$ may be estimated statistically on the basis of measured signals, and thus an adaptive algorithm can be established. Furthermore, digital bandpass filtering may be employed for adaptive frequency-dependent noise cancellation. In tests, three orthogonal field channels and one gradient channel improved the external noise reduction by 40 dB.

Gradiometers may also be made electronically from magnetometers. For example, in the instrument at the University of Ulm, manufactured by Dornier Systems GmbH (see the Appendix for address), 28 magnetometers are used to form 22 effective gradiometers. A similar arrangement has also been tested at the Physikalisch-Technische Bundesanstalt (PTB) in Berlin using their 37-channel magnetometer (Koch *et al.*, 1991), as well as in another study employing a single-sensor magnetometer and a reference magnetometer located 20 cm away (Drung, 1992b). In the latter experiment, a noise reduction of 40 dB was achieved in an unshielded environment. Second-order gradiometers made electronically from first-order gradiometers have also been tested successfully (Vrba *et al.*, 1991, 1993).

Obviously, in order to make electronic gradiometer systems work, a very large dynamic range and a high slew rate (the system's ability to track rapid changes) are needed for the magnetometers. A drawback is that noise in the reference channels sums up vectorially. For example, the effective noise level of the electronically formed gradiometer is increased by a factor of $\sqrt{2}$. Fortunately, the reference signals subtracted from the outputs can be band-limited, which reduces the total random noise. A magnetometer with a low intrinsic noise is, nevertheless, highly desirable for this application.

Electronic noise-cancellation schemes offer an elegant way for reducing environmental disturbances. So far, however, the best results have been achieved with conventional heavy magnetic shields and high-sensitivity first-order gradiometers. Indeed, it is always safer to prevent disturbances than to compensate for them. The main drawbacks of active noise cancellation have so far been the complicated control of channel weights, insufficient dynamics, and a too high noise level of the SQUIDs.

## 4. Filtering and averaging of neuromagnetic data

Bandpass filtering is a simple way to reduce the effect of wideband thermal noise. In magnetoencephalographic studies, a recording passband of a few hundred Hz is typical; in the analysis of most components of evoked responses and of spontaneous activity, even a low-pass

filter with a cutoff at 40–50 Hz is adequate. In the low-frequency end, dc measurements would be useful because very slow shifts may occur, for example, in association with spreading depression, epilepsy, and migraine (Barkley *et al.*, 1991). Because of practical limitations, due to drifts, etc., a high-pass filter below 0.1 Hz is usually employed.

Besides bandpass filtering, averaging is a simple and powerful way of improving the signal-to-noise ratio. This method can, of course, be used only in conjunction with repeating phenomena such as evoked responses. The measured output $u(t)$ is assumed to be the sum of a noiseless signal $s(t)$ and independent random Gaussian noise $n(t)$, viz.,

$$u(t)=s(t)+n(t) . \tag{91}$$

Since noise and external disturbances, including the background activity of the subject, are normally not time-locked to the stimulus, they can be regarded as independent. Thus their influence may be reduced by averaging typically 20–300 responses, with an improvement in the signal-to-noise ratio of $\sqrt{N}$, where $N$ is the number of averaged responses. However, this is strictly true only for "ideal" signals which can be described accurately by Eq. (91). Real signals measured from humans are not perfectly replicable, e.g., because of fatigue in the subject during an experiment. This nonideality may be thought of as non-Gaussian extra noise that cannot be reduced by averaging. A practical limit for $N$ is thus reached when the contribution of random noise is smaller than that of the extra non-Gaussian noise generated by the averaging process.

These methods are simple special solutions to the general problem of extracting a signal from noisy data. More sophisticated filtering and estimation procedures have been developed and, as an example, we discuss here briefly the time-varying filter (de Weerd, 1981; Bertrand *et al.*, 1990), based on continuous estimation of the signal-to-noise ratio in several frequency bands.

If the spectra of the signal $\Gamma_s(f)$ and the noise $\Gamma_n(f)$ are known *a priori,* the optimal linear filter to estimate the signal from an ensemble average is the "*Wiener*" filter with a transfer function (de Weerd, 1981)

$$H(f)=\frac{\Gamma_s(f)}{\Gamma_s(f)+\Gamma_n(f)/N} . \tag{92}$$

However, in practice, $\Gamma_s(f)$ and $\Gamma_n(f)$ are not known, but must be estimated from the ensemble. We then obtain the *a posteriori* "*Wiener*" filter simply by replacing $\Gamma_s(f)$ and $\Gamma_n(f)$ in Eq. (92) by their estimates $\hat{\Gamma}_s(f)$ and $\hat{\Gamma}_n(f)$. Since the evoked responses are transient, and noise may vary with time, it is questionable whether such a time-invariant filter will produce the best results. Therefore, a generalized *a posteriori* "*Wiener*" filter should use time-dependent estimates of the signal and noise spectra, viz.,

$$H(f,t)=\frac{\hat{\Gamma}_s(f,t)}{\hat{\Gamma}_s(f,t)+\hat{\Gamma}_n(f,t)/N} . \tag{93}$$

The power of a signal cannot be estimated with an arbitrarily small resolution simultaneously in the frequency and time domains. In practice, the filter is realized by dividing the frequency range of interest into several bands, using a bank of filters. The signal-to-noise ratio of each band is estimated separately for short periods of time using, for example, normal and alternating averages. The bands are then weighted and recombined. The weights of the filter bank are adjusted on the basis of the time-dependent estimates of the signal-to-noise ratio. The lower the ratio, the more the corresponding band is attenuated.

Although sophisticated filtering methods exist for extracting the signal from noisy data, the main effort should be directed towards noise reduction in the flux sensed by the SQUID. Clean raw data, obtained with proper magnetic shielding, low-noise sensors, and well-designed gradiometers are still the most important ingredients of good MEG results.

#### 5. rf filters and grounding arrangements

A magnetically shielded room can easily be made tight against electrical disturbances. However, strong rf fields may occupy its interior because the room acts as a resonance cavity. External rf fields typically are carried inside by cables from the stimulus-producing equipment, by EEG leads, and by other wires acting as antennae. It is, therefore, essential that all feedthroughs are rf filtered and grounding arrangements are properly made. Careful elimination of ground loops, for example, is a simple and effective method against disturbances, especially for reducing power-line interference. The generation of the stimuli themselves, for example, weak electric somatosensory stimuli, can also give rise to artefacts if the leads are not properly shielded and grounded.

rf filters are necessary in the flux transformer (Ilmoniemi *et al.*, 1984; Seppä, 1987), but possibly in other leads as well, for obtaining reliable and stable low-noise operation. This is not only to suppress external disturbances but also to damp intrinsic resonances excited by high-frequency oscillations in the SQUID itself, as will be discussed in Sec. V.D.3.

### C. Dewars and cryogenics

Construction of the cryogenic system for a neuromagnetometer is a demanding task. Not only must the sensors be brought as close to the source as possible, but also the materials used in the Dewar must be nonmagnetic and the noise generated by thermally induced currents in the electrically conducting parts must be very low.

Fiber-glass-reinforced epoxy has proven a reliable low-noise material in Dewars for biomagnetic research. It allows concave surfaces to be made in order to accommodate the subject's head; even helmet forms are possible.

To minimize the distance from the sensor coils in

liquid helium to the signal source in the brain requires a compromise between thermal noise and the helium boiloff rate. Multiple, vapor-cooled radiation shields and superinsulation cannot be used in the tail section of the Dewar below the sensors: these would lead to wide gaps between the inner and outer surfaces and to large thermal noise currents (Nenonen *et al.*, 1989; Montonen *et al.*, 1992). Instead, a shield made of vapor-cooled coil-foil should be used (Anderson *et al.*, 1961; Lounasmaa, 1974), perhaps with a few layers of striped superinsulation foil. Coil-foil consists of tightly spaced thin insulated wires, glued together to form a sheet; the foil has electrical and thermal conductivity primarily in one dimension only, which prevents the formation of large loops for noise currents. Superinsulation is thin plastic foil with an aluminum film evaporated on one side. A few layers of it wrapped tightly into the vacuum space of the Dewar form "floating" thermal radiation shields, where the temperatures of the layers are determined by radiation equilibrium. In other parts of the Dewar, multiple layers of superinsulation and additional thermally anchored radiation shields can be employed.

The boiloff rate of liquid helium may be a very important practical factor in the design, especially with Dewars intended for hospital use. Typically, a period of 3–4 days between helium transfers can be attained without an unduly massive and clumsy reservoir for the cryogenic liquid.

A vessel containing perhaps several tens of liters of liquid helium, brought in the immediate vicinity of a human subject, is a safety risk. The Dewar must be equipped with proper relief valves to prevent an explosion in case of sudden evaporation of the liquid following an accidental loss of the insulating vacuum. Furthermore, since the Dewar is often operated in the closed space inside a shielded room, effective ventilation is important. Sudden evaporation of helium may rapidly generate cold gas in amounts comparable to or even exceeding the volume of the shielded enclosure; 1.3 liters of liquid helium at 4.2 K is equivalent to 1 $m^3$ of gas at 20 °C!

### D. Superconducting quantum interference devices

The only device with sufficient sensitivity for high-quality biomagnetic measurements is the SQUID magnetometer (Zimmerman *et al.*, 1970), shown schematically in Fig. 28(a). Its basic principles and theory of operation have been described in detail, for example, in review articles (Koch, 1989; Ryhänen *et al.*, 1989) and in textbooks (e.g., Feynman, 1965; Lounasmaa, 1974). In this paper we emphasize aspects that are particularly important in the design of successful instrumentation for neuromagnetic research.

Previously all sensor systems for biomagnetic studies were based on rf SQUIDs because this device was simpler and cheaper to manufacture than its dc counterpart.

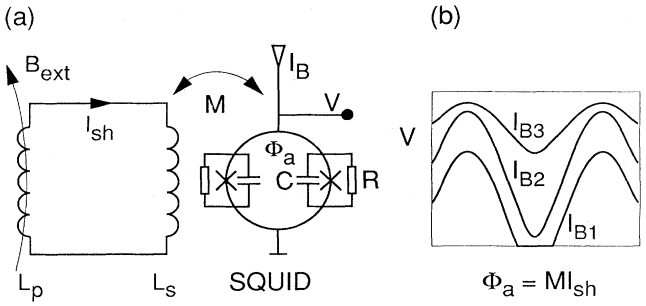


FIG. 28. SQUID basics. (a) Schematic diagram of a dc SQUID magnetometer. The external field $B_{ext}$ is connected via a superconducting flux transformer ($L_p$,$L_s$) to the SQUID. In a gradiometer, there is an additional compensation coil in series with $L_p$. (b) The average voltage $V$ across the SQUID depends on the dc bias current $I_B$ and is a periodic function of the flux $\Phi_a$ coupled to the SQUID ring.

However, advances in thin-film fabrication technology have changed the situation: reliable low-noise dc SQUIDs can be produced now in large quantities and at lower prices than before. Typically, a white noise level can be achieved that is more than an order of magnitude smaller than in rf SQUIDs. Furthermore, the readout electronics for dc SQUIDs is simpler. Therefore, most contemporary instruments are based on dc SQUIDs. In the following, we shall consider these devices only.

#### 1. SQUID basics

The dc SQUID (Jaklevic *et al.*, 1964; Zimmerman and Silver, 1966; Clarke, 1966; Clarke *et al.*, 1975, 1976) consists of a superconducting loop interrupted by two Josephson junctions [Fig. 28(a)]. For simplicity, consider first only the uncoupled noiseless SQUID, i.e., a device without the flux transformer coils $L_p$ (pickup coil) and $L_s$ (signal coil). The Josephson junction is characterized by a critical current $I_c$, and the junction dynamics is governed by the well-known relations (Josephson, 1962)

$$I = I_c \sin\theta \ , \tag{94}$$

$$\frac{\partial\theta}{\partial t} = 2\pi V \frac{2e}{h} = \frac{2\pi V}{\Phi_0} \ , \tag{95}$$

where $\theta$ is the quantum-mechanical phase difference across the junction, $I$ the current, and $V$ the voltage across the junction (see Feynman, 1965). The constant $\Phi_0 = h/2e = 2.07$ fWb is the magnetic-flux quantum.

In practice, there is a capacitance $C$ and a resistance $R$ across the junction. Usually $R$ is determined by an external shunt resistor, much smaller than the equivalent "intrinsic" resistance of the junction, defined by the ratio of the junction voltage to the tunneling current above $I_c$. In the resistively shunted junction (RSJ) model, Eq. (94) becomes

$$I = \frac{V}{R} + I_c \sin\theta + C\frac{dV}{dt} \ . \tag{96}$$

If the current $I$ fed through the junction is smaller than $I_c$, the junction is in zero-voltage regime; but if $I \gg I_c$, $V \simeq RI$ (running state). The transition between these two regimes is hysteretic if the damping due to the resistance $R$ is small. In particular, this happens if the Stewart–McCumber parameter (McCumber, 1968; Stewart, 1968; Ketoja *et al.*, 1984b)

$$\beta_c = \frac{2\pi R^2 I_c C}{\Phi_0} > 0.7 \ . \tag{97}$$

In the dc SQUID, the bias current $I_B$ is the sum of currents through the two junctions, $I_B = I_1 + I_2$. The RSJ equation (96) is applied to both branches separately. For a magnetic flux $\Phi$ threading the ring, the quantization relation obtained by integrating the quantum-mechanical phase around the SQUID ring in the presence of a magnetic field reads

$$\Phi = \frac{\Phi_0}{2\pi}(\theta_1 - \theta_2) = \Phi_a + \frac{L}{2}(I_1 - I_2) \ , \tag{98}$$

where $L$ is the inductance of the ring and $\Phi_a$ is the externally applied magnetic flux. By changing variables to

$$\nu = (\theta_1 + \theta_2)/2 \ ,$$

$$\varphi = (\theta_1 - \theta_2)/2 \ ,$$

$$i = I/2I_c \ ,$$

and

$$\tau = 2\pi R I_c t/\Phi_0 \ ,$$

we obtain the equations of motion,

$$\beta_c \frac{d^2\nu}{d\tau^2} + \frac{d\nu}{d\tau} + \sin\nu\cos\varphi = i \ , \tag{99}$$

$$\beta_c \frac{d^2\varphi}{d\tau^2} + \frac{d\varphi}{d\tau} + \cos\nu\sin\varphi + \frac{2}{\pi\beta_L}(\varphi - \varphi_a) = 0 \ , \tag{100}$$

where $\beta_L = 2LI_c/\Phi_0$, and $\varphi_a = \pi\Phi_a/\Phi_0$. This pair of nonlinear equations must be solved numerically. The voltage across the SQUID is given by $V = RI_c(d\nu/d\tau)$ and the total flux by $\Phi = \Phi_0\varphi/\pi$.

It is common to assume that there is a white-noise source generated solely by thermal fluctuations (Nyquist, 1928) in the shunt resistors. This can be taken into account in the circuit analysis by adding noise terms $i_{n,\nu}(\tau)$ and $i_{n,\varphi}(\tau)$ to the right-hand sides of Eqs. (99) and (100), respectively. Here, the expectation values of the noise terms are

$$E\{i_{n,\nu}(\tau)\} = E\{i_{n,\varphi}(\tau)\} = E\{i_{n,\nu}(\tau) i_{n,\varphi}(\tau)\} = 0$$

and

$$E\{i_{n,\nu}(\tau+\xi) i_{n,\nu}(\tau)\} = E\{i_{n,\varphi}(\tau+\xi) i_{n,\varphi}(\tau)\} = 2\pi k_B T \delta(\xi)/(I_c\Phi_0) \ ,$$

and $\delta(\xi)$ is Dirac's delta function.

In Fig. 28(b), the voltage has been sketched schematically as a function of the applied flux for three different flux bias currents. At the smallest bias, $I_{B1} < 2I_c$, the SQUID stays for part of the cycle in the zero-voltage state: the sum of the current circulating around the SQUID ring plus half of the bias current exceeds the junction critical current only at certain values of the flux. The voltage modulation is maximal at $I_{B2} \geq 2I_c$ and fades away for $I_{B3} \gg 2I_c$. The quantization relation (98) ensures that the response of the SQUID to magnetic flux is periodic in the applied flux $\Phi_a$ with the period $\Phi_0$.

The flux transformer couples the external field $B_{\text{ext}}$ to the SQUID. Since the magnetic flux threading a closed superconducting loop is conserved, a shielding current $I_{\text{sh}} = B_{\text{ext}} A_p/(L_p + L_s)$ is induced [see Fig. 28(a)], with $A_p$ being the effective area of the pickup coil. The flux $\Phi_a = MI_{\text{sh}}$ is coupled to the SQUID through the mutual inductance $M$. The signal coil $L_s$ introduces a parasitic capacitance $C_p$ across the SQUID (see Fig. 29), which substantially complicates the SQUID dynamics but which can be taken into account in numerical analysis by modifying Eqs. (99) and (100) (Ryhänen *et al.*, 1989).

### 2. Thin-film fabrication techniques

The majority of SQUIDs have been made from Pb alloys and pure Nb, typical structures containing layers of both metals. Often the base electrode was fabricated from Nb, with the tunnel barrier formed by oxidizing the Nb surface, and the top electrode made of a Pb alloy. The electrodes were usually separated by a layer of $SiO_2$, except for a window defining the junction area. Nowadays, SQUIDs are manufactured entirely of refractory metals (Kroger *et al.*, 1981; Gurvitch *et al.*, 1983; Raider, 1985; Braginski, 1987): both electrodes are made from Nb or NbN, and they are separated by "artificial" tunnel barriers such as $Al_2O_3$, MgO, or amorphous Si. The $Al_2O_3$ and MgO barriers are superior to conventional materials: they are more stable, the critical current is

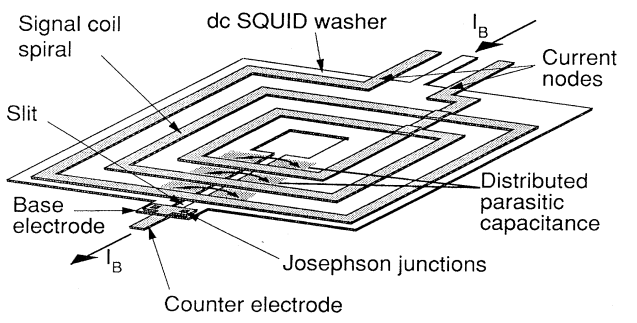


FIG. 29. Simplified structure of a planar thin-film dc SQUID with an input coil. The distributed parasitic capacitances across the SQUID washer and the locations of the current nodes for the microstrip resonance are indicated.

uniform and reproducible, the leakage current at voltages below the gap is negligible, and the junction capacitance is small. For recent developments see, for example, the proceedings of the latest SQUID conference (Koch and Lübbig, 1992).

Sputtering, plasma etching, and self-aligning "full-wafer sandwich" methods, with the junction barrier first formed on the entire wafer and patterned afterwards, are replacing older techniques like evaporation, wet etching, and lift-off. As a result, well-defined and reproducible patterns with smaller dimensions have become possible. The minimum linewidths that can be achieved with the new methods are typically a few micrometers. Advances in semiconductor processing technology have, however, made submicron dimensions feasible in SQUID structures as well (Imamura and Hasuo, 1988; Ketchen, 1991, 1992).

Proper optimization of SQUIDs is, of course, only possible if the critical parameters can be controlled accurately. Fabrication technology poses a number of constraints, including minimum linewidths and conductor separations, required film thicknesses, feasible critical current densities, and specific junction capacitances. All these technology-dependent constraints limit the range of possible parameter values of the SQUID. Since optimization usually leads to very small dimensions (see Sec. V.D.3), it is clear that improvements in fabrication technologies result in better SQUID performance.

### 3. Sensitivity of the dc SQUID

In the literature, the sensitivity of the autonomous SQUID, i.e., a SQUID without any signal-coupling elements, has been thoroughly analyzed (Tesche and Clarke, 1977; Ben-Jacob and Imry, 1981; Ketoja *et al.*, 1984a; Ryhänen *et al.*, 1989). The well-known result for the optimal energy sensitivity is

$$\varepsilon=\gamma k_B T\sqrt{LC} \ , \tag{101}$$

where $L$ is the inductance of the SQUID, $C$ the junction capacitance, and the numerical constant $\gamma\simeq 12$ according to simulations. Clearly, a small size is advantageous. However, the limit given by Eq. (101) cannot be reached in practical devices: many problems appear because of the parasitic effects introduced by the signal-coupling circuits. For example, the spiral-like signal coil (Jaycox and Ketchen, 1981) is deposited over the relatively wide conductor loop, called SQUID washer, forming the SQUID inductance (see Fig. 29). The distributed parasitic capacitance across the washer is seen as an additional capacitance $C_p$ across the SQUID. Computer simulations and experiments have shown (Ryhänen, Cantor, Drung, Koch, and Seppä, 1991; Ryhänen and Seppä, 1992) that the minimum-energy resolution, for $C_p < C$, is then

$$\varepsilon=\gamma k_B T\sqrt{L(C+2C_p)} \ . \tag{102}$$

In modern SQUIDs with small junctions, $C$ can be only a few picofarads, so that $C_p$ easily dominates. This imposes a limit on the number of turns $n_i$ in the signal coil. In addition, since a small inductance is needed for low-noise performance, the output inductance

$$L_i=n_i^2(L-L_{\text{slit}})+L_{\text{strip}} \ , \tag{103}$$

to which the magnetometer or gradiometer coils are connected, remains small. Here $L_{\text{slit}}$ is the parasitic inductance of the SQUID ring, mostly associated with the slits in the washer near the junction area (see Fig. 29), and $L_{\text{strip}}$ is the inductance of the conductor strip in the signal coil. If necessary, the problem of too low $L_i$ can be circumvented with the use of an additional inductance-matching transformer (Muhlfelder *et al.*, 1985, 1986).

The signal coil also gives rise to a variety of resonances. Its inductance and the lumped capacitance form an $LC$ resonance circuit. The SQUID washer itself acts as a $\lambda/2$ resonating antenna; its $Q$ value is enhanced by the signal coil, which reduces radiation losses. For a typical washer with 1-mm circumference, the $\lambda/2$ resonance frequency is on the order of 100 GHz, which is typically above the working point of the SQUID. A microwave transmission line, having its resonance frequency lower than the $\lambda/2$ resonance of the loop, is formed between the SQUID washer and the stripline. The most probable standing waves in the stripline have current nodes at the ends of the signal coil (see Fig. 29), where the line leaves the SQUID washer and the wave impedance changes abruptly (Hilbert and Clarke, 1984; Muhlfelder *et al.*, 1985; Seppä, 1987; Knuutila *et al.*, 1988; Ryhänen *et al.*, 1989). The various resonance frequencies are thus determined by the dimensions of the SQUID washer and by its number of turns. All these resonances can be hazardous to the operation of the SQUID, if they occur near the Josephson oscillation frequency $f_J=V/\Phi_0$ at the working point.

The resonance frequencies can, however, be reasonably well controlled by properly adjusting the geometry. Ideally, the length of the signal coil is first selected by adjusting the number of turns to be high enough to lower the transmission-line and the $LC$ resonance frequencies well below $f_J$. However, a compromise is necessary to prevent $C_p$ from becoming too large. At the same time, the resonances should be properly damped. This is because thermally activated transitions occur between different voltage states, e.g., between zero-voltage and running states. These transitions are enhanced by the presence of resonances, which may lead to substantially increased noise (Seppä, 1987; Knuutila *et al.*, 1988; Ryhänen *et al.*, 1989). Even the relatively low-frequency resonance of the flux transformer circuit, typically at a few MHz, increases the noise significantly if it is not carefully reduced (Knuutila, Ahonen, and Tesche, 1987). The ultimate performance given by Eq. (102) can only be reached if all the above-mentioned conditions are fulfilled and the resonances are properly damped.

Optimization of SQUID structures should take into account all signal-coupling circuits, including their stray in-

ductances and parasitic capacitances. In principle, even the pickup coils should be brought into the analysis. Fortunately, to a large extent, the SQUID can be optimized as a separate unit, provided that the resonances are under control (Knuutila *et al.*, 1988; Cantor *et al.*, 1991). Optimal energy resolution is achieved when

$$\beta_L = 2LI_c/\Phi_0 \simeq 2.6$$

and

$$\beta_c = 2\pi R^2 I_c C/\Phi_0 \simeq 0.7 \ .$$

In practice, energy sensitivities in the range of $10^{-32} Js = 15h$, corresponding to a flux noise well below $10^{-6}\Phi_0/\sqrt{\text{Hz}}$, can be reached (Cantor *et al.*, 1991).

Low-frequency applications of SQUIDs are limited by the $1/f$ noise which is associated with the quality of the device itself. An example of such a noise spectrum is shown in Fig. 30. In many SQUIDs the crossover point, where $1/f$ noise begins to dominate over white noise, shifts towards higher frequencies when the white noise is being reduced (Wellstood *et al.*, 1987). All SQUID elements are potential sources of $1/f$ noise, including the junctions, shunt resistors, the SQUID loop itself, and the signal circuits. Low-frequency fluctuations of junction critical currents, caused by electron trapping and release in the tunnel barrier (Wakai and van Harlingen, 1986; Rogers *et al.*, 1987), are a substantial source of $1/f$ noise. Their contribution can, however, be eliminated by proper electronics (Simmonds, 1980; Koch *et al.*, 1983; Foglietti *et al.*, 1986; Drung *et al.*, 1989). In addition, the critical current fluctuations have been found to scale inversely proportionally to the junction area (Seppä *et al.*, 1993).

The low-frequency flux noise entering the SQUID through the motion of flux lines trapped in the loop materials or in the junctions cannot be reduced by electronic means. Unfortunately, none of the present theories can explain the invariance of the $1/f$ spectral form, appearing in a wide variety of physical systems (Weissman, 1988). Therefore, the origin of the $1/f$ noise in SQUIDs is still a mystery.

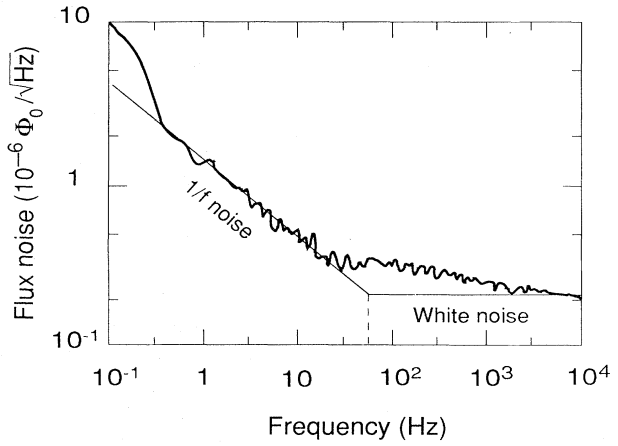


FIG. 30. Example of the flux-noise spectrum of a SQUID as a function of frequency. The $1/f$ noise is dominant below 20 Hz, and the white-noise level above 1 kHz is $2.2\times10^{-7}\Phi_0/\sqrt{\text{Hz}}$. The straight lines show a fit to a simple model consisting of $1/f$ noise plus white noise only. From Grönberg *et al.* (1992).

The ultimate limit of the low-frequency noise cannot be estimated on the basis of existing models. At 1 Hz, $6\times10^{-7}\Phi_0/\sqrt{\text{Hz}}$ in dc SQUIDs with high-quality tunnel junctions and equipped with special electronics for the elimination of critical current fluctuations have been measured (Foglietti *et al.*, 1986). At 0.1 Hz, the flux noise of this uncoupled SQUID was $1\times10^{-6}\Phi_0/\sqrt{\text{Hz}}$. Typical experimental values, however, are near $10^{-5}\Phi_0/\sqrt{\text{Hz}}$. For a coupled SQUID with a high-inductance signal coil and with flux-modulation electronics (see Sec. V.E.1), noise values of $2.5\times10^{-6}\Phi_0/\sqrt{\text{Hz}}$ at 0.1 Hz (Ketchen *et al.*, 1991) have been obtained. The fact that critical current fluctuations scale with the junction area presents the possibility of optimizing the performance with respect to $1/f$ noise as well. Using relatively large-area junctions, a coupled SQUID with a flux noise of $5\times10^{-7}\Phi_0/\sqrt{\text{Hz}}$ at 1 Hz without electronic noise reduction has been realized (Seppä *et al.*, 1993).

### 4. Optimization of flux transformer coils

The flux transformer should be optimized together with the SQUID. However, in existing neuromagnetometers the transformer usually has been realized as a wire-wound coil coupled to an available SQUID; thus the only free design parameters have been the dimensions and numbers of turns of the pickup and compensation coils.

In a gradiometer (see Fig. 26), the flux coupled to the SQUID by the transformer is

$$\Phi_s = k_s \frac{\sqrt{LL_s}}{L_p + L_{\text{comp}} + L_s + L_w} \Phi_{\text{net}} \ . \tag{104}$$

Here $L_p$, $L_{\text{comp}}$, and $L_s$ are the inductances of the pickup, compensation, and signal coils, respectively. The corresponding expression for a magnetometer is obtained from Eq. (104) by setting $L_{\text{comp}}=0$. The SQUID inductance is $L$, $L_w$ denotes the inductance of the connecting wires, and $k_s$ is the coupling coefficient between the signal coil and the SQUID. The difference of the fluxes threading the pickup and compensation coils, $\Phi_{\text{net}}$, depends on the field distribution. The sensitivity of a magnetometer is defined as the local homogeneous field in the pickup coil that would produce at the output of the system a signal equal in magnitude to the system noise over unit bandwidth.

If $\Phi_n$ is the flux noise in the SQUID, the corresponding field noise is ($E\{\cdot\}$ denotes the expectation value)

$$E\{B_n^2\}^{1/2} = \frac{\sqrt{2}(L_p + L_{\text{comp}} + L_s + L_w)}{\sqrt{L_s} n_p A_p} k_s^{-1} \left[ \frac{E\{\Phi_n^2\}}{2L} \right]^{1/2} , \tag{105}$$

where $n_p$ is the number of turns in the pickup coil and

$A_p$ is their average effective area. If we assume that the SQUID and its signal coil are of fixed design, only the pickup and compensation coils can be adjusted. The inductance-matching condition,

$$L_s = L_p + L_{\text{comp}} + L_w \ , \tag{106}$$

maximizes the transfer of energy from the pickup loop to the SQUID. In practice, however, the minimum external field sensitivity, obtained by varying the coil parameters, does not generally fulfill this condition (Ilmoniemi *et al.*, 1984). In particular, this is true if the SQUID and the pickup coil are considered together (Ryhänen *et al.*, 1989). Careful optimization reveals interrelationships between parameters not taken into account by the simple analysis, e.g., screening effects. Furthermore, the diameter and the length of the pickup coil are often determined by other considerations, like the spatial selectivity and the distribution of the field to be measured, and the dimensions of the compensation coil are fixed by the gradiometric balance condition and by space limitations.

For example, assuming that the diameters of the pickup and compensation coils have been selected, the optimum number of turns $n_p$ in the pickup coil is found by differentiating Eq. (105), where the total flux coupled to the pickup and compensation coils is assumed to be proportional to $n_p$ (Ilmoniemi *et al.*, 1984), giving,

$$L_p + L_{\text{comp}} + L_s + L_l - n_p \frac{\partial}{\partial n_p}(L_p + L_c + L_l) = 0 \ . \tag{107}$$

Therefore, the inductance-matching condition, Eq. (106), maximizes the sensitivity for tightly wound coils only. In general, no simple analytical expression exists for the dependence of the inductance on $n_p$. As a result, the optimum number of turns and other coil parameters must be determined numerically. The feasible maximum dimensions must be specified as constraints, often dictated by the space available in the Dewar.

Enlarging the pickup coil increases the field sensitivity but, at the same time, the loop integrates flux from a larger area. Thus the coils can no longer be approximated by point magnetometers. In practice, this effect becomes significant only when the coil diameter exceeds the distance to the source (Romani *et al.*, 1982a; Duret and Karp, 1984). An increased length of the coil, i.e., less tight winding, allows more turns without an excessive increase of inductance. The sensitivity improves, but the signal becomes weaker, because the distance from the source is increased. For cortical current dipoles these two effects tend to cancel, leading to a broad maximum in the signal-to-noise versus coil-length curve (Ilmoniemi *et al.*, 1984; Knuutila, Ahlfors, *et al.*, 1987).

A simple formula has been proposed for optimizing flux transformers; it takes into account the above-mentioned effects (Duret and Karp, 1984; Thomas and Duret, 1988). The figure of merit is defined as

$$G_B = \frac{\Phi_{\text{SQ}}}{B_0 A_{\text{SQ}}} \ , \tag{108}$$

where $\Phi_{\text{SQ}}$ is the net flux coupled to the SQUID, calculated by assuming a certain source geometry, e.g., a current dipole in a conducting sphere. Here, $B_0$ is the field at the center of the loop nearest to the source, and $A_{\text{SQ}}$ is the coupling area of the SQUID. This figure of merit also takes into account the base length via the net flux $\Phi_{\text{SQ}}$.

### 5. Examples of dc SQUIDs for neuromagnetic applications

dc SQUIDs suitable for neuromagnetic measurements have been reported by several groups. They were all fabricated using thin-film techniques and incorporate a densely coupled signal coil (Jaycox and Ketchen, 1981) with an output inductance high enough for use with wire-wound coils; the flux noise is less than $10^{-5}\Phi_0/\sqrt{\text{Hz}}$. We mention here a few illustrative examples, and the list is by no means complete. Integrated structures, incorporating a thin-film pickup coil as well, will be discussed in the next section.

One of the first all-thin-film dc SQUIDs used successfully in neuromagnetic research, at the Helsinki University of Technology, was the $\text{Nb/NbO}_x\text{/Pb}$-alloy-based device fabricated by IBM (Tesche *et al.*, 1985; Knuutila, Ahlfors, *et al.*, 1987). The SQUID features a 0.7-$\mu$H signal coil. When it is operated in a practical setup with flux modulation and a flux-locked loop (see Sec. V.E.1) and connected to a gradiometer coil, a flux sensitivity of $4\text{–}5\times10^{-6}\Phi_0/\sqrt{\text{Hz}}$ is reached, provided that resonances are properly damped (Knuutila, Ahonen, and Tesche, 1987). The onset frequency for the $1/f$ noise is below 0.1 Hz.

A coupled dc SQUID with even smaller white noise and better low-frequency properties was later made by IBM (Foglietti *et al.*, 1989). It employs a modified version of the fabrication process. These SQUIDs are used by the neuromagnetism group at the Istituto di Elettronica dello Stato Solido in Rome in a 28-channel system (Foglietti *et al.*, 1991).

The use of new artificial tunnel barrier materials, $Al_2O_3$ and MgO, is a general trend at present (Daalmans *et al.*, 1991; Dössel *et al.*, 1991; Houwman *et al.*, 1991; Ketchen *et al.*, 1991; Koch and Lübbig, 1992). The quality and properties of SQUIDs processed with these techniques have proven superior over conventional oxide or other deposited-barrier structures. For example, an all-refractory $\text{Nb/Al}_2\text{O}_3\text{/Nb}$ fabrication process was introduced by IBM, resulting in SQUIDs with a flux noise less than $2.5\times10^{-6}\Phi_0/\sqrt{\text{Hz}}$ at 0.1 Hz and a white noise of $0.5\times10^{-6}\Phi_0/\sqrt{\text{Hz}}$ (Ketchen *et al.*, 1991).

The Technical Research Center of Finland has made SQUIDs with low $1/f$ noise (see Sec. V.D.3). Their performance was optimized in the frequency range of 0.1 Hz to 1 kHz. The sensor, fabricated using a 10-mask-level $\text{Nb/Al-AlO}_x\text{/Nb}$ process, has 25-$\mu\text{m}^2$ junctions with $I_c = 50\ \mu\text{A}$. The 7-pH SQUID inductance is matched to an output inductance of 320 nH by means of an inter-

mediate transformer. Resonances have been carefully eliminated, resulting at best in a white flux noise of about $1\times10^{-7}\Phi_0/\sqrt{\text{Hz}}$, corresponding to the intrinsic energy resolution of $4.7h$ (Seppä *et al.*, 1993).

dc SQUID sensors are also available commercially. The first manufacturer was BTi (Biomagnetic Technologies, Inc.; see the Appendix for address), which offered a hybrid SQUID with thin-film junctions, a toroidal cavity machined of Nb, and a wire-wound signal coil. The BTi SQUID has a white-noise level of $1\times10^{-5}\Phi_0/\sqrt{\text{Hz}}$ above 1 Hz, measured using a special bias-current and flux-modulation technique to reduce the contribution of critical-current fluctuations to the low-frequency noise. Presently, all-thin-film structures are also available, for example, from Friedrich-Schiller-University, from 2G/Hypres, and from Quantum Design (see the Appendix for addresses of these suppliers). Typical white noise in these SQUIDs is $5-10\times10^{-6}\Phi_0/\sqrt{\text{Hz}}$, with the $1/f$ corner frequency at 0.1–1 Hz.

### 6. Integrated thin-film magnetometers and gradiometers

To avoid the problems of wire-wound gradiometers, which are expensive to manufacture in large quantities and have only a modest balance, planar integrated sensors have been investigated (Erné and Romani, 1985; Knuutila *et al.*, 1985; Carelli and Leoni, 1986; Bruno and Costa Ribeiro, 1989). The main advantages of thin-film gradiometers are their compact structure and excellent dimensional precision, which provides a good intrinsic balance.

Two main methods have been used for coupling the signal to the SQUID in integrated sensors. In one type, the pickup loop is a part of the SQUID structure. In the first reported integrated gradiometer (Ketchen *et al.*, 1978) the SQUID ring shared a common conductor with a larger field-collecting loop, thus forming an inductively shunted dc SQUID device. The coupling of the flux to the SQUID was poor in this construction because of a mismatch between the inductances of the pickup loop and the SQUID. For a pair of $24\times16$ mm$^2$ coils, connected in parallel, a gradient sensitivity of 20 fT/(cm$\sqrt{\text{Hz}}$) was achieved.

Later, several other experimental first- and second-order gradiometers, in which the pickup loop formed an integral part of the SQUID itself, were reported (de Waal and Klapwijk, 1982; Carelli and Foglietti, 1983; van Nieuwenhuyzen and de Waal, 1985). The early integrated magnetometers have been discussed in several review articles (Donaldson *et al.*, 1985; Ketchen 1985, 1987). A successful magnetometer has been reported in which the SQUID coil is divided into eight loops coupled in parallel to reduce the total inductance (Drung *et al.*, 1990; Drung, 1992a). The field sensitivity of the $7.2\times7.2$ mm$^2$ device is 2.3 fT/$\sqrt{\text{Hz}}$ above 500 Hz and 5 fT/$\sqrt{\text{Hz}}$ at 1 Hz.

Another design possibility is to connect the pickup loop to the SQUID via a signal coil (Jaycox and Ketchen, 1981), which allows good coupling and the necessary inductance matching. The first such fully integrated magnetometer, built for geomagnetic applications, was reported by Wellstood *et al.* (1984). Their device had a pickup-coil area of 47 mm$^2$, and the sensitivity was 5 fT/$\sqrt{\text{Hz}}$ above 10 Hz and 20 fT/$\sqrt{\text{Hz}}$ at 1 Hz. Detectors based on the same signal-coupling principle have been reported by groups working at Karlsruhe University (Drung *et al.*, 1987), at the Electrotechnical Laboratory in Tsukuba (Nakanishi *et al.*, 1987), and at the Helsinki University of Technology (Knuutila *et al.*, 1988).

In the Helsinki device, optimization of the whole structure as a single unit was done for the first time. The predicted energy sensitivity of $1.2\times10^{-31}$ Js was reached within a factor of 2. Although the integrated prototype sensor showed excellent sensitivity and tolerance to external disturbances, technical difficulties in the fabrication process kept the yield low. Thus the 24-channel system (see Sec. V.F.5.a), which was completed in 1989, had to be realized with wire-wound coils.

Integrated magnetometers and gradiometers based on the same optimization principles have been reported by Cantor *et al.* (1991). Their $4\times4$ mm$^2$ magnetometer has a white flux noise of $5\times10^{-7}\Phi_0/\sqrt{\text{Hz}}$, corresponding to a field noise of 3 fT/$\sqrt{\text{Hz}}$ and a coupled energy resolution of $1.5\times10^{-32}$ Js measured with a SQUID preamplifier. The sensitivity of the $11\times17$ mm$^2$ gradiometer is 1.1 fT/(cm$\sqrt{\text{Hz}}$).

The Technical Research Center of Finland has also produced integrated SQUID magnetometers and gradiometers designed according to the principles discussed above. The flux noise of a SQUID magnetometer with 3-$\mu$m$^2$ junctions, a 12-turn signal coil, and a SQUID of 11-pH inductance is $2.8\times10^{-7}\Phi_0/\sqrt{\text{Hz}}$ at 1 kHz and $1.5\times10^{-6}\Phi_0/\sqrt{\text{Hz}}$ at 1 Hz (Grönberg *et al.*, 1992). The SQUID is connected to a pickup loop with an inductance of a few hundred nH by means of an intermediate transformer; the measured white-noise performance corresponds to a gradient sensitivity of 1 fT/(cm$\sqrt{\text{Hz}}$). The device is fabricated using an eight-level process which employs a Nb/Al-AlO$_x$/Nb trilayer.

### 7. High-$T_c$ SQUIDs

The discovery of superconducting ceramic compounds with critical temperatures above 90 K has raised hopes for practical high-temperature SQUIDs. However, the unfavorable mechanical, chemical, and crystalline properties of high-$T_c$ materials complicate the development of good-quality films and wires and well-controlled Josephson junctions. For instance, the extremely short coherence length results in low pinning forces, allowing flux creep. The rough surface structure complicates construction of tunnel junctions; granularity in bulk samples and in polycrystalline thin films leads to phase-locked Josephson junctions between the grains, resulting in fluc-

tuations of current paths and lower critical current densities than in conventional superconductors. In addition, many high-$T_c$ materials are very sensitive to moisture and air. For a recent review, see the article by Braginski (1992).

Nevertheless, high-$T_c$ SQUIDs are being investigated enthusiastically in several laboratories. As an example, an uncoupled energy sensitivity of $1.5\times10^{-30}$ Js, or $6\times10^{-6}\Phi_0/\sqrt{\text{Hz}}$ above 10 kHz and $1.2\times10^{-28}$ Js, or $6\times10^{-5}\Phi_0/\sqrt{\text{Hz}}$ at 10 Hz, both at 77 K, has been achieved with a 60-pH grain-boundary $YBa_2Cu_3O_{7-\delta}$ (YBCO) dc SQUID (Gross *et al.*, 1990, 1991). The lowest uncoupled energy sensitivity, so far reached, is $3\times10^{-31}$ Js at 77 K and 71 kHz (Kawasaki *et al.*, 1992).

Flux transformers made of high-$T_c$ materials have been investigated as well (DiIorio *et al.*, 1991; Wellstood *et al.*, 1991), but they seem to produce excessive low-frequency noise, especially in coils made of films with a low critical-current density. Vortex motion in films is sensed by the SQUID in two ways: directly and indirectly via screening currents induced in the flux transformer. This was clearly seen in the experiments of Wellstood *et al.* (1991), where an YBCO transformer on a separate substrate was sandwiched with a conventional low-$T_c$ SQUID chip. The flux noise at 1 Hz, with the transformer coil at 60 K, was at least two orders of magnitude higher than that of the bare SQUID, resulting in a field sensitivity of 0.9 $\text{pT}/\sqrt{\text{Hz}}$. When the loop was cut and the indirect contribution thus eliminated, the noise dropped by a factor of 10.

At frequencies that are important for neuromagnetism, all high-$T_c$ SQUIDs studied so far have much larger noise levels than expected according to the $\sqrt{T}$ law, which is based on thermal fluctuations alone. Well above several kHz, however, a good agreement has been found with the theory for white noise caused by Nyquist fluctuations in resistive shunts (Gross *et al.*, 1991). The enhanced flux creep, resulting in excess noise, is a consequence of the short coherence length, an inherent property of high-$T_c$ materials (Ryhänen *et al.*, 1989). However, other mechanisms contribute as well and, on the whole, the origin of the excess $1/f$ noise still remains unknown.

Future development of reliable high-$T_c$ SQUIDs depends especially on the solution of two problems: (1) How to fabricate reliable, reproducible, and well-controllable junctions, and (2) how to avoid excess low-frequency noise. For construction of practical devices, however, high-$T_c$ SQUIDs alone are not enough. Other components, such as superconducting wires and contacts, as well as thin-film flux transformers, must be made.

### E. dc SQUID electronics

Electronics for SQUID magnetometers must meet two fundamental requirements. First, the periodic response of the SQUID to applied flux, i.e., the $\Phi-V$ characteristics (Fig. 31), must be linearized. This is achieved by operating the SQUID in a "flux-locked-loop" mode, where negative feedback is used to keep the working point of the SQUID constant. Second, the electronic circuits must be matched to the SQUID output impedance of only a few ohms. The optimal signal impedance (Netzer, 1974, 1981)

$$Z_{\text{opt}}=e_n/i_n \tag{109}$$

of typical preamplifiers is several kilo-ohms at least. Here, $e_n$ and $i_n$ are, respectively, the voltage and current white-noise spectral densities of the amplifier. Therefore, impedance matching is essential.

Several readout schemes have been proposed to meet the requirements, and they have been demonstrated experimentally as well. So far, however, only flux-modulation electronics and direct readout have been used in practical devices. In addition to them, we shall discuss digital readout techniques.

#### 1. Electronics based on flux modulation

In applications where a SQUID monitors a low-frequency magnetic field, the most commonly used technique is flux modulation (Forgacs and Warnick, 1967). This method is illustrated in Fig. 31. Square-wave modulation of $\Phi_0/2$ peak-to-peak amplitude is applied to the SQUID, and the signal is detected by a demodulator circuit. The output at the modulation frequency is proportional to the deviation of the low-frequency flux from a half-multiple of $\Phi_0$. The phase detection scheme helps to eliminate some sources of low-frequency noise, such as electromotive forces, drifts in the junction critical current and in the SQUID parameters, and $1/f$ noise from the preamplifiers. The detected signal is usually fed back to the SQUID ring through a resistor and a coupling coil. Since the high-gain feedback loop tends to

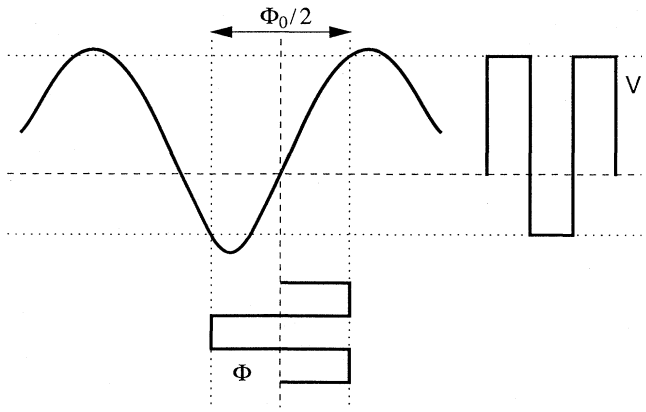


FIG. 31. Flux-to-voltage ($\Phi-V$) characteristics of a current-biased dc SQUID. A modulation of the flux through the SQUID appears as an output voltage at the same frequency. When the working point, indicated by dashed lines, is at a peak or a valley, only the harmonics are seen. In the flux-modulation scheme, the voltage detection is phase sensitive and locked to the fundamental modulation frequency.

maintain a constant flux in the SQUID, the feedback voltage is proportional to the external flux. Thus the periodic SQUID response is converted into a linear one, which is independent of the amplifier gain. In general, well-designed lock-in electronics does not increase the flux noise of the system; but in SQUIDs with complex $\Phi - V$ characteristics, some loss of sensitivity may result.

The feedback electronics can lock the intrinsic flux at any multiple of $\Phi_0/2$. However, a strong external pulse may kick the system from one stable point of operation to another, resulting in a sharp transition in the output voltage. Evidently, the higher the feedback gain, the better the system can screen the SQUID loop against an external flux jump. The increase of the open-loop gain is ultimately limited by the modulation frequency. The feedback loop may become unstable if the gain is very high and if the output of the demodulator circuit is not filtered before feeding the signal back to the SQUID ring. In dc SQUIDs the increase of amplifier noise with frequency limits the range of modulation frequencies. SQUID electronics operated in the lock-in mode have been extensively discussed in the literature (Giffard *et al.*, 1972; Giffard, 1980; Rillo *et al.*, 1987). Only the most important features will be mentioned here.

Usually the feedback loop contains an integrator (proportional plus integrating = PI controller), yielding a feedback gain $G(\omega) \simeq j\omega_{\rm mod}/\omega$. The maximum rate of flux change (slew rate) is limited to the order of $\Phi_0/\omega_{\rm mod}$, but loop stability is easily attained (Giffard *et al.*, 1972). Here $\omega$ is the angular frequency, $\omega_{\rm mod}$ the angular frequency of the flux modulation, and $j = \sqrt{-1}$. By increasing the frequency dependence of the feedback gain, $G(\omega) \simeq (j\omega_{\rm mod}/\omega)^{\delta}$, a higher slew rate can be achieved, but stability against variations in loop parameters is then impaired (Giffard, 1980). A loop filter with $\delta = 1.5$ (Seppä and Sipola, 1990) produces a phase shift of 135°. The realization of such a filter requires, however, many components. Under quiet conditions, for example, inside a magnetically shielded room, a conventional PI controller is sufficient to ensure proper operation. In multichannel applications the electronics should contain a special unit to rebalance any of the SQUIDs after loss of lock.

A transformer is needed to match the SQUID to the optimal input impedance of a few kilo-ohms for a low-noise JFET amplifier. The modulation frequency must be sufficiently high to avoid $1/f$ noise from the preamplifier, but low enough to exclude input current noise which increases drastically with frequency. Many switching transistors with a large gate area provide excellent noise characteristics for reasonable source impedances and are ideal for dc SQUIDs.

The low output impedance can be increased by feeding the signal through a cooled inductor into a capacitor in parallel with the preamplifier (Clarke *et al.*, 1975), or by using an ordinary tuned transformer (with or without a ferrite core) immersed in liquid helium. A transformer is preferable, since an increased output capacitance reduces the bandwidth of the reactive circuit. Using a tuned transformer with a transfer ratio $m$ and a quality factor $Q$, the impedance seen by the preamplifier is

$$Z_s \simeq (R_D + R) m^2 Q^2 , \tag{110}$$

where $R$ is the resistance of the transformer primary and $R_D$ is the dynamic output impedance of the SQUID. The $Q$ value is

$$Q \simeq Z_s \omega_0 C_t \simeq Z_{\rm opt} \omega_0 C_t , \tag{111}$$

where $\omega_0$ is the resonant frequency and $C_t$ the effective capacitance across the secondary of the transformer. Equations (110) and (111) show that it is possible to select independently both the impedance scaling and the bandwidth. With an additional room-temperature transformer, one may increase the bandwidth even further (Wellstood *et al.*, 1984). The slew rate could be improved, as well, by increasing the modulation frequency up to 500 kHz.

A dc SQUID readout circuit is illustrated in Fig. 32 (Knuutila *et al.*, 1988). The signal from the SQUID is fed through a cooled resonant transformer into a preamplifier consisting of two parallel FETs (Toshiba SK146). The synchronous detector contains a switching circuit, an integrator, and a sample-and-hold circuit which can effectively attenuate the modulation frequency and its harmonics without introducing a phase shift at signal frequencies. The output of the synchronous demodulator is fed via the PI controller and a transconductance amplifier (buffer) back to the modulation coil. The electronics is operated at 100 kHz. The cooled input circuits are designed to transform the 10-Ω SQUID impedance to 4 kΩ, which is optimal for this amplifier, whose noise temperature is as low as 2 K at 100 kHz. Since the dynamic range of the dc SQUID may be extremely high, the feedback circuit must be designed with care. In Fig. 32, current sources prevent conductance fluctuations in wires and contacts from adding noise when the system is operated with large feedback currents.

The $1/f$ noise in SQUIDs can be reduced by reversing the bias-current synchronously with flux modulation (Simmonds, 1980; Koch *et al.*, 1983). Many schemes, with effective reduction of low-frequency noise, have been described (Foglietti *et al.*, 1986; Kuriki *et al.*, 1988; Drung *et al.*, 1989). Bias-current modulation, however, complicates the electronics and therefore is not a very tempting solution in devices where the simultaneous operation of a large number of SQUIDs is required.

The rapid progress in instruments with many channels has given much impetus to the development of integrated and cooled readout circuits with multiplexing (Furukawa *et al.*, 1986; Shirae *et al.*, 1988). In this scheme, the voltage across several series-connected SQUIDs, modulated at different frequencies, can be recorded with a single SQUID, and a demodulation circuit at room temperature can separate the different channels (Shirae *et al.*, 1988). Unfortunately, circuits presented in the literature increase the noise level because of the aliasing effect. If the wideband noise extends to frequencies well above the

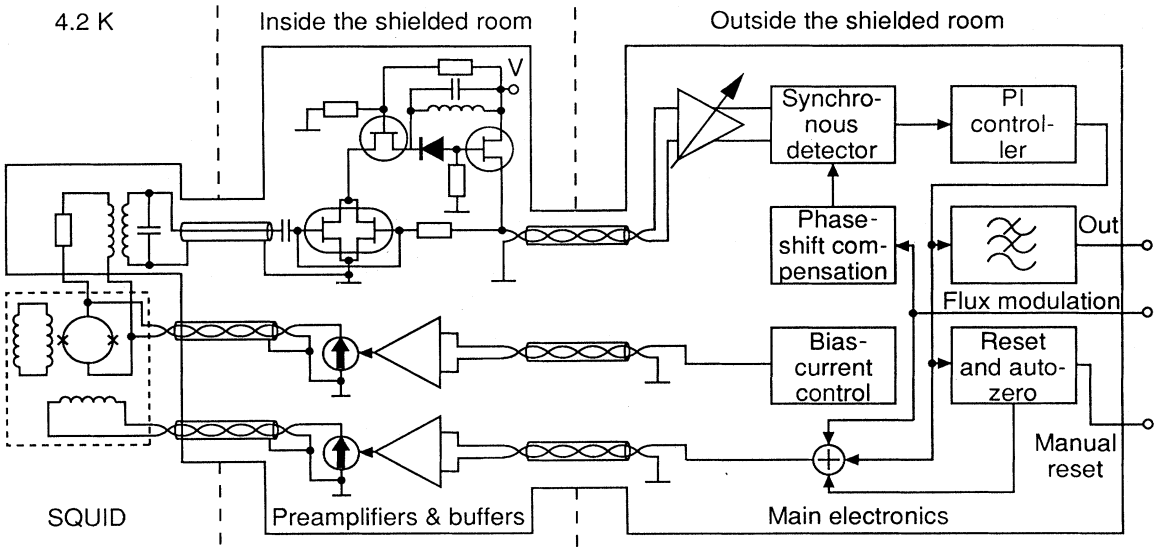


FIG. 32. Block diagram of dc SQUID electronics based on flux modulation and phase-sensitive detection (Knuutila *et al.*, 1988). For more details, see text.

sampling frequency of the multiplexing, high-frequency noise is mixed down to lower frequencies. This effect can be avoided by placing extra filters between the SQUIDs and the readout electronics, but the cooled multichannel unit then becomes rather complex.

### 2. Direct readout

The fact that the preamplifier noise at low frequencies has exceeded that of the SQUID itself has effectively prevented the use of direct readout of the SQUID voltage. However, modern operational amplifiers with a voltage noise of only 1 $nV/\sqrt{Hz}$ down to a few Hz, and SQUIDs with a large $\partial V/\partial\Phi$, have changed the situation. Furthermore, noise performance may be improved even more, either with additional positive feedback (Drung *et al.*, 1990) or with amplifier noise cancellation (Seppä *et al.*, 1991). Successful operation of a high-gain SQUID with a low-noise operational amplifier (Linear Technology LT 1028) has been demonstrated. With additional optimized feedback, noise in the flux-locked loop was decreased to $6.4\times10^{-7}\Phi_0/\sqrt{Hz}$ above 1 kHz (Ryhänen, Cantor, Drung, and Koch, 1991). Similarly, with amplifier noise cancellation, a flux noise of $5\times10^{-7}\Phi_0/\sqrt{Hz}$ above 1 kHz and $2\times10^{-6}\Phi_0/\sqrt{Hz}$ at 1 Hz (Seppä, 1992) have been reached. Reference measurements with a second dc SQUID as a preamplifier have confirmed that the intrinsic SQUID noise can be achieved with both noise-reduction methods. Since there is no need for flux modulation or impedance transformation with reactive components, the bandwidth of the electronics can be increased substantially.

#### *a. Additional positive feedback*

A schematic diagram of a direct readout circuit with positive feedback and current bias is shown in Fig. 33(a).

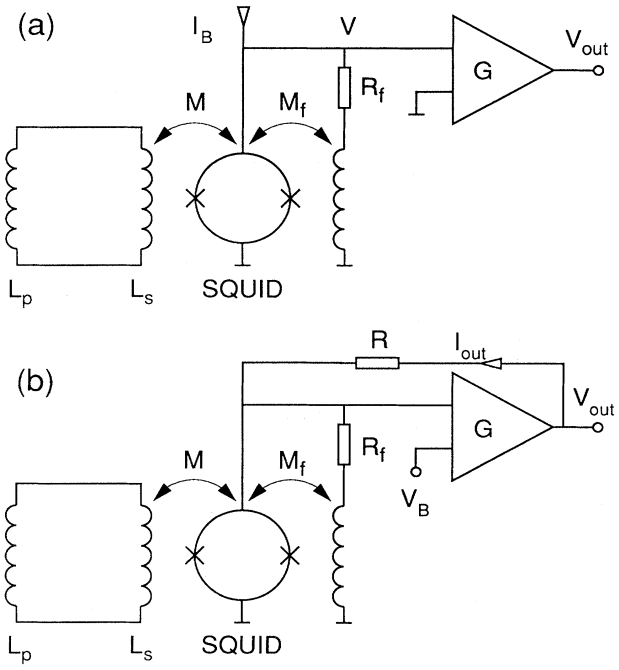


FIG. 33. dc SQUID electronics based on direct readout: (a) current bias with additional positive feedback and (b) voltage bias with amplifier noise cancellation. $I_B$ and $V_B$ are the bias current and the bias voltage, respectively. $V_{out}$ is the output voltage, $I_{out}$ the feedback current of the amplifier, $G$ its gain, and $L_p$ and $L_s$ the inductances of the pickup and signal coils, respectively. Mutual inductances $M$ and $M_f$, between the signal coil and the SQUID, and between the feedback coil and the SQUID, respectively, are shown as well. The compensation coils of gradiometers were omitted for simplicity.

If the external flux to be measured is $\Phi_{\text{ext}}$, the SQUID sees, in the presence of feedback, the flux

$$\Phi=\Phi_{\text{ext}}\Big/\left[1-\frac{M_f}{R_f+R_D}\frac{\partial V}{\partial\Phi}\right], \tag{112}$$

where $R_f$ is the feedback resistance, $R_D$ the dynamic resistance of the SQUID, and $M_f$ is the mutual inductance of the feedback branch. For the small-signal voltage $v$, we obtain

$$v=\frac{\partial V}{\partial\Phi}\Phi_{\text{ext}}\Big/\left[1+\frac{R_D}{R_f}(1-\beta M_f)\right], \tag{113}$$

where $R_D\beta=\partial V/\partial\Phi$. As a result of the feedback branch, the normal $\Phi-V$ characteristics are transformed as illustrated in Fig. 34(a); on the falling slope the effective gain $\partial V/\partial\Phi$ is increased and on the rising slope it is decreased, provided that $|\beta M_f|>1$. If $R_f<(|\beta M_f|-1)R_D$, the system becomes unstable. In the experiment of Drung *et al.* (1990), a fixed resistor was used to set the additional gain. However, by replacing the resistor with an adjustable element, adaptive gain control can be established (Seppä *et al.*, 1991). This technique can effectively prevent instabilities and higher noise. By increasing the gain of the SQUID, the total noise decreases until the limit set by the flux noise of the SQUID is reached; this has been verified experimentally. However, since the flux-to-voltage characteristics are skewed, the linear region of the SQUID is reduced, decreasing the maximum slew rate. Fortunately, this effect is partly compensated by the large bandwidth.

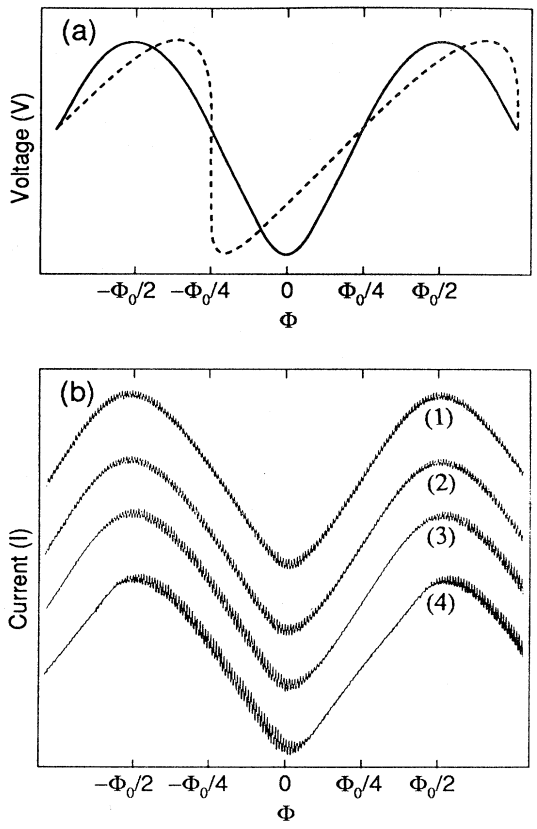


FIG. 34. SQUID characteristics with direct readout. (a) Flux-to-voltage characteristics of a current-biased SQUID without positive feedback (solid line) and with positive feedback (dashed line). The $\Phi-V$ characteristics become skewed with increased gain. (b) Measured flux-to-current characteristics (Seppä, 1992) of a voltage-biased SQUID with amplifier noise cancellation for four different decreasing values of the feedback resistance (see text); curve (1) represents the largest value of $R_f$. To illustrate the noise cancellation, a modulation signal (artificial noise) has been added to the input of the amplifier. Note that the modulation is canceled on the rising slope when $R_f$ is decreased, exactly in the way as the amplifier noise. Curve (3) corresponds to the optimum $R_f=(|\beta M_f|-1)R_D$. The curves have been separated vertically for clarity.

### *b. Amplifier noise cancellation*

Instead of the commonly used current bias, the SQUID can be voltage biased and the total noise reduced by cancellation of the amplifier noise (Seppä, 1992; Seppä *et al.*, 1991). Such a system is depicted in Fig. 33(b). Although the circuitry looks similar to that used in additional positive feedback, no positive feedback can actually take place because the voltage over the SQUID stays constant. Still, the contribution of the preamplifier noise can be reduced. The amplifier noise that is coupled magnetically to the SQUID via the feedback coil is canceled by a signal that is proportional to the amplifier noise but of opposite sign. As previously, an adaptive noise-cancellation system can be constructed when the resistor $R_f$ is replaced by an adjustable component and a controller is set to monitor the amount of cancellation.

With voltage bias, the flux seen by the SQUID is

$$\Phi=\Phi_{\text{ext}}\Big/\left[1+\frac{\beta M_f}{1+R_f[1+G(\omega)+R/R_D]/R}\right]. \tag{114}$$

Here $G(\omega)$ is the gain of the operational amplifier and $R$ the resistance in its feedback branch [see Fig. 33(b)]. Since $G(\omega)\gg R/R_D\gg 1$ at low frequencies, we see that the $\Phi-I$ characteristics are not skewed like the corresponding $\Phi-V$ curve in the current-bias scheme with positive feedback.

If $e_e$ is the noise voltage and $i_n$ the current noise caused by the operational amplifier, $e_f=\sqrt{4k_BTR_f}$ is the noise of the feedback resistor, $e_R=\sqrt{4k_BTR_D}$ is the SQUID voltage noise, and $\Phi_n$ is the flux noise of the SQUID, then the total noise at the output is (considering only small signals)

$$i_{\text{out}}=-\frac{e_R}{R_D}+\left[\frac{1}{R_D}+\frac{1+\beta M_f}{R_f}\right]e_e-\frac{1+\beta M_f}{R_f}e_f+\beta\Phi_n+i_n\ . \tag{115}$$

The contribution of $e_e$ can be canceled exactly if $\beta M_f = -(R_f + R_D)/R_D$. As before, we must have $|\beta M_f| > 1$. The system becomes unstable if $R_f < (|\beta M_f| - 1)R_D$. An example of the amplifier noise cancellation for different values of $R_f$ is given in Fig. 34(b).

The use of voltage bias is convenient because the circuit is simple. Even if the feedback exceeds the critical value by a small amount, no dramatic effects occur contrary to the situation with the current-biased SQUID (Seppä *et al.*, 1991). Since the $\Phi - V$ curve is not skewed, the dynamic range of the voltage-biased SQUID with adaptive noise cancellation is not reduced. A high-quality dc SQUID electronics system (Seppä, 1992) can be realized by employing adaptive noise cancellation and a $PI^{3/2}$ controller, where the feedback loop gain is proportional to $\omega^{-3/2}$ (see also Sec. V.E.1; Seppä and Sipola, 1990). The bandwidth of this device, when connected to an ultra-low-noise SQUID (Grönberg *et al.*, 1992), is 300 kHz in the flux-locked-loop mode, with an open-loop gain of 130 dB at 10 Hz, and with the enormous 170-dB dynamic range at 1 kHz.

Examples of measured flux noise as a function of the amount of feedback or cancellation on both voltage- and current-biased SQUIDs are given in Fig. 35. The use of a direct readout system results in very simple electronics. The promising experimental results obtained so far make this scheme attractive, especially for multichannel magnetometers, as has been demonstrated already by Koch *et al.* (1991).

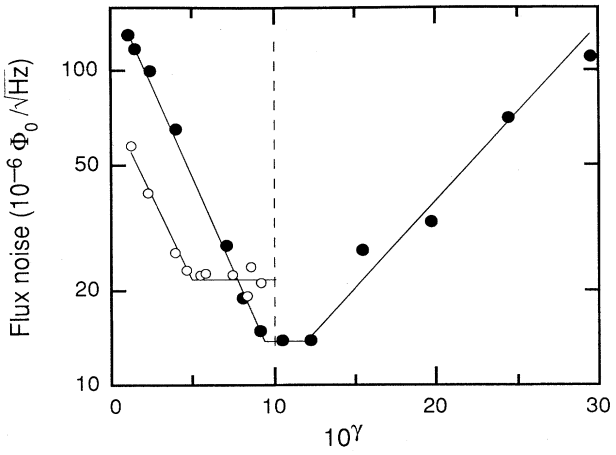


FIG. 35. Flux noise as a function of the parameter $\gamma = R_D(|\beta M_f| - 1)/R_f$ (see text). Open circles refer to additional positive feedback and solid ones to amplifier noise cancellation. The total gain is proportional to $1/(1-\gamma)$. When $\gamma = 0$, no feedback is present, and at $\gamma = 1$ the system becomes unstable. The open circles were measured for a current-biased dc SQUID fabricated at the Friedrich-Schiller-University (Jena, Germany) and connected to a low-noise preamplifier (1 nV/$\sqrt{\text{Hz}}$). The solid circles refer to a voltage-biased IBM SQUID (Tesche *et al.*, 1985), connected to a high-noise preamplifier (17 nV/$\sqrt{\text{Hz}}$). When $\gamma > 1$, no meaningful data can be obtained for the current-biased SQUID because the working point is unstable. The straight lines are only for guiding the eyes. From Seppä *et al.* (1991).

### 3. Digital readout

An interesting alternative to conventional readout techniques is to employ an integrated A/D converter on the same cryogenic chip as the SQUID. The output voltage can then be changed into digital form at low temperatures, for example, with a hysteretic dc SQUID of nonunique flux-to-voltage characteristics, used as a comparator (Drung, 1986; Drung *et al.*, 1989). This is illustrated in Fig. 36(a). The comparator is probed with a current pulse $I_{gk}$ presented at the clock frequency $f_{cl}$. The output $V_k$ switches to the voltage state with a probability of 50% when the sum of the control current, $I_{ck}$, plus a term directly proportional to the voltage over the SQUID, biased with a constant current $I_g$, is constant at the normal working point. However, if the SQUID output changes, the effective control current changes as well and the switching probability is altered very steeply. By connecting an up-down counter (UDC) and a D/A converter to the comparator output, and then by feeding back the converted analog signal $V_0$ to the SQUID as flux, the operating point is locked and the feedback current $I_{fb}$ replicates the external flux to be measured.

Another possibility (Fujimaki *et al.*, 1988) is that the SQUID itself is strongly hysteretic and ac biased with biphasic pulses $I_{ac}$ [Fig. 36(b)]. The distribution of positive and negative pulses $V_{ac}$ then depends on the external flux. These pulses can be used to add or subtract flux

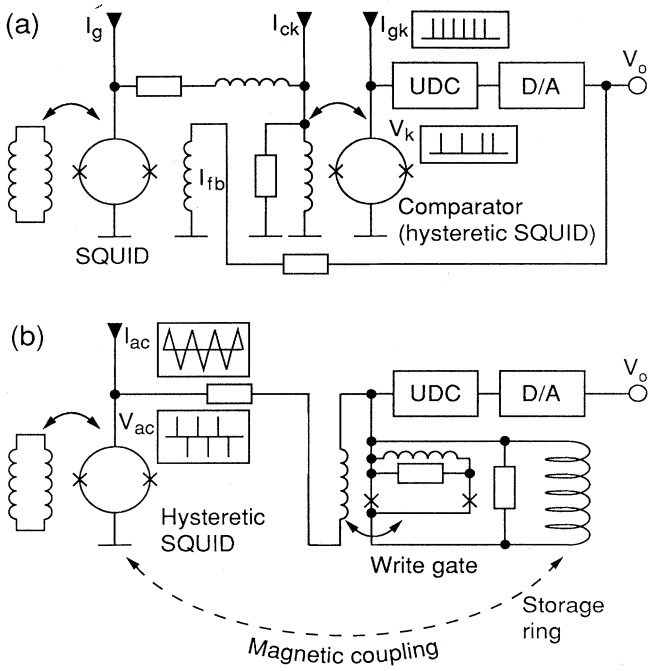


FIG. 36. dc SQUID electronics based on digital readout: (a) with a separate comparator and external feedback and (b) with a hysteretic SQUID and internal feedback, including a magnetically coupled storage loop. Some of the signal wave forms have been indicated schematically in the insets. For details, see text.

quanta trapped in a storage ring which is magnetically coupled to the actual SQUID sensor. The storage consists of a write-gate interferometer which is connected to a large flux-collecting coil. The pulses are coupled magnetically and injected into the write gate. A positive pulse causes the junctions at the gate to switch sequentially and momentarily to the voltage state to allow the entry of one flux quantum, first into the write loop and then into the storage ring. Correspondingly, a negative pulse subtracts one flux quantum. In this way, a negative feedback circuit is established on the SQUID chip, without the need of additional D/A conversion. The output can be deduced from the pulses at room temperature and counted.

Digital readout has been demonstrated to work in a rather promising way. Flux-noise values of $7\times10^{-7}\Phi_0/\sqrt{\text{Hz}}$ above 1 kHz and $5\times10^{-6}\Phi_0/\sqrt{\text{Hz}}$ at 0.1 Hz, when an additional low-frequency noise-compensating modulation scheme was used, have been reported (Drung *et al.*, 1989). The slew rates of digital SQUIDs are below those of conventional devices. However, increasing the clock frequency should improve the situation.

### F. Multi-SQUID systems

Until the middle of the 1980s, almost all biomagnetic measurements were carried out using single-channel magnetometers with pickup and compensation coils wound of superconducting wire on three-dimensional formers. The optimization of the coil parameters, such as their diameter and length, the number of turns, and the base line of the gradiometer followed the principles described in Sec. V.D.4. The optimal configurations have also been discussed by several authors (Romani *et al.*, 1982a; Vrba *et al.*, 1982; Duret and Karp, 1983, 1984; Farrell *et al.*, 1983; Ilmoniemi *et al.*, 1984; Thomas and Duret, 1988). In maximizing the field sensitivity and discrimination against external noise, the spatial distribution of the biomagnetic signal and of the disturbances must be taken into account.

Locating current sources in the brain and the follow-up of their dynamic behavior are the main objectives of the neuromagnetic method. Therefore, the use of a multichannel device for mapping the spatial pattern of the magnetic field caused by these sources is very desirable. Such instruments not only speed up the measurements but also give more reliable data and make possible experiments that require simultaneous recordings over a large area, such as studies of spontaneous brain activity.

#### 1. Optimal coil configuration

Because of the large variety of possible source current distributions in the human brain, general criteria for optimal magnetometer design do not exist. Figures of merit for different configurations can be obtained only by making assumptions about the signal sources and their characteristic field distributions.

In addition to maximum sensitivity in every channel, one has to find a sensor configuration that gives the best locating accuracy. Unfortunately, these two goals are sometimes contradictory. For example, increasing the pickup-coil diameter improves field sensitivity but reduces spatial resolution.

In practice, the freedom of the designer is restricted by several constraints: the size of the Dewar, the properties of the SQUID sensors, the feasible number of channels, the distribution and strength of external noise sources, and the characteristics of the brain signals.

A useful figure of merit for multichannel magnetometers is the precision in locating cortical current sources. To estimate the error limits, a suitable source current model and a volume conductor model must be chosen. A current dipole in a spherically symmetric volume conductor is usually appropriate, as discussed in Sec. III.E.2.

The locating accuracy of a magnetometer may be simulated numerically by adding noise to the calculated field values and by fitting an equivalent dipolar source to the data by means of a least-squares search. Repeated simulations then reveal the average locating error. A more effective way is to determine directly the confidence regions of the least-squares fit, as was discussed in Secs. IV.F.4 and IV.G.4.

The limits depend not only on the signal-to-noise ratio, but also on the depth of the dipole and on the measurement grid. Therefore, the calculated confidence limits can be applied for comparing various magnetometer arrays (Knuutila *et al.*, 1985; Knuutila, Ahlfors, *et al.*, 1987; Knuutila and Hämäläinen, 1989).

In addition to calculation of the confidence limits, spatial sampling theory and information theory can be employed for determining an optimal coil configuration. We shall discuss both methods in detail below.

#### 2. Sampling of neuromagnetic signals

If the spatial frequency content of the signal to be measured is known, multidimensional sampling theory (Petersen and Middleton, 1962, 1964; Montgomery, 1964; Ahonen *et al.*, 1993) can be used to determine the largest spacing allowed for the measurement grid if aliasing is to be avoided. This problem occurs when the grid is not dense enough to capture the spatial variations of the field.

Assume that the vertical component of the magnetic field $B_z$ is sampled at points $\mathbf{r}_n=\sum_{i=1}^{N} n_i\mathbf{a}_i$, where $n_i$ are integers and $\{\mathbf{a}_i, i=1,\ldots,N\}$ form a basis of the space $R^N$, and that $B_z$ is spatially bandlimited, i.e., restricted to a bounded area $S$ of the reciprocal (momentum) space $K^N$. The Fourier transform of a function $B_z(\mathbf{r})$ sampled at discrete points is equal to a set of spectra obtained by shifting the region $S$ in $K^N$ periodically by $\mathbf{k}_n=\sum_{i=1}^{N} n_i\mathbf{b}_i$. Here, $\{\mathbf{b}_i, i=1,\ldots,N\}$ is a base of $K^N$, related to $\{\mathbf{a}_i\}$ by $\mathbf{a}_i\cdot\mathbf{b}_j=\delta_{ij}$; $i,j=1,\ldots,N$, where $\delta_{ij}$ is the Kronecker delta. To obtain a criterion for aliasing,

we try to construct an interpolation function $g(\mathbf{r})$, such that everywhere in $R^N$,

$$B_z(\mathbf{r})=\sum_n B_z(\mathbf{r}_n)g(\mathbf{r}-\mathbf{r}_n) . \quad (116)$$

The exact reconstruction of $B_z(\mathbf{r})$ from the samples $B_z(\mathbf{r}_n)$ is thus reduced to deriving $g(\mathbf{r})$. Equation (116) can be transformed into

$$\mathcal{B}_z(\mathbf{k})=K\sum_n \mathcal{B}_z(\mathbf{k}-\mathbf{k}_n)\mathcal{G}(\mathbf{k}) , \quad (117)$$

where $\mathcal{B}_z$ and $\mathcal{G}$ represent the Fourier transforms of $B_z$ and $g$, respectively, and $K$ is the volume of the unit cell in the reciprocal space. Obviously, Eq. (117) must be an identity for a properly sampled signal.

Equation (117) represents a sum over the periodically extended images $S_p$ of the support $S$: $S_p=\{S+\mathbf{k}_n;\ \mathbf{k}\in S\ \forall\mathbf{k}_n=\sum_{i=1}^N n_i\mathbf{b}_i\}$. If the shifted images $S_p$ do not overlap, Eq. (117) is, indeed, an identity, and no aliasing occurs (Petersen and Middleton, 1962). Thus the sampling grid $\{\mathbf{a}_i\}$ should be dense enough to provide a grid $\{\mathbf{b}_i\}$ which is sufficiently sparse to prevent overlap. Then, one can find $g(\mathbf{r})$ such that the exact reconstruction of $B_z(\mathbf{r})$ from the samples $B_z(\mathbf{r}_n)$ is possible by choosing $\mathcal{G}(\mathbf{k})=1/K$ for $k\in S$ and $\mathcal{G}(\mathbf{k})=0$ when $k\in(S_p-S)$. This is a generalization of the classical one-dimensional Nyquist sampling criterion, stating that the inverse of the sampling interval should be at least twice the largest frequency present in the signal to be sampled.

However, multiple, simultaneous, and independent measurements at one point allow a certain degree of overlap, permitting the use of a less dense sampling grid (Montgomery, 1964; Petersen and Middleton, 1964). Suppose now that we measure, instead of the amplitude of $B_z(\mathbf{r})$, all components of the gradient vector $\nabla B_z(\mathbf{r})$. Interpolation can then, of course, only be carried out up to an additive constant $f_0$. As a result, Eq. (116) is changed to

$$B_z(\mathbf{r})=B_0+\sum_n \nabla B_z(\mathbf{r}_n)\cdot\mathbf{g}(\mathbf{r}-\mathbf{r}_n) . \quad (118)$$

Without loss of generality, we can assume that $B_0=0$. As above, this can be transformed to

$$\mathcal{B}_z(\mathbf{k})=-2\pi jK\sum_n \mathcal{B}_z(\mathbf{k}-\mathbf{k}_n)(\mathbf{k}-\mathbf{k}_n)\cdot\mathcal{G}(\mathbf{k}) , \quad (119)$$

where $j$ is the imaginary unit. To avoid aliasing, we require again that Eq. (119) be an identity. This can be accomplished if

$$-2\pi j\mathbf{k}\cdot\mathcal{G}(\mathbf{k})=A\,;\mathbf{k}\in S,\ \mathbf{k}_n=0 , \quad (120)$$

$$(\mathbf{k}-\mathbf{k}_n)\cdot\mathcal{G}(\mathbf{k})=0;\mathbf{k}\in(S+\mathbf{k}_n),\ \mathbf{k}_n\neq 0 . \quad (121)$$

Here, $A$ is the volume of the unit cell spanned by the base vectors $\mathbf{a}_i$. These conditions can be met, except at some singular points, in an $N$-dimensional space, even when there is at most an $(N-1)$-fold overlap in the images of $S$, i.e., if each point $\mathbf{k}$ belongs at most to $N$ different periodically extended images $S+\mathbf{k}_n$ (Ahonen *et al.*, 1993). If the amplitude is measured together with the gradient vector, the overlap could be $N$-fold (Montgomery, 1964; Petersen and Middleton, 1964).

In particular, if we measure the planar orthogonal derivatives $\partial B_z/\partial x$ and $\partial B_z/\partial y$ at the same point instead of just $B_z$, the sampling grid of these dual sensors can be sparser by a factor of $\sqrt{2}$ compared with what is needed for sampling just $B_z$. Intuitively, the result is obvious: since twice as much information is gathered at each point, the "unit cell" around a point in the sampling grid can be twice as large. This result has practical consequences, especially in designing devices covering the entire head, as will be discussed in Sec. V.F.6.

In practice, typical cortical dipoles are more than 30 mm from the sensors. Thus an appropriate grid spacing for locating a single source would be 30 mm for magnetometers and axial gradiometers and 40 mm for planar gradiometers. But what happens if there are two dipoles, at a separation $l$ which is less than the distance to the detector array: can the two dipoles be resolved from a single dipole? It turns out that the discrimination capability is reduced with decreasing $l$ only because the difference between the amplitudes produced by the pair of dipoles and a single, stronger dipole is reduced below the noise level, but not because of the appearance of short-wavelength spatial variations in the field that would cause aliasing in the sampling grid (Ahonen *et al.*, 1993). Thus we arrive at the conclusion that in practice a grid spacing of 30–40 mm, depending on what types of gradiometers are used, is indeed sufficient to avoid aliasing. After this critical density has been reached, the amount of information gathered increases much more slowly than the number of channels; this limit is thus set by practical constraints.

### 3. Information conveyed by the magnetometers

The angles between the lead fields (see Sec. IV.B) of two channels provide a measure of the amount of different information conveyed by each channel (Ilmoniemi and Knuutila, 1984; Knuutila, Ahlfors, *et al.*, 1987). The lead field $\mathcal{L}_i$ of the magnetometer $i$ measuring the component $B_i$ is defined by [see Eq. (43)]

$$B_i=\int \mathcal{L}_i(\mathbf{r})\cdot\mathbf{J}^p(\mathbf{r})dv\equiv\langle\mathcal{L}_i,J^p\rangle , \quad (122)$$

where $\mathbf{J}^p$ denotes the source (=primary) current density and the integration extends over the source area. The angle $\phi$ between lead fields $\mathcal{L}_1$ and $\mathcal{L}_2$ is then defined as

$$\phi=\arccos\frac{\langle\mathcal{L}_1,\mathcal{L}_2\rangle}{\sqrt{\langle\mathcal{L}_1,\mathcal{L}_1\rangle\langle\mathcal{L}_2,\mathcal{L}_2\rangle}} . \quad (123)$$

The concept of marginal utility, when adding more channels to a given area, may be studied best by computing the information-theoretical channel capacity of a given magnetometer configuration (Kemppainen and Il-

moniemi, 1989). In these calculations, the source currents $\mathbf{J}^p$ are assumed to be completely random with zero mean and a variance $s^2$, and uniformly distributed in the conductor volume. The magnetometer outputs $u_i$ are

$$u_i = b_i(t) + n(t) = \langle \mathcal{L}_i, J^p \rangle + n(t) , \tag{124}$$

where $n(t)$ is Gaussian noise with zero mean and variance $\sigma^2$. The signal-to-noise ratio of one channel is given by

$$P_i = \langle \mathcal{L}_i, \mathcal{L}_i \rangle s^2/\sigma^2 . \tag{125}$$

Here, the inner product of the lead fields $\langle \mathcal{L}_i, \mathcal{L}_i \rangle$ describes the strength of the coupling of channel $i$ to the sources.

To obtain an expression for the channel capacity of a multi-SQUID magnetometer, it is necessary to orthogonalize the lead fields by the transformation

$$\mathcal{L}_i' = \Sigma_j M_{ij} \mathcal{L}_i . \tag{126}$$

Then, the signal-to-noise ratio is

$$P_i' = \langle \mathcal{L}_i', \mathcal{L}_i' \rangle s^2/\sigma'^2 , \tag{127}$$

where $\sigma_i'^2 = \Sigma_j (M_{ij}\sigma_j)^2$. To find the transformation matrix $\mathbf{M}$ with components $M_{ij}$, we compute the matrix $\Pi$ containing the inner products of the lead fields, viz.,

$$\Pi_{ij} = \langle \mathcal{L}_i, \mathcal{L}_j \rangle . \tag{128}$$

Next, we make the spectral decomposition $\mathbf{\Pi} = \mathbf{U}\mathbf{\Lambda}\mathbf{U}^T$, where $\mathbf{\Lambda}$ is a diagonal matrix. One can choose $\mathbf{M} = \mathbf{U}^T$ because then $\mathbf{\Pi}' = \mathbf{M}\mathbf{\Pi}\mathbf{M}^T = \mathbf{\Lambda}$. Finally, the equation for the total channel capacity is

$$I_{\text{tot}} = \frac{1}{2} \sum_{i=1}^{N} \log_2(P_i' + 1) . \tag{129}$$

This figure of merit has the advantage that it properly takes into account the sensing-coil geometry, the noise level, the distance to the source area, as well as the sensor distribution. It has been used for comparison of various multichannel magnetometer configurations (Kemppainen and Ilmoniemi, 1989).

Assume now that we want to cover a certain area with magnetometer units. To find an adequate number of channels $N$, we calculate $I_{\text{tot}}$ as a function of $N$. At first, $I_{\text{tot}}$ increases steadily with $N$. However, after a certain limit, $I_{\text{tot}}$ saturates. This is because of overlap by the lead fields of additional channels when they are brought closer to each other. After this limit, the orthogonalized signal-to-noise ratios $P_i'$ give only a negligible contribution to $I_{\text{tot}}$. By comparing the increase of the channel capacity as a function of $N$ with the additional cost and increased complexity of the construction, we thus obtain a practical optimum for the number of channels.

## 4. Practical aspects

In a multichannel magnetometer, compact modular construction is advantageous. When many channels are used simultaneously, the possibility for computer control of the electronics is important. Furthermore, to keep crosstalk between channels sufficiently low, e.g., below $10^{-2}$, cables must be well shielded and symmetrized. This is also necessary to provide immunity against ambient external noise. For high-sensitivity magnetometers, a robust grounding arrangement is essential. In addition, materials used inside the Dewar must be carefully chosen. For example, careless cabling between the liquid helium and room-temperature parts of the system may increase the boiloff rate excessively.

Making Dewars for wide-area multichannel magnetometers is problematic, too (see Sec. V.C). Because of considerable variations in head shapes, no Dewar cap can be made optimal for all subjects. A spherical bottom is a compromise approximating the average curvature of the head. In addition, a large measuring area requires thick Dewar walls for strength and thus a wide gap between the room-temperature surface and the 4.2-K interior. The fact that some of the channels are rather far from the scalp imposes high demands on the sensitivity of the SQUIDs.

## 5. Examples of multichannel systems

The first multi-SQUID magnetometers had 4–5 channels on an area of only a few cm in diameter (Ilmoniemi *et al.*, 1984; Romani *et al.*, 1985; Williamson *et al.*, 1985). The noise in these devices was about 20 $\text{fT}/\sqrt{\text{Hz}}$. In the second phase of development, 7-channel dc SQUID magnetometers were introduced. The 7-SQUID gradiometer at the Helsinki University of Technology (Knuutila, Ahlfors, *et al.*, 1987) covered a relatively large area, nearly 10 cm in diameter. The first-order axial asymmetric gradiometer coils were laid in a hexagonal array. The noise level of this instrument was 5 $\text{fT}/\sqrt{\text{Hz}}$. Such devices have been discussed in detail in a review on multi-SQUID systems (Ilmoniemi *et al.*, 1989). Several new instruments with 7–9 channels have been reported since (Carelli *et al.*, 1989; Guy *et al.*, 1989; Ohta *et al.*, 1989; Dössel *et al.*, 1991).

In 1989, a new generation of instruments emerged, having typically more than 20 SQUID channels distributed over an area exceeding 10 cm in diameter. We shall now briefly review these devices.

### *a. The 24-channel gradiometer at the Helsinki University of Technology*

Our 24-channel system (Kajola *et al.*, 1989; Ahonen *et al.*, 1991) was in use from 1989 to 1992 when it was replaced by a whole-cortex device (see Sec. V.F.6.a). The device is shown schematically in Fig. 37 and in a photograph in Fig. 10. It has 12 two-gradiometer units, spaced 30 mm from each other and located on a spherical cap with a diameter of 125 mm and a 125-mm radius of curvature. Every unit measures the off-diagonal derivatives $\partial B_z/\partial x$ and $\partial B_z/\partial y$, where $x$, $y$, and $z$ refer to a coordi-

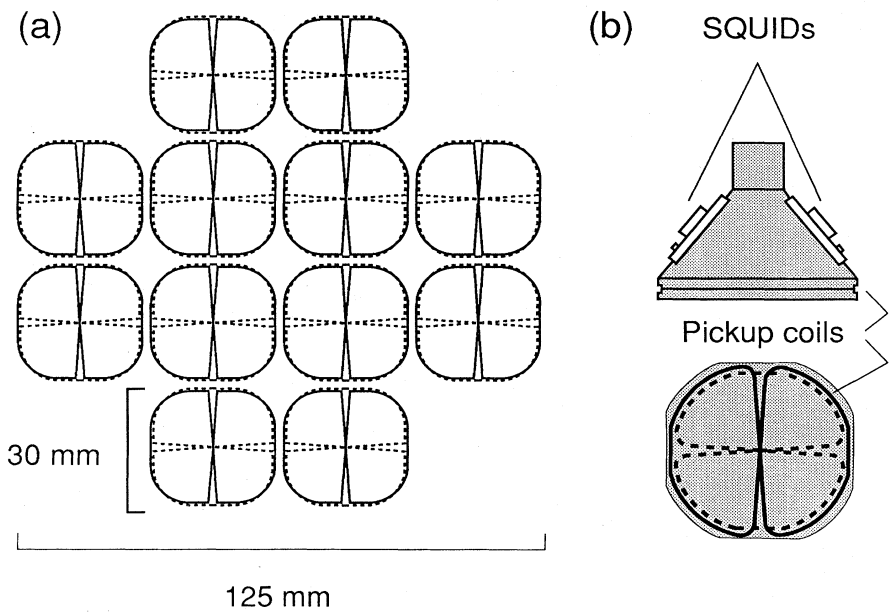


FIG. 37. Schematic illustration of the flux-transformer array in the 24-channel gradiometer at the Helsinki University of Technology: (a) arrangement of the pickup coils, located on a spherical cap, and (b) one of the 12 two-SQUID units. The coils, measuring $\partial B_z/\partial x$ and $\partial B_z/\partial y$, are indicated by solid and dashed lines, respectively. The SQUIDs are above the coils.

nate system local to each sensor separately [see Fig. 7(c)]. As discussed earlier (see Fig. 27), this design produces its maximal response just over the dipole; the direction of the dipole is given by the expression $(\partial B_z/\partial y)\mathbf{e}_x - (\partial B_z/\partial x)\mathbf{e}_y$, where $\mathbf{e}_x$ and $\mathbf{e}_y$ are unit vectors. The base length of the gradiometers is 13 mm and the area of the pickup loops is 3.7 $cm^2$. The SQUIDs, fabricated by IBM (Tesche *et al.*, 1985; see also Sec. V.D.5), are mounted on a conical former above the wire-wound flux-transformer coils. The sensor array is housed in a custom-designed Dewar (CTF Systems, Inc.; see the Appendix for addresses) with a curved and tilted end cap and a 10-liter capacity for liquid helium. This gives a three-day period between refills. The distance from the sensors to the outer surface of the Dewar is 15 mm.

The system uses conventional flux-locked-loop electronics, with a modulation at 90 kHz applied in phase to all channels. The resonant impedance-matching transformers are located in the helium storage area of the Dewar, and the preamplifiers, in groups of eight, are on top of the cryostat in detachable aluminum boxes. The bias, voltage-measurement, and flux-modulation cables from the SQUIDs to the preamplifiers also run in groups of eight inside Cu-Ni tubes. The detector-controller units, each on a Euro-1-sized printed circuit board, are outside the shielded room in an rf-shielded cabinet. The equivalent gradient noise of the sensors is 3–5 $fT/(cm\sqrt{Hz})$. The imbalance of the gradiometers, operated inside our heavily shielded room (see Fig. 9), is typically less than 2%. The crosstalk between channels is below 1%.

The low-pass-filtered results are digitized with a data-acquisition unit and transferred to a computer with a real-time operating system. This computer also calculates averages of evoked responses online and stores the results on disk. Spontaneous data are saved on a digital tape. The results may then be analyzed later off line in UNIX workstations, which are connected to the measurement computer by a local area network.

### *b. The Siemens 37-channel "Krenikon" systems*

Figure 38(a) shows the flat layout of the pickup coils in the 37-channel axial gradiometer manufactured by Siemens AG in Erlangen (Hoenig *et al.*, 1991). This system is intended for use inside a moderately shielded room. The hexagonal arrays of hexagonal first-order gradiometer pickup and compensation coils were fabricated on flexible printed-circuit boards and glued onto a support structure so that axial gradiometers were formed. The pickup area of the coils is 6 $cm^2$; the pickup and compensation coils are within a 19-cm-diameter cylinder in two planes separated by 70 mm. The system includes three additional magnetometers to measure the $x$, $y$, and $z$ components of the external magnetic field for noise cancellation.

The SQUIDs are inside of four separate superconducting shields, each containing one chip with ten dc SQUIDs (Daalmans *et al.*, 1989). The electronics is based on 100-kHz flux modulation, with resonant impedance-matching transformers. The noise of the system is typically less than 10 $fT/\sqrt{Hz}$ at frequencies over 10 Hz. Because of the flat-bottomed Dewar, "Krenikon" is most suitable for cardiomagnetic measurements; some

of the channels, especially the outer ones, would be quite far from the brain. The gap between the liquid-helium space and the outer surface of the Dewar is 20 mm. The capacity of the helium reservoir is 25 liters, requiring refills every four days. The complete installation also includes a Vacuumschmelze shielded room (see Sec. V.B.1) plus a data-acquisition and computer system with software for data analysis. Krenikon systems have been installed in Erlangen and in Stockholm. Figure 38(b) illustrates an example of data obtained with this instrument.

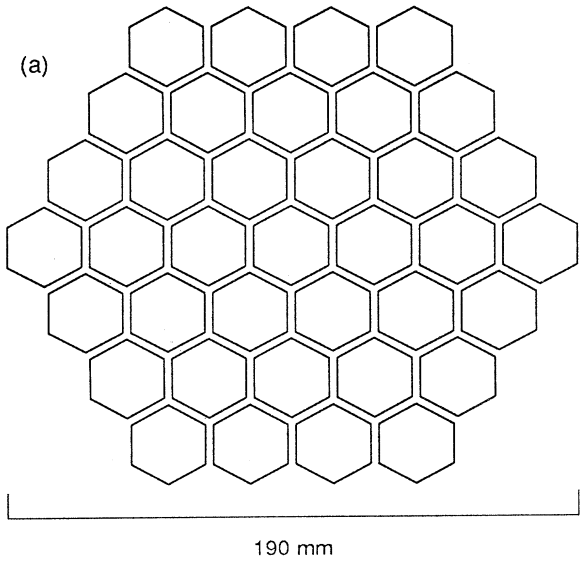


FIG. 38. Siemens "Krenikon" system. (a) Sensor arrangement of the Siemens 37-SQUID "Krenikon" system (Hoenig *et al.*, 1991). The hexagonal first-order axial gradiometer coils are on two flat printed circuit boards, separated by 7 cm. Only one of the boards is shown. (b) Auditory evoked magnetic responses obtained with the Krenikon system over the left hemisphere. Tone bursts (1 kHz, 300 ms) were presented once every 2.2 s to the right ear. The traces are averages of 557 single responses, and they start 100 ms before the stimulus onset. Unpublished data courtesy of Dr. P. Grummich and Dr. E. Herrmann (1992; Department of Experimental Neuropsychiatry and Otorhinolaryngologic Clinic, University of Erlangen, Germany).

*c. The BTi gradiometers*

The first commercial multichannel neuromagnetometer was introduced in 1985 by BTi. It had seven channels in a curved-bottom Dewar on a spherical cap of 55-mm diameter and 100-mm radius of curvature. Some of these installations include two such Dewars that make it possible to record from both hemispheres simultaneously.

The latest BTi model is a 37-channel system ("Magnes"), shown in Fig. 39(a). It has a hexagonal sen-

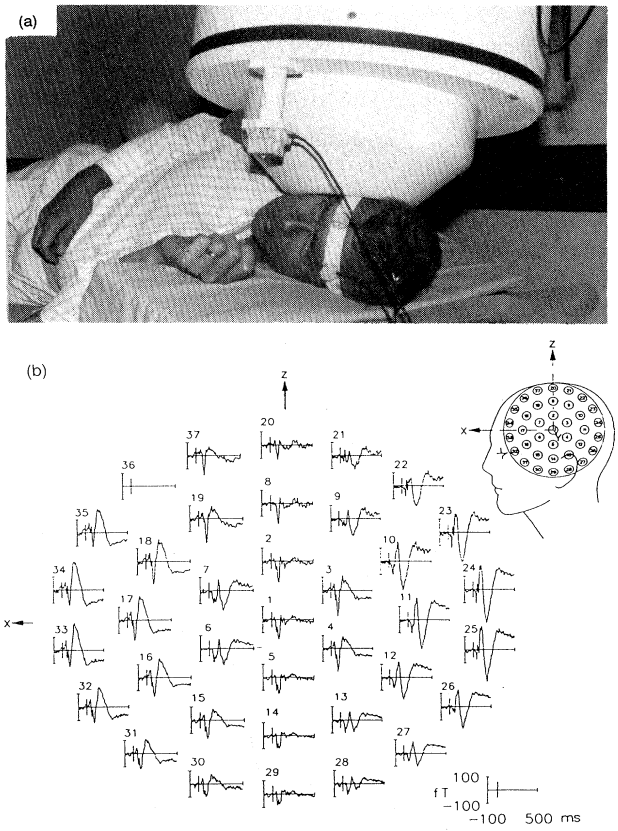


FIG. 39. BTi "Magnes" system. (a) 37-channel gradiometer of the BTi "Magnes" system in a measurement situation. The coils of the probe-position indicator, discussed in Sec. V.F.8, are attached to the subject's head and to the Dewar (courtesy of Biomagnetic Technologies, Inc.). (b) Auditory evoked responses to tone bursts recorded with the BTi 37-channel instrument over the left hemisphere. The approximate positions of the sensors are shown on the schematic head. The interstimulus interval was 4*s* and 384 responses were averaged. From Pantev *et al.* (1991).

sor arrangement similar to the Siemens device, but the coils are wire-wound around 20-mm formers. They are spaced 22 mm apart and are located on a spherical cap with a 120-mm radius of curvature. The diameter of the coil array is 144 mm. In addition to the 37 first-order gradiometers, there are eight additional SQUIDs for cancellation of external disturbances. The noise of the system is 10–20 fT/$\sqrt{\text{Hz}}$. BTi delivers complete systems with shielded rooms, computers, and software. In August 1992, nine installations of the 37-channel device were in use, for instance, in National Institute for Physiological Sciences (Okazaki, Japan), in New York University Medical Center, in Scripps Clinic (San Diego), and in the University of Münster (Germany). Figure 39(b) shows typical auditory evoked responses measured with the BTi instrument (Pantev *et al.*, 1991).

Together with their clinical installations, BTi is developing application protocols intended for routine hospital use. Patient handling and data acquisition and analysis, as well as output presentations, are being standardized so that a system operator/technician should be able to complete an examination procedure in one hour, including preparation of routine information needed by the referring physician.

Two applications are currently being tested by BTi for clinical use. The first is localization of the somatosensory cortex by evoked-response techniques to minimize paralysis caused by surgical injury to the motor cortex. The second application is based on the observation that the spectrum of the spontaneous electrical activity from functionally injured brain tissue often exhibits a shift towards lower frequency, particularly below 8 Hz. In EEG analysis, focal regions of low frequency or slow, rhythmic activity are commonly associated with localized pathology. The diagnostic value of focal slow activity is enhanced when its generators are located with respect to brain anatomy. Situations in which MEG recordings of focal slow activity are believed to be useful include cerebral ischemia, trauma, tumor, and degenerative diseases.

### *d. The PTB 37-channel magnetometer*

A 37-channel instrument is in operation at the Physikalisch-Technische Bundesanstalt in Berlin (Koch *et al.*, 1991). This system was designed mainly for magnetocardiographic measurements inside a heavily shielded room. The device uses integrated multiloop dc SQUID magnetometers, fabricated on individual $9\times9$ mm$^2$ chips (Drung *et al.*, 1990) and then laid out on a planar surface along three concentric circles of 70 mm, 140 mm, and 210 mm in diameter. The SQUIDs have eight loops connected in parallel. Each magnetometer is a separate entity consisting of the SQUID package, a stainless-steel tube with cabling, and an electronics box. Every unit can be mounted into the system individually, enabling easy replacement of sensors. The flat-bottom Dewar, with an inner diameter of 250 mm, was made in-house; the vacuum gap at the tip, when warm, is 27 mm and the noise due to the radiation shields is 2 fT/$\sqrt{\text{Hz}}$. The capacity of the liquid-helium reservoir is 25 liters and the boiloff rate 6 liters/day with all sensor units mounted.

The readout electronics of the SQUIDs is based on low-noise operational amplifiers, with the SQUID gain increased by means of positive feedback (Drung *et al.*, 1990). The field sensitivities at 1 Hz range from 6 to 10 fT/$\sqrt{\text{Hz}}$, with the noise increasing by almost two orders of magnitude at 0.1 Hz. The low-frequency disturbances were found to be mostly environmental. They can be reduced by an order of magnitude by subtracting the signals of two magnetometers, 56 mm apart, from each other, thus forming a gradiometer electronically. The average of the outputs of all SQUIDs or of those on the outer ring can be used as the reference signal (Drung, 1992b).

### *e. The Dornier two-Dewar system*

A $2\times14$ channel rf SQUID system was fabricated by Dornier, in collaboration with CTF, for the University of Ulm. The system has two Dewars, with roughly *D*-shaped curved bottoms, positioned as close to each other as possible with the straight sides adjacent (see Fig. 40). This arrangement is intended for recordings of brain signals over both field extrema of a neuronal source, or for simultaneous measurements from the right and left hemispheres. Both Dewars contain a magnetometer array with the coils wound on 16 cubic formers, spaced 20.5 mm apart, each having pickup loops in three orthogonal directions. Eleven coils are connected to rf SQUIDs via a switching matrix which allows choosing any of the 48 coils to be used in the measurements. The channels cannot, however, be reconnected when the device is operational at liquid-helium temperature. The remaining three SQUIDs are connected to three orthogonal reference coils, 9 cm above the array. A gradiometric response of the device is formed by calculating differences electronically. The equivalent noise of the magnetometers is 15 fT/$\sqrt{\text{Hz}}$ and that of the gradiometers 20–30 fT/$\sqrt{\text{Hz}}$. The radius of curvature of the Dewar bottom is 118 mm.

### *f. 19-channel gradiometers*

Two 19-channel systems, one at the University of Twente in the Netherlands (ter Brake, Flokstra, *et al.*, 1991) and one at the Philips Research Laboratories in Hamburg (Dössel *et al.*, 1992), have been introduced. Both devices have wire-wound gradiometer coils, laid out in a hexagonal grid and covering a spherical cap of 140 mm in diameter and with a 125-mm radius of curvature. The sensing coils are connected to SQUIDs made in-house. The Twente system includes three additional SQUIDs, connected to orthogonal magnetometer loops for active compensation, since the device is intended to be operated in a single-layer $\mu$-metal room, with only 20 dB of shielding at low frequencies (ter Brake, Wieringa, and Rogalla, 1991). The magnetometer at Philips La-

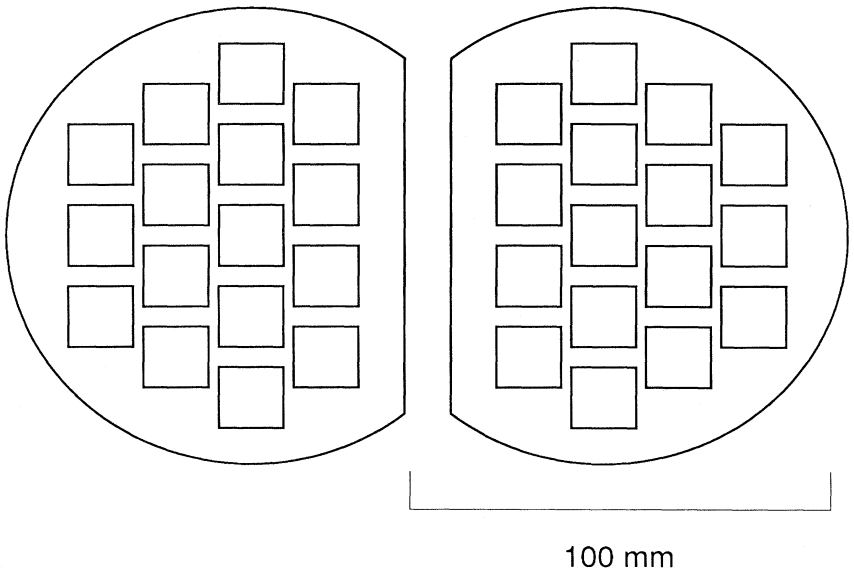


FIG. 40. Sensor arrangement in the Dornier 2×14-SQUID magnetometer. The coils are wound on cubic formers. For details, see text. This coil configuration and those in Figs. 37 and 38 have been drawn on the same scale.

boratories is modularly constructed, allowing each channel to be changed individually, if necessary. Since the device is in a curved-bottom Dewar, radially oriented axial gradiometers cannot be used. Instead, the coils are wound obliquely on formers parallel to the axis of the cylindrically symmetric Dewar to approximate a radial orientation.

#### *g. The 28-channel "hybrid" system in Rome*

A 28-channel system has been developed in Rome at the Istituto di Elettronica dello Stato Solido of CNR (Foglietti *et al.*, 1991; Torrioli *et al.*, 1992). The device has both axial and planar gradiometers. The detectors are located on a spherical surface of 135-mm radius of curvature, covering an area of 160 mm in diameter. In the center and along two surrounding concentric circles there are 16 axial gradiometers with a coil diameter of 18 mm and a base length of 85 mm. On the third, outermost circle, there are 12 planar gradiometers of 10-mm diameter and 15-mm base length, measuring the derivative along the tangent of the circle. The noise of the axial and planar gradiometers is 6–8 $\mathrm{fT}/\sqrt{\mathrm{Hz}}$ and 5–8 $\mathrm{fT}/(\mathrm{cm}\sqrt{\mathrm{Hz}})$, respectively.

The reason for placing the planar sensors on the outer rim is to save space; the Dewar would otherwise be too large, because of the wide volume required by the axial gradiometers. However, the utility of the additional planar channels is marginal in this device, because they measure only one gradient component at each point and because they are on the outer rim. If the device is placed symmetrically above a current dipole, the planar gradiometers detect only small signals, since their maximal response is just above the source, whereas far from the dipole the field is fairly uniform. The planar gradiometers are also less sensitive because they are smaller than the axial ones.

### 6. Whole-head coverage

Multichannel systems described in Sec. V.F.5 possess enough channels spread out on a sufficiently large area for locating cortical sources from measurements without moving the instrument, provided that the magnetometer is correctly positioned initially. However, especially in clinical studies, and during various complex investigations, it is important to measure even over a larger area than has been possible earlier. Two whole-cortex instruments meeting this goal are operational at present.

There are several practical problems in building such a device. The helmetlike Dewar bottom must be large enough to accommodate most heads; evidently, at least some of the channels are then bound to be quite far away from the current sources in the brain. This means that a high sensitivity and low environmental noise level must be achieved, including the noise from construction materials and radiation shields used in the Dewar.

Other important questions are the proper sensor type and their spacing. Obviously, planar gradiometer coils are attractive because of their small size. Another possibility is the use of magnetometers with the gradiometric signals formed electronically. Determining a proper sensor spacing is to a large extent an economic question: in order to have sufficient coverage of the whole head, over a hundred SQUIDs are needed.

#### *a. The "Neuromag-122" system*

In our laboratory, a 122-SQUID system (Ahonen *et al.*, 1992; Knuutila *et al.*, 1993) has been operational

since June 1992. The device employs 61 planar first-order two-gradiometer units, measuring $\partial B_z/\partial x$ and $\partial B_z/\partial y$, as in our 24-channel system [see Sec. V.F.5.a and Fig. 7(c)]. The thin-film pickup coils are deposited on $28\times28$ mm$^2$ silicon chips; they are connected to dc SQUIDs fabricated by IBM (Tesche *et al.*, 1985). The effective area of each oppositely wound loop is 2.6 cm$^2$, and the base length of the gradiometer is 16.5 mm. The separation between two double-sensor units is about 43 mm. As was discussed in Sec. V.F.2, this is sufficient, because measuring two planar gradients simultaneously corresponds to a conventional axial-gradiometer sampling grid that is denser by a factor of $\sqrt{2}$. The sensors have an equivalent gradient noise of 3–5 fT/(cm$\sqrt{\text{Hz}}$).

The Dewar bottom is helmet-shaped, covering the entire scalp (see Figs. 9 and 41). The interior is broader in the parietal than in the frontal regions, thus fitting better to the typical shape of human skulls. The dimensions, with radii of curvature between 83 and 91 mm, have been chosen to accommodate about 95% of adult heads. The distance from the outer surface of the Dewar to the gradiometer coils is 16 mm.

Modular construction is employed throughout the probe unit of "Neuromag-122," leading to a very reliable construction, which is easy to test and assemble. The instrument (see Fig. 41) consists of a top plate made of fiber glass and a printed circuit board, a neck plug of fiber-glass-coated foam plastic, four connector boards, and a wiring unit onto which the 61 gradiometer components are mounted. The two-gradiometer chips, together with the dc SQUIDs, are encapsulated into identical plug-in units. A special elastic construction guarantees a well-defined position and orientation of the gradiometer coils; they are within 1 mm of the Dewar bottom.

The electronics is based on direct readout with amplifier noise cancellation (see Sec. V.E.2.b). This eliminates the need for separate preamplifiers; the entire electronics is placed outside the magnetically shielded room. The operation of the electronics, including the tuning of the SQUIDs, is remotely controlled by a dedicated processor. Data handling is distributed among workstations, connected via a local area network: one for data acquisition and the rest for analysis. The acquisition computer also controls the electronics of the probe-position indicator (see Sec. V.F.8) that is employed to determine the position of the subject's head with respect to the sensors. The acquisition computer can be used to generate stimulus sequences, but it is also possible to employ external triggering.

Figure 42 shows results from an auditory evoked measurement. Tone pips at 1 kHz, with 50-ms duration, were presented to the left ear of the subject. The N100m response could be recorded simultaneously from both hemispheres. Planar gradiometers couple strongest to current dipoles located directly underneath the pickup coil. This can be seen clearly in Fig. 42(a) as prominent deflections near the right and left temporal lobes.

To locate the sources for the auditory evoked response, a two-dipole fit was applied to the magnetic-field data at

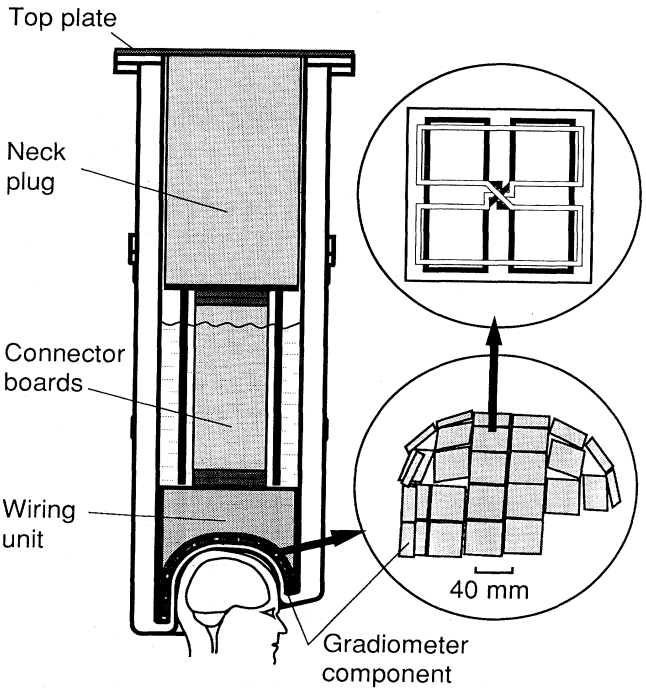


FIG. 41. The 122-channel gradiometer ("Neuromag-122") built in Helsinki. The main modules inside the Dewar are the top plate made of fiber glass and a printed circuit board, the neck plug of fiber-glass-coated foam plastic, the four connector boards, and the wiring unit with 61 two-channel plug-in gradiometer components. Multipair shielded cables are laminated into the surface layer of the neck plug and lead from the top plate to the connector boards where the components for the SQUID gain control are located. On the right, the distribution of the sensors (below) and the gradiometer chip (above) with the two orthogonal figure-of-eight coils are illustrated schematically.

108 ms after the stimulus. The initial guesses for dipole positions were obtained by fitting single dipoles to the left- and right-hemisphere measurements separately. Thereafter, a full two-dipole fit was used to find the globally best solution. Figure 42(b) shows a rough estimate for the source currents in both hemispheres. The result was obtained by rotating the two-dimensional field gradients by 90°. This gives the approximate locations of the sources directly from the measured data, which is a significant advantage of an array of planar gradiometer sensors over more conventional axial gradiometers. In Fig. 42(c) the equivalent current dipoles resulting from a fit to the field patterns are shown for both hemispheres. The field distributions were obtained from the measured data using the minimum-norm estimate (see Sec. IV.I.1). The lower maps show the calculated field patterns.

Neuromag Ltd. (see the Appendix) has produced the prototype system, which is now being used for basic research in our laboratory. Similar instruments are available commercially; these systems employ Finnish dc SQUIDs (see Secs. V.D.3 and V.D.5).

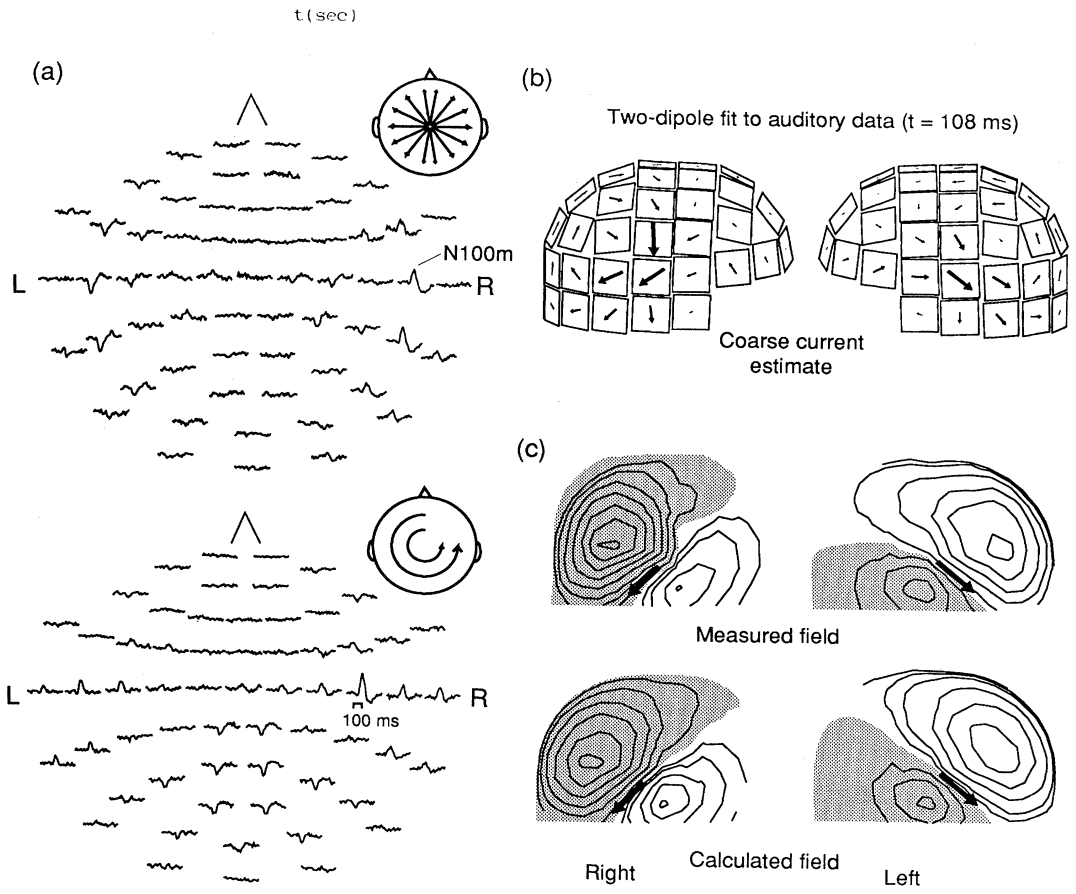


FIG. 42. Auditory data recorded and analyzed using the "Neuromag-122" system (see Fig. 41). (a) Responses to 50-ms 1-kHz sine-wave tone pips presented to the left ear with an interstimulus interval of 1 s; 211 responses were averaged and digitally filtered with a passband of 0.03–45 Hz. The two sets of data (nose up, $L$ =left, $R$ =right) show the two independent tangential derivatives of $B_z$. Along the longitudes and the latitudes [see inset heads and also Fig. 41], the field component normal to the helmet-shaped bottom of the Dewar at each of the 61 measurement sites. (b) Coarse estimate for the source currents at $t = 108$ ms after the stimulus; the estimate was obtained by rotating the two-dimensional field gradient by 90°. (c) Measured and calculated field patterns of the source dipoles at 108 ms (the N100m auditory response; see Fig. 1) over the right and left hemispheres. The upper field pattern was obtained from the measured data using the minimum-norm estimate (Hämäläinen and Ilmoniemi, 1993). The lower part of the figure shows the calculated field. Note that the field is stronger over the right hemisphere, contralateral to the stimulated left ear.

### *b. The CTF instrument*

CTF Systems Inc. has built an instrument covering the whole head with 64 axial symmetric first-order gradiometers on a quasiregular grid (Vrba *et al.*, 1993). The 2-cm-diameter wire-wound coils have a base length of 5 cm, and the average center-to-center separation is 4 cm. The system also contains 16 reference channels to measure three field components as well as first- and second-order gradient components to characterize the background fields. The electronics is based on digital signal processors, and with the help of the reference SQUIDs second- or third-order gradiometers can be created electronically to make operation possible even without a magnetically shielded room. The electronic cancellation is carried out digitally in real time with a time-independent, nonadaptive algorithm (Vrba *et al.*, 1991). The magnetometer architecture allows expansion up to 80 sensor channels.

The helmet-shaped lower portion of the Dewar has a distance of 15–16 mm between the 300-K and 4-K surfaces in the area under the signal channels; the helium boiloff rate is 12 liters/day, giving a period of 5–7 days between refills. The all-niobium SQUIDs have a white-noise level below $10^{-5}\Phi_0/\sqrt{\text{Hz}}$. The onset of the $1/f$ noise is at 1–5 Hz. A noise level of 10 $\text{fT}/\sqrt{\text{Hz}}$ in the frequency range from a few Hz to 60 Hz was reached in an unshielded environment (Vrba *et al.*, 1993).

Another whole-head system planned by CTF will have magnetometers inside a whole-body high-$T_c$ superconductor shield, to be made in collaboration with

Furukawa Electric Corporation (see the Appendix for address; Matsuba *et al.*, 1992).

### c. Japanese plans

The most extensive project to develop whole-head magnetometer systems has been announced by the Superconducting Sensor Laboratory of Japan (see the Appendix for address). The project is sponsored by the Japan Key Technology Center and nine private companies. The plans include most aspects related to building a magnetoencephalographic system suitable for brain studies, such as magnetic shielding, cryogenics, SQUID sensor development, software, and system design.

## 7. Calibration of multichannel magnetometers

Shielding currents in superconducting flux transformers distort the magnetic field. As a result, an individual channel does not sense the original external field. If the inductances of flux transformers and their mutual inductances are known, a correction can be calculated easily. In doing so, one must note that the effective inductance of a flux transformer coil is affected by feedback. Let us assume that there are $N$ channels and that the mutual inductances are described by an $N\times N$ matrix $\mathbf{M}$. Let us further define the transpose of a vector of net flux values $\mathbf{\Phi}'=(\Phi'_1,\ldots,\Phi'_N)^T$ measured by the flux transformers, and let $\mathbf{\Phi}$ represent the undistorted applied flux values. Then,

$$\mathbf{\Phi}=(\mathbf{I}+\mathbf{M}\mathbf{L}^{-1})\mathbf{\Phi}' , \tag{130}$$

where $\mathbf{L}=\mathrm{diag}(L_1,\ldots,L_N)$ is a diagonal matrix containing the total inductances of the flux transformers and $\mathbf{I}$ is the identity matrix.

In practice, one measures the output voltages

$$\mathbf{V}=(V_1,\ldots,V_N)^T ,$$

which are related to $\mathbf{\Phi}'$ via the calibration coefficients $K_1,\ldots,K_N$. Since in MEG experiments the field distribution generally differs from that used during the calibration, the effects of coupling also differ. Consequently, the calibrations $K_i$ cannot be calculated simply from $\Phi_i/V_i$, where now the applied flux $\mathbf{\Phi}$ is obtained from the geometry of the experimental setup. Instead, the *true* calibration $\Phi'_i/V_i$ can be calculated from Eq. (130).

Of the $N(N-1)/2$ independent mutual inductances between $N$ channels, usually only the nearest neighbors need to be taken into account. Nevertheless, the situation becomes complicated if the mutual inductances cannot be measured directly. In this case, the best solution is to calibrate the device with a phantom head, with the sources in the phantom generating a field distribution which resembles that elicited by the brain. This automatically takes into account the interchannel coupling corrections during the measurement of the calibration coefficients.

An alternative method, based on feedback, was first proposed by Claassen (1975). Feedback is applied to the flux transformer rather than to the SQUID. This procedure keeps the current in the transformer effectively constant. Therefore, crosstalk between the detection coils is eliminated. The method has been used successfully (Hoenig *et al.*, 1991; ter Brake, Flokstra, *et al.*, 1991).

Accurate calibration also requires a well-designed experimental setup with no external field distortions and an exact geometry. In practice, reaching an accuracy of 1% or better with a single calibrator source may be difficult. Best results have been achieved using multiple sources, the relative positions of which were accurately known with respect to each other. For example, a small coil may be consecutively placed in several positions on a grid (Buchanan and Paulson, 1989), or three or more small coils fixed on a planar plate by means of printed-circuit techniques may be employed.

## 8. Probe-position indicator systems

The accuracy with which the position of the magnetometer can be determined in relation to the subject's head affects the calculated location of cortical sources in an essential way. In single-channel experiments, the uncertainty in the position of the field point may be considered as a source of extra noise. This introduces a random error in the location of the current dipole determined on the basis of the experimental field values. In multichannel devices this problem is simpler to solve because the relative sites of the different channels are known *a priori*. The position and orientation of the Dewar must, however, be found with respect to a coordinate system defined by at least three fixed points on the subject's head. Possible uncertainties then cause systematic errors in the location of the current dipole.

Traditionally, the single-channel magnetometer has been positioned with some alignment marks on the Dewar and on the subject's head. The shape of the skull may also be digitized to provide 3D information. When a multichannel magnetometer covers an extended area, however, the Dewar bottom is quite large and its accurate positioning according to markers becomes difficult.

Fixed points on the head that have been used in defining coordinate frames include the ear canals, the nasion (the deepest point of the nasal bone between the eyes), the inion (the protrusion of the occipital bone at the back of the head), and the front teeth. One possibility for defining a coordinate system is, for example, an orthogonal Cartesian frame of reference determined by both ear canals and the nasion.

The accurate position and orientation of the Dewar with respect to the head can be found by measuring the magnetic field produced by currents in small coils attached to the scalp (Knuutila *et al.*, 1985; Erné *et al.*, 1987). This approach was first used with the 7-channel magnetometer in Helsinki (Knuutila, Ahlfors *et al.*, 1987). Three small coils were mounted on a thin fiber-

glass plate; the same system is also employed with our 24-channel device (Kajola *et al.*, 1989; Ahonen *et al.*, 1991) and with the new 122-channel system. The plate is attached to the subject's head at a known point in the measurement area, the Dewar is positioned, the coils are energized sequentially, and the resulting fields are measured. The position of the coil set with respect to the ear canals and the nasion is determined with the help of a 3D digitizer (Polhemus Navigational Sciences; see the Appendix for address). The location and orientation of the head with respect to the 122-SQUID gradiometer array is found by a least-squares fit of magnetic dipoles to the test data. The position of the Dewar can be determined with an rms error of about 1 mm. The method provides direct information on the locations of the measuring sensors themselves and does not rely on knowledge of the relative position of the gradiometer array with respect to the Dewar. Modified versions of this approach use units containing three orthogonal coils each (Ahlfors and Ilmoniemi, 1989; Higuchi *et al.*, 1989; van Hulsteyn *et al.*, 1989).

Another device employed in neuromagnetic measurements (BTi) is based on an inductive magnetometer using three orthogonal coils in the receiver and in the transmitter. It is a modified version of a commercial 3D digitizer (Polhemus), but constructed without ferrous materials. The receiver coils are attached to the subject's head with a stretch band and the set of transmitter coils are secured to the Dewar (see Fig. 39). The position and the orientation of the magnetometer can be found from the measured mutual inductances. The locations of the head coils are obtained by a reference measurement: the 3D coordinates of chosen landmarks on the head are determined by touching them with a pointer that has a similar orthogonal-coil transmitter. The system may also include a laser-based position-control device, which gives an alarm if the subject has moved his head during the measurement.

#### 9. Data acquisition and experiment control

In a neuromagnetic measurement, the signal of interest is usually limited to the frequency band below a few hundred Hz. After proper anti-aliasing, often in connection with an additional high-pass filter, sampling frequencies up to 1–2 kHz are needed to take into account the finite rolloff of the filters. This means, for example, a maximum flow rate of 2–4 kbytes/s per channel. This amount of data can be gathered easily, even in a system with over 100 channels. However, since the signal must, at least in part, be processed and analyzed in real time, a reasonably fast computer is needed. For example, in evoked-field studies, running averages and statistics should be calculated and displayed during the measurement. In addition, if real-time data must be stored for later analysis, as in studies of spontaneous brain activity, a large amount of memory is needed. Various stimulus generators, the magnetometer electronics, probe-positioning devices, etc., must be controlled as well. This means that the computer system has to be equipped with real-time interrupt handling capabilities.

A typical off-line analysis of the results includes digital bandpass filtering of the data, displays of the measurement results as time traces and field distributions, and most importantly, the solution of the inverse problem based on source-modeling calculations (see Sec. IV).

Modern multi-SQUID instruments produce large quantities of measurement data; therefore, easy use and effectiveness of the analysis system is vital. Since the new devices are intended to be employed outside research laboratories and operated by personnel other than the programmers themselves, an intuitively clear and uniform user interface is necessary. Although the main emphasis in this section has been on the hardware, including shielded rooms, Dewars, SQUID gradiometers, and electronics, proper design and realization of the software is of equal importance and requires extensive development work.

## VI. EXAMPLES OF NEUROMAGNETIC RESULTS

In the following, we describe recordings of evoked and spontaneous magnetic fields of the human brain. The examples arise mainly from our own work at Helsinki, but the reader can become acquainted with many other interesting experiments by consulting the references given. All our measurements were carried out within a magnetically shielded room (see Fig. 9). The early recordings were made with a 4- or a 7-channel axial first-order gradiometer and the more recent studies with the 24- and 122-SQUID planar gradiometers (see Figs. 10 and 37). All the data were high-pass filtered at 0.05 Hz.

### A. Auditory evoked responses

#### 1. Responses to sound onsets

The experience gained during the last ten years has shown that MEG is well suited for studies of the auditory cortex (Hari, 1990). Any abrupt sound or a change in a continuous auditory stimulus evokes a typical response, with the most prominent deflection N100m peaking about 100 ms after the sound onset, offset, or a change in the sound (see Figs. 1 and 43). The generation site of N100m is specific to the stimulus: its location depends, for example, on the tone frequency, thereby indicating tonotopic organization of the human auditory cortex (Pantev *et al.*, 1988). Similar tomotopy was observed earlier with recordings of MEG responses to amplitude-modulated continuous tones (Romani *et al.*, 1982b).

The earliest auditory response to a click peaks 19 ms after the stimulus. The equivalent source is deep inside the Sylvian fissure, in the primary auditory cortex (Scherg *et al.*, 1989). The activity continues for a few

hundred milliseconds, as evidenced by several deflections of the auditory evoked magnetic field (AEF); the source areas change slightly as a function of time (see Fig. 43). The equivalent dipole of N100m is perpendicular to the course of the Sylvian fissure and points towards the neck, thereby reflecting activation of the auditory cortex in the superior surface of the temporal lobe. This result, originally based on a comparison of source locations and external landmarks on the skull (Elberling *et al.*, 1980; Hari *et al.* 1980), has received support from combined MEG and MRI studies (Yamamoto *et al.*, 1988; Pantev *et al.*, 1990). As is evident from Fig. 42(a), N100m is larger in amplitude in the hemisphere contralateral to the stimulated ear.

The electric scalp potentials originating at the auditory cortex in the upper surface of the temporal lobe (see Fig. 2) are recorded best on the head midline. From EEG data, it is thus difficult to differentiate between responses from the two hemispheres unless proper source-modeling techniques are used (Scherg, 1990). The special advantage of MEG in the study of the auditory system is that activity of both hemispheres can be detected separately and that hemispheric differences are often directly evident from the raw data.

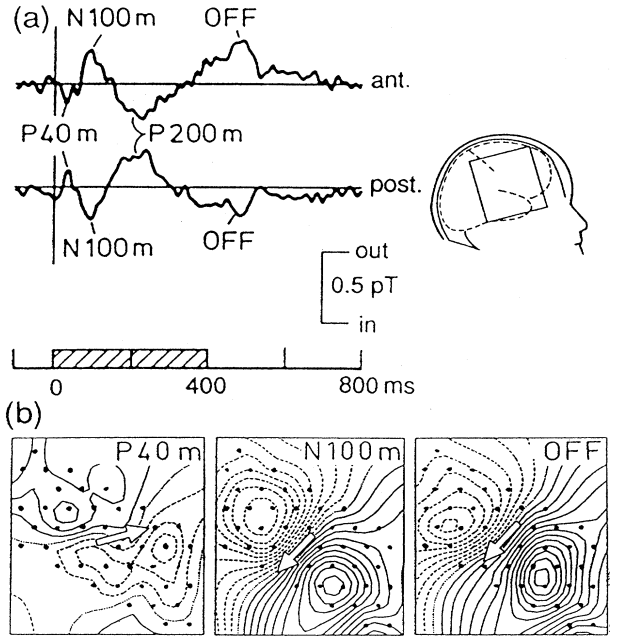


FIG. 43. Magnetic responses to noise bursts. (a) Responses of one subject to 400-ms noise bursts repeated once every 1.1 s. The upper recording (ant.) is from the frontotemporal and the lower one (post.) from the parietotemporal area over the right hemisphere. In addition to the onset responses (deflections P40m, N100m, and P200m), the response to sound offset (OFF) is also seen. The data have been digitally low-pass filtered at 45 Hz. (b) Isofield contour maps during three deflections; the measurement area is shown by the head insert. Solid lines indicate flux out of, and dashed lines flux into, the head. Gradiometer positions are shown by small dots, and the white arrows illustrate the locations of the equivalent current dipoles. Adjacent isofield contour lines are separated by 20 fT. The data were obtained using the lowest three channels of a 4-channel axial gradiometer (Ilmoniemi *et al.*, 1984). Modified from Hari *et al.* (1987).

Equivalent current dipoles (ECDs; see Sec. III.C) in the auditory cortex can be employed to explain qualitatively the scalp distribution of the electric 100-ms deflection, N100, with maximum signals recorded in the frontocentral midline. However, the sources of the electric and magnetic responses do not seem identical: when the interstimulus interval (ISI) is increased from 1 to 16 s, the amplitude ratio changes between the magnetic N100m, recorded from one extremum of the field pattern, and the electric N100, measured at the head midline. If the underlying sources were identical, the amplitude ratios should have been stable (Hari *et al.*, 1982). This behavior can be explained by assuming that N100 and N100m reflect activity of approximately the same sources at short ISIs, but an additional generator is operating at long ISIs. Recently an extra source of magnetic responses has been found in the auditory association cortex (Lü, Williamson, and Kaufman, 1992).

### 2. Responses to transients within the sound stimulus

Recordings applying short words and noise/square-wave sequences as stimuli have indicated that the auditory cortex is very sensitive to changes in sounds (Kaukoranta *et al.*, 1987; Mäkelä *et al.*, 1988). The brain also reacts strongly to amplitude and frequency modulations (Mäkelä *et al.*, 1987). Moreover, the auditory cortex responds even to small changes in directional stimuli, for example, to the time difference between clicks brought to each ear (McEvoy *et al.*, 1993; Sams, Hämäläinen, *et al.*, 1993).

In one experiment, two 320-ms stimuli, a word and a noise burst, were alternately presented to the subject with a constant 1-s interval (Kaukoranta *et al.*, 1987). The word was the Finnish greeting *hei* (pronounced *hay* and meaning *hi*), produced by a speech synthesizer. The fricative consonant *h* lasted for 100 ms. Subjects were lying in the magnetically shielded room with their eyes open and counting the stimuli to maintain vigilance.

As shown in Fig. 44, the main deflections of the AEF to noise bursts peaked at 100 ms and 200 ms (N100m and P200m, respectively). Polarity reversal of the signal is obvious from the two responses, which are from extreme measurement locations, indicating that the equivalent dipole is somewhere in the middle. The dipolar field pattern of the N100m deflection was interpreted as activation in the auditory cortex, about 25 mm beneath the scalp.

The word *hei* elicited a clearly different response: N100m was followed by another deflection of the same polarity. This response, N100m′, peaked at 210 ms, i.e., 110 ms after the vowel onset. N100m′ was seen in all

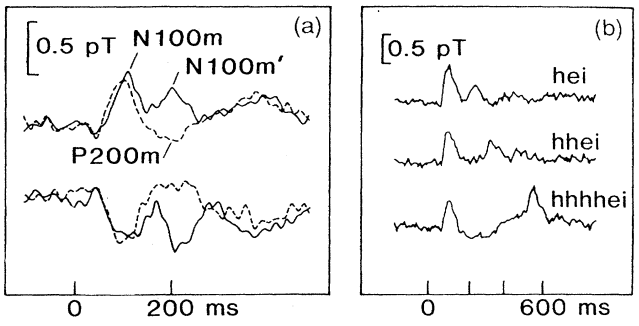


FIG. 44. Auditory responses to noise and word stimuli. (a) Magnetic responses to noise bursts (dashed lines) and to *hei* words (solid lines). The upper and lower traces are from the two ends of the Sylvian fissure, and each trace is an average of 120 responses. (b) Averaged magnetic responses to three words, all generated by a speech synthesizer. The recordings were made from the right frontotemporal field extremum; the passband was 0.05–70 Hz. Modified from Kaukoranta *et al.* (1987).

subjects and on both hemispheres. In eight of the 14 hemispheres studied, the dipole for N100m′ was statistically significantly anterior to that of N100m, suggesting different generators for these two deflections. However, separations between the source locations never exceeded 15 mm.

Several control experiments were performed to ascertain which features of the stimulus determine the occurrence of N100m′. When the duration of the fricative *h* was increased from 100 ms to 200 ms and then to 400 ms by replacing *hei* with *hhei* or *hhhhei*, the N100m′ deflection increased in latency consistently with the length of the fricative, peaking always about 110 ms after the vowel onset (see Fig. 44). Only words beginning with voiceless fricatives, *f*, *h*, or *s*, and followed by vowels resulted in an N100m′-type deflection of similar magnitude and wave-form as that observed for *hei*. Furthermore, the finding that only *ssseee* and not its mirror word *eeesss* elicited an N100m′-type signal indicates that this response is not generated by the change as such, but is dependent on the direction of the change. The type of the vowel was not critical for the occurrence of N100m′.

Later, noise/square-wave sounds were used to mimic acoustically the *hei* word, and very similar pairs of responses were observed: N100m after the sound onset and N100m′ after the noise/square-wave transition (Mäkelä *et al.*, 1988). Consequently, the N100m′ response was interpreted to be related to the acoustic rather than phonetic features of the stimuli. In other words, although N100m′ was originally elicited by words, it was not related to the speech character of the stimuli. In fact, research is still in progress to discover responses that are specific to speech sounds. For example, it would be interesting to see whether it is possible to detect in the human brain phoneme maps which have been suggested to evolve as a result of self-organization in neural networks (Kohonen, 1990).

### 3. Mismatch fields

An effective method for studying the reactivity of the human brain is to use an "oddball paradigm" in which infrequent deviants are randomly interspersed among monotonously repeated standard stimuli. Different types of deviations within a sound sequence evoke strong magnetic responses, so-called mismatch fields (MMFs). For a description of the electric counterpart of this response, see the review by Näätänen and Picton (1987). Figure 45 illustrates such a MMF, in this case triggered by a change in the periodicity pitch, determined by the gating frequency of a noise burst. MMF peaked later and was stronger in amplitude than the response to the standard stimuli. MMF-type deflections have been recorded in response to small and rare changes in frequency, intensity, or in the duration of a tone, and to changes in the interstimulus interval. Using magnetic recordings, the brain areas where these effects take place have been localized. The slightly more anterior sites for MMF, in comparison with N100m (Sams, Kaukoranta *et al.*, 1991; Hari, *et al.*, 1992), suggest the existence of two different subpopulations of neurons, one giving rise to N100m and the other to MMF.

MMFs are not present in responses to deviants delivered in the absence of standards. Thus MMF depends, in addition to the physical quality of the sound, also on the sound's position in a sequence. MMF may reflect a mismatch process between the neuronal representation of the standard stimuli and the input caused by the deviant (Näätänen, 1984). This type of comparison process may be associated with the auditory sensory

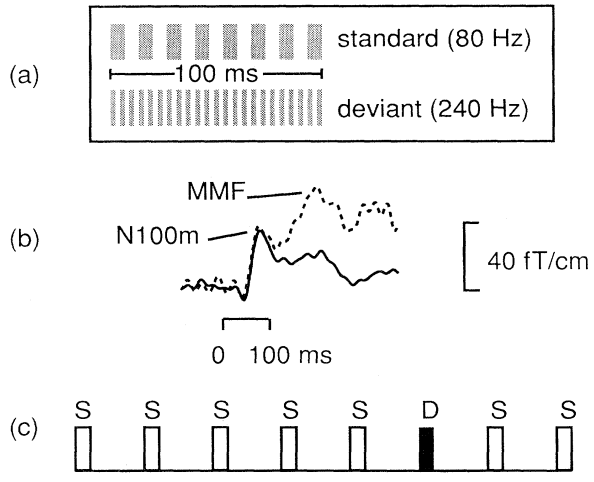


FIG. 45. Periodicity pitch experiment: (Top) amplitude-modulated (depth 100%) noise bursts were used as stimuli; (Middle) responses of one subject to 80-Hz standards (solid line) and to 240-Hz deviants (dashed line); (Bottom) principle of the oddball experiment: *S* = standard, *D* = deviant.

memory. The storing accuracy of this hypothetical short-duration memory trace seems to be good, since an MMF is elicited by very small deviations which are near the psychophysiological detection thresholds. Sams, Hari, *et al.* (1993) recently showed that MMF data agree with behavioral experiments conducted to determine the duration of the auditory sensory memory, both giving estimates of about 10 s. We can thus conclude that recordings of MMFs may give important objective information on the human sensory memory. In the above example of an MMF produced by a change in the periodicity pitch (see Fig. 45), the result indicates that information on the stimulus (gating frequency of the noise burst) is kept in memory for a few seconds.

An extreme example of deviance is the omission of a stimulus in an otherwise monotonous sequence of tones. Joutsiniemi and Hari (1989) recorded responses in a situation where 10% of the otherwise regularly presented tones were omitted randomly. Figure 46 shows magnetic responses of one subject to regularly occurring tones and to tone omissions. Clear deflections could be detected 90–250 ms after the omission, with large interindividual variability. The omission responses depended strongly on the attentional state of the subjects and were often missing if they ignored the tones. The response to the omitted stimulus reflects the brain's reaction to the expected, but missing, input.

Figure 46 also illustrates, on a schematic brain, the approximate source areas for responses to tones and to omissions in five subjects. The ECDs of the omission responses are anterior and superior to those of N100m. Therefore, the frontal lobe seems to be involved in this experiment associated with time perception. This agrees with regional cerebral blood-flow studies where cortical areas in the frontal lobe were activated while the subject paid attention to the rhythm of auditory stimuli (Roland *et al.*, 1981). Since most responses recorded earlier have arisen from primary projection areas of the cortex, the possibility of recording responses outside these areas is promising for the future of MEG.

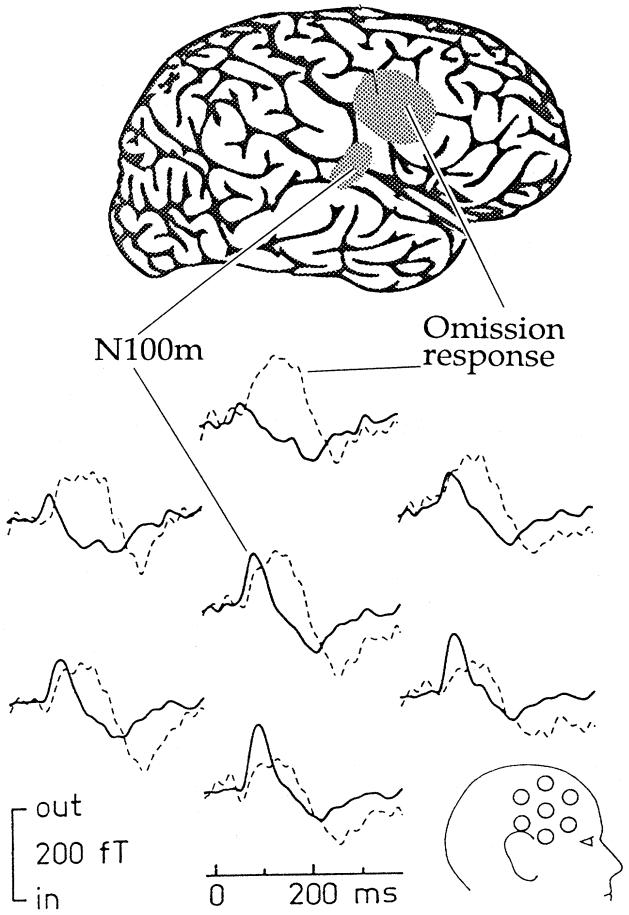


FIG. 46. Omission experiment. (Bottom) Magnetic responses of one subject to regularly occurring tones (continuous lines) and to stimulus omissions (dashed lines), recorded at one end of the right Sylvian fissure. A 7-channel magnetometer was used, and 580 responses to tones and 80 to omissions were averaged. Adapted from Joutsiniemi and Hari (1989). (Top) Regions of source locations for responses to tones (N100m) and to omissions are shown schematically, based on data from five subjects.

### 4. Effects of attention

Attention is an important cognitive function, which has been studied extensively by means of electric evoked potential measurements (Näätänen, 1990, 1992). Selective attention is needed, for example, to pick up a desired discussion among mixtures of sounds during a party. In single-cell recordings made directly from the cortex, selective listening has changed the neuronal activity in monkey and human auditory cortices (Benson and Hienz, 1978; Creutzfeldt, 1987).

We have studied the effects of selective listening on the auditory MEG responses evoked by simple words (Hari, Hämäläinen *et al.*, 1989). The stimuli were five-letter Finnish words, like *kukko*, *koivu*, *kalja*, all beginning with *k* and ending with a vowel. Altogether 58 words presented in random order at an interval of 2.3 s; half of the words were targets, names of animals or plants, and the rest other meaningful Finnish words. The task of the subject was either to ignore all the words by concentrating on reading a book or, in the listening condition, to pay attention to the stimuli by counting the target words.

Figure 47 illustrates some results of this word categorization test. The transient response peaks 100 ms after the onset of the word and is followed by a sustained field (SF), which outlasts the stimulus. The responses to attended and ignored stimuli start to differ at about 120 ms. The field maps and the ECDs suggest activation of the auditory cortex at the upper surface of the temporal lobe. During attention the sustained field (long downwards deflection) was considerably stronger. A very similar increase of activity during the stimulus was seen in a duration classification task with 425-ms and 600-ms

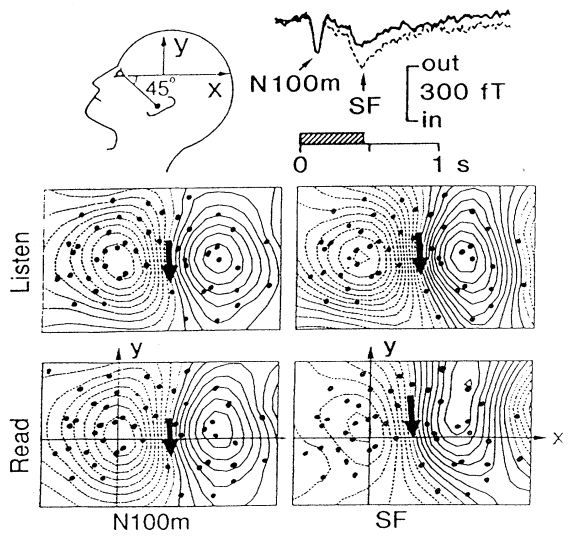


FIG. 47. Effect of attention on responses evoked by auditorily presented words. The subject was either ignoring the stimuli by reading (solid trace) or listening to the sounds during a word categorization task (dotted trace); the mean duration of the words is given by the hatched bar on the time axis. The field maps are shown during the N100m deflection and the sustained field (SF) for both conditions. The isofield contours are separated by 20 fT and the dots illustrate the measurement locations. The origin of the coordinate system, shown on the schematic head, is 7 cm backwards from the eye corner, and the $x$ axis forms a 45° angle with the line connecting the ear canal to the eye corner. Modified from Hari *et al.* (1989).

tones, indicating that the observed effect is not speech-specific. Furthermore, no statistically significant hemispheric differences were observed, suggesting that both temporal lobes participate in the early analysis of speech signals, not just the left hemisphere, which is usually dominant for speech production and perception.

Further studies have indicated that the activities of at least two areas in the supratemporal cortex are modified by attention, depending on the interstimulus interval (Hari, Hämäläinen *et al.*, 1989; Arthur *et al.*, 1991; Rif *et al.*, 1991). In the study of Rif and co-workers, tones of two different pitches, 1 kHz and 3 kHz, were presented to the left ear in a random sequence, but with equal probability, while magnetic responses were recorded over the right hemisphere (see Fig. 48). The majority (80%) of the tones of both pitches were 50 ms in duration, whereas 20% were 100 ms long. The task of the subject was to count the number of longer tones among either the high- or low-pitch stimuli. Only responses to the standard 50-ms tones, both attended and ignored, were analyzed. Responses to attended tones differed from those obtained during the ignoring condition; the difference peaked at 200 ms. Field patterns indicated that the change in the response wave form reflected an altered stimulus processing site at the auditory cortex, about 1 cm anterior to the area that was activated 100 ms after any tone.

Voluntary attention seems to gate relevant input entering the cortex and to inhibit processing of the ignored input. MEG is particularly suitable for this type of study in which good spatial and temporal resolution are needed. Neuromagnetic measurements can thus be used, not only for picking up evoked responses from specific sensory areas, but also for investigating the neurophysiological basis of cognitive activity.

### 5. Audio-visual interaction

Seeing the articulatory movements of a speaker's face provides complementary information for speech comprehension. The benefits from lip reading become particularly evident in a noisy environment or when hearing is defective. One interesting example of the integration of auditory and visual speech perception is the striking illusion called the "McGurk effect" (McGurk and MacDonald, 1976). We recently applied this phenomenon to find out at which level the information obtained from seen and heard speech is integrated (Sams, Aulanko, *et al.*, 1991). The experimental setup is illustrated in Fig. 49. The auditory stimulus was the Finnish syllable *pa* presented once every second. The sounds were delivered to both ears simultaneously and a videotaped female face, seen through a hole in the wall of the shielded room, was articulating, in 84% of the cases, the concordant syllable *pa* but, in 16% of the cases, the visual articulation was the discordant syllable *ka*. The subjects reported that they heard the discordant stimulus as *ta*, in a few cases as *ka*, but never as *pa*.

Magnetic responses to both stimuli are shown in Fig. 50. The signal consisted, typically, of three consecutive

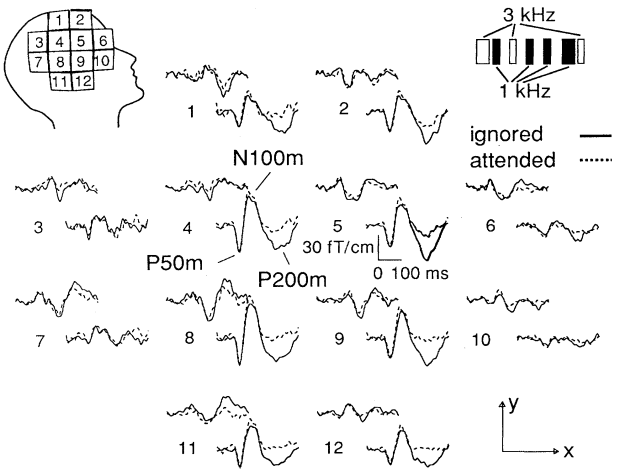


FIG. 48. Auditory evoked magnetic responses from one subject in an attention experiment. The stimulus sequence is shown schematically in the upper right corner: 3-kHz and 1-kHz tones were presented randomly to the same ear. The responses are shown to 1-kHz tones when they were ignored (solid lines) or attended (dotted lines). The traces are averages of about 150 single responses, digitally low-pass filtered at 45 Hz. The recording location of the 24-channel instrument is depicted on the schematic head. Modified from Rif *et al.* (1991).


FIG. 49. Stimuli employed in the MEG study of the McGurk effect. For details, see text.

main deflections, peaking around 50, 100, and 200 ms, respectively. All these signals could be explained by activity in the auditory cortex. Responses to the discordant stimulus, visual ≠ auditory, showed the same initial behavior. However, the later part of the signal was clearly changed in relation to responses elicited by the concordant stimuli (V=A); the difference peaked at 200–300 ms. The source of the difference wave form (responses in the discordant condition subtracted from those in the concordant condition) was about 0.5 cm anterior to sources of N100m. When the same auditory sound sequence was presented in the absence of the visual input, all stimuli evoked identical deflections, but visual stimuli shown alone did not produce any magnetic activity at the auditory cortex.

The results indicate that visual information has an entry into the human auditory cortex, in agreement with the very vivid auditory nature of the McGurk illusion. Interestingly, Cahill and Scheich (1991) recently showed that visual conditioning changes the activity of the gerbil's auditory cortex. Their study utilized 2-deoxyglucose labeled with a radioactive marker to indicate brain areas of increased glucose consumption.

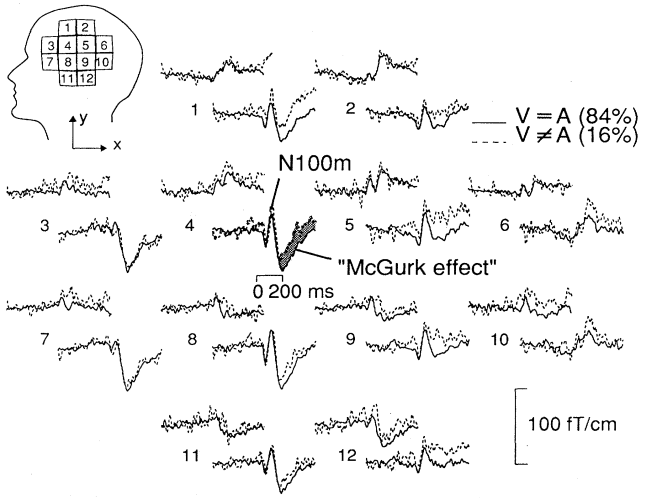


FIG. 50. Data from the McGurk experiment. The solid lines indicate responses to auditory *pa* stimuli when visual and auditory inputs were congruent (V=A), whereas the dotted lines show responses to the same auditory stimuli when the visual input was the incongruous *ka* (V≠A). Eighty responses to deviants and 500 to standards were averaged. Modified from Sams, Aulanko, *et al.* (1991a).

In face-to-face communication, speech can be seen before it is heard: the lips are in the required position even hundreds of milliseconds before the syllable emerges as a sound. The visual *ka* information might prime in the supratemporal auditory cortex those neurons that are tuned to the presence of the *k* and *t* consonants followed by a vowel. These units evidently develop during childhood as a result of learning a language. The auditory *pa* would then activate more vigorously the *ka* or *ta* than the *pa* detectors, giving rise to the "wrong" perception and thus producing the McGurk effect. It is interesting to note that the observed neural activity correlated with the auditory perception rather than with the sound.

Auditory perception is biased by vision also during "ventriloquism": speech sounds are perceived as coming from the visually observed speaker (Jack and Thurlow, 1973), which may even be a puppy with a moving mouth. It remains to be seen whether activity of the auditory cortex is modified also during this phenomenon. Furthermore, it will be of interest to study interactions of stimuli arising from the other sensory modalities. Such experiments will become easy to perform with instruments covering the whole head.

### B. Visual evoked responses

#### 1. Responses from occipital areas

Visually evoked fields (VEFs) were reported for the first time in 1975 (Brenner *et al.*, 1975; Teyler *et al.*, 1975). MEG has been used to study the retinotopic organization of the occipital visual cortex V1 (see Fig. 2), in which different parts of the visual field are mapped to different areas; for example, information from the left visual field goes to the right hemisphere and vice versa, and the lower visual field is mapped to the upper visual

cortex and vice versa. In MEG studies, the ECD moved deeper with increasing stimulus eccentricity, i.e., with the distance from the central visual field, indicating retinotopic organization (Maclin *et al.*, 1983). MEG data can also be employed to estimate the cortical magnification factor (Ilmoniemi and Ahlfors, 1990), which previously was based on less direct information, e.g., on knowledge about the distribution of retinal receptors and on psychophysical experiments. The magnification factor tells how much of the cortical surface is devoted to a certain part of the visual field, and it is largest for central vision.

Figure 51 shows responses to an octant checkerboard pattern in the right visual field. The maximum signals were obtained over the left hemisphere near the midline, with the main deflection peaking at 130 ms.

## 2. Responses to faces

Recognizing one's fellow citizens is fundamental to human social life, and our brains probably contain areas that are specifically activated when we see people's faces. Humans are very good at this task, even under adverse conditions, but the job is difficult for computers. One convincing piece of evidence for the existence of face-specific brain regions is prosopagnosia, the inability to recognize previously known familiar faces; in severe cases patients may be unable even to identify spouses. This disorder is usually associated with bilateral brain damage in the occipito-temporal region.

In monkeys, several visual areas are known to exist in addition to the primary visual cortex in the occipital lobe. Some evidence for similar areas has been obtained in humans as well by using positron-emission tomography (Lueck *et al.*, 1989) and by MEG in the experiment to be discussed next.

Lu *et al.* (1991) presented black-and-white pictures of laboratory personnel for 300 ms, once every second in a random sequence. The response over the sides of the head consisted of two transient deflections at 150 and 270 ms and a late, slow deflection around 500 ms (see Fig. 52). During each peak, the field patterns suggested activation of areas outside the occipital visual cortex. The lower part of Fig. 52 illustrates the mean source locations for six subjects on the left hemisphere and for 15 subjects on the right. For reference, the position of the source of the auditory N100m response to short tones is also shown. The depths of the sources of face-evoked responses varied between 34 and 38 mm.

The first source area was near the junction of the oc-

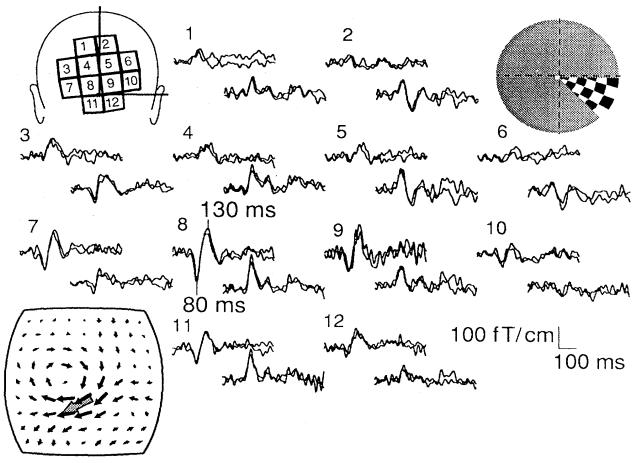


FIG. 51. Responses to stimulation of the lower right visual field with an octant checkerboard pattern 1.5° in extension. Twenty responses were averaged for each set of traces. The schematic head shows the measurement locations at the back of the head, while the inset below illustrates the minimum-norm current estimate (small arrows; see Sec. IV.I.1) and the location of the equivalent current dipole (shadowed arrow). Modified from Ahlfors *et al.* (1992).

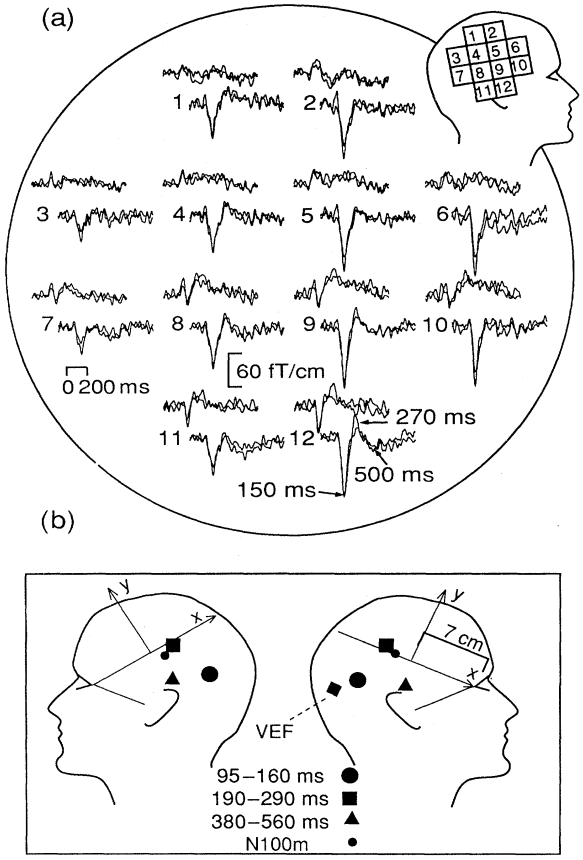


FIG. 52. Responses to faces. (a) Neuromagnetic responses to face stimuli over the right hemisphere for one subject, measured with a 24-channel gradiometer. The superimposed traces depict two successive measurements at each site. The approximate location of the instrument is shown on the schematic head. (b) The average *xy* locations of the ECDs over the left hemisphere (six subjects) and the right hemisphere (15 subjects) for the three main peaks in the responses to face stimuli. VEF indicates the source of the 100-ms response in the occipital visual cortex. Modified from Lu *et al.* (1991).

cipital and temporal lobes, the second in the lower part of the parietal lobe, and the third in the middle of the temporal lobe. All three locations were significantly different from each other and clearly separated from the occipital visual areas. The parietal source was also activated by pictures of birds and simple drawings, but the two other sources were not.

Three areas outside the occipital visual cortex, on both sides of the head, were thus oberved to become sequentially active by the face stimuli. Interestingly, the first source location agrees with clinical observations on humans showing that prosopagnosia can result from damage in the occipito-temporal junction. The source of the late (380–560 ms) activity might correspond to the superior temporal sulcus in monkeys, an area which shows considerably stronger responses to faces than to other complex visual stimuli. These sites had not been located earlier in humans.

This investigation is a good example of how magnetoencephalography can be used for noninvasive studies of signal processing in the brain. The same stimulus activated four brain areas (see Fig. 52) in the sequence: 100 ms (occipital lobe)→150 ms (occipital-temporal junction)→270 ms (inferior parietal lobe)→500 ms (temporal lobe).

### C. Somatosensory evoked responses

#### 1. Responses from S1

The organization of the primary somatosensory cortex S1 (see Fig. 3) is well reflected in the distribution of somatosensory evoked fields (SEFs). The early studies (Brenner *et al.*, 1978; Hari *et al.*, 1984; Okada *et al.*, 1984) already indicated different representations for the thumb and the little finger, and showed that the sources activated by stimulation of the ankle were in the inner wall of the contralateral hemisphere. Figure 53 illustrates responses to alternate wrist and tongue stimulation. The response to median nerve stimulation has two prominent peaks, one at 20 ms (N20m) and the other at 30 ms (P30m), whereas the main deflection of the response to tongue stimulation peaks at 55 ms (P55m). The corresponding ECD locations (see also Suk *et al.*, 1991) agree, in general, with the known somatosensory homunculus (Penfield and Rasmussen, 1950; Penfield and Jasper, 1954; see Fig. 3). The same is true for stimulation of other parts of the body. Recording of MEG responses is completely noninvasive, in contrast to direct stimulation of the cortex applied during brain surgery. With MEG it may thus be possible to monitor plastic changes of cortical organization following various lesions in peripheral nerves or in limbs.

#### 2. Responses from S2

MEG recordings have indicated that peripheral stimuli also activate other sources bilaterally, close to the upper

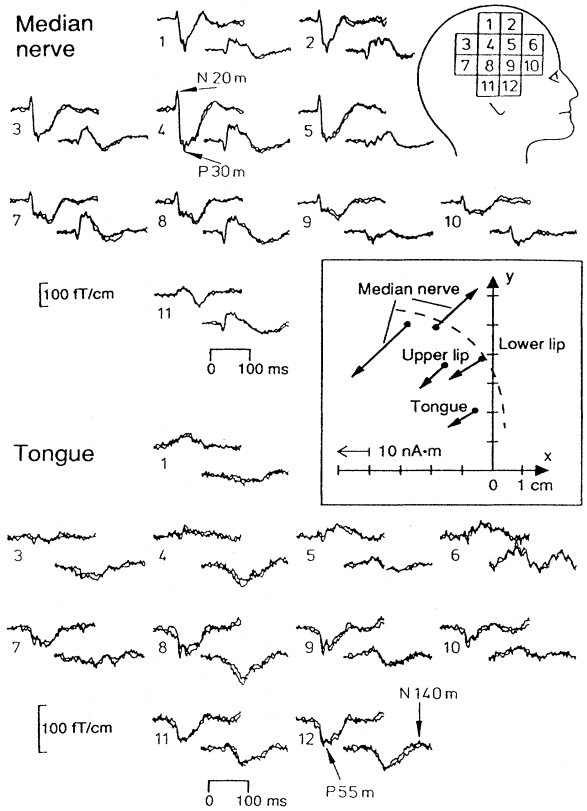


FIG. 53. Somatosensory responses to stimulation of the median nerve at the wrist (above) and to the lingual nerve in the tongue (below). The traces are averages of about 350 responses, digitally low-pass filtered at 190 Hz. The inset shows the approximate locations, strengths, and orientations of the ECDs to median nerve and tongue stimulation, as well as to upper and lower lip stimulation; in the former case the sources are shown for the two main deflections. The dashed line in the inset illustrates the approximate course of the Rolandic fissure. Adapted from Karhu *et al.* (1991).

lip of the Sylvian fissure, most probably in the second somatosensory area S2 (Hari *et al.*, 1984, 1990; Kaukoranta, Hari *et al.*, 1986). Figure 54 gives a schematic illustration about the differences of MEG and EEG recordings in differentiating between activities of S1 and S2. It is assumed that the left ankle was stimulated, resulting in activation of S1 on the inner surface of the opposite hemisphere within the longitudinal fissure (see Fig. 3) and of the S2 areas in both hemispheres. The magnetic patterns are clearly separate over each source, whereas the electric potential is more widely distributed. Consequently, it is not easy to see directly from the EEG patterns that there are three underlying sources. However, when this information is available from other experiments, the correct solution can be found from the EEG pattern as well.

Differentiation between temporally overlapping S1 and S2 activities can be done by a two-dipole time-varying model: the source locations are first found and their

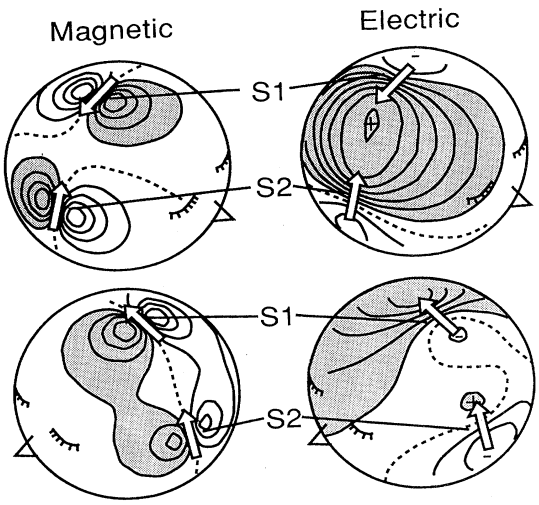


FIG. 54. Schematic illustration of electric and magnetic patterns due to activity in the first and second somatosensory cortices S1 and S2. In the simulations, the head was assumed to be a spherical conductor with four layers of different conductivities, corresponding to the brain, the cerebrospinal fluid, the skull, and the scalp. The situation corresponds to that observed after left-sided peroneal nerve stimulation at the ankle, with simultaneous activity at S1 in the inner central wall of the right hemisphere and at both S2 areas. The dipole strengths were assumed equal at S1 and at the right S2, and $\frac{1}{3}$ smaller at the left S2. The shadowed areas indicate magnetic flux out of the head and positive electric potential. Modified from Kaukoranta, Hari, *et al.* (1986).

strengths are allowed to change as a function of time (see Sec. IV.H). After thumb stimulation, for example, such a model shows maximum activity in S1 at 45 ms and at 145 ms, whereas activity in S2 reaches its maximum at 115 ms (see Fig. 55).

Differentiation between signals arising at the S1 and S2 cortices is very clear in Fig. 56 which shows responses to stimulation of the left tibial nerve at the ankle, measured with the 122-channel whole-head magnetometer (see Fig. 41). The first cortical response, peaking at 42 ms, is visible at the top of the head, above the foot area in S1. On both sides, a long-latency peak is seen at 130–140 ms. reflecting activity at the left and right S2 cortices. When the median nerve was stimulated at the wrist, the source area of the earliest response was, in agreement with the somatotopical order of S1, a few centimeters lateral to the midline in the contralateral hand S1 area, whereas long-latency signals were still seen over both S2 cortices.

In an earlier study (Hari *et al.*, 1990), responses from S2 were obtained using an oddball paradigm. The standards (90%) were presented to the thumb and the deviant stimuli (10%) to the middle finger, and vice versa. The S2 responses, peaking at about 100 ms, were almost 3 times as high in amplitude to deviants than to standards (see Fig. 57). A similar amplitude enhancement was obtained when the deviants were presented without the intervening standards but with the same long interstimulus interval. In other words, the stimuli applied to one finger did not have an observable effect on neural populations responding to stimulation of the other finger. These results indicate that an accurate functional representation of different body parts is maintained in the human S2 as well.

#### 3. Painful stimulation

Responses have also been recorded to painful stimuli; the activated areas were around S2. Electrical stimulation of the tooth pulp, carbon dioxide stimulation of the nasal mucosa, and electrical stimulation of the skin were used (Hari *et al.*, 1983; Huttunen *et al.*, 1986; Joseph *et al.*, 1991). Consequently, it can be concluded that painful stimuli activate certain cortical areas, but no evidence has been obtained for a localized cortical "pain center." In objective evaluation of different pain-killer drugs, it might be valuable to monitor these pain-related responses whose source areas are now known.

### D. Spontaneous activity

#### 1. Alpha rhythm

Studies of spontaneous brain activity benefit greatly from recordings with multisensor arrays. In evoked-response experiments, discussed so far, data from several sites measured at different times can be combined fairly safely; but in recordings of spontaneous activity, this is not possible because every event is unique. On the other hand, many spontaneous brain signals are so strong that they can be recorded without averaging.

The appearance of the magnetoencephalogram of an awake subject resembles the well-known EEG: the parieto-occipital areas show 8–13-Hz $\alpha$ activity, which is damped by opening of the eyes. In the first study of the human magnetic $\alpha$ rhythm (Cohen, 1968), a phase reversal was observed between signals measured from the right and left hemispheres, and the oscillating source currents were suggested to be parallel to the longitudinal fissure between the hemispheres. Chapman *et al.* (1984) used the relative covariance method with an electric reference at the vertex. The map showed two extrema, one at each parieto-occipital area. The distribution agreed with a two-dipole model, with the sources in the vicinity of the calcarine fissure (the site of the primary visual cortex), symmetric with respect to the cortical midline and 4–6 cm beneath the scalp. The magnetic $\alpha$ signal was selectively suppressed on one side by stimulation of the left or right visual fields separately.

Later, a multitude of $\alpha$ sources were found for signals measured with a 4-channel magnetometer (Vvedensky, Ilmoniemi, and Kajola, 1985) and with two 7-channel magnetometers simultaneously (Ilmoniemi *et al.*, 1988). In a comparison of the $\alpha$ sources and anatomical information obtained from MR images (Williamson and Kaufman,

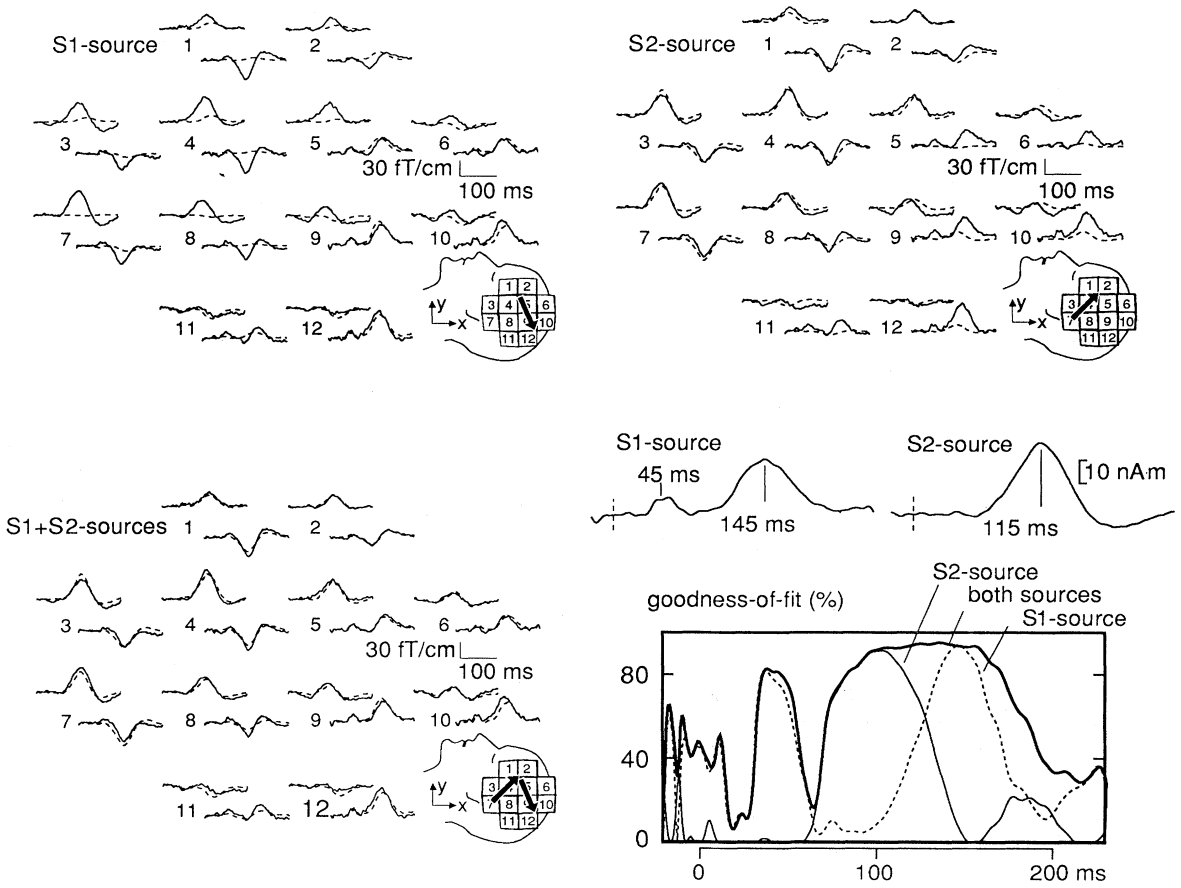


FIG. 55. Responses over the left hemisphere to electric stimulation of the right thumb; the stimuli were presented once every 2 s. The signals were digitally low-pass filtered at 90 Hz, and 55 responses were averaged. Three different source models were applied: a single dipole at the primary somatosensory hand area S1, a single dipole at the second somatosensory cortex S2, and these two sources operating simultaneously. The continuous traces illustrate the original measured signals and the dotted lines those predicted by the models. The figure at the lower right corner depicts the dipole moments of the two sources as a function of time and the goodness-of-fit values for the three models. Adapted from Hari *et al.* (1993).

1989), sources of strong oscillations were found in the region of the fissure between the parietal and occipital lobes (see Fig. 2), with most sources within 2 cm from the midline. No dipoles were observed with orientations that would suggest activation of the wall of the longitudinal fissure. Either this part of the visual cortex does not display $\alpha$ oscillations or their fields were canceled out due to bilateral activity on the opposite walls of the same fissure.

Kaufman *et al.* (1990) have demonstrated that the occipital magnetic $\alpha$ activity is suppressed for about 1 s during a visual memory task. This effect was found by monitoring the average field variance at the $\alpha$ frequency.

Figure 58 shows recordings of spontaneous magnetic signals in one subject over the right occipital lobe. Rhythmic 10-Hz activity is prominent when the eyes are closed, but it is blocked by the opening of the eyes. The maximum field gradient during the eyes-closed condition was about 0.5 pT/cm. This corresponds to a magnetic-field strength of several picoteslas at the maxima. The equivalent dipoles of the signals were clustered at the same vertical height as the sources of the visually evoked responses to checkerboard stimuli, but about 1 cm deeper. The detected $\alpha$ oscillations, therefore, most probably arise from the calcarine fissure or from its immediate surroundings. These MEG results confirm in humans the generation sites of the $\alpha$ rhythm, detected earlier by microelectrode studies in animals.

### 2. Mu and tau rhythms

Another well-known spontaneous EEG activity, the $\mu$ rhythm, has a magnetic counterpart as well. This signal, which can be recorded over the Rolandic fissure, consists of 10- and 21-Hz components (Tiihonen *et al.*, 1989); they are clearly damped by a clenching of the fist. The ECDs of the $\mu$ rhythm were within 1 cm of the source area of the 20-ms SEF deflection N20m, evoked by stimulation of the median nerve at the wrist (see Fig. 53). The

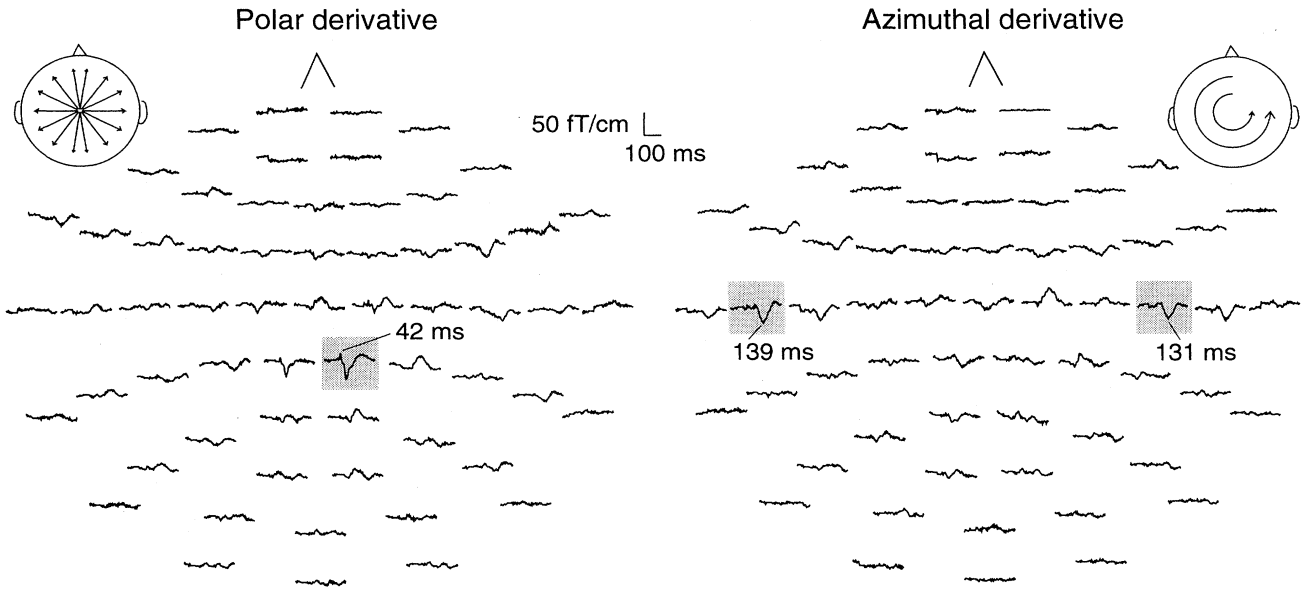


FIG. 56. Responses to stimulation of the left tibial nerve at the ankle. The recording was made with the whole-head 122-SQUID magnetometer (see Figs. 41 and 42). The ISI was 2 s, the recording passband 0.05–180 Hz, and about 150 single responses were averaged. The traces were digitally low-pass filtered at 140 Hz. The field gradients are shown separately in the polar direction (left) and in the azimuthal direction (right). From Hari *et al.* (1993).

rhythm thus seems to be most prominent in the somatomotor hand area, thereby reflecting the importance of the hand, and especially the thumb, for human sensorimotor organization. Other types of rhythmic magnetic signals at the somatomotor area, 6 and 12 Hz in frequency, have been recorded by Narici *et al.* (1990) after sensory stimulation.

Recently, another spontaneous MEG activity, the $\tau$ rhythm, was detected (Tiihonen *et al.*, 1991; Hari, 1993). This is also an 8–10-Hz oscillation, best seen in the planar gradiometric recordings just over the auditory cortex (see Fig. 59). Occasionally the $\tau$ rhythm was reduced by sound stimuli, such as bursts of noise, but it was not damped by opening of the eyes, behaving thus clearly differently from the occipital $\alpha$ rhythm. The spatial distribution of the $\tau$ rhythm suggested activity near the auditory cortex, with the dipole locations within 2 cm from the source area of the 100-ms auditory evoked response (see Fig. 60).

The $\tau$ rhythm may affect the reactivity of the cortex to external stimuli. In fact, an enhancement of evoked responses to the second tone in a pair of tones occurs when the sound onset asynchrony is 100–200 ms, which would correspond to intrinsic frequencies of 5–10 Hz (Loveless *et al.*, 1989). Spontaneous 10-Hz rhythms may either have an idling function, helping the system to avoid starting from "cold" when stimulus processing becomes necessary, or they may synchronize neuronal populations which are necessary for perception.

### 3. Spontaneous activity during sleep

During sleep, characteristic changes are seen in the amplitude and frequency of the spontaneous EEG activity (Rechtschaffen and Kales, 1968). The first multichannel MEG recordings of sleep were reported only recently (Lu, Kajola, *et al.*, 1992). Figure 61 illustrates 24-channel magnetic recordings and some electric derivations on one subject during different stages of sleep, which were classified on the basis of both EEG and MEG data. During light drowsiness (stage 1a), rhythmic $\tau$ activity appeared over the temporal lobe. During deep drowsiness and light sleep (stages 1b and 2), sharp vertex waves ("V-waves") of short duration were seen in the frontocentral EEG leads (Fz and Cz) and on several MEG channels. Magnetic spindles of 11–15 Hz in frequency appeared during stage 2 as well. The spindles were occasionally superposed on high-amplitude transients, thereby resembling the typical electric "K-complexes." During deep sleep (stages 3 and 4, 0.5–2-Hz polymorphic slow-wave activity was widely spread over the measurement area. During REM sleep, defined on the basis of rapid eye movements and decreased muscular tone, MEG activity was lower in amplitude and faster in frequency than during the other stages of sleep.

Figure 62 shows source locations for two subjects during the V-waves and K-complexes. The ECDs are clustered in an area of $4\times4$ cm$^2$ in the $xy$ plane, a few

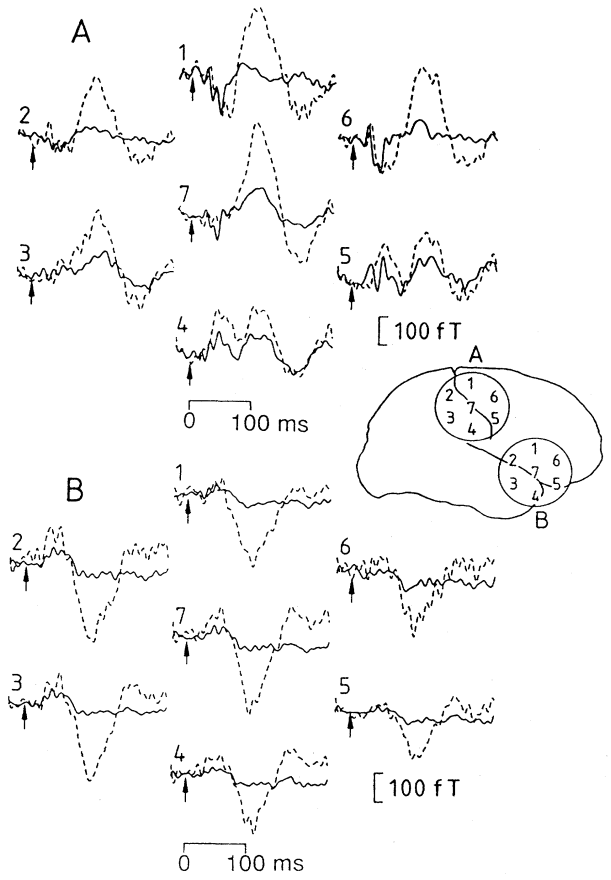


FIG. 57. Seven-channel recordings of responses at two locations (shown schematically on the inset brain) to frequent electric pulses presented on the left thumb (solid lines) and to infrequent pulses delivered to the middle finger (dashed lines). The responses have been digitally low-pass filtered at 90 Hz. The small vertical arrows define the time of stimulus presentation.

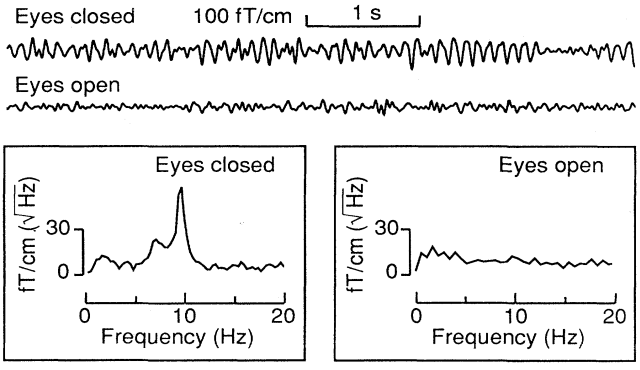


FIG. 58. Alpha rhythm on one gradiometer channel from the occipital area when the subject had his eyes closed or open. The frequency spectra were calculated from 20-s time sequences.

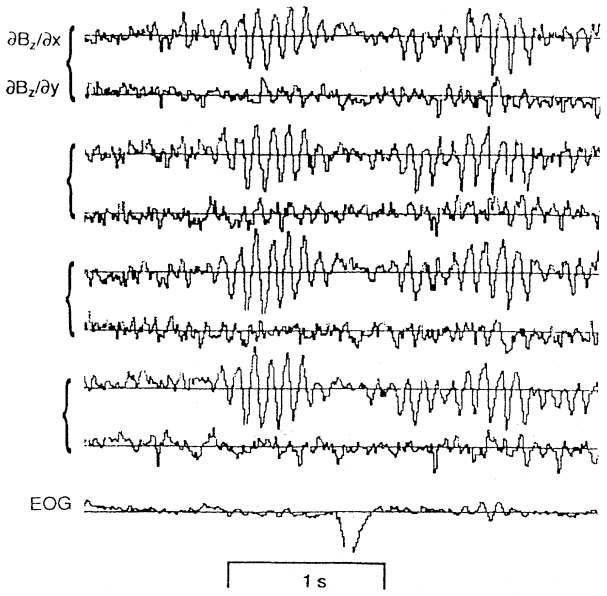


FIG. 59. Spontaneous magnetic activity recorded by eight MEG channels ($\partial B_z/\partial x$ above and $\partial B_z/\partial y$ below for each pair) over the right temporal area from a subject who had his eyes open. EOG refers to electro-oculogram. The signals were low-pass filtered at 40 Hz. Prominent $\tau$ oscillations can be seen. Modified from Hari (1993).

centimeters toward the parietal lobe from the sources of N100m. Since the MEG signals originate primarily from currents in the fissural cortex (see Sec. III.E.2), the figure also shows the estimated course of the fissure from which the signals might be generated. These estimates were obtained by drawing lines orthogonal to the main orientation of the ECDs. These "fissures" form an angle of about 45° with the Sylvian fissure (see Fig. 2), whose course was derived from the orientation of the ECD for the N100m deflection of the auditory evoked response.

The sources of the V-waves and K-complexes are in the lower part of the parietal lobe, which may thus be transiently activated during sleep. This region of the brain is involved in the regulation of attention, and its activation seems to agree with the early hypothesis that K-complexes are linked to arousal and orientation during sleep (Roth *et al.*, 1956).

During slow-wave sleep, the ECDs were distributed more widely, but they were still concentrated in the lower parts of the lateral recording sites. The sources underlying the sleep spindles were complex: it was not possible to account for their distribution with a single-dipole model, nor with a two-dipole time-varying model. Complexity of spindle generation, with a multitude of sources and frequencies, has also been suggested on the basis of animal experiments (Buser, 1987) and by depth-electrode and scalp-topography studies on humans (Niedermeyer, 1982).

In order to be confident that the ECDs really are physiologically meaningful, and to compare electric and

magnetic wave forms, simultaneous EEG and MEG recordings covering the whole head are necessary, especially as the sources in both hemispheres seem to function separately. We expect that these studies will result in a better understanding of changes in the functional organization of the human brain during different stages of sleep.

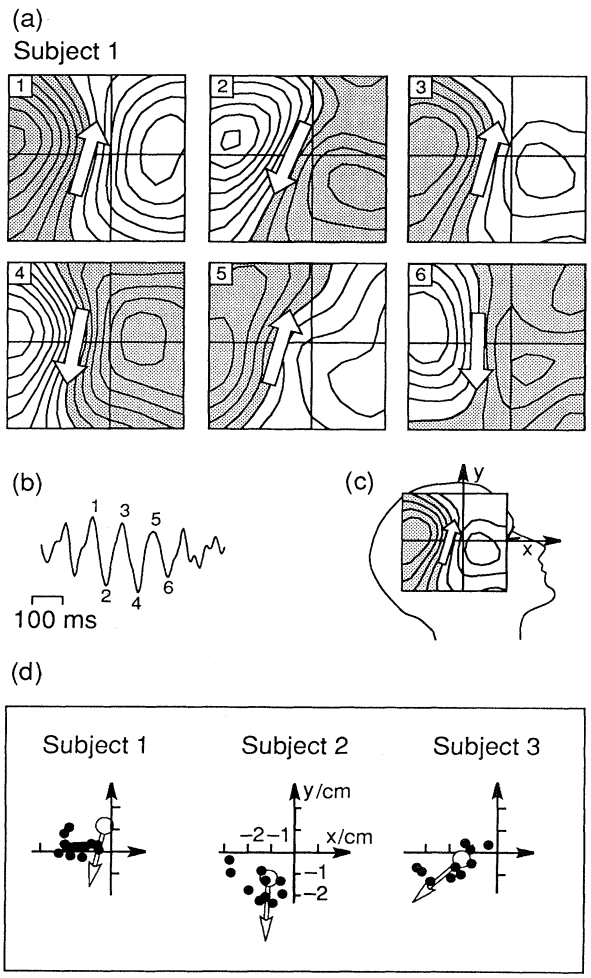


FIG. 60. Source locations of the $\tau$ rhythm. Maps in (a) show the magnetic-field component perpendicular to the head during the six successive peaks 1–6 in a representative section of the $\tau$ rhythm shown in (b). The inset (c) depicts the measurement region with respect to the subject's head. The shadowed areas indicate magnetic flux out of, and the white areas flux into, the head. The isocontours are separated by 100 fT. The white arrows in (a) show the locations and orientations of the equivalent current dipoles. For the coordinate system, see Fig. 47. Shown in (d) are the locations of the equivalent dipoles (solid circles) for ten peak deflections of the spontaneous 8–10-Hz oscillation for three subjects. The open circles and the white arrows show the dipole locations and orientations for the 100-ms auditory response. Modified from Tiihonen *et al.* (1991).

### E. Magnetoencephalography in epilepsy

#### 1. Background and data analysis

The most important clinical application of MEG so far is the localization of irritative brain areas in patients suffering from epilepsy. Studies of this type were first carried out at the University of California in Los Angeles (Barth *et al.*, 1982) and at the University of Rome (Modena *et al.*, 1982). In focal epilepsy, small areas of brain tissue may trigger the epileptic seizure. In western countries 0.5–1% of the population suffers from epilepsy. In spite of advances in antiepileptic medication, seizures in some patients cannot be controlled adequately and surgical treatment must be considered. For the successful outcome of an operation, it is necessary that there be only one trigger area that can be located accurately and that it be situated in a cortical region that may be removed without serious side effects to the patient. These requirements necessitate extensive preoperative tests, often including invasive recordings directly from the cortex. Therefore, attempts have been made to obtain from MEG data additional information for selection and noninvasive preoperative evaluation of candidates for epilepsy surgery.

Since the early 1980s, a number of epileptic patients have been studied in several MEG laboratories, as reviewed by Rose *et al.* (1987) and by Sato (1990). During the last few years, multichannel devices have considerably speeded up the recordings and improved their accuracy (Stefan *et al.*, 1989, 1991; Paetau *et al.*, 1990, 1991, 1992; Tiihonen *et al.*, 1990).

The epileptogenic focus manifests itself as an abnormal spontaneous activity, including spikes, spike-and-wave complexes, sharp waves, and irregular slow activity which can often be recorded also during the time between the seizures. These signals are typically an order of magnitude stronger than the evoked cerebral responses and can thus be measured in real time. To find the trigger location, spontaneous brain activity should be recorded simultaneously from large areas over the head. Owing to lack of suitable multichannel instruments in the past, a common approach was to apply signal averaging, which is necessary if the data are obtained sequentially from several locations. The simultaneously measured EEG signal can be used as a trigger for MEG wave forms. With this method, both single sources and multiple irritative brain areas have been found (Barth *et al.*, 1982, 1984).

Interesting results have been obtained by using spikes from electrodes on the scalp and/or in other structures as triggers for MEG averaging. A consistent depth difference was observed in the source areas of two groups of magnetic spikes, triggered by activity recorded on the scalp and by electrodes put directly into the brain (Sutherling and Barth, 1989). This result illustrates propagation of the epileptic discharge between the superficial and the deeper brain areas.

In the preoperative evaluation of patients it is essential

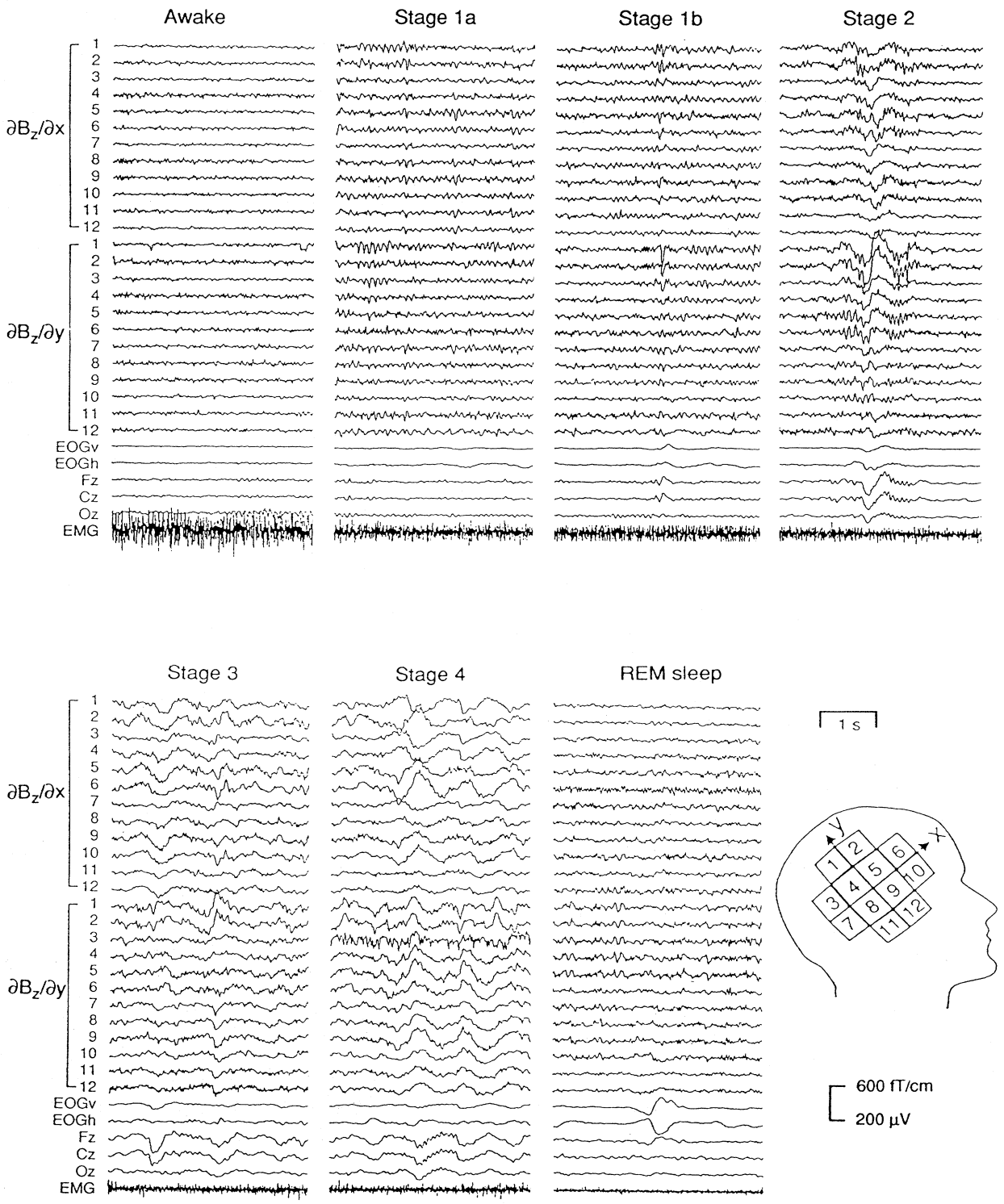


FIG. 61. Comparison of spontaneous MEG activity over the right temporal lobe during wakefulness and sleep. The recording site is indicated on the schematic head. The $x$ gradients at 12 locations are plotted above and the $y$ gradients below. In the electric channels, EOGv and EOGh are recordings of the vertical and horizontal oculograms, respectively. The electric amplitude scale refers to all other electric recordings except the EMG (electromyogram), for which only relative amplitudes are of importance. Fz, Cz, and Oz refer to frontal, central, and occipital midline locations of EEG recordings, respectively. Modified from Lu *et al.* (1992).

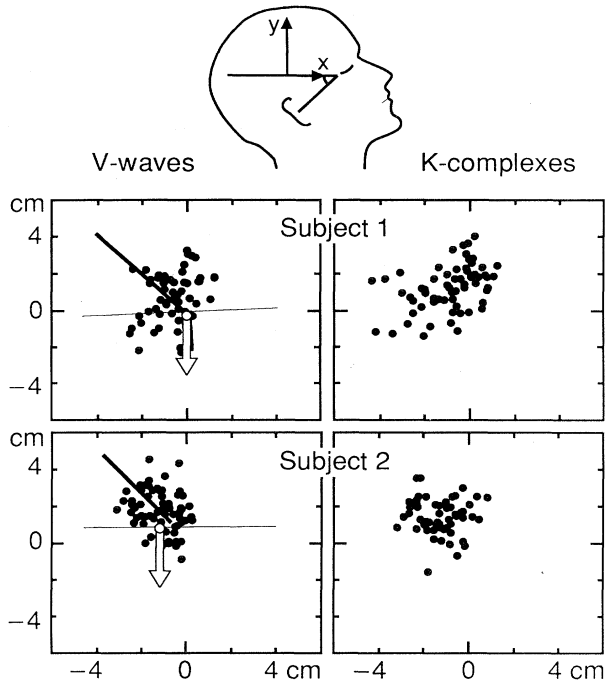


FIG. 62. Source locations (black dots) for V waves and K complexes in two subjects. Only ECDs with goodness-of-fit values exceeding 90% have been included. For the coordinate system, see Fig. 47. The thin lines in the V-wave boxes illustrate the course of the Sylvian fissure, assumed to be orthogonal to the orientation of N100m, and the thick lines the "fissures" of the ECDs of V waves (see text for more details). The orientation of ECDs for the N100m responses are shown by white arrows, and their locations by open circles. Modified from Lu *et al.* (1992).

to determine how close the irritative focus is to crucial brain areas that should not be damaged during surgery; these include, for example, cortical regions involved in motor control as well as in speech production and perception. In this task, well-established landmarks are needed. Functional localization with respect to source areas of known evoked responses (Tiihonen *et al.*, 1990) has now become routine in several MEG laboratories. The usefulness of this approach is also supported by results showing that recordings of somatosensory evoked magnetic fields agree with electrocorticographic data in determining the course of the central sulcus (Sutherling *et al.*, 1988); with combined MEG and scalp EEG data, the localization accuracy approached that of direct recordings from the cortex.

### 2. Example: boy with disturbed speech understanding

Figure 63 illustrates epileptic 3-Hz spike-and-wave activity recorded from a 7-year-old boy who suffers from the syndrome of Landau and Kleffner (Paetau *et al.*, 1991). He first developed normally but started to lose his ability to understand speech at the age of 3, owing to severe defects in auditory discrimination. The boy had normal hearing thresholds and intelligence, but he could not identify speech, not even his own name, nor could he discriminate between telephone ringing and other sounds. Auditory evoked magnetic fields to tones and syllables were absent over the right hemisphere and contaminated by spikes on the left side. In Fig. 63, the strongest epileptic discharges, about 1 pT/cm, are seen on the $x$ derivative of units 8 and 11, while the next largest signals are observed over the neighboring units 4, 7, 9, and 12. The

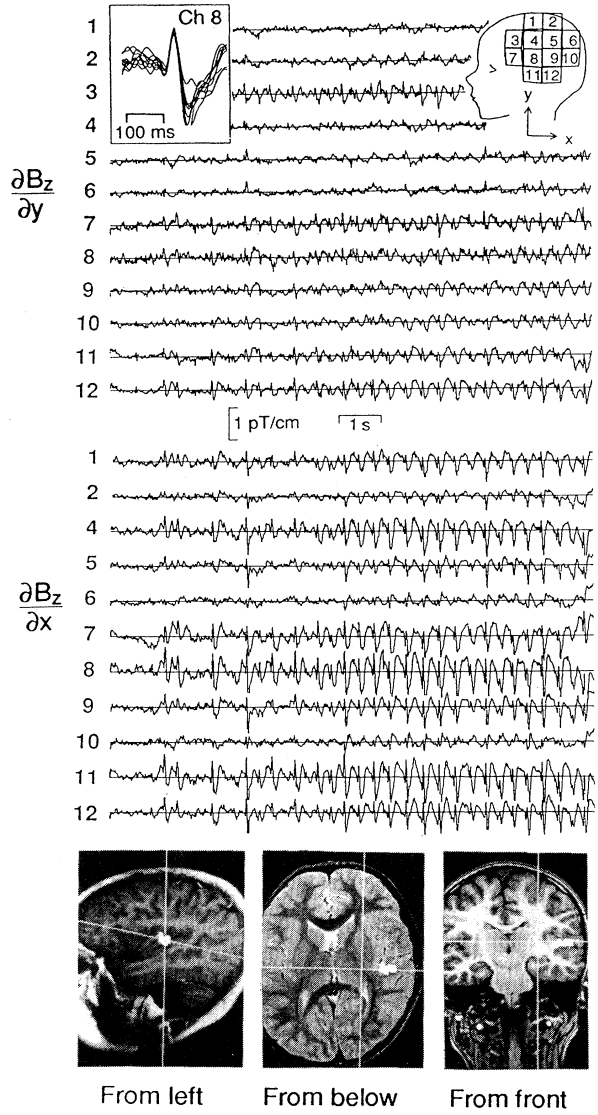


FIG. 63. Study of an epileptic patient. (Top) Examples of spontaneous spike-and-wave discharges from the left hemisphere of a child with the Landau–Kleffner syndrome. The upper traces reflect the vertical and the lower ones the horizontal gradients. The inset illustrates ten superimposed single spikes from the $y$ derivative of unit 8. (Bottom) ECD locations, shown by white squares of ten single spikes superimposed on MRI slices. The white lines indicate transsection levels of the two other slices. The $y$ channel of unit 3 was not functioning properly and is omitted. Modified from Paetau *et al.* (1991).

*y* derivatives show much smaller signals. The currents causing the epileptic spikes are under the maximum signals and are approximately vertical in orientation. Spikes were detected only on the left hemisphere.

The single-dipole model explained 90–99% of the field variance during all spikes, and the spatial distribution of the field was very stable. The source locations, superimposed on three MRI scans (see the bottom part of Fig. 63), fall in all projections on a narrow strip in the auditory cortex along the upper surface of the temporal lobe. Most probably a local epileptic focus has disturbed the normal functioning of the child's auditory cortical areas.

When extended or multiple source areas are simultaneously active, as often happens during the epileptic discharge, the single-dipole model is not always satisfactory. However, even if the source localization fails, useful information can be obtained by studying the field pattern at different time instances. Clear changes from one irritative phenomenon to another suggest the existence of several sources, although they do not rule out a deeper common trigger. This type of "qualitative" measurement, which resembles the classical use of EEG recordings, can be of value in screening patients for surgery.

### F. Other patient studies

Besides epilepsy, several other clinical applications of MEG are emerging. Proper functioning of sensory pathways from the periphery to the brain, the main focus of the clinical evoked-potential research at present, can be assessed by magnetic evoked responses. Some recordings have been made from deaf patients who use an implanted cochlear prosthesis (Pelizzone *et al.*, 1987; Hari, Pelizzone *et al.*, 1988; Hoke, Pantev *et al.*, 1989). In these patients the auditory nerve is directly stimulated by an electrode put into the cochlea, with the normal receptor mechanisms bypassed. In spite of this very artificial input, the patients learn to respond to the stimuli in a similar way as they earlier reacted to real sounds, and some of them start to understand speech even without lip reading. Similarly, the responses of their auditory cortex may resemble closely those of subjects with normal hearing.

Strokes associated with insufficient or blocked blood flow to the temporal lobe often cause marked defects in speech perception and production. Both AEFs and spontaneous activity have been recorded recently in patients with different types of cerebrovascular accidents. A lesion in the supratemporal auditory cortex resulted in the disappearance of the N100m deflection of the auditory evoked response only when the damaged area extended deep into the temporal lobe (Leinonen and Joutsiniemi, 1989; Mäkelä *et al.*, 1991). Figure 64 illustrates the evoked responses and the extent of the lesion of one such patient. Focal slowing of the spontaneous MEG activity has been detected in patients with brain infarctions, hemorrhages, and transient ischemic attacks (Vieth, 1990).

Hoke *et al.* (1989) have suggested the interesting possibility of using AEFs as objective signs of tinnitus (ringing of the ears). For example, the amplitude ratio of P200m and N100m had decreased in a patient with tinnitus that was caused by an acute noise trauma, but returned to normal during the period of recovery (Pantev *et al.*, 1989). Several experimental factors do, however, affect this amplitude ratio, and contradictory results have been reported recently (Jacobson *et al.*, 1991).

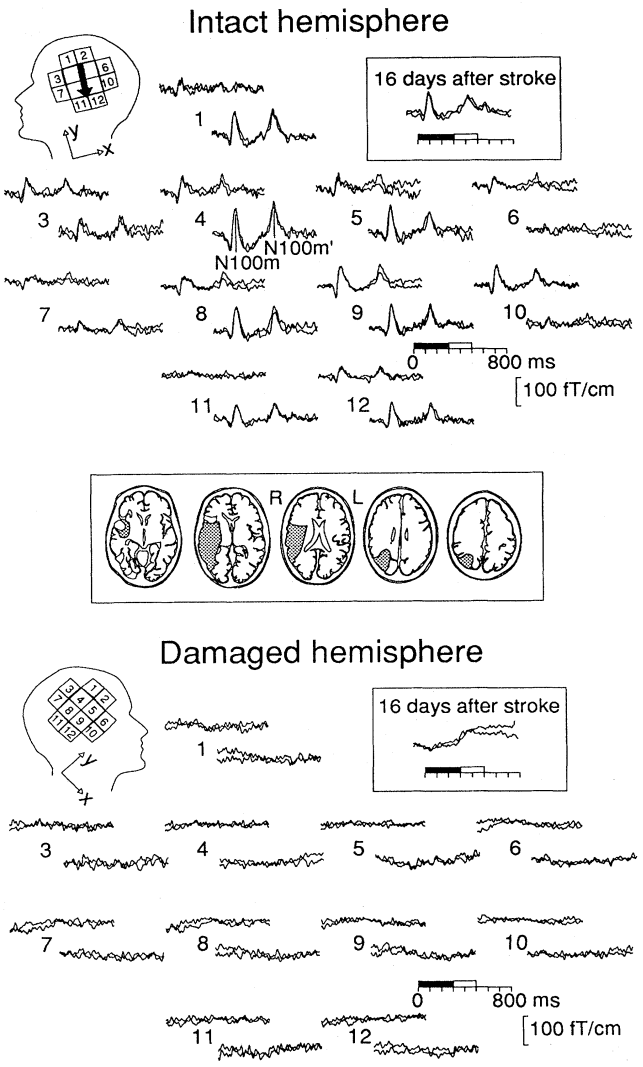


FIG. 64. Auditory responses of a patient over both hemispheres 16 months after a stroke. The black and white bars on the time scale indicate noise and square-wave parts of the stimuli, respectively. Sixty single responses to contralateral stimuli were averaged and two independent sets of measurements are superimposed. The arrow in the upper head inset shows the equivalent dipole for N100m and N100m'. The sites of the two dipoles differ by less than 1 mm. Responses from the channels that recorded the maximum signal 16 days after the stroke, i.e., $15\frac{1}{2}$ months earlier, are displayed in the boxes. The CT data in the middle illustrate the extent of the lesion, extrapolated to a standard series of anatomical pictures. Adapted from Mäkelä and Hari (1992).

Abnormalities have been observed in SEFs of patients with clinically diagnosed multiple sclerosis (Karhu, Hari, Mäkelä *et al.*, 1992). The N20m deflection was reduced and delayed by 2.5–3 ms, in agreement with evoked potential data. Additional abnormalities were common in the middle-latency responses: the 60-ms deflection was often of larger amplitude than that in control subjects. Field mappings indicated that the sources of N20m and P60m were in the somatosensory hand area; their locations agreed with those found in a control group of healthy subjects. Therefore, the responses and especially their electric counterparts can be utilized safely in clinical testing.

In patients with progressive myoclonus epilepsy, SEFs are 3–6 times larger when compared with the response of a normal subject, but the source locations agree with activation of the somatosensory hand area (Karhu, Hari, Kajola *et al.*, 1992). The cortical hyperreactivity of these patients is not extended to the auditory system.

Further attempts to develop MEG's clinical applications include dc recordings on patients suffering from migraine to detect magnetic signals associated with the spreading depression (Barkley *et al.*, 1991).

## VII. CONCLUSIONS

MEG has already proven itself a useful tool in studies of human neurophysiology and information processing. The results have confirmed features of cortical functions that earlier were observed only in animals and have also revealed information about entirely new functional principles. Better knowledge of normal brain functions is the necessary basis for advances in understanding the mechanisms of different brain disorders as well. Furthermore, recordings of both electric and magnetic signals under similar conditions have been important in identifying the neural sources of various evoked responses and of spontaneous brain rhythms. Neuromagnetic studies are thus increasing considerably our knowledge of brain activity.

EEG recordings are routinely made in thousands of laboratories of both clinical and basic neuro- and psychophysiology, but the number of MEG installations is less than 50. We believe, however, that the understanding that has resulted from MEG recordings is useful for everybody working on EEG, independent of one's access to MEG facilities. Since both electric and magnetic signals are generated by the same neuronal activity, one should pay attention to the available MEG data when making conclusions about cerebral functions on the basis of EEG recordings.

Multi-SQUID magnetometers are being actively developed in several countries with considerable industrial backing. High-quality instruments will be installed in many leading hospitals, and future clinical applications of MEG will depend strongly on experience obtained with these devices. When such magnetometers are fully operational, a completely new era of clinical MEG should emerge, since patients can then be studied more rapidly and more conveniently, and both the accuracy and the reliability of the data will improve. Emphasis will be put on combining information from diverse brain imaging methods, applied on large patient populations, to assess reliably the clinical value of MEG.

With the new whole-head-covering instruments, the activity in different parts of the brain can be monitored simultaneously. In precise work, the actual shape of the subject's cerebral cortex, as determined by magnetic-resonance imaging, must be taken into account. Advanced signal-analysis techniques can be applied to reduce coherent noise, and more sophisticated solutions of the inverse problem than the dipole models will become feasible. With these developments, the spatial accuracy of MEG will improve and the method will thereby complement PET studies, which have resolved brain areas activated during different behavioral tasks and during language processing.

It is certain that during the present Decade of the Brain considerable progress will be made in human neuroscience. MEG will probably play an important role in studies of basic neurophysiology, since it can follow changes on a millisecond time scale, characteristic for cortical signal processing. With MEG it is possible to study neurophysiological processes underlying mental acts in healthy and awake humans, including simultaneous stimulation of different sensory modalities, in a totally noninvasive way.

## ACKNOWLEDGMENTS

This work was financially supported by the Academy of Finland, the Körber-Stiftung (Hamburg), and by the Sigrid Jusélius Foundation. We express our gratitude to Dr. Riitta Salmelin and Professor Claudia Tesche, for reading the entire manuscript, and to Professor Heikki Seppä for studying parts of it. We also thank Ms. Karin Portin for preparing many of the illustrations.

## APPENDIX

Amuneal Corporation, 4737 Darrah Str., Philadelphia, PA 19124-2705.

Biomagnetic Technologies, Inc., 9727 Pacific Heights Boulevard, San Diego, CA 92121.

CTF Systems, Inc., 15-1750 McLean Avenue, Port Coquitlam, BC, Canada V3C 1M9.

Dornier Systems GmbH, P.O. Box 1360, D-7990 Friedrichshafen, Germany.

Friedrich-Schiller-University, Goetheallee 1, Jena, Germany.

Furukawa Electric Corporation, 2-4-3 Okano, Nishi-ku, Yokohama 220, Japan.

Neuromag, Ltd., c/o Low Temperature Laboratory, Helsinki University of Technology, 02150 Espoo, Finland.

Polhemus Navigational Sciences, 1 Hercules Drive, Colchester, VT 05446.

Quantum Design, 11578 Sorrento Valley Road, San

Diego, CA 92121.
Superconducting Sensor Laboratory of Japan, 1-6-5 Higashi-Nihonbashi, Chuo-ku, Tokyo 103, Japan.
Takenaka Corporation, 1-13, 4-chome, Hommachi, Chuo-ku, Osaka 541, Japan.
2G/Hypres, 2G Enterprises, 897 Independence Avenue, Mountain View, CA 94043.
Vacuumschmelze GmbH, Grüner Weg 37, D-6450 Hanau, Germany.

## REFERENCES

Ahlfors, S., and R. J. Ilmoniemi, 1989, "Magnetometer position indicator for multichannel MEG," in *Advances in Biomagnetism,* edited by S. J. Williamson, M. Hoke, G. Stroink, and M. Kotani (Plenum, New York), pp. 693–696.

Ahlfors, S. P., R. J. Ilmoniemi, and M. S. Hämäläinen, 1992, "Estimates of visually evoked cortical currents," Electroencephalogr. Clin. Neurophysiol. **82**, 225–236.

Ahonen, A. I., M. S. Hämäläinen, R. J. Ilmoniemi, M. J. Kajola, J. E. T. Knuutila, J. T. Simola, and V. A. Vilkman, 1993, "Sampling theory for neuromagnetic detector arrays (Helsinki University of Technology, Finland), IEEE Trans Biomed. Eng. (in press).

Ahonen, A. I., M. S. Hämäläinen, M. J. Kajola, J. E. T. Knuutila, O. V. Lounasmaa, J. T. Simola, C. D. Tesche, and V. A. Vilkman, 1991, "Multichannel SQUID systems for brain research," IEEE Trans. Magn. **27**, 2786–2792.

Ahonen, A. I., M. S. Hämäläinen, M. J. Kajola, J. E. T. Knuutila, P.L. Laine, O. V. Lounasmaa, J. T. Simola, C. D. Tesche, and V. A. Vilkman, 1992, "A 122-channel magnetometer covering the whole head," in *Proceedings of the Satellite Symposium on Neuroscience and Technology, 14th Annual Conference of the IEEE Engineering in Medicine and Biology Society,* edited by A. Dittmar and J. C. Froment (IEEE Engineering and Medicine and Biology Society, Lyon), pp. 16–20.

Aittoniemi, K., P. J. Karp, T. Katila, M-L. Kuusela, and T. Varpula, 1978, "On balancing superconducting gradiometric magnetometers," J. Phys. (Paris) **39** (C6) 1223–1225.

Albert, A., 1972, *Regression and the Moore-Penrose Pseudoinverse,* Vol. 94 of *Mathematics in Science and Engineering* (Academic, New York).

Anderson, A. C., G. L. Salinger, and J. C. Wheatley, 1961, "Thermal conductivity of liquid $He^3$," Phys. Rev. Lett. **6**, 443–446.

Anogianakis, G., J.-M. Badier, G. Barrett, S. Erné, R. Fenici, P. Fenwick, F. Grandori, R. Hari, R. Ilmoniemi, F. Mauguière, D. Lehmann, F. Perrin, M. Peters, G.-L. Romani, and P. M. Rossini, 1992, "A consensus statement on relative merits of EEG and MEG," Electroencephalogr. Clin. Neurophysiol. **82**, 317–319.

Arthur, D. L., P. S. Lewis, P. A. Medwick, and E. R. Flynn, 1991, "A neuromagnetic study of selective auditory attention," Electroencephalogr. Clin. Neurophysiol. **78**, 348–360.

Arthur, R. M., and D. B. Geselowitz, 1970, "Effect of inhomogeneities on the apparent location and magnitude of a cardiac current dipole source," IEEE Trans. Biomed. Eng. **BME-17**, 141–146.

Atsumi, K., M. Kotani, S. Ueno, T. Katila, and S. J. Williamson, 1988, eds., *Biomagnetism '87* (Tokyo Denki University, Tokyo).

Barkley, G. L., J. E. Moran, Y. Takanashi, and N. Tepley, 1991, "Techniques for dc magnetoencephalography," J. Clin. Neurophysiol. **8**, 189–199.

Barnard, A. C. L., I. M. Duck, M. S. Lynn, and W. P. Timlake, 1967, "The application of electromagnetic theory to electrocardiography. II. Numerical solution of the integral equations," Biophys. J. **7**, 463–491.

Barth, D. S., W. Sutherling, J. Engel, Jr., and J. Beatty, 1982, "Neuromagnetic localization of epileptiform spike activity in the human brain," Science **218**, 891–894.

Barth, D. S., W. Sutherling, J. Engel, Jr., and J. Beatty, 1984, "Neuromagnetic evidence of spatially distributed sources underlying epileptiform spikes in the human brain," Science **223**, 293–296.

Belliveau, J. W., D. N. Kennedy, R. C. McKinstry, B. R. Buchbinder, R. M. Weisskoff, M. S. Cohen, J. M. Vevea, T. J. Brady, and B. R. Rosen, 1991, "Functional mapping of the human visual cortex by magnetic resonance imaging," Science **254**, 716–719.

Ben-Jacob, E., and Y. Imry, 1981, "Dynamics of the dc-SQUID," J. Appl. Phys. **52**, 6806–6815.

Benson, D. A., and R. D. Hienz, 1978, "Single-unit activity in the auditory cortex of monkeys selectively attending left vs. right ear stimuli," Brain Res. **159**, 307–320.

Bertrand, O., J. Bohorquez, and J. Pernier, 1990, "Technical requirements for evoked potential monitoring in the intensive care unit," Vol. EEG Suppl. 41 of *New Trends and Advanced Techniques in Clinical Neurophysiology,* edited by P. M. Rossini and F. Maugui'ere (Elsevier, Amsterdam), pp. 51–70.

Braginski, A. I., 1987, "Recent advances in Josephson junction materials," in *Extended Abstracts of 1987 International Superconductivity Electronics Conference (ISEC '87)* (Japan Society of Applied Physics, Tokyo), pp. 63–67.

Braginski, A. I., 1992, "Toward a technology of electronic circuits with high-$T_c$ supeconductors," in *Superconducting Devices and Their Applications,* Springer Proceedings in Physics, Vol. 64, edited by H. Koch and H. Lübbig (Springer, Berlin), pp. 3–18.

Brenner, D., J. Lipton, L. Kaufman, and S. J. Williamson, 1978, "Somatically evoked magnetic fields of the human brain," Science **199**, 81–83.

Brenner, D., S. J. Williamson, and L. Kaufman, 1975, "Visually evoked magnetic fields of the human brain," Science **190**, 480–482.

Bruno, A. C., and P. Costa Ribeiro, 1989, "Designing planar gradiometer arrays: Preliminary considerations," in *Advances in Biomagnetism,* edited by S. J. Williamson, M. Hoke, G. Stroink, and M. Kotani (Plenum, New York), pp. 649–652.

Buchanan, D. S., and D. N. Paulson, 1989, "Neuromagnetometer calibration using an array of small coils," in *Advances in Biomagnetism,* edited by S. J. Williamson, M. Hoke, G. Stroink, and M. Kotani (Plenum, New York), pp. 705–708.

Buser, P., 1987, "Thalamocortical mechanisms underlying synchronized EEG activity," in *A Textbook of Clinical Neurophysiology,* edited by A. M. Halliday, S. R. Butler, and R. Paul (Wiley, Chichester), pp. 595–621.

Cabrera, B., 1982, "First results from a superconductive detector for moving magnetic monopoles," Phys. Rev. Lett. **48**, 1378–1381.

Cahill, L., and H. Scheich, 1991, "Activation of auditory cortex with visual stimulation through sensory-sensory conditioning," in *Soc. Neurosci. Abstr.,* Vol. 17, Part 2 (Society for Neuroscience, Washington, DC), p. 659.

Cantor, R., T. Ryhänen, D. Drung, H. Koch, and H. Seppä,

1991, "Design and optimization of dc SQUIDs fabricated using a simplified four-level process," IEEE Trans. Magn. **27**, 2927–2931.

Carelli, P., C. Del Gratta, V. Foglietti, I. Modena, A. Pasquarelli, V. Pizzella, M. Pullano, G. L. Romani, and G. Torrioli, 1989, "A nine channel DC SQUID system for biomagnetism," in *Advances in Biomagnetism,* edited by S. J. Williamson, M. Hoke, G. Stroink, and M. Kotani (Plenum, New York), pp. 665–668.

Carelli, P., and V. Foglietti, 1983, "A second derivative gradiometer integrated with a dc superconducting interferometer," J. Appl. Phys. **54**, 6065–6067.

Carelli, P., and R. Leoni, 1986, "Localization of biological sources with arrays of superconducting gradiometers," J. Appl. Phys. **59**, 645–650.

Chapman, R. M., R. J. Ilmoniemi, S. Barbanera, and G. L. Romani, 1984, "Selective localization of alpha brain activity with neuromagnetic measurements," Electroencephalogr. Clin. Neurophysiol. **58**, 569–572.

Claassen, J. H., 1975, "Coupling considerations for SQUID devices," J. Appl. Phys. **46**, 2268–2275.

Clarke, C. J. S., 1989, "Probabilistic methods in a biomagnetic inverse problem," Inverse Problems **5**, 999–1012.

Clarke, C. J. S., A. A. Ioannides, and J. P. R. Bolton, 1989, "Localized and distributed source solutions for the biomagnetic inverse problem I," in *Advances in Biomagnetism,* edited by S. J. Williamson, M. Hoke, G. Stroink, and M. Kotani (Plenum, New York), pp. 587–590.

Clarke, J., 1966, "A superconducting galvanometer employing Josephson tunneling," Philos. Mag. **13**, 115–127.

Clarke, J., 1983, "Geophysical applications of SQUIDs," IEEE Trans. Magn. **MAG-19**, 288–294.

Clarke, J., W. M. Goubau, and M. B. Ketchen, 1975, "Thin-film dc SQUID with low noise and drift," Appl. Phys. Lett. **27**, 155–156.

Clarke, J., W. M. Goubau, and M. B. Ketchen, 1976, "Tunnel junction dc SQUID fabrication, operation, and performance," J. Low Temp. Phys. **25**, 99–144.

Cohen, D., 1968, "Magnetoencephalography: Evidence of magnetic fields produced by alpha-rhythm currents," Science **161**, 784–786.

Cohen, D., 1970a, "Large-volume conventional magnetic shields," Rev. Phys. Appl. **5**, 53–58.

Cohen, D., 1970b, "Low-field room built at high-field magnet lab," Phys. Today **23**, 56–57.

Cohen, D., 1972, "Magnetoencephalography: Detection of the brain's electrical activity with a superconducting magnetometer," Science **175**, 664–666.

Cohen, D., 1979, "Magnetic measurement and display of current generators in the brain. Part I: The 2-D detector," in *Digest of the 12th International Conference on Medical and Biological Engineering, Jerusalem* (Beilinson Medical Center, Petah Tikva, Israel), pp. 15–16.

Cohen, D., and B. N. Cuffin, 1983, "Demonstration of useful differences between magnetoencephalogram and electroencephalogram," Electroencephalogr. Clin. Neurophysiol. **56**, 38–51.

Cohen, D., B. N. Cuffin, K. Yunokuchi, R. Maniewski, C. Purcell, G. R. Cosgrove, J. Ives, J. G. Kennedy, and D. L. Schomer, 1990, "MEG versus EEG localization test using implanted sources in the human brain," Ann. Neurol. **28**, 811–817.

Creutzfeldt, O., 1987, "Single neuron activity in the right and left human temporal lobe during listening and speaking," in *Fundamental Mechanisms of Human Brain Function,* edited by J. Engel, Jr. (Raven, New York), pp. 69–81.

Crowley, C. W., R. E. Greenblatt, and I. Khalil, 1989, "Minimum norm estimation of current distributions in realistic geometries," in *Advances in Biomagnetism,* edited by S. J. Williamson, M. Hoke, G. Stroink, and M. Kotani (Plenum, New York), pp. 603–606.

Cuffin, B. N., 1985, "A comparison of moving dipole inverse solutions using EEG's and MEG's," IEEE Trans. Biomed. Eng. **BME-32**, 905–910.

Cuffin, B. N., and D. Cohen, 1977, "Magnetic fields of a dipole in special volume conductor shapes," IEEE Trans. Biomed. Eng. **BME-24**, 372–381.

Daalmans, G., H. Seifert, F. Bömmel, and H. E. Hoenig, 1989, "Dc-SQUIDs for a 31-channel SQUID-gradiometer array for biomagnetic diagnosis," in *Proceedings of the 2nd Workshop on High-Temperature Superconducting Electron Devices, Shikabe, Hokkaido, Japan* (R&D Association for Future Electron Devices, Shikabe), pp. 219–222.

Daalmans, G. M., L. Bär, F. R. Bömmel, R. Kress, and D. Uhl, 1991, "Ultra low noise all niobium dc-SQUIDs," IEEE Trans. Magn. **27**, 2997–3000.

Damadian, R., 1972, "Apparatus and method for detecting cancer in tissue," U.S. Pat. 3,789,832.

de Munck, J. C., 1988, "The potential distribution in a layered anisotropic spheroidal volume conductor," J. Appl. Phys. **64**, 464–470.

de Munck, J. C., 1990, "The estimation of time-varying dipoles on the basis of evoked potentials," Electroencephalogr. Clin. Neurophysiol. **77**, 156–160.

de Munck, J. C., 1992, "A linear discretization of the volume conductor boundary integral equation using analytically integrated elements," IEEE Trans. Biomed. Eng. **39**, 986–990.

de Waal, V. J., and T. M. Klapwijk, 1982, "Compact integrated dc SQUID gradiometer," Appl. Phys. Lett. **41**, 669–671.

de Weerd, J. P. C., 1981, "*A Posteriori* time-varying filtering of averaged evoked potentials I. Introduction and conceptual basis," Biol. Cybern. **41**, 211–222.

DiIorio, M. S., K.-Y. Yang, J. Zhang, S. Yoshizumi, and M. Maung, 1991, "SQUID magnetometer noise measurements of $YBa_2Cu_3O_7$ thin films and input coils," IEEE Trans. Magn. **27**, 2573–2577.

Donaldson, G. B., C. M. Pegrum, and R. J. P. Bain, 1985, "Integrated thin film SQUID instruments," in *SQUID'85: Superconducting Quantum Interference Devices and their Applications,* edited by H. D. Hahlbohm and H. Lübbig (Walter de Gruyter, Berlin), pp. 729–759.

Dössel, O., B. David, M. Fuchs, W. H. Kullmann, and K.-M. Lüdeke, 1991, "A modular low noise 7-channel SQUID-magnetometer," IEEE Trans. Magn. **27**, 2797–2800.

Dössel, O., B. David, M. Fuchs, W. H. Kullmann, K.-M. Lüdeke, and J. Krüger, 1992, "A multi-channel SQUID system for current density imaging," in *Biomagnetism: Clinical Aspects,* edited by M. Hoke, S. N. Erné, Y. C. Okada, and G. L. Romani (Elsevier, Amsterdam), pp. 837–841.

Drung, D., 1986, "Digital feedback loops for D.C. SQUIDs," Cryogenics **26**, 623–627.

Drung, D., 1992a, "Investigation of a double-loop dc SQUID magnetometer with additional positive feedback," in *SQUID '91: Superconducting Devices and Their Applications,* Springer Proceedings in Physics, Vol. 64, edited by H. Koch and H. Lübbig (Springer, Berlin), pp. 351–356.

Drung, D., 1992b, "Performance of an electronic gradiometer in noisy environments," in *SQUID '91: Superconducting Devices and Their Applications,* Springer Proceedings in Physics,

edited by H. Koch and H. Lübbig (Springer, Berlin), pp. 542–546.

Drung, D., R. Cantor, M. Peters, H. J. Scheer, and H. Koch, 1990, "Low-noise high-speed dc superconducting quantum interference device magnetometer with simplified feedback electronics," Appl. Phys. Lett. **57**, 406–408.

Drung, D., E. Crocoll, R. Herwig, A. Knüttel, M. Neuhaus, and W. Jutzi, 1987, "Experimental gradiometer with a digital feedback loop," in *Extended Abstracts of 1987 International Superconductivity Electronics Conference (ISEC '87),* edited by (Japan Society of Applied Physics, Tokyo), pp. 21–24.

Drung, D., E. Crocoll, R. Herwig, M. Neuhaus, and W. Jutzi, 1989, "Measured performance parameters of gradiometers with digital output," IEEE Trans. Magn. **25**, 1034–1037.

Duret, D., and P. Karp, 1983, "Instrumentation for biomagnetism," Nuovo Cimento D **2**, 123–141.

Duret, D., and P. Karp, 1984, "Figure of merit and spatial resolution of superconducting flux transformers," J. Appl. Phys. **56**, 1762–1768.

Elberling, C., C. Bak, B. Kofoed, J. Lebech, and K. Særmark, 1980, "Magnetic auditory responses from the human brain: A preliminary report," Scand. Audiol. **9**, 185–190.

Erné, S. N., G. Curio, L. Trahms, Z. Trontelj, and P. Aust, 1988, "Magnetic activity of a single peripheral nerve in man," in *Biomagnetism '87,* edited by K. Atsumi, M. Kotani, S. Ueno, T. Katila, and S. J. Williamson (Tokyo Denki University, Tokyo), pp. 166–169.

Erné, S. N., H.-D. Hahlbohm, and H. Lübbig, 1981, Eds., *Biomagnetism,* Proceedings, Third International Workshop on Biomagnetism, Berlin (Walter de Gruyter, Berlin).

Erné, S. N., H.-D. Hahlbohm, H. Scheer, and Z. Trontelj, 1981, "The Berlin magnetically shielded room (BMSR): Section B—performances," in *Biomagnetism,* edited by S. N. Erné, H.-D. Hahlbohm, and H. Lübbig (Walter de Gruyter, Berlin), pp. 79–87.

Erné, S. N., L. Narici, V. Pizzella, and G. L. Romani, 1987, "The positioning problem in biomagnetic measurements: A solution for arrays of superconducting sensors," IEEE Trans. Magn. **MAG-23**, 1319–1322.

Erné, S. N., and G. L. Romani, 1985, "Performances of higher order planar gradiometers for biomagnetic source localization," in *SQUID '85 Superconducting Quantum Interference Devices and their Applications,* edited by H. D. Hahlbohm and H. Lübbig (Walter de Gruyter, Berlin), pp. 951–961.

Farrell, D. E., J. H. Tripp, G. M. Brittenham, E. H. Danish, J. W. Harris, and A. E. Tracht, 1983, "A clinical system for accurate assessment of tissue iron concentration," Nuovo Cimento D **2**, 582–593.

Fenici, R. R., G. L. Romani, and S. N. Erné, 1983, "High-resolution magnetic measurements of human cardiac electrophysiological events," Nuovo Cimento D **2**, 231–247.

Feynman, R. P., R. B. Leighton, and M. Sands, 1965, *The Feynman Lectures on Physics,* Vol. 3 (Addison-Wesley, Reading, MA), pp. 21.1–18.

Foglietti, V., C. Del Gratta, A. Pasquarelli, V. Pizzella, G. Torrioli, G. L. Romani, W. J. Gallagher, M. B. Ketchen, A. W. Kleinsasser, and R. L. Sandstrom, 1991, "28-channel hybrid system for neuromagnetic measurements," IEEE Trans. Magn. **27**, 2959–2962.

Foglietti, V., W. J. Gallagher, M. B. Ketchen, A. W. Kleinsasser, R. H. Koch, S. I. Raider, and R. L. Sandstrom, 1986, "Low-frequency noise in low $1/f$ noise dc SQUID's," Appl. Phys. Lett. **49**, 1393–1395.

Foglietti, V., W. J. Gallagher, M. B. Ketchen, A. W. Kleinsasser, R. H. Koch, and R. L. Sandstrom, 1989, "Performance of dc SQUIDs with resistively shunted inductance," Appl. Phys. Lett. **55**, 1451–1453.

Forgacs, R. L., and A. Warnick, 1967, "Digital-analog magnetometer utilizing superconducting sensor," Rev. Sci. Instrum. **38**, 214–220.

Fraser-Smith, A. C., and J. L. Buxton, 1975, "Superconducting magnetometer measurements of geomagnetic activity in the 0.1 to 14 Hz frequency range," J. Geophys. Res. **80**, 3141–3147.

Freeman, W. J., 1975, *Mass Action of the Nervous System* (Academic, New York).

Fujimaki, N., H. Tamura, T. Imamura, and S. Hasuo, 1988, "A single-chip SQUID magnetometer," IEEE Trans. Electron Devices **35**, 2412–2418.

Furukawa, H., M. Katayama, H. Emoto, and K. Shirae, 1986, "Vector measurement of the heart magnetic field," in *Proceedings of the 6th Sensor Symposium,* edited by S. Kataoka (Institute of Electrical Engineers in Japan, Tsukuba), pp. 319–322.

George, J. S., P. S. Jackson, D. M. Ranken, and E. R. Flynn, 1989, "Three-dimensional volumetric reconstruction for neuromagnetic source localization," in *Advances in Biomagnetism,* edited by S. J. Williamson, M. Hoke, G. Stroink, and M. Kotani (Plenum, New York), pp. 737–740.

Geselowitz, D. B., 1967, "On bioelectric potentials in an inhomogeneous volume conductor," Biophys. J. **7**, 1–11.

Geselowitz, D. B., 1970, "On the magnetic field generated outside an inhomogeneous volume conductor by internal current sources," IEEE Trans. Magn. **MAG-6**, 346–347.

Giffard, R. P., 1980, "Fundamentals for SQUID applications," in *SQUID '80: Superconducting Quantum Interference Devices and their Applications,* edited by H.-D. Hahlbohm and H. Lübbig (Walter de Gruyter, Berlin), pp. 445–471.

Giffard, R. P., R. A. Webb, and J. C. Wheatley, 1972, "Principles and methods of low-frequency electric and magnetic measurements using an rf-biased point-contact superconducting device," J. Low. Temp. Phys. **6**, 533–610.

Goldman, D. E., 1943, "Potential, impedance, and rectification in membranes," J. Gen. Physiol. **27**, 37–60.

Golub, G. H., and C. F. van Loan, 1989, *Matrix Computations,* 2nd ed. (The Johns Hopkins University, Baltimore).

Grandori, F., M. Hoke, and G. L. Romani, 1990, Eds., *Auditory Evoked Magnetic Fields and Potentials,* Vol. 6 of *Advances in Audiology* (Karger, Basel).

Grönberg, L., H. Seppä, R. Cantor, M. Kiviranta, T. Ryhänen, J. Salmi, and I. Suni, 1992, "A low noise dc SQUID based on Nb/Al-$AlO_x$/Nb Josephson junctions," in *SQUID '91: Superconducting Devices and Their Applications,* Springer Proceedings in Physics, Vol. 64, edited by H. Koch and H. Lübbig (Springer, Berlin), pp. 281–285.

Gross, R., P. Chaudhari, M. Kawasaki, M. B. Ketchen, and A. Gupta, 1990, "Low noise $YBa_2Cu_3O_{7-\delta}$ grain boundary junction dc SQUIDs," Appl. Phys. Lett. **57**, 727–729.

Gross, R., P. Chaudhari, M. Kawasaki, M. B. Ketchen, and A. Gupta, 1991, "Characteristics of $YBa_2Cu_3O_{7-\delta}$ grain boundary junction dc-SQUIDs," IEEE Trans. Magn. **27**, 2565–2568.

Grummich, P., and E. Herrmann, 1992, unpublished.

Grynszpan, F., and D. B. Geselowitz, 1973, "Model studies of the magnetocardiogram," Biophys. J. **13**, 911–925.

Gurvitch, M., M. A. Washington, and H. A. Huggins, 1983, "High quality refractory Josephson tunnel junctions utilizing thin aluminum layers," Appl. Phys. Lett. **42**, 472–474.

Guy, C. N., A. Cayles, S. Walker, and K. Leedham-Green, 1989, "A multi-channel biomagnetometer," in *Advances in*

*Biomagnetism,* edited by S. J. Williamson, M. Hoke, G. Stroink, and M. Kotani (Plenum, New York), pp. 661–664.
Hämäläinen, M., 1991, "Anatomical correlates for magnetoencephalography: integration with magnetic resonance images," Clin. Phys. Physiol. Meas. Suppl. A **12**, 29–32.
Hämäläinen, M. S., H. Haario, and M. S. Lehtinen, 1987, "Interferences about sources of neuromagnetic fields using Bayesian parameter estimation" (Helsinki University of Technology, Finland), Technical Report TKK-F-A620.
Hämäläinen, M. S., and R. J. Ilmoniemi, 1984, "Interpreting measured magnetic fields of the brain: Estimates of current distributions" (Helsinki University of Technology, Finland), Technical Report TKK-F-A559.
Hämäläinen, M. S., and R. J. Ilmoniemi, 1993, "Interpreting magnetic fields of the brain: Minimum-norm estimates," Phys. Med. Biol. Comp. (in press).
Hämäläinen, M. S., and J. Sarvas, 1989, "Realistic conductivity geometry model of the human head for interpretation of neuromagnetic data," IEEE Trans. Biomed. Eng. **36**, 165–171.
Hari, R., 1990, "The neuromagnetic method in the study of the human auditory cortex," in *Auditory Evoked Magnetic Fields and Electric Potentials,* Vol. 6 of *Advances in Audiology,* edited by F. Grandori, M. Hoke, and G. L. Romani (Karger, Basel), pp. 222–282.
Hari, R., 1991a, "A neurophysiologist's view on biomagnetic source localization," in *Biomagnetic Localization and 3D Modelling,* edited by J. Nenonen, H.-M. Rajala, and T. Katila (Helsinki University of Technology, Espoo) pp. 32–43.
Hari, R., 1991b, "On brain's magnetic responses to sensory stimuli," J. Clin. Neurophysiol. **8**, 157–169.
Hari, R., 1993, "Magnetoencephalography as a tool of clinical neurophysiology," in *Electroencephalography. Basic Principles, Clinical Applications, and Related Fields,* edited by E. Niedermeyer and F. Lopes da Silva (Williams and Wilkins, Baltimore, in press).
Hari, R., K. Aittoniemi, M.-L. Järvinen, T. Katila, and T. Varpula, 1980, "Auditory evoked transient and sustained magnetic fields of the human brain: Localization of neural generators," Exp. Brain Res. **40**, 237–240.
Hari, R., J. Hällström, J. Tiihonen, and S.-L. Joutsiniemi, 1989, "Multichannel detection of magnetic compound action fields of median and ulnar nerves," Electroencephalogr. Clin. Neurophysiol. **72**, 277–280.
Hari, R., H. Hämäläinen, M. Hämäläinen, J. Kekoni, M. Sams, and J. Tiihonen, 1990, "Separate finger representations at the human second somatosensory cortex," Neurosci. **37**, 245–249.
Hari, R., M. Hämäläinen, R. Ilmoniemi, and O. V. Lounasmaa, 1991, "MEG versus EEG localization test (Letter to the Editor)," Ann. Neurol. **30**, 222–224.
Hari, R., M. Hämäläinen, E. Kaukoranta, J. Mäkelä, S.-L. Joutsiniemi, and J. Tiihonen, 1989, "Selective listening modifies activity of the human auditory cortex," Exp. Brain Res. **74**, 463–470.
Hari, R., and R. J. Ilmoniemi, 1986, "Cerebral magnetic fields," CRC Crit. Rev. Biomed. Eng. **14**, 93–126.
Hari, R., S.-L. Joutsiniemi, and J. Sarvas, 1988, "Spatial resolution of neuromagnetic records: theoretical calculations in a spherical model," Electroencephalogr. Clin. Neurophysiol. **71**, 64–72.
Hari, R., K. Kaila, T. Katila, T. Tuomisto, and T. Varpula, 1982, "Interstimulus-interval dependence of the auditory vertex response and its magnetic counterpart: Implications for their neural generation," Electroencephalogr. Clin. Neurophysiol. **54**, 561–569.
Hari, R., J. Karhu, M. Hämäläinen, J. Knuutila, O. Salonen, M. Sams M, and V. Vilkman, 1993, "Functional organization of the human first and second somatosensory cortices: A nueromagnetic study," Eur. J. Neurosci. (in press).
Hari, R., E. Kaukoranta, K. Reinikainen, T. Huopaniemi, and J. Mauno, 1983, "Neuromagnetic localization of cortical activity evoked by painful dental stimulation in man," Neurosci. Lett. **42**, 77–82.
Hari, R., and O. V. Lounasmaa, 1989, "Recording and interpretation of cerebral magnetic fields," Science **244**, 432–436.
Hari, R., M. Pelizzone, J. P. Mäkelä, J. Hällström, J. Huttunen, and J. Knuutila, 1988, "Neuromagnetic responses from a deaf subject to stimuli presented through a multichannel cochlear prosthesis," Ear and Hearing **9**, 148–152.
Hari, R., M. Pelizzone, J. P. Mäkelä, J. Hällström, L. Leinonen, and O. V. Lounasmaa, 1987, "Neuromagnetic responses of the human auditory cortex to on- and offsets of noise bursts," Audiology **26**, 31–43.
Hari, R., K. Reinikainen, E. Kaukoranta, M. Hämäläinen, R. Ilmoniemi, A. Penttinen, J. Salminen, and D. Teszner, 1984, "Somatosensory evoked cerebral magnetic fields from SI and SII in man," Electroencephalogr. Clin. Neurophysiol. **57**, 254–263.
Hari, R., J. Rif, J. Tiihonen, and M. Sams, 1992, "Neuromagnetic mismatch fields to single and paired tones," Electroencephalogr. Clin. Neurophysiol. **82**, 152–154.
Heller, L., 1990, "Computation of the return current in encephalography: the auto solid angle," in *Digital Image Synthesis and Inverse Optics, Proc. SPIE 1351,* edited by A. F. Gmitro, P. S. Idell, and I. J. LaHaie (SPIE International Society for Optical Engineering, Bellingham), pp. 376–390.
Helmholtz, H. von, 1853, "Ueber einige Gesetze der Vertheilung elektrischer Ströme in körperlichen Leitern, mit Anwendung auf die thierisch-elektrischen Versuche," Ann. Phys. Chem. **89**, 211–233, 353–377.
Higuchi, M., K. Chinone, N. Ishikawa, H. Kado, N. Kasai, M. Nakanishi, M. Koyanagi, and Y. Ishibashi, 1989, "The positioning of magnetometer pickup coil in dewar by artificial signal source," in *Advances in Biomagnetism,* edited by S. J. Williamson, M. Hoke, G. Stroink, and M. Kotani (Plenum, New York), pp. 701–704.
Hilbert, C., and J. Clarke, 1984, "Input impedance of an amplifier based on a dc superconducting quantum interference device," Appl. Phys. Lett. **45**, 799–801.
Hinshaw, W. S., and A. H. Lent, 1983, "An introduction to NMR imaging: From the Bloch equation to the imaging equation," Proc. IEEE **71**, 338–350.
Hinz, T., 1988, "Utilization of reconstruction algorithms in transmission and emission computed tomography," in *Imaging Techniques in Biology and Medicine* (Academic, New York), pp. 257–299.
Hoenig, H. E., G. M. Daalmans, L. Bär, F. Bömmel, A. Paulus, D. Uhl, H. J. Weisse, S. Schneider, H. Seifert, H. Reichenberger, and K. Abraham-Fuchs, 1991, "Multi channel dc SQUID sensor array for biomagnetic applications," IEEE Trans. Magn. **27**, 2777–2785.
Hoke, M., 1988, "SQUID-based measuring techniques—a challenge for the functional diagnostics in medicine," in *The Art of Measurement: Metrology in Fundamental and Applied Physics,* edited by B. Kramer (VCH Verlagsgesellschaft, Weinheim), pp. 287–335.
Hoke, M., S. N. Erné, Y. C. Okada, and G. L. Romani, 1992, Eds., *Biomagnetism: Clinical Aspects* (Elsevier, Amsterdam).
Hoke, M., H. Feldman, C. Pantev, B. Lütkenhöner, and K.

Lehnertz, 1989, "Objective evidence of tinnitus in auditory evoked magnetic fields," Hearing Res. **37**, 281–286.

Hoke, M., C. Pantev, B. Lütkenhöner, K. Lehnertz, and W. Sürth, 1989, "Magnetic fields from the auditory cortex of a deaf human individual occurring spontaneously or evoked by stimulation through a cochlear prosthesis," Audiology **28**, 152–170.

Horacek, B. M., 1973, "Digital model for studies in magnetocardiography," IEEE Trans. Magn. **MAG-9**, 440–444.

Houwman, E. P., D. Veldhuis, J. Flokstra, H. J. M. ter Brake, W. Jaszczuk, A. Martinez, and H. Rogalla, 1991, "Dc-SQUID sensor system for multichannel neuromagnetometry," IEEE Trans. Magn. **27**, 2955–2958.

Hutchinson, J. M. S., and M. A. Foster, 1987, "General principles," *Practical NMR Imaging,* edited by M. A. Foster and J. M. S. Hutchinson (IRL, Oxford), pp. 1–48.

Huttunen, J., G. Kobal, E. Kaukoranta, and R. Hari, 1986, "Cortical responses to painful $CO_2$ stimulation of nasal mucosa; a magnetoencephalographic study in man," Electroencephalogr. Clin. Neurophysiol. **64**, 347–349.

Ilmoniemi, R. J., and S. Ahlfors, 1990, "Visually evoked magnetic fields: Retinotopy and cortical magnification factor," in *Soc. Neurosci. Abstr.,* Vol. 16, Part 1 (Society for Neuroscience, Washington, DC), p. 568.

Ilmoniemi, R. J., M. S. Hämäläinen, and J. Knuutila, 1985, "The forward and inverse problems in the spherical model," in *Biomagnetism: Applications & Theory,* edited by H. Weinberg, G. Stroink, and T. Katila (Pergamon, New York), pp. 278–282.

Ilmoniemi, R., R. Hari, and K. Reinikainen, 1984, "A four-channel SQUID magnetometer for brain research," Electroencephalogr. Clin. Neurophysiol. **58**, 467–473.

Ilmoniemi, R., and J. Knuutila, 1984, "Remarks on the design of a four-channel SQUID magnetometer for brain research," in *Proceedings of the Tenth International Cryogenic Engineering Conference,* edited by H. Collan, P. Berglund, and M. Krusius (Butterworth, Guildford, Surrey), pp. 457–460.

Ilmoniemi, R., J. Knuutila, T. Ryhänen, and H. Seppä, 1989, "Multi-SQUID devices and their applications," Vol. 12 of *Progress in Low Temperature Physics,* edited by D. F. Brewer (North-Holland, Amsterdam), pp. 271–339.

Ilmoniemi, R. J., S. J. Williamson, and W. E. Hostetler, 1988, "New method for the study of spontaneous brain activity," in *Biomagnetism '87,* edited by K. Atsumi, M. Kotani, S. Ueno, T. Katila, and S. J. Williamson (Tokyo Denki University, Tokyo), pp. 182–185.

Imamura, T., and S. Hasuo, 1988, "A submicrometer $Nb/AlO_x/Nb$ Josephson junction," J. Appl. Phys. **64**, 1586–1588.

Ioannides, A. A., J. P. R. Bolton, and C. J. S. Clarke, 1990, "Continuous probabilistic solutions to the biomagnetic inverse problem," Inverse Probl. **6**, 523–542.

Ioannides, A. A., J. P. R. Bolton, R. Hasson, and C. J. S. Clarke, 1989, "Localized and distributed source solutions for the biomagnetic inverse problem II," in *Advances in Biomagnetism,* edited by S. J. Williamson, M. Hoke, G. Stroink, and M. Kotani (Plenum, New York), pp. 591–594.

Iversen, L. L., 1979, "The chemistry of the brain," Sci. Am. **241**, 118–129.

Jack, C. E., and W. R. Thurlow, 1973, "Effects of degree of visual association and angle of displacement on the 'ventriloquism' effect," Percept. Mot. Skills **37**, 967–979.

Jacobson, G. P., B. K. Ahmad, J. Moran, C. W. Newman, N. Tepley, and J. Wharton, 1991, "Auditory evoked cortical magnetic field ($m_{100}/m_{200}$) measurements in tinnitus and normal groups," Hearing Res. **56**, 44–52.

Jacklevic, R. C., J. Lambe, A. H. Silver, and J. E. Mercereau, 1964, "Quantum interference effects in Josephson tunneling," Phys. Rev. Lett. **12**, 159–160.

Jaszczak, R. J., 1988, "Tomographic radiopharmaceutical imaging," Proc. IEEE **76**, 1079–1094.

Jaycox, J. M., and M. B. Ketchen, 1981, "Planar coupling scheme for ultra low noise dc SQUIDs," IEEE Trans. Magn. **MAG-17**, 400–403.

Joseph, J., E. W. Howland, R. Wakai, M. Backonja, O. Baffa, F. M. Potenti, and C. S. Cleeland, 1991, "Late pain-related magnetic fields and electric potentials evoked by intracutaneous electric finger stimulation," Electroencephalogr. Clin. Neurophysiol. **80**, 46–52.

Josephson, B. D., 1962, "Possible new effects in superconductive tunneling," Phys. Lett. **1**, 251–253.

Joutsiniemi, S.-L., and R. Hari, 1989, "Omissions of auditory stimuli may activate frontal cortex," Eur. J. Neurosci. **1**, 524–528.

Kajola, M., S. Ahlfors, G. J. Ehnholm, J. Hällström, M. S. Hämäläinen, R. J. Ilmoniemi, M. Kirviranta, J. Knuutila, O. V. Lounasmaa, C. D. Tesche, and V. Vilkman, 1989, "A 24-channel magnetometer for brain research," in *Advances in Biomagnetism,* edited by S. J. Williamson, M. Hoke, G. Stroink, and M. Kotani (Plenum, New York), pp. 673–676.

Kandel, E. R., J. H. Schwartz, and T. M. Jessel, 1991, *Principles of Neural Science,* 3rd ed. (Elsevier, Amsterdam).

Karhu, J., R. Hari, M. Kajola, E. Mervaala, and R. Paetau, 1992, "Cortical reactivity in patients with progressive myoclonic epilepsy," Neurology **42**, Suppl. 3, 353.

Karhu, J., R. Hari, S.-T. Lu, R. Paetau, and J. Rif, 1991, "Cerebral magnetic fields to lingual stimulation," Electroencephalogr. Clin. Neurophysiol. **80**, 459–468.

Karhu, J., R. Hari, J. Mäkelä, J. Huttunen, and J. Knuutila, 1992, "Somatosensory evoked magnetic fields in multiple sclerosis," Electroencephalogr. Clin. Neurophysiol. **83**, 192–200.

Katila, T. E., 1983, "On the current multipole presentation of the primary current distributions," Nuovo Cimento D **2**, 660–664.

Kaufman, L., B. Schwartz, C. Salustri, and S. J. Williamson, 1990, "Modulation of spontaneous brain activity during mental imagery," J. Cogn. Neurosci. **2**, 124–132.

Kaufman, L., and S. J. Williamson, 1987, "Recent developments in neuromagnetism," in *Evoked Potentials III: The Third International Evoked Potentials Symposium,* edited by C. Barber and T. Blum (Butterworth, Boston), pp. 100–113.

Kaukoranta, E., M. Hämäläinen, J. Sarvas, and R. Hari, 1986, "Mixed and sensory nerve stimulations activate different cytoarchitechtonic areas in the human primary somatosensory cortex SI," Exp. Brain Res. **63**, 60–66.

Kaukoranta, E., R. Hari, M. Hämäläinen, and J. Huttunen, 1986, "Cerebral magnetic fields evoked by peroneal nerve stimulation," Somatosens. Res. **3**, 309–321.

Kaukoranta, E., R. Hari, and O. V. Lounasmaa, 1987, "Responses of the human auditory cortex to vowel onset after fricative consonants," Exp. Brain Res. **69**, 19–23.

Kawasaki, M., P. Chaudhari, T. Newman, and A. Gupta, 1992, "Sub-micron $YBa_2Cu_3O_{7-\delta}$ grain boundary junction dc SQUID's," in *Superconducting Devices and Their Applications,* Springer Proceedings in Physics, Vol. 64, edited by H. Koch and H. Lübbig (Springer, Berlin), pp. 150–154.

Kelhä, V. O., J. M. Pukki, R. S. Peltonen, A. J. Penttinen, R. J.

Ilmoniemi, and J. J. Heino, 1982, "Design, construction, and performance of a large-volume magnetic shield," IEEE Trans. Magn. **MAG-18**, 260–270.

Kemppainen, P. K., and R. J. Ilmoniemi, 1989, "Channel capacity of multichannel magnetometers," in *Advances in Biomagnetism,* edited by S. J. Williamson, M. Hoke, G. Stroink, and M. Kotani (Plenum, New York), pp. 635–638.

Kessler, R. M., C. L. Partain, R. R. Price, and E. James, 1987, "Positron emission tomography: Prospects for clinical utility," Invest. Radiol. **22**, 529–537.

Ketchen, M. B., 1985, "Design of improved integrated thin-film planar dc SQUID gradiometers," J. Appl. Phys. **58**, 4322–4325.

Ketchen, M. B., 1987, "Integrated thin-film dc SQUID sensors," IEEE Trans. Magn. **MAG-23**, 1650–1657.

Ketchen, M. B., 1991, "Design considerations for dc SQUIDs fabricated in deep submicron technology," IEEE Trans. Magn. **27**, 2916–2919.

Ketchen, M. B., 1992, "Design and fabrication considerations for extending integrated dc SQUIDs to the deep sub-micron regime," in *Superconducting Devices and Their Applications,* Springer Proceedings in Physics, Vol. 64, edited by H. Koch and H. Lübbig (Springer, Berlin), pp. 256–264.

Ketchen, M. B., M. Bhushan, S. B. Kaplan, and W. J. Gallagher, 1991, "Low noise dc SQUIDs fabricated in Nb-$Al_2O_3$-Nb trilayer technology," IEEE Trans. Magn. **27**, 3005–3008.

Ketchen, M. B., W. M. Goubau, J. Clarke, and G. B. Donaldson, 1978, "Superconducting thin-film gradiometer," J. Appl. Phys. **49**, 4111–4116.

Ketoja, J. A., J. Kurkijärvi, and R. K. Ritala, 1984a, "Instabilities and chaotic solutions of the current biased dc superconducting quantum interference device," Phys. Rev. B **30**, 3757–3764.

Ketoja, J. A., J. Kurkijärvi, and R. K. Ritala, 1984b, "Tangential bifurcation and critical indices in a Josephson junction," Phys. Lett. A **105**, 425–428.

Knoll, G. F., 1983, "Single-photon emission computed tomography," Proc. IEEE **71**, 320–329.

Knuutila, J., S. Ahlfors, A. Ahonen, J. Hällström, M. Kajola, O. V. Lounasmaa, V. Vilkman, and C. Tesche, 1987, "Large-area low-noise seven-channel dc SQUID magnetometer for brain research," Rev. Sci. Instrum. **58**, 2145–2156.

Knuutila, J., A. I. Ahonen, M. S. Hämäläinen, R. J. Ilmoniemi, and M. J. Kajola, 1985, "Design considerations for multichannel SQUID magnetometers, in *SQUID '85: Superconducting Quantum Interference Devices and their Applications,* edited by H. D. Hahlbohm and H. Lübbig (Walter de Gruyter, Berlin), pp. 939–944.

Knuutila, J. E. T., A. I. Ahonen, M. S. Hämäläinen, M. J. Kajola, P.O. Laine, O. V. Lounasmaa, L. T. Parkkonen, J. T. A. Simola, and C. D. Tesche, 1993, "A 122-channel whole cortex SQUID system for measuring the brain's magnetic fields," IEEE Trans. Magn. (submitted).

Knuutila, J., A. Ahonen, and C. Tesche, 1987, "Effects on dc SQUID characteristics of damping of input coil resonances," J. Low Temp. Phys. **68**, 269–284.

Knuutila, J., and M. S. Hämäläinen, 1988, "Characterization of brain noise using a high sensitivity 7-channel magnetometer," in *Biomagnetism '87,* edited by K. Atsumi, M. Kotani, S. Ueno, T. Katila, and S. J. Williamson (Tokyo Denki University, Tokyo), pp. 186–189.

Knuutila, J., and M. S. Hämäläinen, 1989, "On the spatial locating accuracy of multichannel magnetometers," in *Advances in Biomagnetism,* edited by S. J. Williamson, M. Hoke, G. Stroink, and M. Kotani (Plenum, New York), pp. 713–716.

Knuutila, J., M. Kajola, H. Seppä, R. Mutikainen, and J. Salmi, 1988, "Design, optimization, and construction of a DC SQUID with complete flux transformer circuits," J. Low Temp. Phys. **71**, 369–392.

Koch, H., 1989, "SQUID sensors," in *Magnetic Sensors,* Vol. 5 of *Sensors—A Comprehensive Survey,* edited by W. Göpel, J. Hesse, and J. N. Zemel (VCH Verlagsgesellschaft, Weinheim), pp. 381–445.

Koch, H., R. Cantor, D. Drung, S. N. Erné, K. P. Matthies, M. Peters, T. Ryhänen, H. J. Scheer, and H. D. Hahlbohm, 1991, "A 37 channel dc SQUID magnetometer system," IEEE Trans. Magn. **27**, 2793–2796.

Koch, R. H., J. Clarke, W. M. Goubau, J. M. Martinis, C. M. Pegrum, and D. J. van Harlingen, 1983, "Flicker ($1/f$) noise in tunnel junction dc SQUIDs," J. Low Temp. Phys. **51**, 207–224.

Koch, H. and H. Lübbig, 1992, Eds., *"Superconducting Devices and Their Applications,"* Springer Proceedings in Physics, Vol. 64 (Springer, Berlin).

Kohonen, T., 1988, "An introduction to neural computing," Neural Networks **1**, 3–16.

Kohonen, T., 1990, "The self-organizing map," Proc. IEEE **78**, 1464–1480.

Kraut, M., J. C. Arezzo, and H. G. Vaughan, 1985, "Intracortical generators of the flash VEP in monkeys," Electroencephalogr. Clin. Neurophysiol. **62**, 300–312.

Kroger, H., L. N. Smith, and D. W. Jillie, 1981, "Selective niobium anodization process for fabricating Josephson tunnel junctions," Appl. Phys. Lett. **39**, 280–282.

Kuffler, S. W., J. G. Nicholls, and A. R. Martin, 1984, *From Neuron to Brain,* 2nd ed. (Sinauer Associates, Sunderland).

Kullmann, W., and W. J. Dallas, 1987, "Fourier imaging of electrical currents in the human brain from their magnetic fields," IEEE Trans. Biomed. Eng. **BME-34**, 837–842.

Kuriki, S., M. Matsuda, and A. Matachi, 1988, "Effects of alternating bias current on the low-frequency noise in dc SQUIDs," J. Appl. Phys. **64**, 239–241.

Lauterbur, P. C., 1973, "Image formation by induced local interactions: Examples employing nuclear magnetic resonance," Nature **242**, 190–191.

Leinonen, L., and S.-L. Joutsiniemi, 1989, "Auditory evoked potentials and magnetic fields in patients with lesions of the auditory cortex," Acta Neurol. Scand. **79**, 316–325.

Lounasmaa, O. V., 1974, *Experimental Principles and Methods Below 1K* (Academic, London).

Loveless, N., R. Hari, M. Hämäläinen, and J. Tiihonen, 1989, "Evoked responses of human auditory cortex may be enhanced by preceding stimuli," Electroencephalogr. Clin. Neurophysiol. **74**, 217–227.

Lu, S.-T., M. S. Hämäläinen, R. Hari, R. J. Ilmoniemi, O. V. Lounasmaa, M. Sams, and V. Vilkman, 1991, "Seeing faces activates three separate areas outside the occipital visual vortex in man," Neurosci. **43**, 287–290.

Lu, S.-T., M. Kajola, S.-L. Joutsiniemi, J. Knuutila, and R. Hari, 1992, "Generator sites of spontaneous MEG-activity during sleep," Electroencephalogr. Clin. Neurophysiol. **82**, 182–196.

Lü, Z.-L., S. J. Williamson, and L. Kaufman, 1992, "Human auditory primary and association cortex have differing lifetimes for activation traces," Brain Res. **572**, 236–241.

Lueck, C. J., S. Zeki, K. J. Friston, M.-P. Deiber, P. Cope, V. J. Cunningham, A. A. Lammertsma, C. Kennard, and R. S. J. Frackowiak, 1989, "The colour centre in the cerebral cortex of

man," Nature **340**, 386–389.

Lynn, M. S., and W. P. Timlake, 1968, "The use of multiple deflations in the numerical solution of singular systems of equations with applications to potential theory," SIAM J. Numer. Anal. **5**, 303–322.

Maclin, E., Y. C. Okada, L. Kaufman, and S. J. Williamson, 1983, "Retinotopic map on the visual cortex for eccentrically placed patterns: First noninvasive measurement," Nuovo Cimento D **2**, 410–419.

Mager, A., 1981, "The Berlin magnetically shielded room (BMSR), Section A: Design and construction," in *Biomagnetism,* edited by S. N. Erné, H.-D. Hahlbohm, and H. Lübbig (Walter de Gruyter, Berlin), pp. 51–78.

Mäkelä, J. P., and R. Hari, 1992, "Neuromagnetic auditory evoked responses after a stroke in the right temporal lobe," NeuroReport **3**, 94–96.

Mäkelä, J. P., R. Hari, and L. Leinonen, 1988, "Magnetic responses of the human auditory cortex to noise/square wave transitions," Electroencephalogr. Clin. Neurophysiol. **69**, 423–430.

Mäkelä, J. P., R. Hari, and A. Linnankivi, 1987, "Different analysis of frequency and amplitude modulations of a continuous tone in the human auditory cortex: A neuromagnetic study," Hearing Res. **27**, 257–264.

Mäkelä, J., R. Hari, L. Valanne, and A. Ahonen, 1991, "Auditory evoked magnetic fields after ischemic brain lesions," Ann. Neurol. **30**, 76–82.

Malmivuo, J., 1976, *On the Detection of the Magnetic Heart Vector—An Application of the Reciprocity Theorem,* Acta Polytechnica Scandinavica, Electrical Engineering Series No. 39 (The Finnish Academy of Technical Sciences, Helsinki).

Malmivuo, J., P. Heinonen, M. Tuomola, and J. Lekkala, 1981, "Thick-walled conducting shield in biomagnetic experiments," in *Biomagnetism,* edited by S. N. Erné, H.-D. Hahlbohm, and H. Lübbig (Walter de Gruyter, Berlin), pp. 107–112.

Maniewski, R., I. Derka, T. Katila, T. Ryhänen, and M. Seppänen, 1985, "DC-SQUID system for high-resolution biomagnetic measurements," Med. Biol. Eng. Comput. Suppl. 23, Part 1, 9–10.

Marquardt, D. W., 1963, "An algorithm for least-squares estimation of nonlinear parameters," J. Soc. Ind. Appl. Math. **11**, 431–441.

Matsuba, H., D. Irisawa, and A. Yahara, 1992, "Superconducting shield for biomagnetism measurements coupled with ferro-magnetic," *Biomagnetism: Clinical Aspects,* edited by M. Hoke, S. N. Erné, Y. C. Okada, and G. L. Romani (Elsevier, Amsterdam), pp. 863–868.

McCumber, D. E., 1968, "Effect of ac impedance on dc voltage-current characteristics of superconductor and weak-link junctions," J. Appl. Phys. **39**, 3113–3118.

McEvoy, L., R. Hari, T. Imada, and M. Sams, 1993, "Human auditory cortical mechanisms of sound lateralization. II. Directional selectivity," Hearing Res. (in press).

McGurk, H., and J. MacDonald, 1976, "Hearing lips and seeing voices," Science **264**, 746–748.

Meijs, J., 1988, "The influence of head geometries on electro- and magnetoencephalograms," Ph.D. thesis (University of Twente, The Netherlands).

Meijs, J. W. H., F. G. C. Bosch, M. J. Peters, and F. H. L. da Silva, 1987, "On the magnetic field distribution generated by a dipolar current source situated in a realistically shaped compartment model of the head," Electroencephalogr. Clin. Neurophysiol. **66**, 286–298.

Meijs, J. W. H., M. J. Peters, A. van Oosterom, and H. B. K. Boom, 1987, "The application of the Richardson extrapolation in simulation series of EEG's," Med. Biol. Eng. Comput. **25**, 222–226.

Modena, I., G. B. Ricci, S. Barbanera, R. Leoni, G. L. Romani, and P. Carelli, 1982, "Biomagnetic measurements of spontaneous brain activity in epileptic patients," Electroencephalogr. Clin. Neurophysiol. **54**, 622–628.

Montgomery, W. D., 1964, "The gradient in the sampling of $N$-dimensional band-limited functions," J. Electron. Control **17**, 437–447.

Montonen, J., J. Nenonen, J.-P. Hovi, M. Leiniö, and T. Katila, 1992, "Evaluation and reduction of the thermal noise of a biomagnetic measurement dewar," in *Advances in Biomagnetism '91: Clinical Aspects,* edited by M. Hoke, S. N. Erné, Y. C. Okada, and G. L. Romani (Elsevier, Amsterdam), in press.

Mosher, J. C., P. S. Lewis, and R. Leahy, 1992, "Multiple dipole modeling and localization from spatio-temporal MEG data," IEEE Trans. Biomed. Eng. **39**, 541–557.

Mosher, J. C., P. S. Lewis, R. Leahy, and M. Singh, 1990, "Multiple dipole modeling of spatio-temporal MEG data," in *Digital Image Synthesis and Inverse Optics,* Proc. SPIE 1351, edited by A. F. Gmitro, P. S. Idell, and I. J. LaHaie (SPIE International Society for Optical Engineering, Bellingham), pp. 364–375.

Muhlfelder, B., J. A. Beall, M. W. Cromar, and R. H. Ono, 1986, "Very low noise, tightly coupled, dc SQUID amplifiers," Appl. Phys. Lett. **49**, 1118–1120.

Muhlfelder, B., J. A. Beall, M. W. Cromar, R. H. Ono, and W. W. Johnson, 1985, "Well coupled, low noise, dc SQUIDs," IEEE Trans. Magn. **MAG-21**, 427–429.

Näätänen, R., 1984, "In search for short-duration memory trace of a stimulus in the human brain," in *Human Action and Personality,* edited by L. Pulkkinen and P. Lyytinen (University of Jyväskylä, Finland), pp. 22–36.

Näätänen, R., 1990, "The role of attention in auditory information processing as revealed by event-related potentials and other brain measures of cognitive function," Behav. Brain Sci. **13**, 201–288.

Näätänen, R., 1992, "Attention and Brain Function" (Lawrence Erlbaum, Hillsdale).

Näätänen, R., and T. Picton, 1987, "The $N1$ wave of the human electric and magnetic response to sound: a review and analysis of the component structure," Psychophysiology **84**, 375–425.

Nakanishi, M., M. Koyanagi, S. Kosaka, A. Shoji, M. Aoyagi, and F. Shinoki, 1987, "Integrated dc-SQUID magnetometer," Jpn. J. Appl. Phys. **26**, 1050–1055.

Narici, L., V. Pizzella, G. L. Romani, G. Torrioli, R. Traversa, and P. M. Rossini, 1990, "Evoked $\alpha$- and $\mu$-rhythm in humans: a neuromagnetic study," Brain Res. **520**, 222–231.

Nenonen, J., and T. Katila, 1988, "Thermal noise in a magnetically shielded room," in *Biomagnetism '87,* edited by K. Atsumi, M. Kotani, S. Ueno, T. Katila, and S. J. Williamson (Tokyo Denki University, Tokyo), pp. 426–429.

Nenonen, J., and T. Katila, 1991a, "Noninvasive functional localization by biomagnetic methods, part I," J. Clin. Eng. **16**, 423–434.

Nenonen, J., and T. Katila, 1991b, "Noninvasive functional localization by biomagnetic methods, part II," J. Clin. Eng. **16**, 495–503.

Nenonen, J., T. Katila, and J. Montonen, 1989, "Thermal noise of a biomagnetic measurement dewar," in *Advances in Biomagnetism,* edited by S. J. Williamson, M. Hoke, G. Stroink, and M. Kotani (Plenum, New York), pp. 729–732.

Nenonen, J., C. J. Purcell, B. M. Horacek, G. Stroink, and T.

Katila, 1991, "Magnetocardiographic functional localization using a current dipole in a realistic torso," IEEE Trans. Biomed. Eng. **38**, 658–664.

Netzer, Y., 1974, "A new interpretation of noise reduction by matching," Proc. IEEE **62**, 404–406.

Netzer, Y., 1981, "The design of low-noise amplifiers," Proc. IEEE **69**, 728–741.

Nicolas, P., D. Duret, D. Teszner, and T. Tuomisto, 1983, "Neuromagnetic measurements at hospital: Instrumentation and preliminary tests," Nuovo Cimento D2, 184–194.

Niedermeyer, E., 1982, "Depth electroencephalography," in *Electroencephalography. Basic Principles, Clinical Applications and Related Fields,* edited by E. Niedermeyer and F. Lopes da Silva (Urban & Schwarzenberg, Baltimore/Munich), pp. 519–536.

Nyquist, H., 1928, "Thermal agitation of electric charge in conductors," Phys. Rev. **32**, 110–113.

Ogawa, S., D. W. Tank, R. Menon, J. M. Ellermann, S.-G. Kim, H. Merkle, and K. Ugurbil, 1992, "Intrinsic signal changes accompanying sensory stimulation: Functional brain mapping with magnetic resonance imaging," Proc. Natl. Acad. Sci. USA **89**, 5951–5955.

Ohta, H., M. Takahata, Y. Takahashi, K. Shinada, Y. Yamada, T. Hanasaka, Y. Uchikawa, M. Kotani, T. Matsui, and B. Komiyama, 1989, "Seven-channel rf SQUID with $1/f$ noises only at very low frequencies," IEEE Trans. Magn. **25**, 1018–1021.

Okada, Y., 1985, "Discrimination of localized and distributed current dipole sources and localized single and multiple sources," in *Biomagnetism: Applications & Theory,* edited by H. Weinberg, G. Stroink, and T. Katila (Pergamon, New York), pp. 266–272.

Okada, Y. C., R. Tanenbaum, S. J. Williamson, and L. Kaufman, 1984, "Somatotopic organization of the human somatosensory cortex revealed by neuromagnetic measurements," Exp. Brain Res. **56**, 197–205.

Oostendorp, T. F., and A. van Oosterom, 1989, "Source parameter estimation in inhomogeneous volume conductors of arbitrary shape," IEEE Trans. Biomed. Eng. **36**, 382–391.

Paetau, R., M. Kajola, and R. Hari, 1990, "Magnetoencephalography in the study of epilepsy," Neurophysiologie Clinique **20**, 169–187.

Paetau, R., M. Kajola, J. Karhu, U. Nousiainen, J. Partanen, J. Tiihonen, M. Vapalahti, and R. Hari, 1992, "MEG localization of epileptic cortex—impact on surgical treatment," Ann. Neurol. **32**, 106–109.

Paetau, R., M. Kajola, M. Korkman, M. Hämäläinen, M.-L. Granström, and R. Hari, 1991, "Landau-Kleffner syndrome: epileptic activity in the auditory cortex," NeuroReport **2**, 201–204.

Palfreyman, N. M., K. D. Singh, and S. J. Swithenby, 1989, "Rule-based location of multiple current-dipole sources from biomagnetic data," in *Advances in Biomagnetism,* edited by S. J. Williamson, M. Hoke, G. Stroink, and M. Kotani (Plenum, New York), pp. 567–570.

Pantev, C., M. Hoke, K. Lehnertz, B. Lütkenhöner, G. Anogianakis, and W. Wittkowski, 1988, "Tonotopic organization of the human auditory cortex revealed by transient auditory evoked magnetic fields," Electroencephalogr. Clin. Neurophysiol. **69**, 160–170.

Pantev, C., M. Hoke, K. Lehnertz, B. Lütkenhöner, G. Fahrendorf, and U. Stöber, 1990, "Identification of sources of brain neuronal activity with high spatiotemporal resolution through combination of neuromagnetic source localization (NMSL) and magnetic resonance imaging (MRI)," Electroencephalogr. Clin. Neurophysiol. **75**, 173–184.

Pantev, C., M. Hoke, B. Lütkenhöner, K. Lehnertz, and W. Kumpf, 1989, "Tinnitus remission objectified by neuromagnetic measurements," Hearing Res. **40**, 261–264.

Pantev, C., S. Makeig, M. Hoke, R. Galambos, S. Hampson, and C. Gallen, 1991, "Human auditory evoked gamma-band magnetic fields," Proc. Natl. Acad. Sci. USA **88**, 8996–9000.

Pechura, C. M., and J. B. Martin, 1991, Eds., *Mapping the Brain and its Functions* (National Academy, Washington, DC).

Pelizzone, M., R. Hari, J. Mäkelä, E. Kaukoranta, and P. Montandon, 1987, "Cortical activity evoked by a multichannel cochlear prosthesis," Acta Otolaryngol. **103**, 632–636.

Penfield, W., and H. Jasper, 1954, *Epilepsy and the Functional Anatomy of the Human Brain* (Little, Brown, Boston).

Penfield, W., and T. Rasmussen, 1950, *The Cerebral Cortex of Man* (MacMillan, New York).

Petersen, D. P., and D. Middleton, 1962, "Sampling and reconstruction of wave-number-limited functions in $N$-dimensional Euclidean spaces," Inf. Control. **5**, 279–323.

Petersen, D. P., and D. Middleton, 1964, "Reconstruction of multidimensional stochastic fields from discrete measurements of amplitude and gradient," Inf. Control. **7**, 445–476.

Press, W. H., B. P. Flannery, S. A. Teukolsky, and W. T. Vetterling, 1992, *Numerical Recipes in C,* 2nd ed. (Cambridge University, Cambridge).

Raider, S. I., 1985, "Josephson tunnel junctions with refractory electrodes," IEEE Trans. Magn. **MAG-21**, 110–117.

Rechtschaffen, A., and A. Kales, 1968, "A manual of standardized terminology, techniques and scoring system for sleep stages in human subjects" (U.S. GPO, Washington, DC).

Ribary, U., A. A. Ioannides, K. D. Singh, R. Hasson, J. P. R. Bolton, F. Lado, A. Mogilner, and R. Llinás, 1991, "Magnetic field tomography of coherent thalamo cortical 40-Hz oscillations in humans," Proc. Natl. Acad. Sci. USA **88**, 11037–11041.

Richardson, L. F., and J. A. Guant, 1927, "The deferred approach to the limit," Philos. Trans. R. Soc. London **226**, 299–361.

Rif, J., R. Hari, M. S. Hämäläinen, and M. Sams, 1991, "Auditory attention affects two different areas in the human supratemporal cortex," Electroencephalogr. Clin. Neurophysiol. **79**, 464–472.

Rillo, C., D. Veldhuis, and J. Flokstra, 1987, "Optimization of the dynamic behavior of a SQUID system using an electronic simulation," IEEE Trans. Instrum. Meas. **IM-36**, 770–775.

Robinson, S. E., 1989, "Environmental noise cancellation for biomagnetic measurements," in *Advances in Biomagnetism,* edited by S. J. Williamson, M. Hoke, G. Stroink, and M. Kotani (Plenum, New York), pp. 721–724.

Rogers, C. T., R. A. Buhrman, W. J. Gallagher, S. I. Raider, A. W. Kleinsasser, and R. L. Sandstrom, 1987, "Electron trap states and low frequency noise in tunnel junctions," IEEE Trans. Magn. **MAG-23**, 1658–1661.

Roland, P. E., E. Skinhøj, and N. A. Lassen, 1981, "Focal activations of human cerebral cortex during auditory discrimination," J. Neurophysiol. **45**, 1139–1151.

Romani, G. L., R. Leoni, and C. Salustri, 1985, "Multichannel instrumentation for biomagnetism," in *SQUID '85: Superconducting Quantum Interference Devices and their Applications,* edited by H. D. Hahlbohm and H. Lübbig (Walter de Gruyter, Berlin), pp. 919–932.

Romani, G. L., and L. Narici, 1986, "Principles and clinical validity of the biomagnetic method," Med. Progr. Technol. **11**,

123–159.
Romani, G. L., and S. J. Williamson, 1983, Eds., *Proceedings of the Fourth International Workshop on Biomagnetism* (Nuovo Cimento D **2**, 121–664).
Romani, G. L., S. J. Williamson, and L. Kaufman, 1982a, "Biomagnetic instrumentation," Rev. Sci. Instrum. **53**, 1815–1845.
Romani, G. L., S. J. Williamson, and L. Kaufman, 1982b, "Tonotopic organization of the human auditory cortex," Science **216**, 1339–1340.
Rose, D. F., P. D. Smith, and S. Sato, 1987, "Magnetoencephalography and epilepsy research," Science **238**, 329–335.
Roth, B. J., and J. P. Wikswo, Jr., 1985, "The magnetic field of a single axon," Biophys. J. **48**, 93–109.
Roth, M., J. Shaw, and J. Green, 1956, "The form, voltage distribution and physiological significance of the K-complex," Electroencephalogr. Clin. Neurophysiol. **8**, 385–402.
Ryhänen, T., R. Cantor, D. Drung, and H. Koch, 1991, "Practical low-noise integrated dc superconducting quantum interference device magnetometer with additional positive feedback," Appl. Phys. Lett. **59**, 228–230.
Ryhänen, T., R. Cantor, D. Drung, H. Koch, and H. Seppä, 1991, "Effect of parasitic capacitance on dc SQUID performance," IEEE Trans. Magn. **27**, 3013–3016.
Ryhänen, T., and H. Seppä, 1992, "Effect of parasitic capacitance and inductance on the dynamics and noise of dc superconducting quantum interference devices," J. Appl. Phys. **71**, 6150–6166.
Ryhänen, T., H. Seppä, R. Ilmoniemi, and J. Knuutila, 1989, "SQUID magnetometers for low-frequency applications," J. Low Temp. Phys. **76**, 287–386.
Sams, M., R. Aulanko, M. Hämäläinen, R. Hari, O. V. Lounasmaa, S.-T. Lu, and J. Simola, 1991, "Seeing speech: visual information from lip movements modifies activity in the human auditory cortex," Neurosci. Lett. **127**, 141–145.
Sams, M., M. Hämäläinen, R. Hari, and L. McEvoy, 1993, "Human auditory cortical mechanisms of sound lateralization. I. Response to changes in interaural time difference," Hearing Res. (in press).
Sams, M., R. Hari, J. Rif, and J. Knuutila, 1993, "The human auditory sensory memory trace persists about 10 s: neuromagnetic evidence," J. Cogn. Neurosci. (in press).
Sams, M., E. Kaukoranta, M. Hämäläinen, and R. Näätänen, 1991, "Cortical activity elicited by changes in auditory stimuli: Different sources for the magnetic N100m and mismatch responses," Psychophysiology **28**, 21–29.
Sarvas, J., 1987, "Basic mathematical and electromagnetic concepts of the biomagnetic inverse problem," Phys. Med. Biol. **32**, 11–22.
Sato, S., 1990, Ed., *Magnetoencephalography,* Vol. 54 (Raven, New York).
Scherg, M., 1990, "Fundamentals of dipole source potential analysis," in *Auditory Evoked Magnetic Fields and Electric Potentials,* Vol. 6 of *Advances of Audiology,* edited by F. Grandori, M. Hoke, and G. L. Romani (Karger, Basel), pp. 40–69.
Scherg, M., R. Hari, and M. Hämäläinen, 1989, "Frequency-specific sources of the auditory N19-P30-P50 response detected by a multiple source analysis of evoked magnetic fields and potentials," in *Advances in Biomagnetism,* edited by S. J. Williamson, M. Hoke, G. Stroink, and M. Kotani (Plenum, New York), pp. 97–100.
Schmidt, R. O., 1986, "Multiple emitter location and signal parameter estimation," IEEE Trans. Antennas Propag. **AP-34**, 276–280.
Schneider, S., K. Abraham-Fuchs, G. Daalmans, W. Folberth, H. E. Hoenig, H. Reichenberger, G. Röhrlein, H. Seifert, and A. Wirth, 1989, "Development and performance of a multichannel system for studies of biomagnetic signals of brain and heart," in *Advances in Biomagnetism,* edited by S. J. Williamson, M. Hoke, G. Stroink, and M. Kotani (Plenum, New York), pp. 669–672.
Scott, A. C., 1977, *Neurophysics* (Wiley, New York).
Seppä, H., 1987, "Influence of the signal coil on dc-SQUID dynamics," IEEE Trans. Magn. **MAG-23**, 1083–1086.
Seppä, H., 1992, "Dc-SQUID electronics based on adaptive noise cancellation and high open-loop gain controller," in *Superconducting Devices and Their Applications,* Springer Proceedings in Physics, Vol. 64, edited by H. Koch and H. Lübbig (Springer, Berlin), pp. 346–350.
Seppä, H., A. Ahonen, J. Knuutila, J. Simola, and V. Vilkman, 1991, "Dc-SQUID electronics based on adaptive positive feedback: Experiments," IEEE Trans. Magn. **27**, 2488–2490.
Seppä, H., M. Kiviranta, A. Satrapinski, L. Grönberg, J. Salmi, and I. Suni, 1993, "A coupled DC SQUID with low $1/f$ noise," IEEE Trans. Magn. (in press).
Seppä, H., and H. Sipola, 1990, "A high open-loop gain controller," Rev. Sci. Instrum. **61**, 2449–2451.
Shirae, K., H. Furukawa, M. Katayama, and T. Katayama, 1988, "Proposal of multichannel SQUID amplifiers for biomagnetic measurement," in *Biomagnetism '87,* edited by K. Atsumi, M. Kotani, S. Ueno, T. Katila, and S. J. Williamson (Tokyo Denki University, Tokyo), pp. 470–473.
Silvey, S. O., 1978, *Statistical Inference* (Chapman and Hall, London).
Simmonds, M., 1980, "Ac biasing of a dc SQUID," U.S. Patent No. 4389612.
Stefan, H., S. Schneider, K. Abraham-Fuchs, J. Bauer, H. Feistel, U. Neubauer, and W. J. Huk, 1989, "Application of a multichannel MEG-system in temporal lobe epilepsy," in *Advances in Biomagnetism,* edited by S. J. Williamson, M. Hoke, G. Stroink, and M. Kotani (Plenum, New York), pp. 279–282.
Stehling, M. K., R. Turner, and P. Mansfield, 1991, "Echo-planar imaging: Magnetic resonance imaging in a fraction of a second," Science **254**, 43–50.
Stewart, W. C., 1968, "Current-voltage characteristics of Josephson junctions," Appl. Phys. Lett. **12**, 277–280.
Stok, C. J., 1987, "The influence of model parameters on EEG/MEG single dipole source estimation," IEEE Trans. Biomed. Eng. **BME-34**, 289–296.
Stroink, G., B. Blackford, B. Brown, and M. Horacek, 1981, "Aluminum shielded room for biomagnetic measurements," Rev. Sci. Instrum. **52**, 463–468.
Suk, J., J. Cappell, U. Ribary, T. Yamamoto, and R. R. Llinás, 1989, "Magnetic localization of somatically evoked responses in the human brain," in *Advances in Biomagnetism,* edited by S. J Williamson, M. Hoke, G. Stroink, and M. Kotani (Plenum, New York), pp. 165–168.
Suk, J., U. Ribary, J. Cappell, T. Yamamoto, and R. Llinás, 1991, "Anatomical localization revealed by MEG recordings of the human somatosensory system," Electroencephalogr. Clin. Neurophysiol. **78**, 185–196.
Supek, S., and C. J. Aine, 1993, "Model order determination and limits of source resolution for multi-source neuromagnetic data: Simulation studies," IEEE Trans. Biomed. Eng. (in press).
Sutherling, W. W., and D. S. Barth, 1989, "Neocortical propagation in temporal lobe spike foci on magnetoencephalography and electroencephalography," Ann. Neurol. **25**, 373–381.

Sutherling, W. W., P. H. Crandall, T. M. Darcey, D. P. Becker, M. F. Levesque, and D. S. Barth, 1988, "The magnetic and electric fields agree with intracranial localizations of somatosensory cortex," Neurology **38**, 1705–1714.

Tarantola, A., 1987, *Inverse Problem Theory* (Elsevier, New York).

Tarantola, A., and B. Valette, 1982, "Inverse problems = quest for information," J. Geophys. **50**, 159–170.

ter Brake, H. J. M., J. Folkstra, W. Jaszczuk, R. Stammis, G. K. van Ancum, A. Martinez, and H. Rogalla, 1991, "The UT 19-channel dc squid based neuromagnetometer," Clin. Phys. Physiol. Meas. **12**, Suppl. B, 45–50.

ter Brake, H. J. M., H. J. Wieringa, and H. Rogalla, 1991, "Improvement of the performance of a $\mu$-metal magnetically shielded room by means of active compensation," Meas. Sci. Technol. **2**, 596–601.

ter-Pogossian, M. M., M. E. Phelps, E. J. Hoffman, and N. A. Mullani, 1975, "A positron emission transaxial tomograph for nuclear medicine imaging (PETT)," Radiology **114**, 89–98.

Tesche, C. D., K. H. Brown, A. C. Callegari, M. M. Chen, J. H. Greiner, H. C. Jones, M. B. Ketchen, K. K. Kim, A. W. Kleinsasser, H. A. Notarys, G. Proto, R. H. Wang, and T. Yogi, 1985, "Practical dc SQUIDs with extremely low $1/f$ noise," IEEE Trans. Magn. **MAG-21**, 1032–1035.

Tesche, C. D., C. C. Chi, C. C. Tsuei, and P. Chaudhari, 1983, "Inductive monopole detector employing planar high order superconducting gradiometer coils," Appl. Phys. Lett. **43**, 384–386.

Tesche, C. D., and J. Clarke, 1977, "Dc SQUID: Noise and optimization," J. Low Temp. Phys. **29**, 301–331.

Teyler, T. J., B. N. Cuffin, and D. Cohen, 1985, "The visual evoked magnetoencephalogram," Life Sci. **17**, 683–692.

Thomas, T., and D. Duret, 1988, "High resolution single channel neuromagnetometry and minimal approach for multichannel systems," Cryogenics **28**, 783–795.

Thompson, R. F., 1985, *The Brain—An Introduction to Neuroscience* (Freeman, New York).

Tiihonen, J., R. Hari, M. Kajola, J. Karhu, S. Ahlfors, and S. Tissari, 1991, "Magnetoencephalographic 10-Hz rhythm from the human auditory cortex," Neurosci. Lett. **129**, 303–305.

Tiihonen, J., R. Hari, M. Kajola, U. Nousiainen, and M. Vapalahti, 1990, "Localization of epileptic foci using a large-area magnetometer and functional brain anatomy," Ann. Neurol. **27**, 283–290.

Tiihonen, J., M. Kajola, and R. Hari, 1989, "Magnetic mu rhythm in man," Neurosci. **32**, 793–800.

Torrioli, G., S. Casciardi, C. Del Gratta, V. Foglietti, W. J. Gallagher, M. B. Ketchen, A. W. Kleinsasser, A. Pasquarelli, V. Pizzella, G. L. Romani, and R. L. Sandstrom, 1992, "28 channel hybrid neuromagnetometer," in *Biomagnetism: Clinical Aspects,* edited by M. Hoke, S. N. Erné, Y. C. Okada, and G. L. Romani (Elsevier, Amsterdam), pp. 843–846.

Tripp, J. H., 1983, "Physical concepts and mathematical models," in *Biomagnetism: An Interdisciplinary Approach,* edited by S. J. Williamson, G.-L. Romani, L. Kaufman, and I. Modena (Plenum, New York), pp. 101–139.

Tuomisto, T., R. Hari, T. Katila, T. Poutanen, and T. Varpula, 1983, "Studies of auditory evoked magnetic and electric responses: Modality specificity and modelling," Nuovo Cimento D **2**, 471–483.

Urankar, L., 1990, "Common compact analytical formulas for computation of geometry integrals on a basic Cartesian subdomain in boundary and volume integral methods," Eng. Anal. Boundary Elements **7**, 124–129.

van den Noort, S., P. Altrocchi, M. F. Brin, J. Ferguson, J. Greenberg, L. Jacobs, F. Kittredge, C. Markham, M. Nuwer, and R. Tindall, 1992, "Assessment: Magnetoencephalography (MEG). Report of the therapeutics and technology assessment subcommittee of the American Academy of Neurology."

van Hulsteyn, D. B., L. McGavran, L. Heller, J. George, P. Medvick, and E. Flynn, 1989, "The LANL gradiometer orientation device," in *Advances in Biomagnetism,* edited by S. J. Williamson, M. Hoke, G. Stroink, and M. Kotani (Plenum, New York), pp. 689–692.

van Nieuwenhuyzen, G. J., and V. J. de Waal, 1985, "Second order gradiometer and dc SQUID integrated on a planar substrate," Appl. Phys. Lett. **46**, 439–443.

van Oosterom, A., and J. Strackee, 1983, "The solid angle of a plane triangle," IEEE Trans. Biomed. Eng. **BME-30**, 125–126.

Varpula, T., and T. Poutanen, 1984, "Magnetic field fluctuations arising from thermal motion of electric charge in conductors," J. Appl. Phys. **55**, 4015–4021.

Vieth, J., 1990, "Magnetoencephalography in the study of stroke (cerebrovascular accident)," in *Magnetoencephalography,* Vol. 54 of *Advances in Neurology,* edited by S. Sato (Raven, New York), pp. 261–269.

Vladimirov, V. S., 1971, *Equations of Mathematical Physics* (Marcel Dekker, New York).

Vrba, J., K. Betts, M. Burbank, T. Cheung, A. A. Fife, G. Haid, P. R. Kubik, S. Lee, J. McCubbin, J. McKay, D. McKenzie, P. Spear, B. Taylor, M. Tillotson, D. Cheyne, and H. Weinberg, 1993, "Whole cortex, 64 channel SQUID biomagnetometer system," IEEE Trans. Magn. (in press).

Vrba, J., A. A. Fife, M. B. Burbank, H. Weinberg, and P. A. Brickett, 1982, "Spatial discrimination in SQUID gradiometers and 3rd order gradiometer performance," Can. J. Phys. **60**, 1060–1073.

Vrba, J., G. Haid, S. Lee, B. Taylor, A. A. Fife, P. Kubik, J. McCubbin, and M. B. Burbank, 1991, "Biomagnetometers for unshielded and well shielded environments," Clin. Phys. Physiol. Meas. **12**, Suppl. B **81-86**,

Vrba, J., J. McCubbin, S. Lee, A. A. Fife, and M. B. Burbank, 1989, "Noise cancellation in biomagnetometers," in *Advances in Biomagnetism,* edited by S. J. Williamson, M. Hoke, G. Stroink, and M. Kotani (Plenum, New York), pp. 733–736.

Vvedensky, V. L., R. J. Ilmoniemi, and M. J. Kajola, 1985, "Study of the alpha rhythm with a 4-channel SQUID magnetometer," Med. Biol. Eng. Comput. 23, Suppl., Part 1, 11–12.

Vvedensky, V. L., S. P. Naurzakov, V. I. Ozhogin, and S. Y. Shabanov, 1985, "Measurement of the tangential component of the magnetic field associated with rhythmic alpha activity in the human brain," in *Biomagnetism: Applications & Theory,* edited by H. Weinberg, G. Stroink, and T. Katila (Pergamon, New York), pp. 57–60.

Wakai, R. T., and D. J. van Harlingen, 1986, "Low-frequency noise and discrete charge trapping in small-area tunnel junction dc SQUID's" Appl. Phys. Lett. **49**, 593–595.

Wang, J.-Z., S. J. Williamson, and L. Kaufman, 1992, "Magnetic source images determined by a lead-field analysis: the unique minimum-norm least-squares estimation," IEEE Trans. Biomed. Eng. **39**, 665–675.

Wax, M., and T. Kailath, 1985, "Detection of signals by information theoretic criteria," IEEE Trans. Acoust. Speech Signal Process. **ASSP-33**, 387–392.

Weinberg, H., G. Stroink, and T. Katila, 1985, Eds., *Biomagnetism: Applications and Theory* (Pergamon, New York).

Weissman, M. B., 1988, "$1/f$ noise and other slow, nonexponential kinetics in condensed matter," Rev. Mod. Phys. **60**,

537–571.
Wellstood, F., C. Heiden, and J. Clarke, 1984, "Integrated DC SQUID magnetometer with a high slew rate," Rev. Sci. Instrum. **55**, 952–957.
Wellstood, F. C., J. J. Kingston, M. J. Ferrari, and J. Clarke, 1991, "Thin-film flux transformers of $YBa_2Cu_3O_{7-x}$," IEEE Trans. Magn. **27**, 2569–2572.
Wellstood, F. C., C. Urbina, and J. Clarke, 1987, "Low-frequency noise in dc superconducting quantum interference devices below 1 K," Appl. Phys. Lett. **50**, 772–774.
Wikswo, J. P., Jr., 1985, "Magnetic measurements on single nerve axons and nerve bundles," Med. Biol. Eng. Comput. **23**, Suppl., Part 1, 3–6.
Wikswo, J. P., Jr., G. S. Abraham, and V. R. Hentz, 1985, "Magnetic assessment of regeneration across a nerve graft," in *Biomagnetism: Applications & Theory,* edited by H. Weinberg, G. Stroink, and T. Katila (Pergamon, New York), pp. 88–92.
Wikswo, J. P., Jr., J. P. Barach, and J. A. Freeman, 1980, "Magnetic field of a nerve impulse: First measurements," Science **208**, 53–55.
Wikswo, J. P., Jr., W. P. Henry, P. C. Samson, and R. P. Giffard, 1985, "Current probe system for measuring cellular action currents," in *Biomagnetism: Applications & Theory,* edited by H. Weinberg, G. Stroink, and T. Katila (Pergamon, New York), pp. 83–87.
Wikswo, J. P., Jr., and B. J. Roth, 1985, "Magnetic measurement of propagating action potentials in isolated, one-dimensional cardiac tissue preparations," in *Biomagnetism: Applications & Theory,* edited by H. Weinberg, G. Stroink, and T. Katila (Pergamon, New York), pp. 121–125.
Williamson, S., 1991, "MEG versus EEG localization test (Letter to the Editor)," Ann. Neurol. **30**, 222.
Williamson, S. J., M. Hoke, G. Stroink, and M. Kotani, 1989, Eds., *Advances in Biomagnetism* (Plenum, New York).
Williamson, S. J., and L. Kaufman, 1981, "Biomagnetism," J. Magn. Magn. Mat. **22**, 129–201.
Williamson, S. J., and L. Kaufman, 1989, "Advances in neuromagnetic instrumentation and studies of spontaneous brain activity," Brain Topogr. **2**, 129–139.
Williamson, S. J., M. Pelizzone, Y. Okada, L. Kaufman, D. B. Crum, and J. R. Marsden, 1985, "Five channel SQUID installation for unshielded neuromagnetic measurements," in *Biomagnetism: Applications & Theory,* edited by H. Weinberg, G. Stroink, and T. Katila (Pergamon, New York), pp. 46–51.
Williamson, S. J., G. L. Romani, L. Kaufman, and I. Modena, 1983, Eds., *Biomagnetism: An Interdisciplinary Approach,* Vol. 66 of *NATO Advanced Science Institutes Series. Series A: Life Sciences* (Plenum, New York).
Yamamoto, T., S. J. Williamson, L. Kaufman, C. Nicholson, and R. Llinás, 1988, "Magnetic localization of neuronal activity in the human brain," Proc. Natl. Acad. Sci. USA **85**, 8732–8736.
Yin, Y. Q., and P. R. Krishnaiah, 1987, "On some nonparametric methods for detection of the number of signals," IEEE Trans. Acoust. Speech Signal Process. **ASSP-35**, 1533–1538.
Zimmerman, J. E., 1977, "SQUID instruments and shielding for low-level magnetic measurements," J. Appl. Phys. **48**, 702–710.
Zimmerman, J. E., and A. H. Silver, 1966, "Macroscopic quantum interference effects through superconducting point contacts," Phys. Rev. **141**, 367–375.
Zimmerman, J. E., P. Thiene, and J. T. Harding, 1970, "Design and operation of stable rf-biased superconducting point-contact quantum devices and a note on the properties of perfectly clean metal contacts," J. Appl. Phys. **41**, 1572–1580.

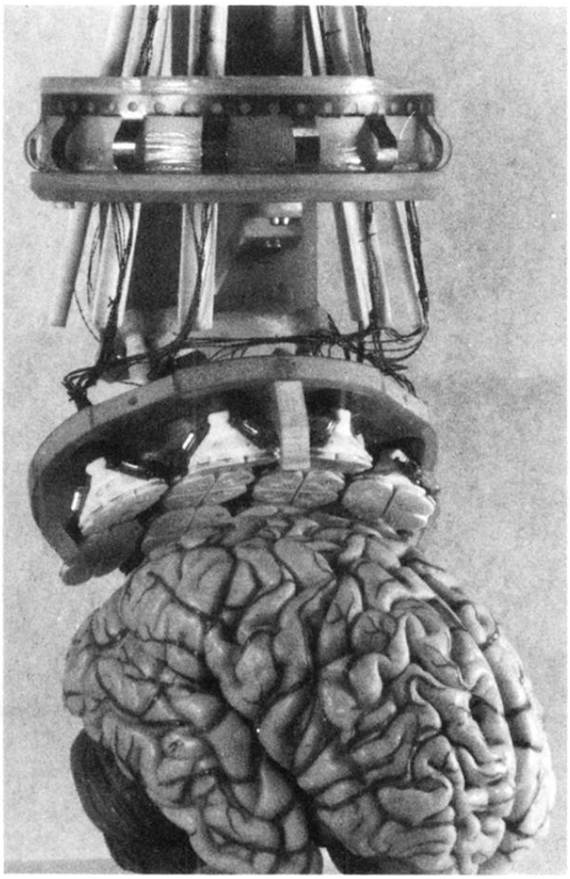

FIG. 10. The 24-channel neurogradiometer in Helsinki (Kajola *et al.*, 1989; Ahonen *et al.*, 1991) at a typical measurement distance above a model of the brain. During an actual measurement the instrument is, of course, in a helium dewar and the brain is inside the skull! The measuring head of the gradiometer and the tip of the dewar are concave so that they fit as closely as possible to the subject's head.

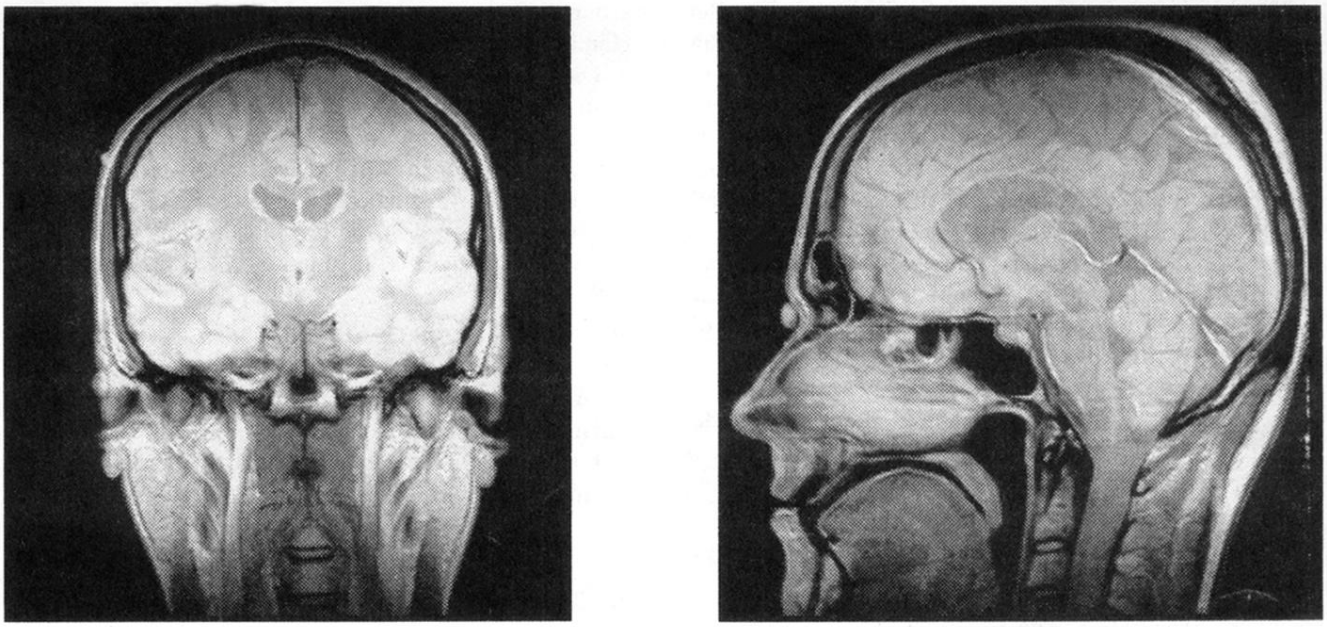

FIG. 13. Coronal section (a) at the level of the ears and sagittal (longitudinal) section (b) near the head midline of MRI's made on one of the authors; many important brain structures are clearly seen. The images were acquired with the Siemens 1.0-T MRI system at the Helsinki University Central Hospital.

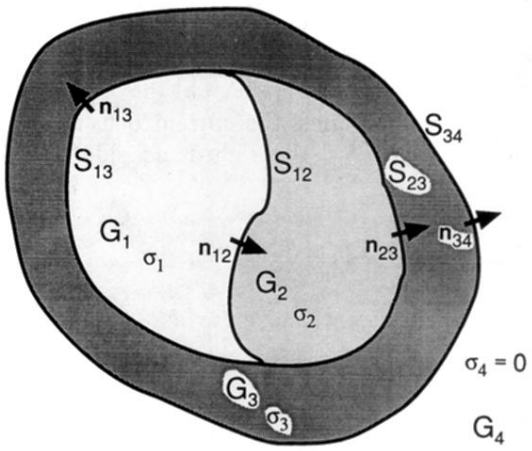


FIG. 18. Multicompartment conductivity model. Each region $G_i$ has uniform conductivity $\sigma_i$. Unit vectors normal to the surfaces are denoted by $\mathbf{n}_{ij}$.

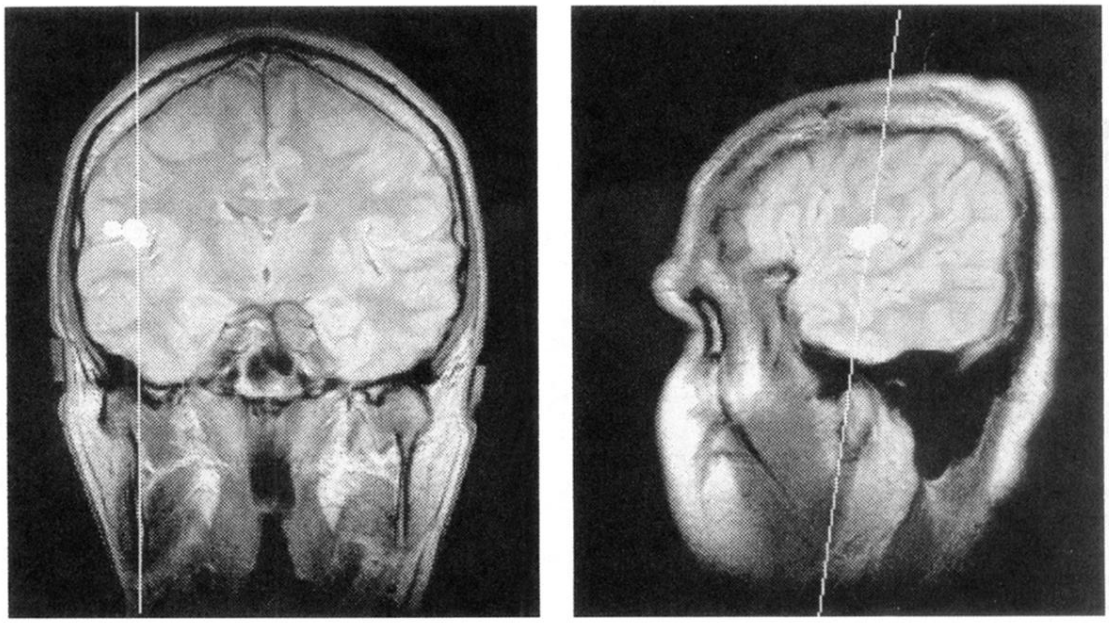

FIG. 20. Example of source locations superimposed on coronal (a) and sagittal (b) MR images. The white lines indicate transsection levels of the companion slice. The white dots show positions of equivalent current dipoles corresponding to the 100-ms deflections of auditory evoked responses in independent repeated measurements. All source locations are within a sphere of 15 mm in diameter (Hämäläinen, 1991).

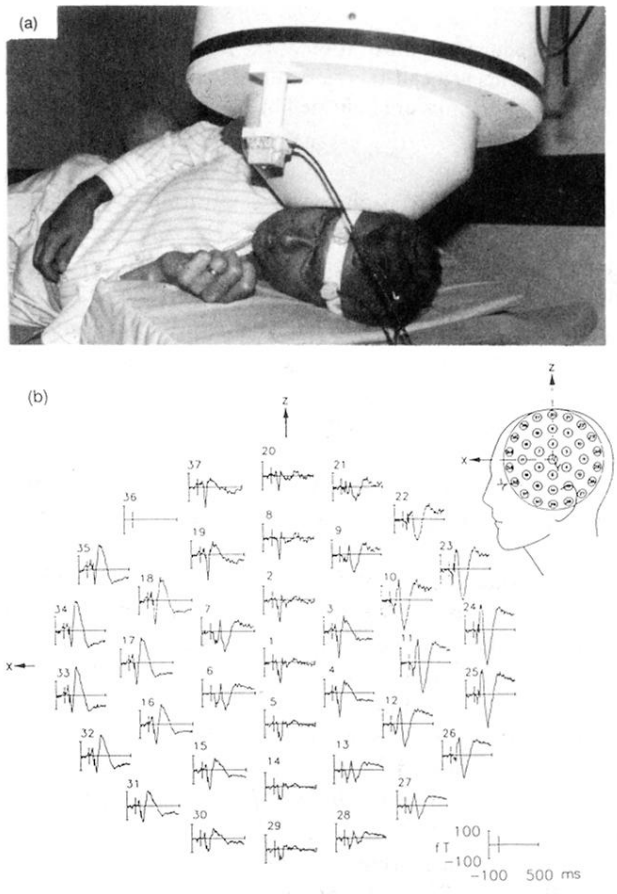


FIG. 39. BTi "Magnes" system. (a) 37-channel gradiometer of the BTi "Magnes" system in a measurement situation. The coils of the probe-position indicator, discussed in Sec. V.F.8, are attached to the subject's head and to the Dewar (courtesy of Biomagnetic Technologies, Inc.). (b) Auditory evoked responses to tone bursts recorded with the BTi 37-channel instrument over the left hemisphere. The approximate positions of the sensors are shown on the schematic head. The interstimulus interval was 4*s* and 384 responses were averaged. From Pantev *et al.* (1991).

| | | | | |
|---|---|---|---|---|
| Articulation: | *pa* | *pa* | *ka* | *pa* |
| Sound: | *pa* | *pa* | *pa* | *pa* |
| Perception: | *pa* | *pa* | *ta* | *pa* |

FIG. 49. Stimuli employed in the MEG study of the McGurk effect. For details, see text.

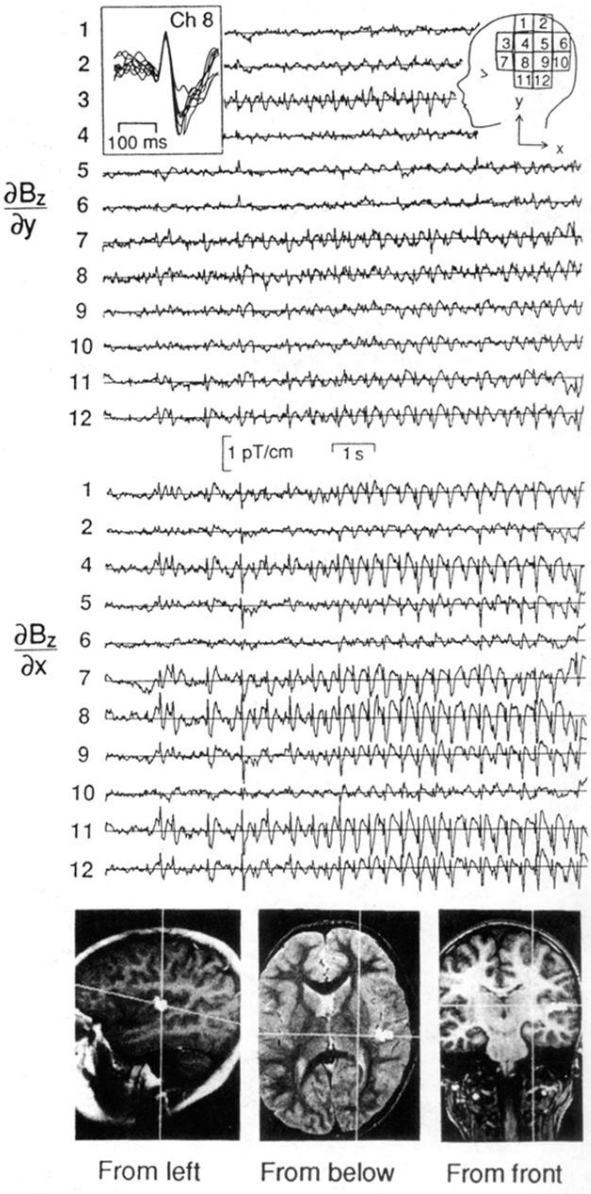


FIG. 63. Study of an epileptic patient. (Top) Examples of spontaneous spike-and-wave discharges from the left hemisphere of a child with the Landau–Kleffner syndrome. The upper traces reflect the vertical and the lower ones the horizontal gradients. The inset illustrates ten superimposed single spikes from the $y$ derivative of unit 8. (Bottom) ECD locations, shown by white squares of ten single spikes superimposed on MRI slices. The white lines indicate transsection levels of the two other slices. The $y$ channel of unit 3 was not functioning properly and is omitted. Modified from Paetau *et al.* (1991).

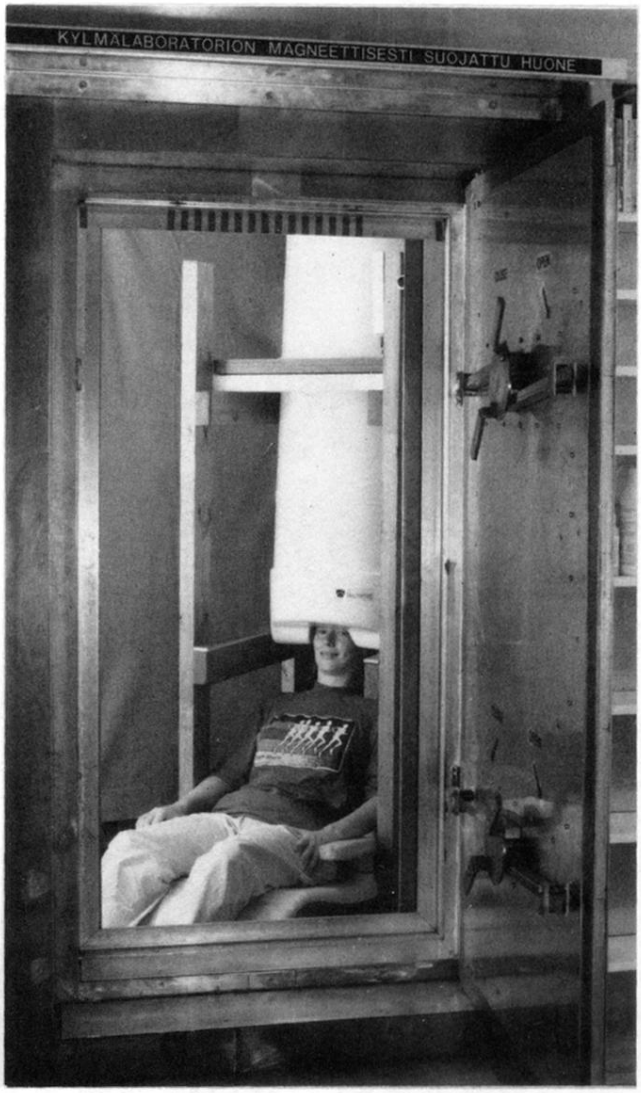


FIG. 9. View of the interior of the magnetically shielded room at the Helsinki University of Technology (Kelhä *et al.*, 1982). During actual measurements the subject is usually left alone and the double doors are closed. The room is a cube of 2.4-m inner dimensions with three layers of $\mu$-metal, which are effective for shielding at low frequencies of the external magnetic noise spectrum (particularly important for biomagnetic measurements), and three layers of aluminum, which attenuate very well the high-frequency band. The shielding factor is $10^3$–$10^4$ for low-frequency magnetic fields and about $10^5$ for fields of 10 Hz and above. The subject has her head inside a 122-channel neuromagnetometer (see Fig. 41 and Sec. V.F.6).